UNIVERSITY OF CALIFORNIA

Los Angeles

Experimental and Analytical Studies of Moderate Aspect Ratio Reinforced Concrete Structural Walls

A dissertation submitted in partial satisfaction of the

requirements for the degree Doctor of Philosophy

in Civil Engineering

by

Thien Anh Tran

2012

ABSTRACT OF THE DISSERTATION

Experimental and Analytical Studies of Moderate Aspect Ratio

Reinforced Concrete Structural Walls

by

Thien Anh Tran

Doctor of Philosophy in Civil Engineering

University of California, Los Angeles, 2012

Professor John W. Wallace, Chair

Experimental and analytical investigations were conducted to provide insight into the nonlinear cyclic response of moderate aspect ratio reinforced concrete structural walls. Five large-scale cantilever structural wall specimens, subjected to combined constant axial load and reversed cyclic lateral loading, were designed, constructed, instrumented, and tested. The wall specimens were designed to yield in flexure prior to loss of lateral load capacity. Primary test variables included aspect ratio (1.5 and 2.0), axial load level ($0.025A_g f_c^{'}$ and $0.10A_g f_c^{'}$), and wall shear stress level (between approximately 4 and $8\sqrt{f_c^{'}}$ psi).

Test results showed that substantial loss of lateral load capacity was observed for a variety of reasons, such as diagonal tension, diagonal compression, sliding shear, concrete crushing, and

buckling of vertical reinforcement. Test results also indicated that significant strength loss was impacted by wall aspect ratio, axial load level, and wall shear stress level. Although various failure modes were observed for five wall specimens, drift ratio at substantial loss of lateral load capacity was approximately 3.0% for all tests. The average contribution of nonlinear shear deformations to the top lateral displacement varied between approximately 20 and 50%, with lower values for the aspect ratio 2.0 walls.

Modeling parameters recommended by ASCE 41-06 and FEMA 356, including effective flexural and shear stiffness values, deformation capacities, and residual strengths, are compared with the corresponding values derived from test results. Current modeling approaches, including both uncoupled (P-M and V independent) and coupled (interaction between P-M and V) models, were used to assess their ability to capture the measured responses for the moderate aspect ratio structural walls. The investigation indicates that both models overestimate lateral load capacity and lateral stiffness, but with notable differences. In general, results for the uncoupled models are less consistent with the test results, indicating that coupled models are needed to adequately capture the responses of moderate aspect ratio walls. The primary shortcoming of the coupled model was the lack of cyclic material models. The detailed response information obtained from the heavily instrumented walls tested in this study provide essential data to develop robust analytical models, including models that account for cyclic nonlinear shear-flexure interaction.

The dissertation of Thien Anh Tran is approved.

Scott J. Brandenberg

William S. Klug

Jian Zhang

John W. Wallace, Committee Chair

University of California, Los Angeles

2012

TABLE OF CONTENTS

LIST OF FIGURES

LIST OF TABLES

ACKNOWLEDGEMENTS

I would particularly like to express my gratitude to my research advisor, Professor John W. Wallace, for his invaluable guidance and support during my PhD studies at the University of California, Los Angeles. Special appreciation is extended to the members of the Doctoral Committee, Professors Scott J. Brandenberg, William S. Klug, and Jian Zhang for their insightful advice and comments.

This research was conducted with funding provided from the National Science Foundation under Grant NSF CMMI-0825347, and also in a collaboratory renovated by the National Science Foundation under Grant No. 0963183, which is an award funded under the American Recovery and Reinvestment Act of 2009 (ARRA). Further, my great appreciation goes to the Ministry of Education and Training of Vietnam for providing partial financial support for my PhD studies.

I would like to thank UCLA Senior Development Engineer Steve Keowen for his valuable help with specimen construction, strain gauge installation, and test setup. Special thanks are given to Dr. Alberto Salamanca for his support and assistance with specimen testing and data acquisition. Thanks also go to Senior Development Engineer Harold Kasper for his help with material testing.

Thanks are extended to laboratory assistants Christopher Hilson, Bradley Gerlick, Ryon Marapao, Kyle Weiland, Saul Garcia, Ian Wallace, Luis Herrera, Jesse Diaz, Felipe Cifelli, Khoi

Pham, and Gregg Schwartz for their help with specimen construction, test preparation and test completion.

Finally, I would like to thank my parents Tan Tran and Thanh T. Pham for their love and support throughout my life. Special thanks are reserved for my wife Duyen Pham for her understanding and support throughout my PhD studies. Her love and encouragement gave me the will to finish this work. I would also like to thank my little daughter Khanh Tran for her lovely smiles that always refresh my mind; she is the joy of our lives.

VITA

1998	B.S., Civil Engineering Danang University of Technology, University of Danang, Vietnam
2003	M.Eng., Structural Engineering University of Technology, Sydney Australia
1998-2008	Lecturer, Danang University of Technology, University of Danang, Vietnam
2008-2012	Graduate Student Researcher Department of Civil and Environmental Engineering University of California, Los Angeles
2011-2012	Teaching Assistant Department of Civil and Environmental Engineering University of California, Los Angeles

PUBLICATIONS AND PRESENTATIONS

Tran, T.A. and Wallace, J.W., "Experimental Study of the Lateral Load Response of Moderate Aspect Ratio Reinforced Concrete Structural Walls", Report No. UCLA SGEL 2012/XX, Department of Civil and Environmental Engineering, University of California, Los Angeles (In preparation).

Kolozvari, K.; Tran, T.; Wallace, J.; and Orakcal, K., "Modeling of Cyclic Shear-Flexure Interaction in Reinforced Concrete Structural Walls," Proceedings of the 15th World Conference on Earthquake Engineering, Lisbon, Portugal, September 2012, (Accepted for publication and presentation).

Tran, T.A. and Wallace, J.W., "Experimental Study of Nonlinear Flexural and Shear Deformations of Reinforced Concrete Structural Walls", Proceedings of the 15th World Conference on Earthquake Engineering, Lisbon, Portugal, September 2012, (Accepted for publication and presentation).

Tran, T.A. and Wallace, J.W., "Nonlinear Cyclic Response of Special Structural Walls", Student Researcher Symposium, Quake Summit 2012, Boston, Massachusetts, July 2012.

Tran, T.A. and Wallace, J.W., "Behavior and Response of Moderate-Aspect Ratio RC Structural Walls", Quake Summit 2012, Boston, Massachusetts, July 2012.

Tran, T.A. and Wallace, J.W., "Experimental Study of Shear-Flexure Interaction for Moderate-Aspect Ratio Special Structural Walls", CEE 249 - Selected Topics in Structural Engineering, Mechanics, and Geotechnical Engineering, University of California, Los Angeles, January 2012.

CHAPTER 1 INTRODUCTION

1.1 General

Reinforced concrete structural walls are very effective in resisting lateral loads, such as wind loads or seismic loads, due to their high strength and stiffness. Practically, using structural walls to resist lateral loads in high seismic regions is very common (Eberhard and Meigs, 1995). Designing a structural wall such that it remains elastic during a strong earthquake is not feasible; therefore, inelastic deformations are expected. The distribution and magnitude of the inelastic deformations within the building depend on the attributes of the structural system. Well-established provisions incorporating thorough knowledge of the wall strength, stiffness, and deformation behavior for the given system, geometry, materials, and loading are necessary to design efficient structural walls.

A significant body of experimental work is available to address these issues for slender cantilever walls with rectangular or flanged cross sections (e.g., Thomsen and Wallace, 1995 and 2004; Wood and Sittipunt, 1996; Wight et al., 1996; Adebar et al., 2007; Brueggen, 2009; Brueggen and French, 2010; Johnson, 2010; Birely et al., 2008 and 2010), as well as slender walls with openings (Ali and Wight, 1990 and 1991; Taylor et al., 1998). Based on these works, as well as prior work, provisions for special structural walls have been updated in ACI 318. Examples include the introduction of displacement-based design for walls into ACI 318-99 and the application of strut-and-tie models, which are effective for design of walls with openings

(Appendix A, ACI 318-11). Despite this significant body of work, damage observed in recent tests and earthquakes (Wallace, 2012) indicate that important issues remain unresolved.

A significant number of tests have been also conducted for squat walls which have aspect ratio smaller than 1.5 (Barda et al., 1977; Paulay et al., 1982; Gupta and Rangan, 1998; Kabeyasawa and Hiraishi, 1998; Salonikios et al., 1999 and 2000; Hidalgo et al., 2002; Palermo and Vecchio, 2002; Massone, 2006; Farvashany et al., 2008; Orakcal et al., 2009). These low-rise walls are usually governed by shear. Again, despite this significant body of prior work, significant issues remain, such as the role of axial load on wall shear strength and the deformation capacity of low-rise walls.

For moderate-aspect ratio walls, i.e., walls with aspect ratios between about 1.5 and 2.5, nonlinear shear behavior may be significant, leading to lower effective elastic stiffness and modestly lower flexural strength (Massone et al., 2006), and larger longitudinal concrete compressive strains at wall boundaries (Wallace, 2007); however, these factors are not typically considered in analysis and design. Although a relatively significant number of tests have been conducted on moderate-rise walls (see Cardenas et al., 1973; Oesterle et al., 1976 and 1979; Corley et al., 1981; Wood, 1990; Pilakoutas and Elnashai, 1995; Kabeyasawa and Hiraishi, 1998; Mickleborough et al., 1999; Salonikios et al., 1999 and 2000; Zhang and Wang, 2000; Dazio et al., 2009), the prior tests generally focused on the determination of wall shear strength, typically without axial load, and in many cases, provided web reinforcement or boundary transverse reinforcement that did not satisfy ACI 318-83 (and later) requirements for special structural walls. In addition, and significantly, deformations associated with the test setup were not always

measured and detailed instrumentation was rarely provided; therefore, the measured results may not be reliable for assessing deformation responses associated with different damage states (e.g., cracking, yielding, spalling, buckling, strength loss, residual strength, loss of vertical load carrying capacity). The lack of sufficient and precise instrumentation inhibits the development of robust analysis and design tools to enable development and use of more elegant and cost-effective approaches, such as Performance-Based Seismic Design.

Several macroscopic analytical models have been developed to describe the inelastic response of reinforced concrete structural walls (Kabeyasawa et al., 1983; Vulcano and Bertero, 1987; Vulcano et al., 1988; Fischinger et al., 1990 and 1992; Vulcano, 1992; Kabeyasawa, 1997; Orakcal et al., 2004; Orakcal and Wallace, 2006). Although these models have been shown to reasonably capture global (lateral load versus top displacement) and local (plastic hinge rotation), the responses are uncoupled, i.e., flexural and shear behaviors are described independently. Observations from tests conducted by Oesterle et al. (1976 and 1979) and Thomsen and Wallace (1995) clearly show coupling between nonlinear flexural responses and nonlinear shear responses for walls tested with aspect ratios of 2.4 and 3.0, respectively. Various analytical models have been proposed to incorporate "shear-flexure interaction" (Colotti, 1993; Elwood, 2002; Orakcal et al., 2006; Massone et al., 2006 and 2009; Jiang and Kurama, 2010; Beyer et al., 2011). The models proposed by Colotti (1993), Massone et al. (2006, 2009), and Jiang and Kurama (2010) are based on the use of fiber-type models with interaction incorporated with a biaxial material model (e.g., modified compression field approach), whereas the approach proposed by Beyer et al. (2011) determines the degree of interaction from an empirical relations derived from test results. The model by Elwood (2002) is derived from column data and has not

been validated for structural walls. In general, relatively little model validation has been reported. Massone et al. (2006, 2009) provide comparisons for monotonic model results with test results for the aspect ratio (shear span ratio) three tests conducted by Thomsen and Wallace (2004) and the shear span ratio 0.5 tests conducted by Massone (2006). Monotonic results are compared because the model does not include cyclic material models. Jiang and Kurama (2010) provide comparisons between model results and 2.4 aspect ratio wall tests; however, the comparisons included are for lateral load versus top displacement and for boundary longitudinal reinforcement strain, both of which are not overly sensitive to shear-flexure interaction (Orakcal and Wallace, 2006). Additional test results are needed to enable more robust model validation studies. These tests should be conducted on walls expected to have modest to significant shear-flexure interaction, include the detailed instrumentation needed to enable validation on global and local responses, and include data to assess damage associated with significant loss of lateral load capacity and loss of axial load carrying capacity.

1.2 Objectives

Five large-scale reinforced concrete shear wall specimens were designed, constructed, and tested. The test specimens were designed to yield in flexure prior to reaching their shear capacity; however, nonlinear shear deformations were expected to contribute significantly to lateral displacement responses. Walls subjected to both high and moderate shear stresses were tested, and all walls were detailed to satisfy ACI 318-11 S21.9.6.4 requirements for special boundary elements. The test specimens were heavily instrumented to obtain detailed response information, as well as to provide data for development and validation of analytical models, including models

that account for cyclic nonlinear shear-flexure interaction. Primary test variables were wall aspect ratio, wall axial stress, and wall shear stress. The main objectives of this study are to.

(1) provide insight into the nonlinear cyclic response of moderate aspect ratio structural walls where shear deformations impact the global behavior, including damage states, failure modes, and load versus deformation relations.

(2) determine the distribution and magnitude of deformations due to flexure, shear, shear sliding at the wall-foundation interface, and anchorage.

(3) provide detailed response information for development and validation of analytical models, including models that account for cyclic nonlinear shear-flexure interaction.

(4) investigate the ability of the wall elements to sustain axial loads following the onset of lateral strength degradation; i.e. testing will be continued until loss of axial load capacity is observed.

(5) determine and compare flexural and shear stiffness and backbone relations of moderate-aspect ratio walls to those of current standard provisions.

(6) compare test results with analytical results using current uncoupled and coupled (shear-flexure interaction) models

1.3 Organization

This dissertation is divided into nine chapters and three appendices. Chapter 1 presents an overview of the research program, identifies the key issues, and summarizes primary objectives. Chapter 2 summarizes relevant research on slender and moderate aspect ratio reinforced concrete structural walls, including research work related to instrumentation of walls, and research on

interaction of axial-flexure-shear responses. Design methodology and details of test specimens are provided in Chapter 3, whereas Chapter 4 introduces test setup and design of foundation blocks for wall specimens. Chapter 5 summarizes instrumentation and data acquisition, testing protocols, construction procedures, and as-tested mechanical properties of concrete and reinforcement. Experimental results for wall specimens, including summary of test results, experimentally observed damage and behavior, lateral load versus top total displacement responses, profiles of total displacement over the wall height, average horizontal strain, and wall vertical growth are presented in Chapter 6. Chapter 7 analyzes components of lateral displacement, including flexural, shear, and sliding shear deformations, as well as slip and extension of boundary longitudinal reinforcement. Chapter 8 presents flexural and shear stiffness, backbone relations, and comparison of test and model results using uncoupled and coupled models for monotonic loading. Finally, research findings are summarized and recommendations are provided in Chapter 9.

CHAPTER 2 LITERATURE REVIEW

This chapter summarizes prior research on slender and moderate aspect ratio reinforced concrete structural walls, including research related to instrumentation configurations needed to measure flexural and shear deformations and research associated with modeling shear-flexure interaction.

2.1 Slender and Moderate Aspect Ratio Reinforced Concrete Structural Walls

Cardenas et al. (1973) summarized experimental results of thirteen cantilever shear walls with rectangular cross sections, including four 3.36 aspect ratio, two 1.92 aspect ratio, and seven 1.0 aspect ratio wall specimens tested at the laboratories of the Portland Cement Association. The primary objectives of this research were to provide background and supporting documentation for the ACI 318-71 code provisions related to assessing flexural and shear strengths of structural walls. Test specimens with aspect ratios of 3.36 or 1.92 were subjected to combined constant axial load, which was either 0.06 or $0.07A_g f_c^{'}$, and monotonic quasi-static lateral loading. These walls had identical rectangular cross-section of 3×75 in. (76×1905 mm) and were provided with the horizontal web reinforcement ratio of 0.27%, which was just above the minimum of 0.25% required by the provisions of Section 11.16 of the 1971 ACI 318 Building Code. Concrete compressive strengths were between 5,900 and 7,420 psi (40.7 and 51.2 MPa), while the reinforcement yield strengths ranged from 60,000 to 70,000 psi (414 to 483 MPa). The results of the study showed that the code provisions could predict satisfactorily the flexural and shear strengths of cantilever walls with rectangular cross sections. However, the test results indicated that special attention to detailing at wall boundaries was necessary to achieve significant

nonlinear deformations, i.e., ductility with stable energy dissipation, required to obtain satisfactory structural performance.

A comprehensive experimental research program, consisting of testing sixteen approximately 1/3 scale solid walls, was conducted by Oesterle et al. (1976 and 1979) to study the behavior of reinforced concrete shear walls for earthquake resistant structures. The primary test variables included wall section shape (rectangular, barbell, and flanged), amount of flexural reinforcement, amount of web horizontal reinforcement, amount of boundary transverse reinforcement, axial load level (either zero or constant axial load, ranging from 0.06 to $0.13A_g f_c^{'}$), concrete strength (between 3,165 and 7,775 psi; or 21.8 and 53.6 MPa), and load history (monotonic and reversed cyclic lateral loading). All wall specimens had the aspect ratio of 2.4, and were 4 in. (102 mm) thick, 75 in. (1.91 m) long, and 15 ft. (4.57 m) tall. The barbell cross section walls had 12 in. (305 mm) square boundary columns, whereas the flanged cross section walls had 4 in. (102 mm) thick and 36 in. (914 mm) long flanges at both ends of the wall web. Longitudinal boundary reinforcement ratios varied from 1.1 to 4.4%. Vertical and horizontal web reinforcement ratios ranged from 0.25 to 0.31% and from 0.31 to 1.38%, respectively. The reinforcement yield strengths varied between 59.5 and 74.2 ksi (410 and 512 MPa).

The results of the research program indicated that the shear stress level had a significant impact on the behavior of shear walls. For walls with maximum shear stresses less than $3.0\sqrt{f_c^{'}}$ psi ($0.25\sqrt{f_c^{'}}$ MPa), inelastic performance was governed by buckling of flexural reinforcement and

crushing of core concrete. For walls with maximum shear stresses larger than $7.0\sqrt{f_c'}$ psi ($0.58\sqrt{f_c'}$ MPa), web crushing limited the wall nonlinear deformation capacity. It also was concluded that the decrease in nominal shear stress led to the increase in wall ductility and the contribution of shear deformations within the hinge region to the total wall top displacement was significant. Furthermore, shear distortions within the hinge region were coupled to flexural rotations, where increasing shear distortions occurred with increasing flexural deformations within the hinge regions. The study also revealed that using web horizontal reinforcement beyond the requirements by the 1971 ACI Building Code did not substantially improve wall strength or ductility in cases where web crushing occurred. Inelastic deformation capacities of the walls were increased substantially by use of stiff boundary elements or confinement reinforcement within the hinge region of the wall. It also was shown that for flexure-controlled walls, strength and deformation capacity of walls subjected to reversed cyclic loading were less than similar walls subjected to monotonic loading, although the impact of reversed cyclic loading was not as significant for walls governed by web crushing failure (Corley et al., 1981). All wall specimens reached top lateral displacements in excess of 1.5% drift. However, these specimens were not heavily-instrumented, so detailed response information of wall specimens were not recorded.

Thomsen and Wallace (1995 and 2004) tested four relatively slender cantilever shear walls with 3.0 aspect ratio at the Structural Laboratory at Clarkson University. These approximately one-quarter scale structural walls, including two walls with rectangular and two walls with T-shaped cross-sections, were 4 in. (102 mm) thick, 4 ft. (1.22 m) long, and 12 ft. (3.66 m) tall. The flange

of T-shaped walls also had a cross-section of 4×48 in. (102 mm $\times$ 1.22 m). All test specimens were subjected to an axial load of around $0.1A_g f_c^{'}$ and reversed cyclic, quasi-static lateral load. Transverse reinforcement at the wall boundaries was determined using a displacement-based design approach and was varied slightly in an attempt to produce different failure modes. The concrete compressive strengths ranged from 4,156 to 8,462 psi (28.7 to 58.3 MPa) while the reinforcing steel yield strengths ranged from 63 to 65 ksi (434 to 448 MPa). Test results showed that the walls reached lateral top displacements in excess of 2% of the wall height. It also was concluded that shear deformations contributed approximately 20 to 30% to the first story total lateral displacement (Massone and Wallace, 2004), but less than 5% to the top lateral displacement. This research program proved that detailing using a displacement-based approach was a powerful and flexible tool for design of reinforced concrete structural walls; a displacement-based design approach for assessing detailing requirements at boundaries of slender structural walls was introduced into ACI 318-99 based primarily on this research (see Wallace, 1994; Wallace, 1995; Wallace and Thomsen, 1995).

Pilakoutas and Elnashai (1995) conducted tests of six cantilever walls with aspect ratio of 2.0. Reversed cyclic lateral load was applied to these 1/2.5 scale rectangular walls; however, no axial load was applied. All specimens were 60 mm (2.4 in.) thick, 0.6 m (23.6 in.) long, and 1.2 m (47.2 in.) tall. Boundary longitudinal reinforcement ratio was approximately 3%. Web vertical and horizontal reinforcement ratios varied from 0.31 to 0.47%, satisfying the minimum of 0.25% required by ACI 318-11 provisions; however, boundary transverse reinforcement did not meet the requirement from ACI code provisions for special boundary elements. Concrete with

compressive strength ranging from 31.8 to 45.8 MPa (4.6 to 6.7 ksi), and reinforcing steel with yield strength ranging from around 400 to 550 MPa (58 to 80 ksi) were used for the test specimens. Various failure modes were observed in this study, depending mainly on the amount and distribution of web horizontal reinforcement. Maximum lateral drift ratios of approximately 2% were reached for all specimens prior to substantial loss of lateral load capacity, with a majority of the energy dissipation due to flexural deformations, versus shear deformations. It also was noted that wall strength and deformation were not substantially affected by horizontal web reinforcement in excess of the amount required, supporting the findings of the PCA tests. Vertical growth of the wall occurred mainly after flexural yielding due to irrecoverable strains accumulated mostly within the plastic hinge zone.

Mickleborough et al. (1999) investigated structural walls subjected to combined constant axial load (between 0.07 to $0.17A_g f_c^{'}$) and monotonic lateral loading. Six rectangular walls, including two 2.0 and two 1.5 aspect ratio walls, with cross-sections of 125 by 750 mm (4.9 by 29.5 in.) were tested; however, no boundary elements existed in these specimens. Web vertical and horizontal reinforcement ratios were 1.17 and 0.39%, respectively. The concrete compressive strengths ranged from 29.5 to 57.3 MPa (4.3 to 8.3 ksi) whereas the steel yield strengths were approximately 460 MPa (67 ksi). The main purpose of this testing program was to further develop the effective stiffness method from a full-scale beam testing program (Ning, 1998) and to enable the prediction of the lateral flexural deflections of structural walls under service loads.

Salonikios et al. (1999 and 2000) investigated the validity of design provisions of Eurocode 8 (EC8) and ACI 318-95 for cyclic loading of reinforced concrete walls. Eleven approximately 1/2.5 scale wall specimens with rectangular cross sections of 10×120 cm (3.9×47.2 in.) were tested, including six with 1.5 aspect ratio and the other five with 1.0 aspect ratio. All walls were detailed according to the provisions of EC8. Wall shear reinforcement consisted of orthogonal grids of web reinforcement, sometimes with additional cross-inclined bidiagonal bars. Axial load of either zero or $0.07 A_g f_c^{'}$, along with cyclic lateral load, were applied to the walls. Boundary vertical reinforcement ratio was either 1.3 or 1.7%, while web reinforcement ratios were either 0.28 or 0.56%. Concrete compressive strengths ranging from around 21.6 to 27.5 MPa (3.1 to 4.0 ksi) and reinforcement yield strengths ranging from 585 to 610 MPa (84.8 to 88.5 ksi) were used for the test specimens. The study indicated that the predictions of diagonal tension capacities from ACI 318 were higher than those from EC8, whereas the predictions of sliding shear capacities from EC8 were substantially underestimated. It also was concluded that use of bidiagonal bars intersecting at the wall-foundation block interface resulted in higher sliding shear capacities, while use of bidiagonal bars intersecting above the wall-foundation interface increased strength and energy dissipation capacity. Although the contributions of various deformations to total lateral displacement also were measured and analyzed to assess wall deformation and ductility, the simple instrumentation installed in the wall specimens inhibited the collection of sufficient and precise test data.

Dazio et al. (2009) performed cyclic tests on six half-scale reinforced concrete walls at the ETH Zurich. This research investigated the effects of the amount and ductility level of vertical

reinforcement on deformation response and failure mechanisms of structural walls. These specimens were 150 mm (5.9 in.) thick, 2.0 m (78.7 in.) long, and 4.56 or 4.52 m (15.0 or 14.8 ft.) tall, resulting in aspect ratios of 2.28 and 2.26, with axial load levels ranging from 0.051 to $0.128A_g f_c^{'}$. The concrete compressive strengths ranged from approximately 38 to 46 MPa (5.5 to 6.7 ksi) and the steel yield strengths varied from around 500 to 650 MPa (72.5 to 94.3 ksi). It was revealed from the study that wall deformation capacities decreased with low amount of longitudinal reinforcement, and this trend became more significant if using low ductility reinforcement. The results also showed that the ratios of shear to flexural displacements at the peaks of the cycles for all six specimens remained almost constant throughout the loading history and were in the range from approximately 5 to 15%. Test specimens constructed were typical for regions of moderate seismicity in Central Europe; therefore, their detailing did not meet the requirements for special structural walls from ACI 318-11 Code provisions.

Although a relatively large number of moderate-aspect ratio reinforced concrete structural walls have been tested, the tests have primarily focused on the investigation of wall flexural and shear strengths and in many cases, no axial load was applied and/or the requirements for special boundary elements from ACI 318-11 Code provisions were not satisfied. Furthermore, wall specimens and their test setup were not always well-instrumented, leading to the lack of sufficient and precise test data necessary for the development and validation of analytical models and the application of Performance-Based Seismic Design.

The instrumentation configuration used in research program described in subsequent chapters was influenced by results presented by Massone and Wallace (2004), which provided recommended practices associated with determining the relative contributions of flexural and shear deformations to inelastic lateral displacements. According to this paper, the common approach of using two diagonal LVDTs (Linear Variable Differential Transformers) to determine shear deformations tended to overestimate shear distortions in the wall yielding region by as much as 30%. This error can be minimized by using multiple pairs of vertical displacement transducers along two walls edges within the plastic hinge region. The study showed that use of 4 to 6 pairs of vertical displacement transducers would give reasonable results.

2.2 Interaction of Axial-Flexure-Shear Responses

Analytical modeling of reinforced concrete structural walls can be achieved by using either microscopic (detailed) or macroscopic (simplified) models. While microscopic models are based on a detailed description of geometry and local responses, macroscopic models are based on capturing overall wall behavior with acceptable accuracy. Micro-models, such as detailed nonlinear, three-dimensional, finite element models, can provide a refined and detailed local response; however, they usually require substantial computational effort. Therefore, macro-models are more practical and effective in analyzing and designing reinforced concrete structural systems because they are relatively simple to implement and can reduce significantly computational effort.

Several macroscopic models have been developed for analytical modeling of reinforced concrete shear walls. A simple approach, which was common prior to the late 1990's, was to use a beam-column element along the centroidal axis of the wall (Figure 2-1). This model includes a linear elastic beam-column with nonlinear rotational springs at the ends and in some cases nonlinear axial springs, with prescribed moment-rotation and force-deformation relationships, respectively. The drawbacks associated with this model include the inability to capture the variation of the neutral axis along the depth of the wall cross section, rocking of the wall, and interaction with the frame members connected to the wall, which are very important for inelastic response of the walls (Orakcal et al., 2006).

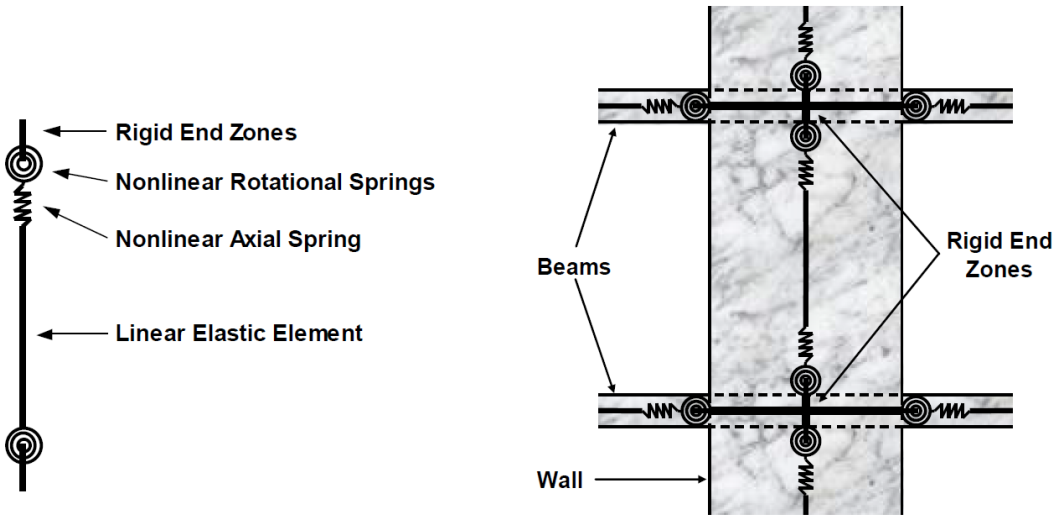

(a) Beam-column element (b) Model configuration

Figure 2-1 Beam-column element model (Orakcal et al., 2006)

Kabeyasawa et al. (1983) developed a three vertical line element model after examining experimental results of a full-scale seven-story reinforced concrete frame-wall building (Figure

2-2). The wall model included three vertical line elements with infinitely rigid beams at the top and bottom floor levels. Two outside vertical springs simulated the axial stiffness of wall boundaries, whereas the central vertical element combining vertical, horizontal, and rotational springs simulated the response of the wall web. In this study, an axial-stiffness hysteresis model was used to idealize the hysteretic behavior of the three vertical elements of the wall model under axial load reversals (Figure 2-3), whereas the origin-oriented hysteresis model was used to describe the force-deformation relationships for the rotational and horizontal springs of the central vertical element, which present the flexural and shear behavior of the wall, respectively (Figure 2-4).

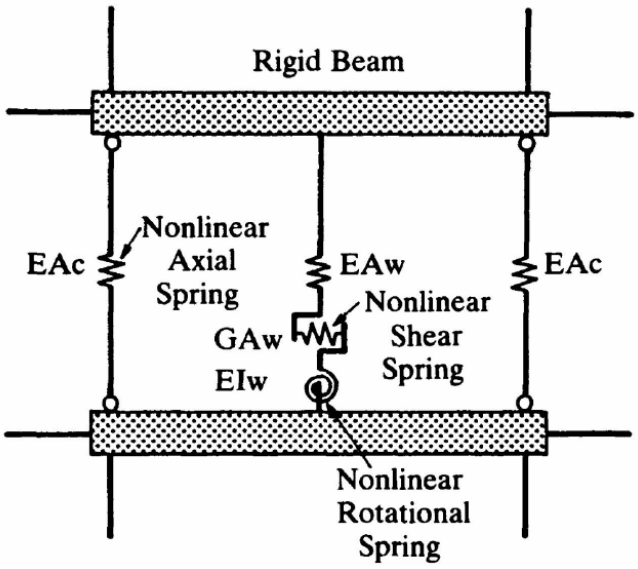

Figure 2-2 Three vertical line element model (Kabeyasawa et al., 1983)

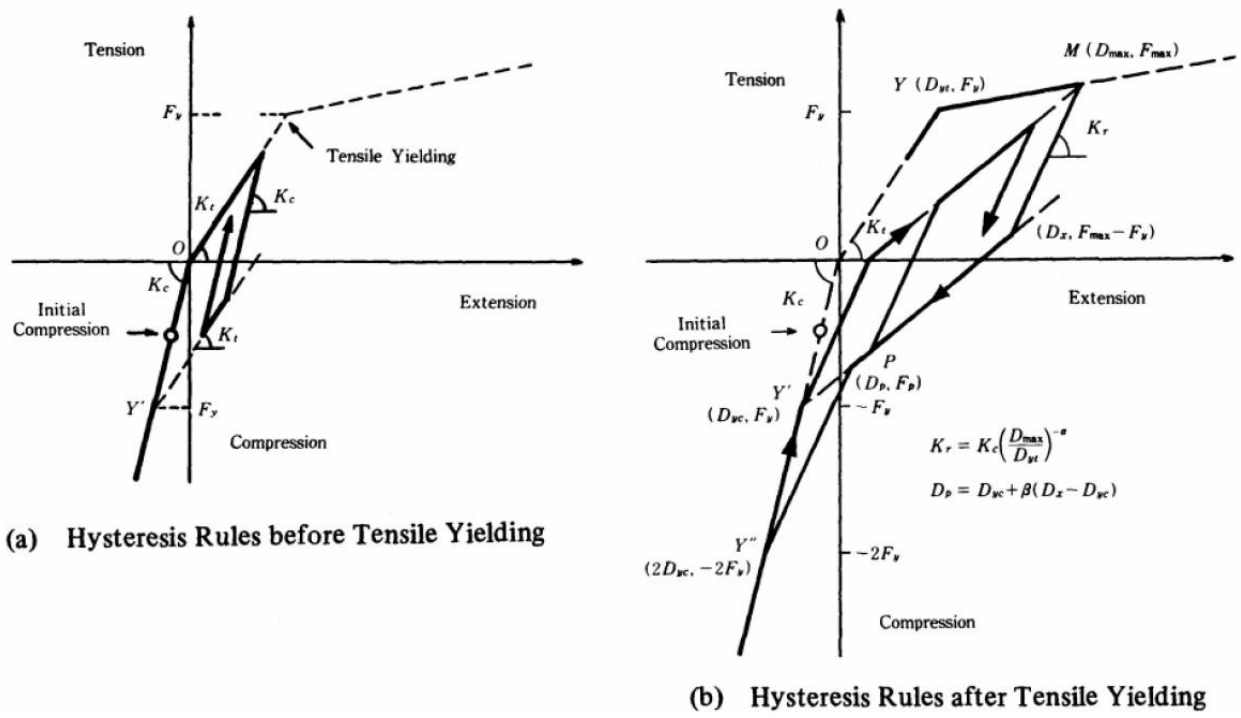

Figure 2-3 Axial-stiffness hysteresis model (Kabeyasawa et al., 1983)

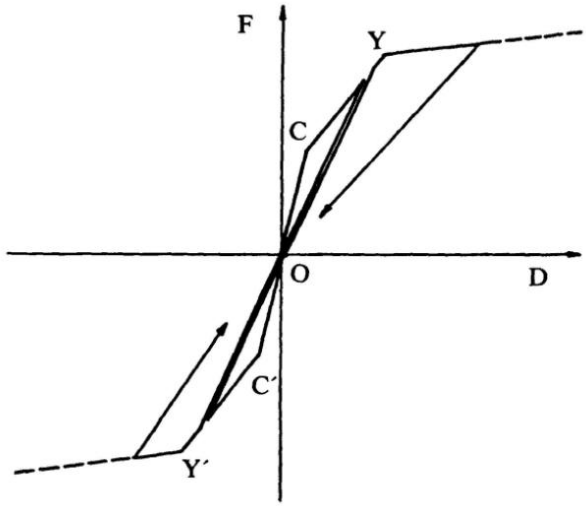

Figure 2-4 Origin-oriented hysteresis model (Kabeyasawa et al., 1983)

Notes: F = Force, D = Displacement, C = Cracking, Y = Yielding

Although relatively simple, the three vertical line element model incorporates main features of the experimentally observed behavior, i.e., shifting of the neutral axis along the wall cross-section during loading, rocking of the wall, and the interaction of the wall with surrounding frames. However, its disadvantages come from the difficulties in defining the properties and physical representation of the springs representing the panel, and the incompatibility between the panel and the boundary columns (Vulcano and Bertero, 1987; Orakcal et al., 2006).

The Multiple-Vertical-Line-Element-Model (MVLEM) (Vulcano et al., 1988) is a robust macro-model for walls (Figure 2-5). In this model, a structural wall is represented as a stack of MVLEs, which are placed on top of each other. The flexural response of each MVLE is simulated by a series of parallel uniaxial elements connected to infinitely rigid beams at the top and bottom levels, which enforces the plane section assumption. While the two outside elements model the axial stiffness k_1 and k_n of the boundary columns, the interior elements (at least two), with axial stiffness k_2, …, k_{n-1}, represent globally the axial and flexural stiffness values of the central panel. The horizontal spring, with stiffness k_H and hysteretic behavior described by the origin-oriented hysteresis model, simulated the nonlinear shear response of the wall element. This horizontal spring placed at the center of rotation of each MVLE at a height of ch. Flexural and shear behaviors are incorporated but uncoupled in the MVLEM.

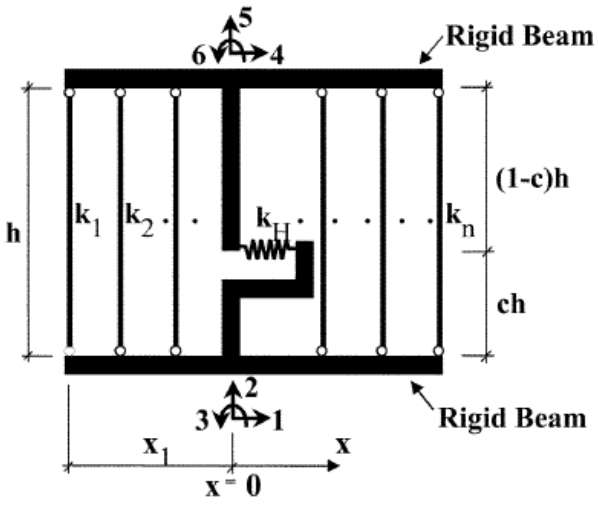

Figure 2-5 MVLEM element (Vulcano et al., 1988)

The MVLEM was improved by implementing refined hysteretic uniaxial, cyclic constitutive models instead of simplified force-deformation rules to predict the inelastic response of slender RC walls (Orakcal, 2004; Orakcal et al., 2004; Orakcal and Wallace, 2006). The stress-strain model for reinforcing steel was the hysteretic model of Menegotto and Pinto (1973), as extended by Filippou et al. (1983) to include isotropic strain hardening effects (Figure 2-6). For concrete, the hysteretic constitutive model by Chang and Mander (1994) was used in the study (Figure 2-7). This constitutive model has the capabilities of addressing important features such as the hysteretic behavior in both cyclic compression and tension, the progressive degradation of stiffness of the unloading and reloading curves for increasing values of strain, and the effects of confinement, tension stiffening and gradual crack closure.

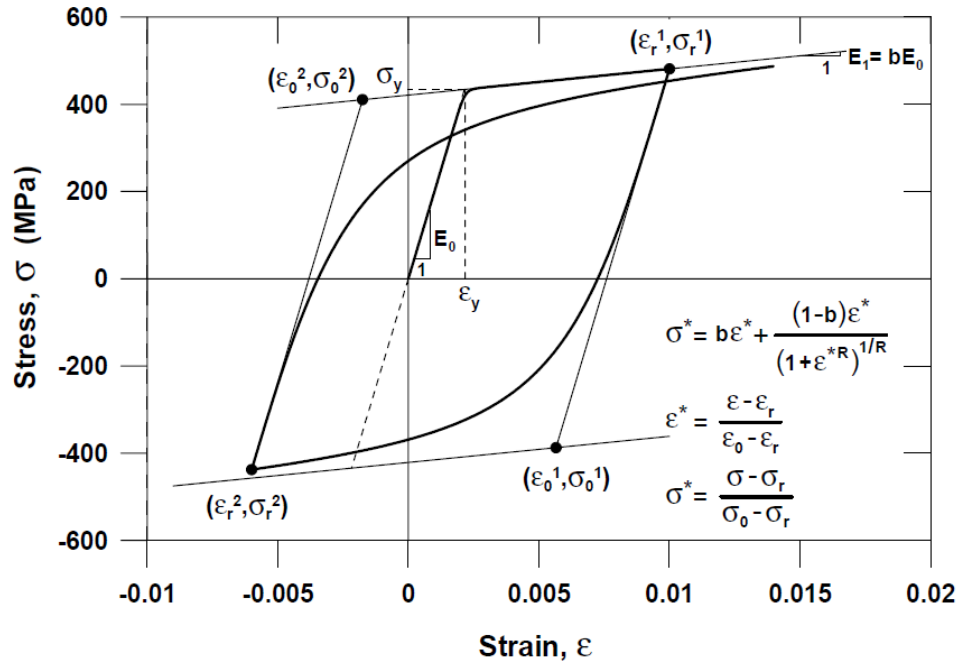

(a) Governing equation

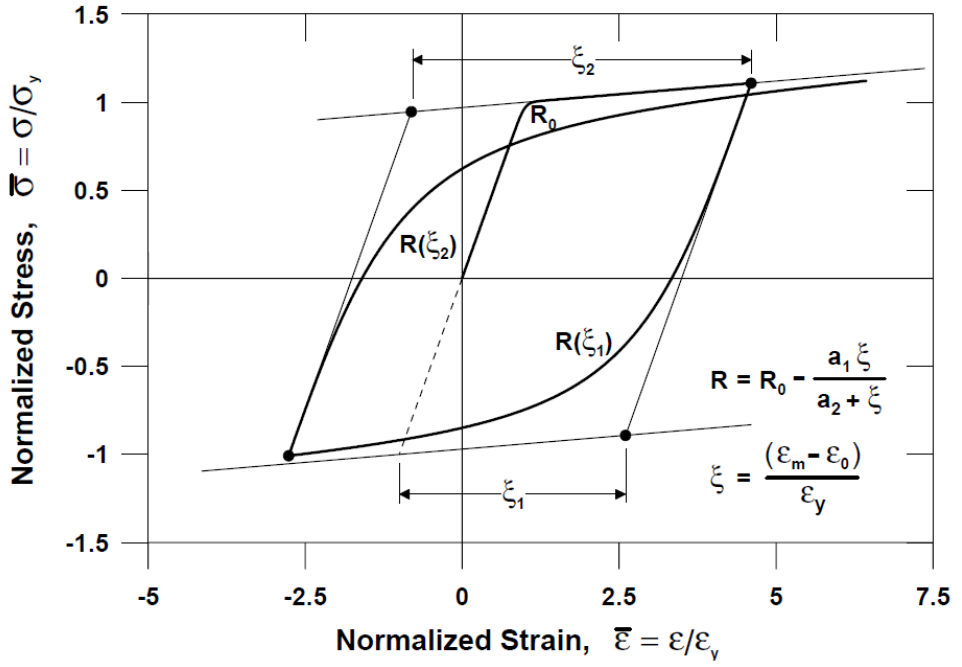

(b) Degradation of cyclic curvature

Figure 2-6 Steel, uniaxial, cyclic, constitutive model (Orakcal et al., 2004)

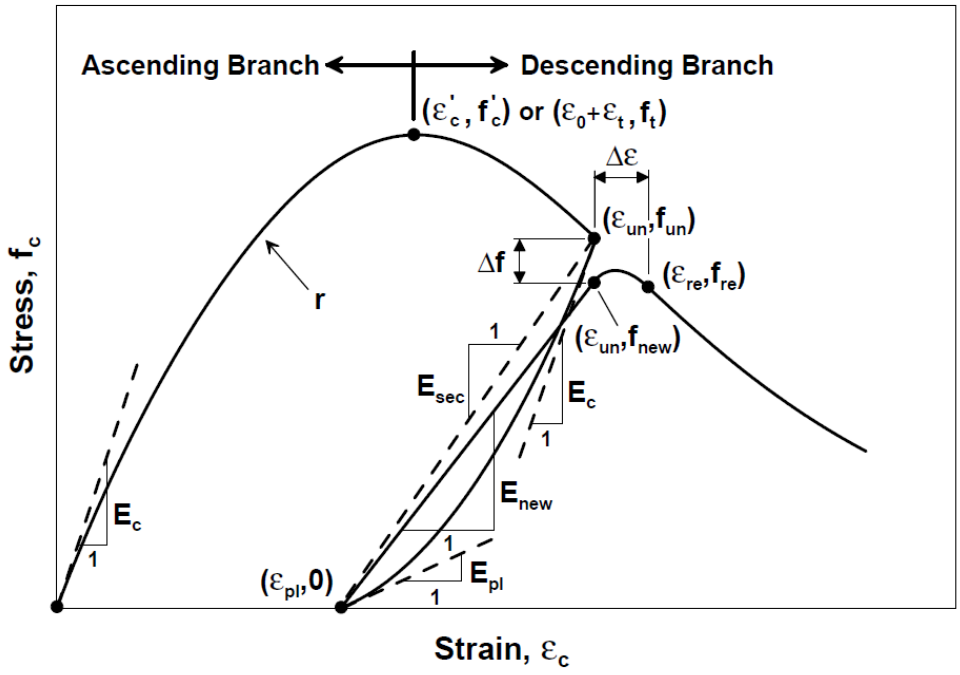

(a) Hysteretic parameters

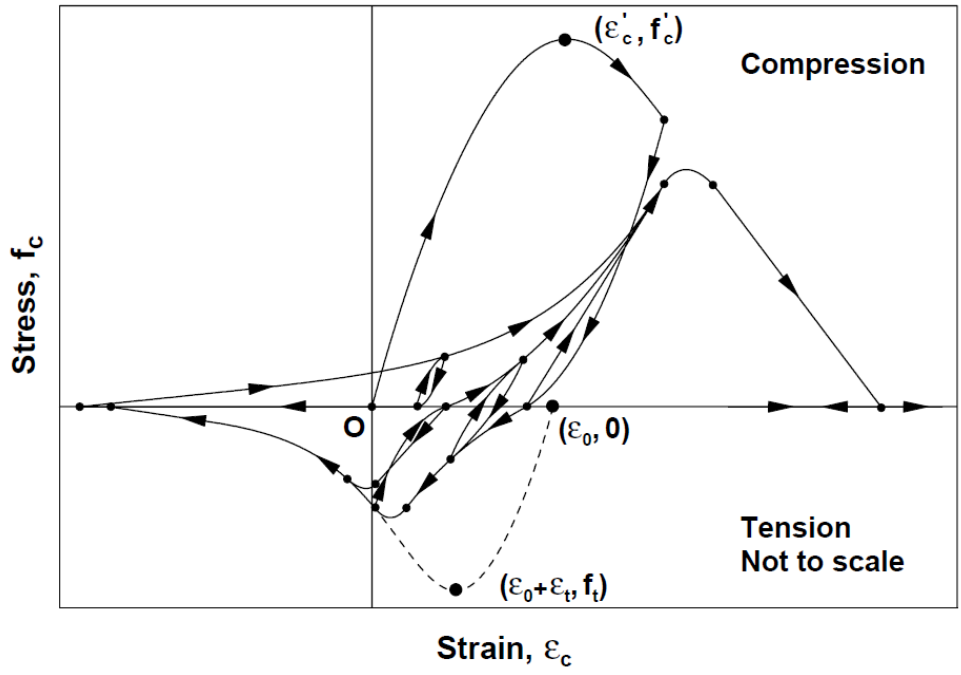

(b) Hysteresis in compression and tension

Figure 2-7 Concrete, uniaxial, cyclic constitutive model (Orakcal et al., 2004)

The models mentioned are capable of capturing axial, flexural and shear responses; however, axial-flexural behavior (P-M interaction) and shear behavior (V) are uncoupled. Other macroscopic models have been developed for flexural-shear interaction. Colotti (1993) modified the MVLEM by replacing the horizontal shear spring with a shear panel model. The response of this shear panel model is determined by using the Modified Compression-Field Theory (MCFT) (Vecchio and Collins, 1986). The stress state in the vertical direction is considered uniform and is assumed to be related to the value of the vertical strain corresponding to the centroidal axis of the panel. The effective shear area of the wall is defined as the product of the panel thickness and the length between the geometrical axes of two boundary elements. Although there are some discrepancies between the results from the model and test data, this model proved to be more accurate than other macro-models. The main shortcoming is that it is incapable of coupling flexural and shear behavior, since it can couple axial and shear responses only.

Massone et al. (2006, 2009) proposed a macroscopic model that can couple flexural and shear responses in reinforced concrete walls. This model, based on the methodology developed by Petrangeli et al. (1999) and Petrangeli (1999), incorporates reinforced concrete panel behavior into the MVLEM (Figure 2-8).

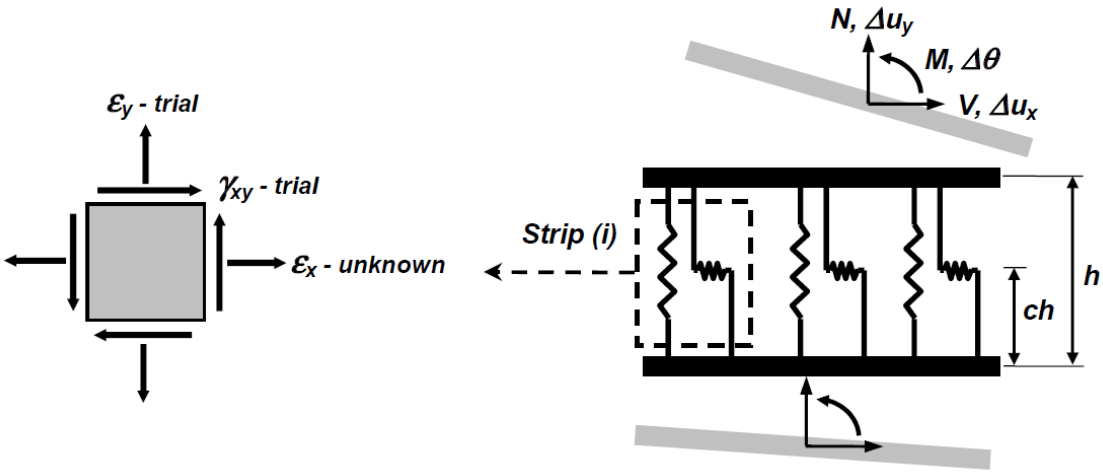

Figure 2-8 Coupled model element (Massone et al., 2006 and 2009)

The model formulation involves modifying the MVLEM by assigning a shear spring to each uniaxial element, which is then treated as a reinforced concrete panel element subjected to membrane actions that are in-plane uniform normal and shear stresses. As a result, the coupling between flexural and shear responses is incorporated at the fiber level. A rotating-angle modeling approach, such as the Modified Compression-Field Theory (MCFT) (Vecchio and Collins, 1986) or the Rotating-Angle Softened-Truss-Model (RA-STM) (Hsu, 1993; Belarbi and Hsu, 1994 and 1995; Pang and Hsu, 1995), can be used to model the constitutive panel behavior. It is assumed that plane section remains plane; strain fields acting on concrete and reinforcing steel are identical, i.e., perfect bond between reinforcement and concrete; shear strains are uniformly distributed along the length of the wall; principle stress and strain directions are identical; and dowel action on reinforcement is neglected, i.e., no shear stress on reinforcing steel. Material constitutive models for reinforcing steel and for concrete in tension and compression used in this

study are presented in Figures 2-9, 2-10, and 2-11, respectively. The comparison of the analytical results with the test data shows that the model is able to incorporate the shear-flexure interaction (Orakcal et al., 2006) and provides improved comparisons with experimental results compared to results produced with an uncoupled model; however, the model does not account for cyclic behavior.

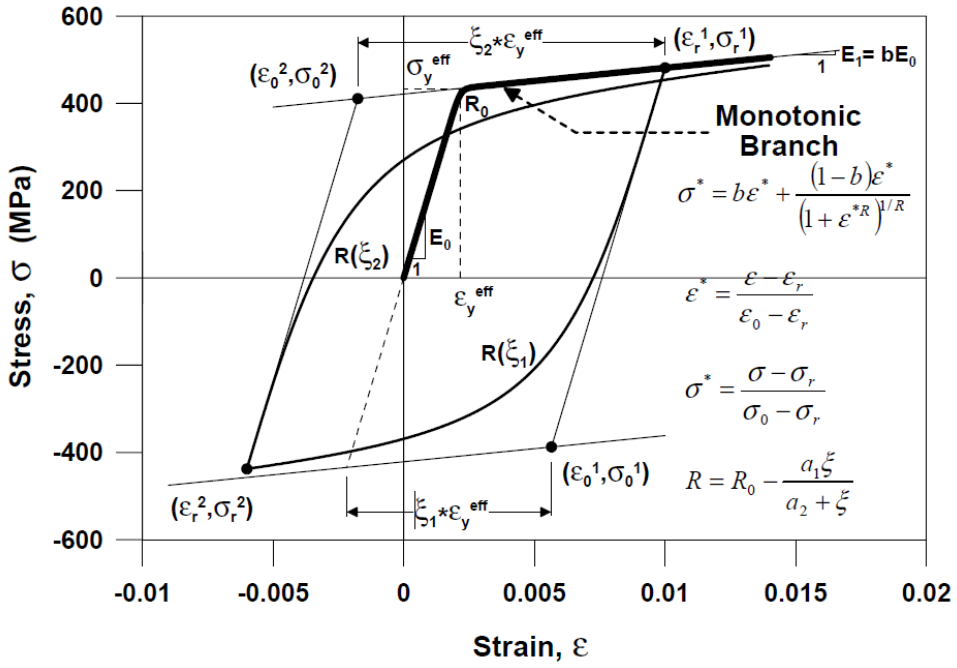

Figure 2-9 Constitutive model for reinforcing steel (Massone et al., 2006)

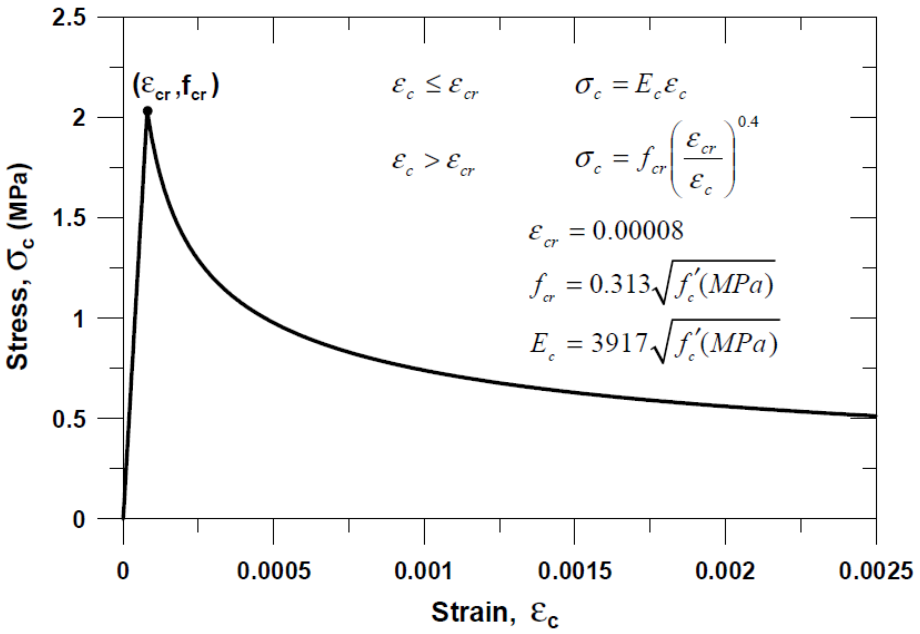

Figure 2-10 Constitutive model for concrete in tension (Massone et al., 2006)

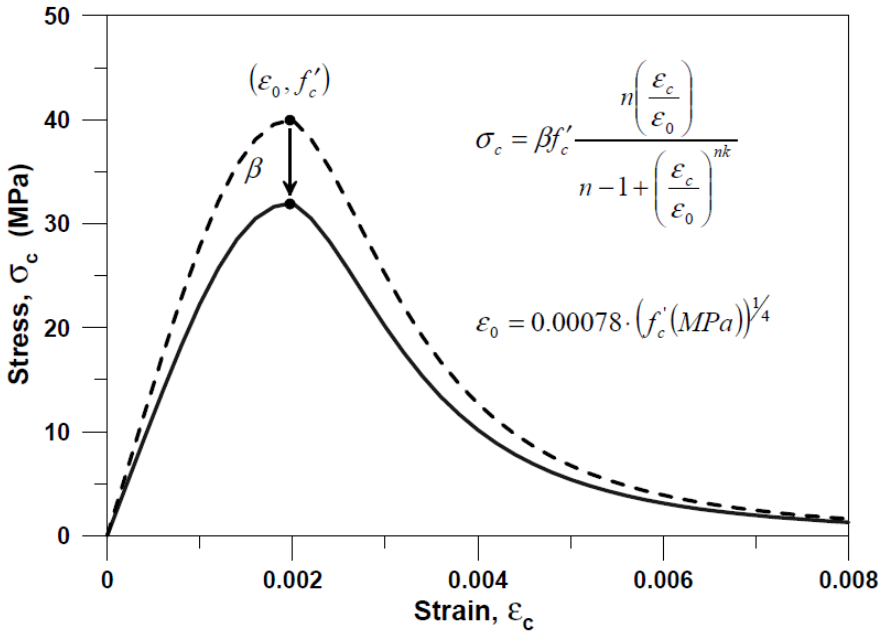

Figure 2-11 Constitutive model for concrete in compression (Massone et al., 2006)

Beyer et al. (2011) accounted for shear-flexure interaction by studying the ratio of shear-to-flexural deformations. Based on assessing experimental results from quasi-static reversed cyclic tests on 34 slender reinforced concrete shear walls, the following empirical relation between shear and flexural deformations was derived.

$$\frac{\Delta_s}{\Delta_f} = C_1 \frac{\varepsilon_m}{\phi \tan\beta} \frac{1}{H_n}$$

where ε_m and ϕ are respectively the mean axial strain and curvature of the wall over the height of the plastic hinge length, assumed to be constant; β is the cracking angle outside the fanned crack pattern, as observed within the plastic zone, where cracks are approximately parallel; H_n is the distance from the top of the wall to the centroid of the plastic hinge; C_1 is the correction factor, accounting for the reduction of the ratio $\frac{1}{\tan\beta}$ compared to $\frac{1}{\tan\overline{\beta}}$, where $\overline{\beta}$ is the cracking angle representative of the fanned crack pattern within the plastic zone, and estimated to be 1.5 from the database considered in the study.

The comparison of the shear-to-flexural deformations predicted with the above equation and by experimental results is presented in Figure 2-12. As can be seen from the figure, although the empirical relation between shear and flexural deformations is capable of capturing the general trend of the Δ_s/Δ_f ratio, a significant variation between the model and test results still exists.

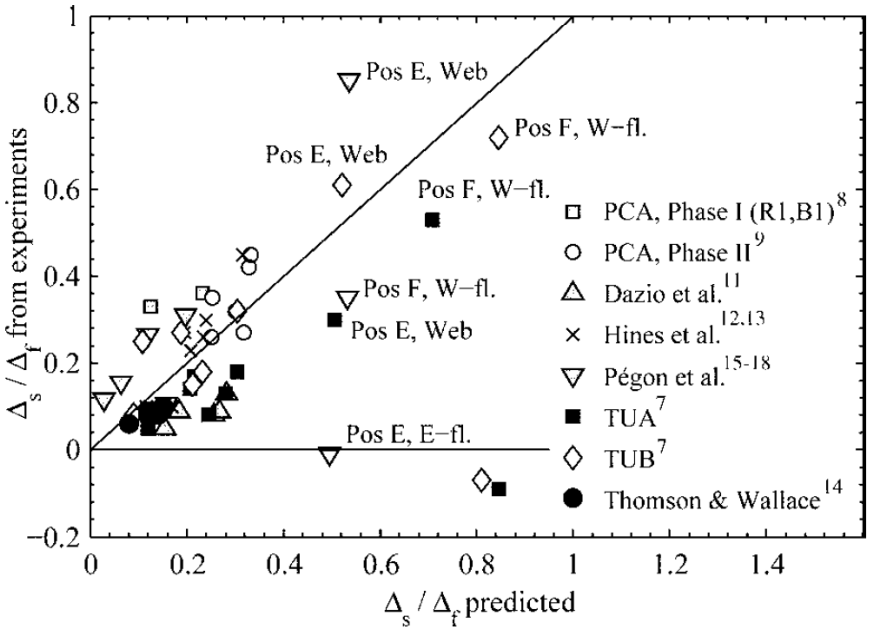

Figure 2-12 Comparison of predicted Δ_s/Δ_f ratios to ones determined from experimental measurements (Beyer et al., 2011)

One of the primary goals of this comprehensive research program is to design and test five large-scale moderate-aspect ratio reinforced concrete shear walls where nonlinear shear deformation contributes significantly to the lateral deformations and there is significant interaction between flexural and shear responses. The specimens are detailed to satisfy requirements for special structural walls from ACI 318-11 Code provisions. A combined constant axial load and reversed cyclic loading was applied to the walls. Shear stress level also was considered as one of the primary test variables. Detailed instrumentation was applied to the walls to provide detailed response information, including various lateral displacement components (flexural displacement, slip and extension of longitudinal boundary reinforcement, shear displacement, and sliding shear displacement at the wall-foundation block interface). Instrumentation also was provided to

measure rotation and sliding of the foundation block and any test setup deformations. Investigation on failure modes, wall strength, stiffness, and deformation capacity, as well as crack patterns and crack widths are performed to provide insight into the nonlinear cyclic response of moderate aspect ratio reinforced concrete structural walls. Analytical results using current uncoupled and coupled models of flexural and shear behavior also are assessed for their ability to predict the inelastic response of this type of reinforced concrete structural walls.

CHAPTER 3 DESIGN OF WALL SPECIMENS

This chapter provides details of the design methodology used for the test specimens and summarizes the test program for five reinforced concrete structural wall specimens. Cross-section and reinforcement details of five wall specimens are also described.

3.1 Text Matrix

Five large-scale cantilever structural wall specimens, subjected to combined constant axial load and reversed cyclic lateral loading, were designed and tested. The wall specimens were designed to yield in flexure prior to loss of lateral load strength. Primary test variables included aspect ratio (1.5 and 2.0), which is equal to the shear-span ratio for these tests, axial load level ($0.025A_g f_c^{'}$ and $0.10A_g f_c^{'}$), and wall shear stress level (between approximately 4 and $8\sqrt{f_c^{'}}$ psi). The ratio of the lateral load corresponding to nominal moment capacity over the nominal shear strength determined using ACI 318-11 S21.9.4, $V@M_n/V_n$, varied from 0.79 to 0.88 for design material strengths, or very close to the design limit (for $\phi = 1.0$). A primary objective of the test program was to assess the impact of wall aspect ratio, level of axial stress, and average shear stress on the wall failure modes and deformation capacity at significant loss of lateral load capacity, including various components of lateral displacement, as well as the influence of these parameters on loss of axial load capacity.

The five cantilever wall specimens are 6 in. (150 mm) thick and 48 in. (1.22 m) long, with lateral load applied at either 72 in. (1.83 m) or 96 in. (2.44 m) above the wall-foundation block

interface. Axial load levels of $0.10A_g f_c^{'}$ and $0.025A_g f_c^{'}$ were applied to the first four specimens and the fifth specimen, respectively, where A_g is the gross cross-section area of shear walls and $f_c^{'}$ is the specified concrete compressive strength. Average shear stress of all specimens was designed in the range from 3.8 to $7.8\sqrt{f_c^{'}}$ psi (0.32 to $0.65\sqrt{f_c^{'}}$ MPa). The ratios of horizontal and vertical web reinforcement of each wall, ρ_t and $\rho_{l,}$ respectively, were equal and varied from 0.0027 to 0.0073, which exceeded the 0.0025 minimum required by ACI 318-11. The ratio of the area of vertical boundary reinforcement to the area of the boundary element ρ_b varied between 0.0323 and 0.0711. Transverse reinforcement at wall boundaries satisfied ACI 318-11 S21.9.6.4 requirements of special structural walls.

Table 3-1 shows the test matrix for all five shear wall specimens. Identifiers were established for the test specimens, e.g., specimen **RW-A20-P10-S38**, describes a **R**ectangular **W**all with **A**spect ratio of **2.0** under design axial load **P** of **10**% $A_g f_c^{'}$, and design average **S**hear stress of **3.8** $\sqrt{f_c^{'}}$ psi ($0.32\sqrt{f_c^{'}}$ MPa).

For actual concrete and reinforcement properties, which are presented briefly in Section 5.4 and in more detail in Appendix C, the ratio $V@M_n/V_n$ ranged from 0.79 to 0.91, which is very closed to its range for design material strengths, i.e. from 0.79 to 0.88. The axial load level using actual material strengths (see Table 3-1) ranged from $0.064A_g f_c^{'}$ to $0.077A_g f_c^{'}$ for the first four

walls and $0.016A_g f_c^{'}$ for the fifth wall, respectively. Similarly, the actual wall shear stress varied from 3.6 to $7.0\sqrt{f_c^{'}}$ psi (0.30 to $0.58\sqrt{f_c^{'}}$ MPa).

Table 3-1 Wall specimen attributes

Test No.	Specimen code	$\frac{h_w}{l_w}$	$\rho_t = \rho_l$ (%)	ρ_b (%)	$\frac{P^{des}}{A_g f_c^{'des}}$	$\frac{V@M_n^{des}}{V_n^{des}}$	$\frac{V@M_n^{des}}{A_{cv}\sqrt{f_c^{'des}}}$	$\frac{P^{act}}{A_g f_c^{'act}}$	$\frac{V@M_n^{act}}{V_n^{act}}$	$\frac{V@M_n^{act}}{A_{cv}\sqrt{f_c^{'act}}}$
1	RW-A20-P10-S38	2.0	0.27	3.23	0.10	0.80	3.8	0.073	0.81	3.6
2	RW-A20-P10-S63		0.61	7.11	0.10	0.88	6.3	0.073	0.91	6.1
3	RW-A15-P10-S51	1.5	0.32	3.23	0.10	0.80	5.1	0.077	0.83	4.9
4	RW-A15-P10-S78		0.73	6.06	0.10	0.84	7.8	0.064	0.85	7.0
5	RW-A15-P2.5-S64		0.61	6.06	0.025	0.79	6.4	0.016	0.79	5.8

Notes: $\frac{h_w}{l_w}$ is the aspect ratio; ρ_t is the horizontal web reinforcement ratio; ρ_l is the vertical web reinforcement ratio; ρ_b is the boundary longitudinal reinforcement ratio; $\frac{P^{des}}{A_g f_c^{'des}}$ is the design axial load ratio using the design axial load and design compressive strength of concrete; $\frac{V@M_n^{des}}{V_n^{des}}$ is the design ratio of the lateral load corresponding to the nominal moment capacity over the nominal shear strength using the specified compressive strength of concrete and specified yield strength of reinforcement; $\frac{V@M_n^{des}}{A_{cv}\sqrt{f_c^{'des}}}$ is the design ratio of the average shear stress at nominal moment capacity over $\sqrt{f_c^{'}}$ using the design material strengths, for $f_c^{'}$ in psi unit;

$\frac{P^{act}}{A_g f_c^{'act}}$ is the actual axial load ratio using the actual axial load and actual compressive strength of concrete; $\frac{V@M_n^{act}}{V_n^{act}}$ is the actual ratio of the lateral load corresponding to the nominal moment capacity over the nominal shear strength using the actual material strengths; $\frac{V@M_n^{act}}{A_{cv}\sqrt{f_c^{'act}}}$ is the actual ratio of the average shear stress at nominal moment capacity over $\sqrt{f_c^{'}}$ using the actual material strengths, for $f_c^{'}$ in psi unit.

3.2 Description of Test Specimens

Geometry and reinforcement used in the test specimens are described in this section. The foundation block of specimens will be described in Section 4.4 because the design of foundation blocks is impacted significantly by the laboratory test setup, i.e., the spacing and capacity of the strong floor anchors.

Cross-section and reinforcement details of the five wall specimens are shown in Figures 3-1 through 3-5. Concrete with specified compressive strength of 5,000 psi (34.5 MPa) was used for all specimens, including the wall and the foundation block. Concrete clear cover over boundary vertical reinforcement was selected to be greater than or equal to one vertical boundary bar diameter (either US #4, #5, or #6; 12.7, 15.9, or 19.1 mm); therefore, a maximum aggregate size of 3/8 in. (9.5 mm) was specified to limit problems associate with improper concrete consolidation.

All reinforcement used for wall specimens were deformed bars except for smooth bars used as boundary transverse reinforcement. Boundary longitudinal reinforcement for each wall consisted of eight, A706 Grade 60 (414 MPa), vertical bars (either #4, #5, or #6) . These longitudinal bars were continuous over the wall height and had heads at both of their ends. Headed bars were used to help avoid the congestion of reinforcement and to reduce anchorage lengths at the top of specimens. Web vertical and horizontal reinforcement were identical and included 6 mm-diameter bars, equivalent to #2 (6.4 mm) U.S. bars, and A615

Grade 60 (414 MPa) #3 (9.5 mm) bars. Deformed #2 bars are not produced in the U.S.; therefore, deformed 6mm-diameter bars, imported from Sweden and Australia, were used instead. 6 mm-diameter deformed bars from Sweden, denoted as D6a, had specified yield strength of 400 MPa (58 ksi) whereas 6 mm-diameter deformed bars from Australia, denoted as D6b, had specified yield strength of 500 MPa (72.5 ksi). Web reinforcement consisted of two curtains of either D6a bars, which were used for RW-A20-P10-S38 and RW-A15-P10-S51, or #3 bars, which were used for the other three specimens. A615 Grade 40 (276 MPa) #2 smooth bars with were used as boundary transverse reinforcement, which included one hoop and one cross-tie at each height level. All bars of each type (diameter) of reinforcement were produced from only one heat so that they had identical mechanical properties.

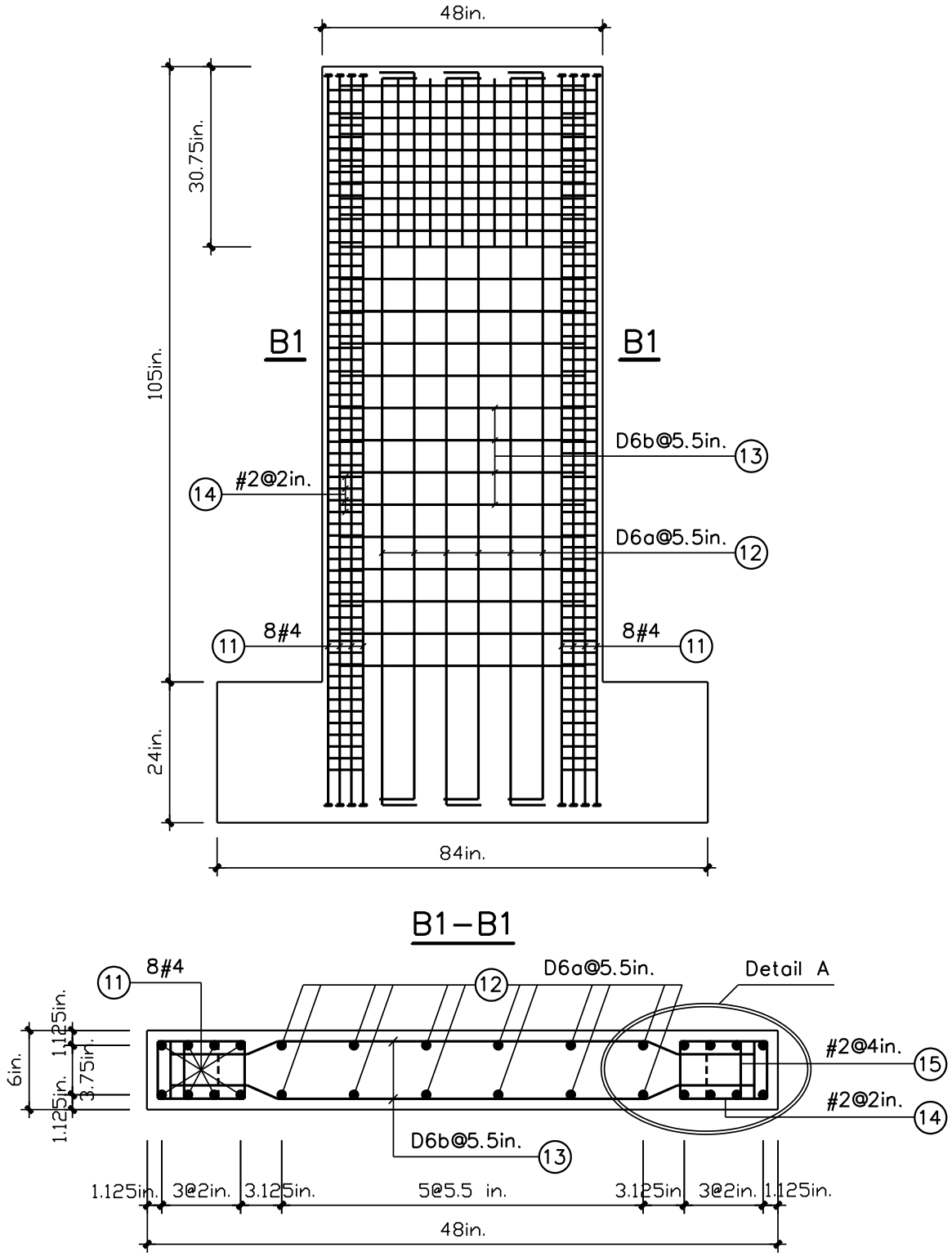

Figure 3-1 Reinforcement details for RW-A20-P10-S38

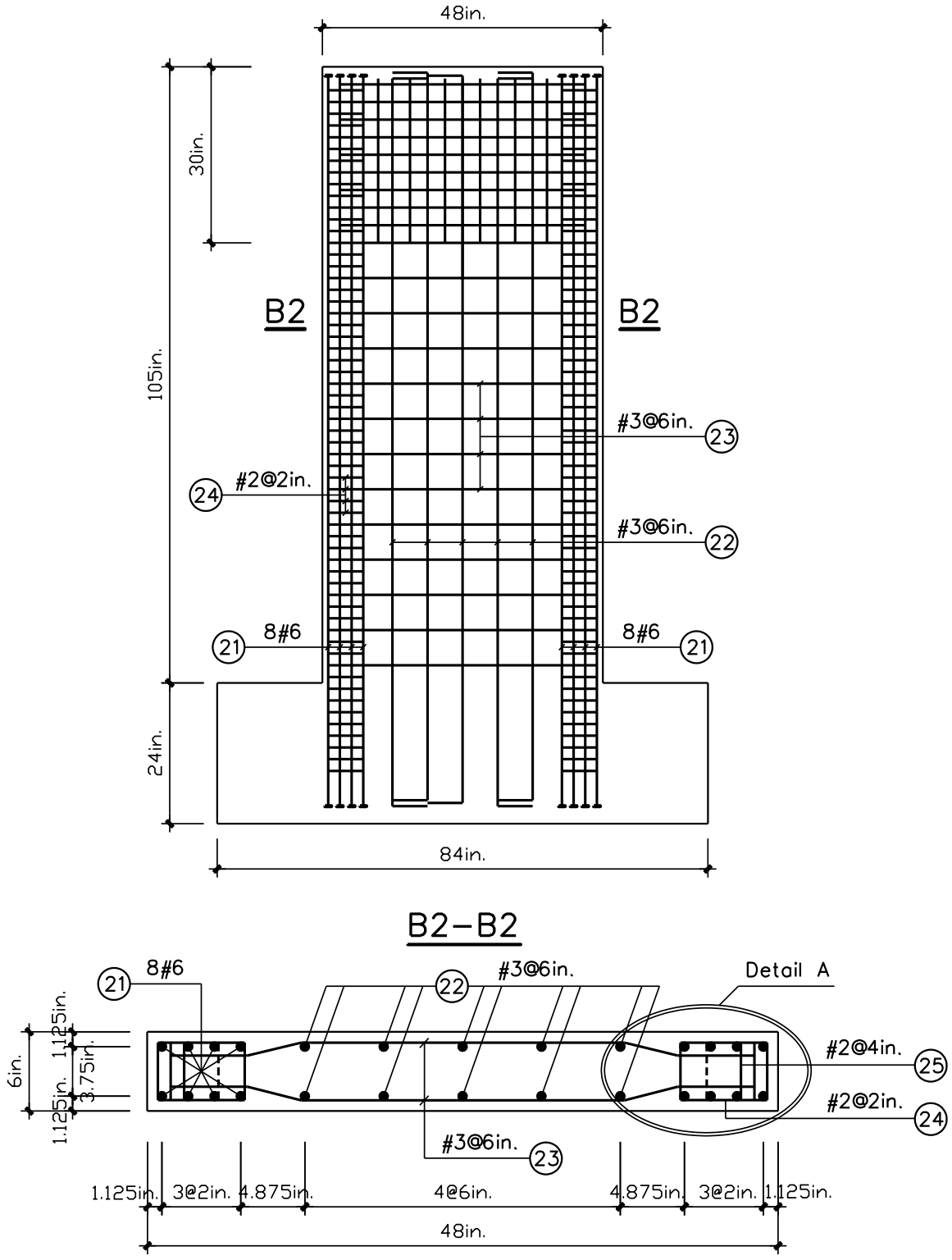

Figure 3-2 Reinforcement details for RW-A20-P10-S63

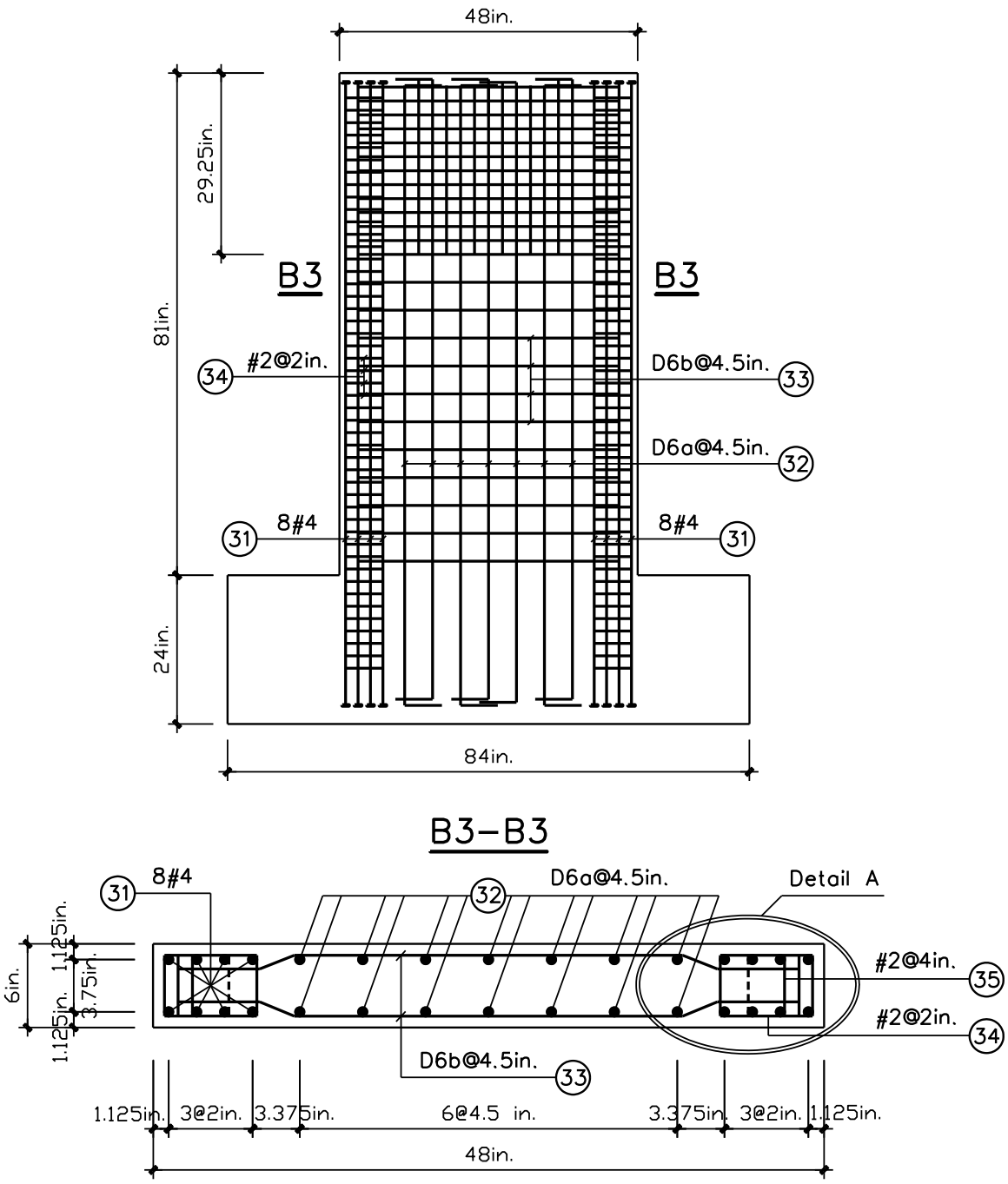

Figure 3-3 Reinforcement details for RW-A15-P10-S51

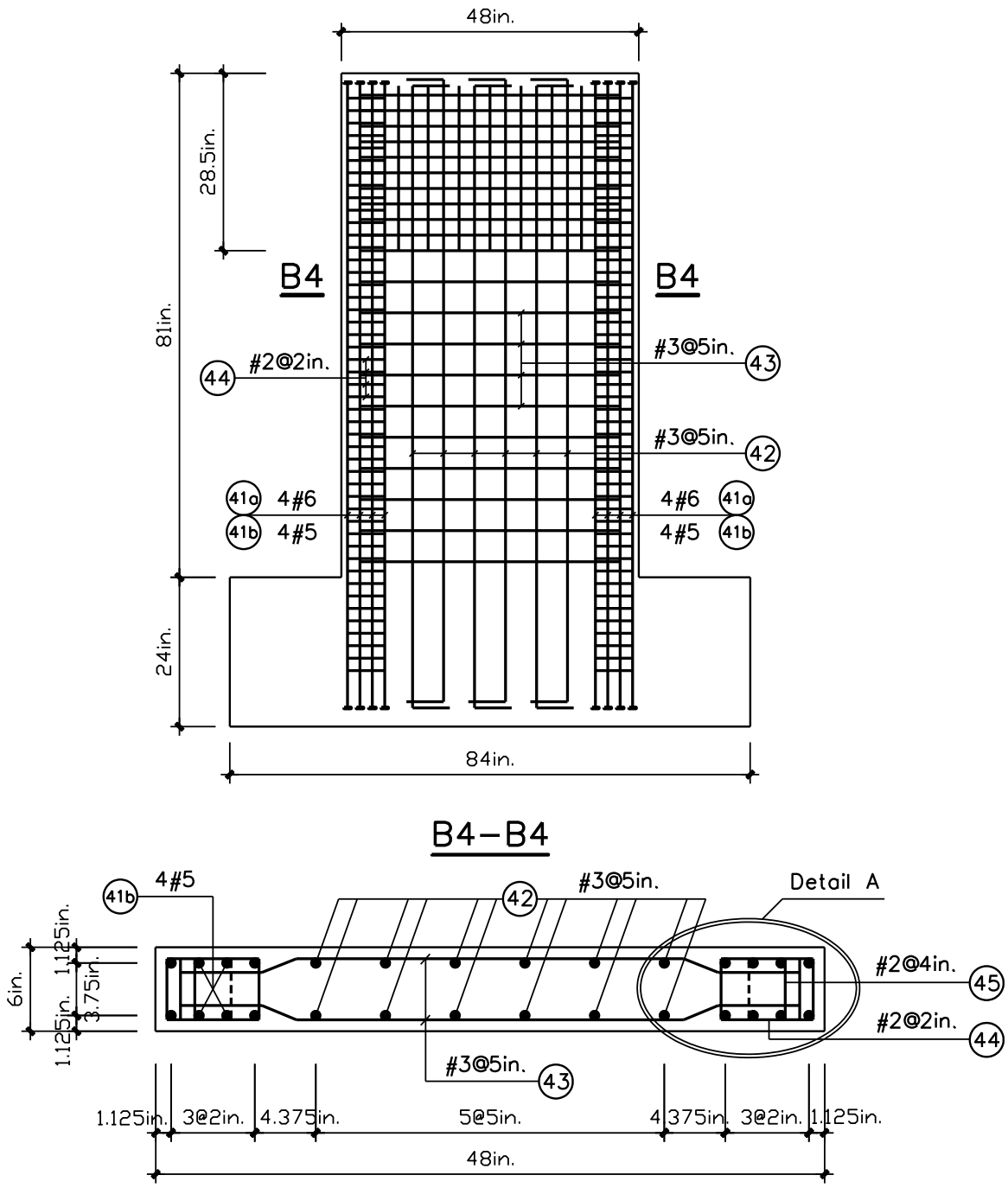

Figure 3-4 Reinforcement details for RW-A15-P10-S78

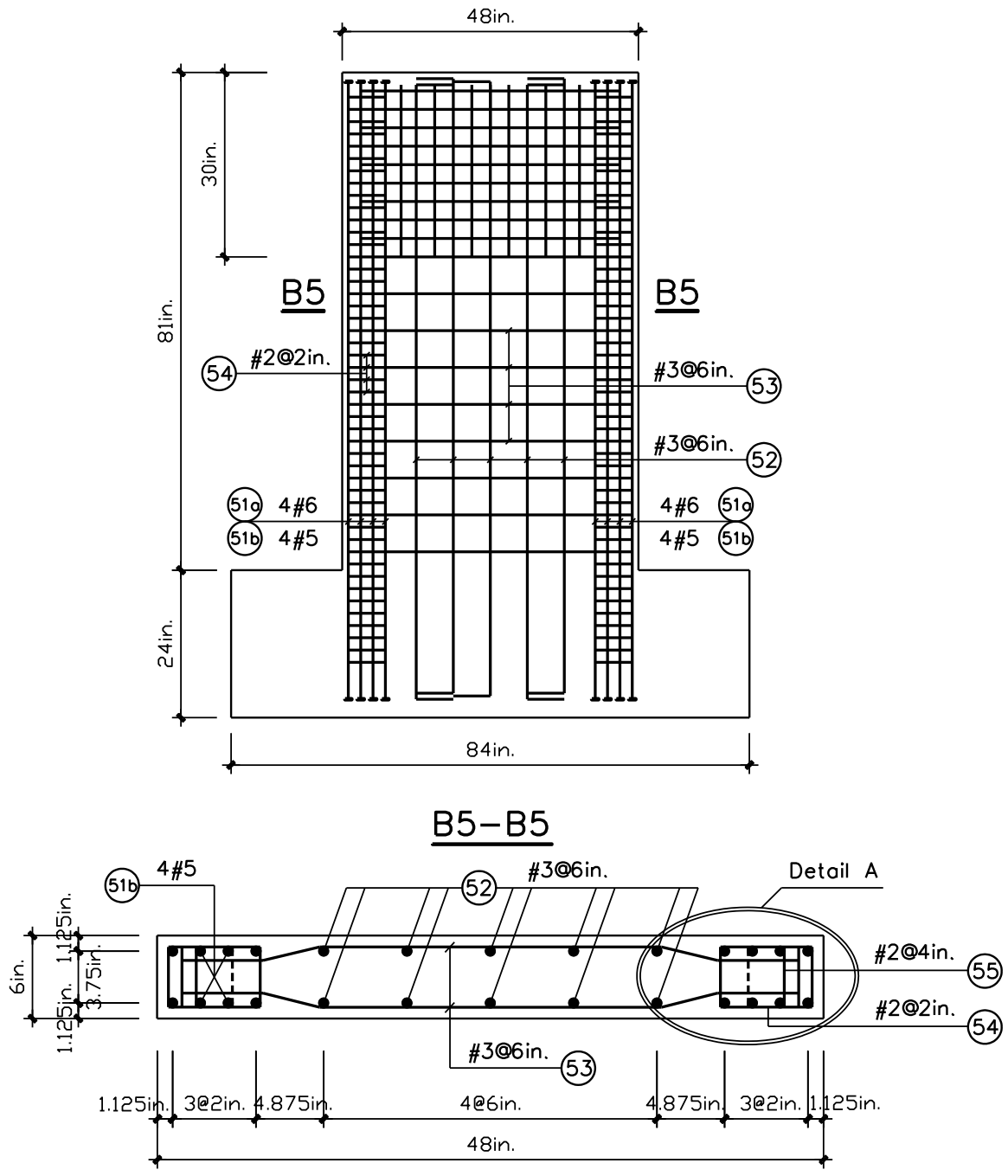

Figure 3-5 Reinforcement details for RW-A15-P2.5-S64

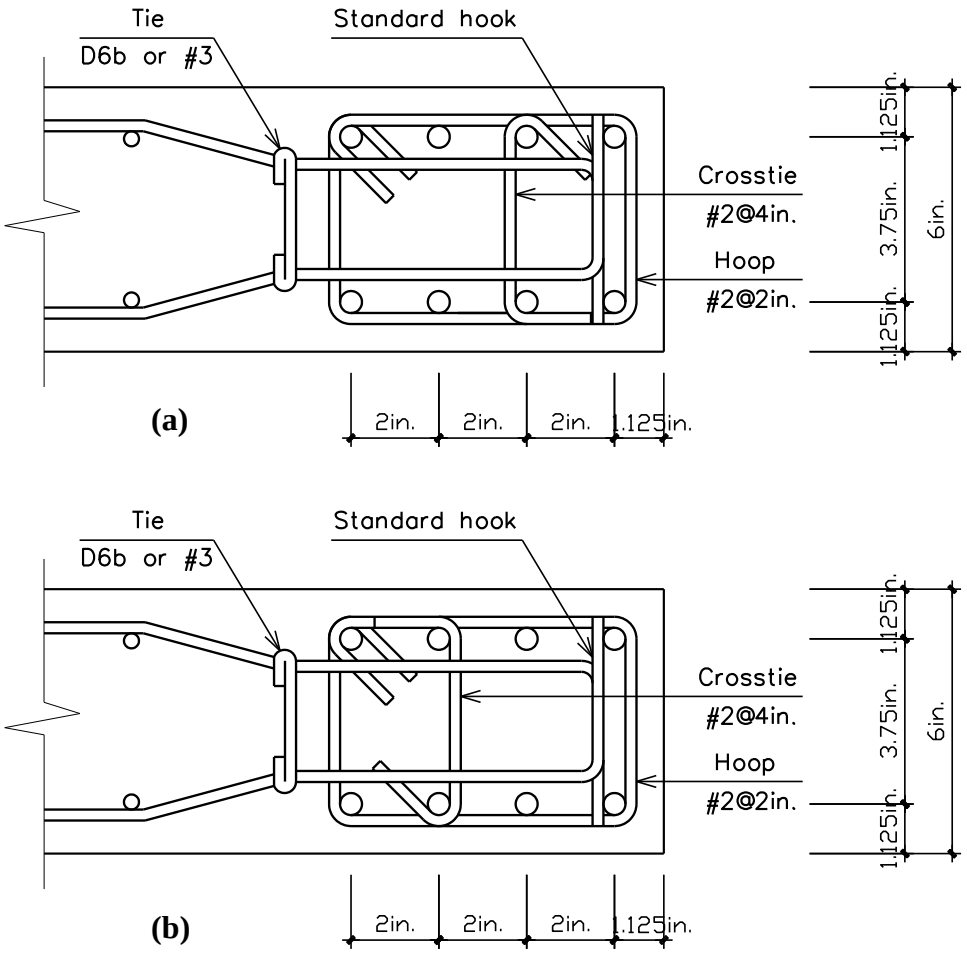

Figure 3-6 Detail A

Figure 3-6 (Detail A) shows details of the special boundary elements used in test specimens. According to the current code provisions ACI 318-11 S21.9.6, the need for special boundary elements at the edges of structural walls can be evaluated by using the stress-based approach or displacement-based approach. Since the displacement-based approach is based on the assumption that inelastic response of the wall is dominated by flexural behavior, this method is only considered as a reference for this study. The calculations using stress-based approach showed that all specimens needed special boundary elements; therefore, special boundary elements were required for all specimens. Wall boundary transverse reinforcement was

designed to satisfy ACI 318-11 S21.9.6.4 requirements for special boundary elements, which includes a requirement that the horizontal web reinforcement be developed within the confined core of the boundary element using the following relation:

$$l_{dh} = \frac{f_y d_b}{65\sqrt{f_c'}} = \frac{60{,}000 d_b}{65\sqrt{5000}} = 13.05 d_b \geq [8 d_b; 6'']$$

The requirement of 6 in. (152 mm) governed for #2 and #3 horizontal web bars, which was satisfied for all five specimens (see Figure 3-6). In addition, a standard 90-degree hook with $12d_b$ extension is required. This length ($12d_b$) was 3 in. (76 mm) for #2 bars and 4.5 in. (114 mm) for #3 bars. Due to the small thickness of wall specimens, a hook extension length of 3 in. (76 mm) was used for both #2 and #3 horizontal web reinforcement in all five specimens.

A hoop (#2) and a single crosstie (#2) were used at each at level of all wall special boundary elements; the crosstie was alternated between pairs of boundary longitudinal reinforcement over the height of the special boundary element as shown in Figures 3-6a and 3-6b. Each crosstie ends with a 90-degree hook at one side and with a 135-degree hook at the other side; adjacent crossties (over the height) also were alternated. According to ACI 318-11 S21.6.4.2, the extension of the hook is not less than $6d_b$ and 3 in. (76 mm); 3in. controls for #2 bars. Due to limited space, the extension of the hook was reduced to 2 in. (51 mm) for all hoops and crossties in the special boundary elements for all five walls. Figure 3-7 and Table 3-2 provide a summary of the wall geometry and reinforcement for all five specimens, whereas Table 3-3 summarizes general properties of the reinforcement.

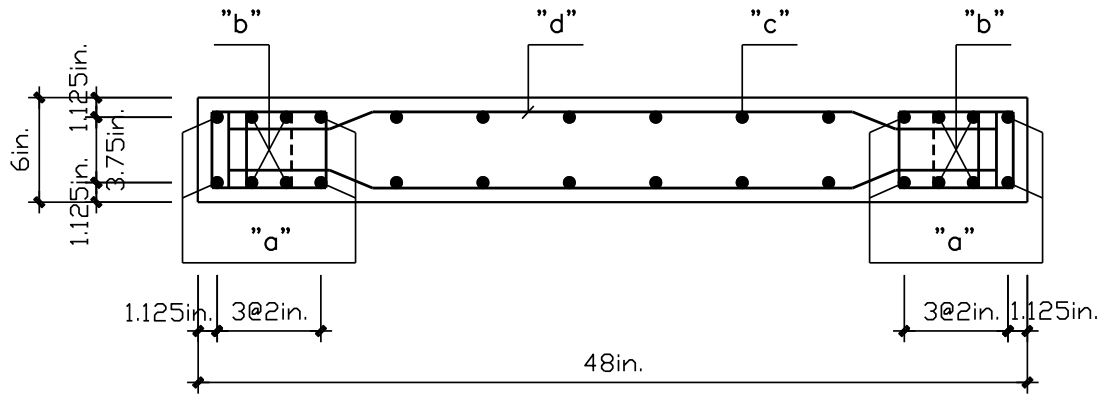

Figure 3-7 Typical wall cross-section

Table 3-2 Wall reinforcement details

Wall specimen	"a"	"b"	"c"	"d"
RW-A20-P10-S38	4#4	4#4	6D6a @140 (@5.5in.)	D6b @140 (@5.5in.)
RW-A20-P10-S63	4#6	4#6	5#3 @152 (@6in.)	#3 @152 (@6in.)
RW-A15-P10-S51	4#4	4#4	7D6a @114 (@4.5in.)	D6b @114 (@4.5in.)
RW-A15-P10-S78	4#6	4#5	6#3 @127 (@5in.)	#3 @127 (@5in.)
RW-A15-P2.5-S64	4#6	4#5	5#3 @152 (@6in.)	#3 @152 (@6in.)

Table 3-3 Bar details

Reinforcement	Grade	Specified yield strength f_y ksi (MPa)	Deformed or smooth bars
#4, #5, #6 (Headed bars)	GR60	60 (414)	Deformed
D6a	400MPa	58 (400)	Deformed
D6b	500MPa	72.5 (500)	Deformed
#2	GR40	40 (276)	Smooth
#3	GR60	60 (414)	Deformed

CHAPTER 4 TEST SETUP

This chapter presents test setup of structural wall specimens, including anchorage of walls to the strong floor, application of lateral and axial load, and prevention of twisting of specimens during testing. As well, the design of the foundation block is provided.

The cantilever wall specimens were tested in an upright position at the UCLA Structural/Earthquake Engineering Laboratory. Figures 4-1 and 4-2 show a schematic and a photograph of test setup for a typical wall specimen.

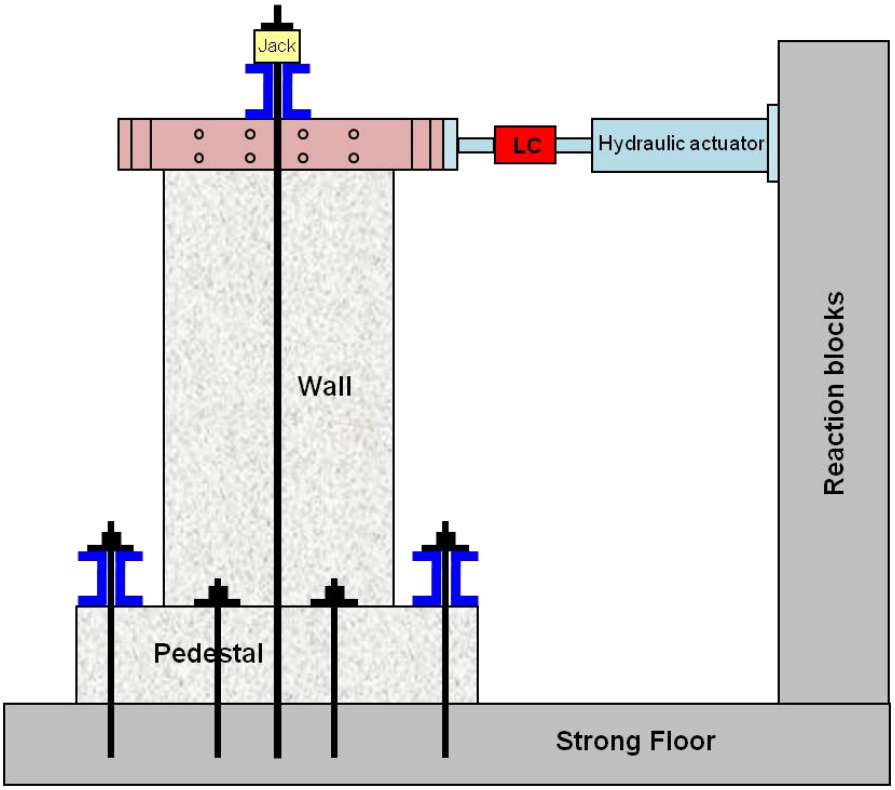

Figure 4-1 Scheme of test setup

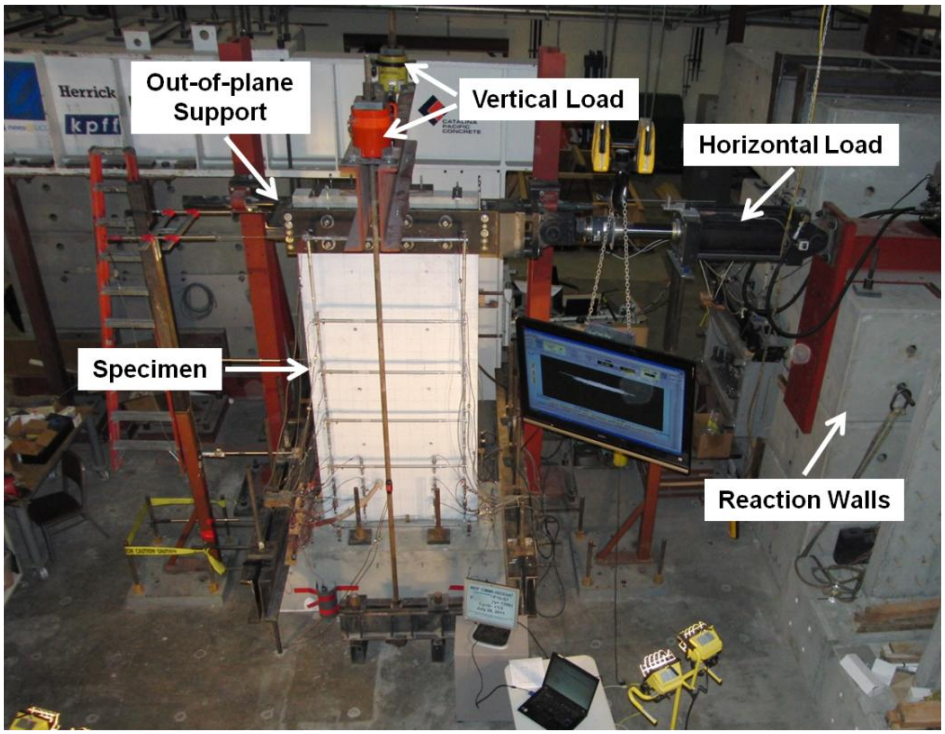

Figure 4-2 Photograph of test setup for a typical wall specimen

4.1 Anchorage of Wall Specimens to the Strong Floor

A thin layer of hydrostone grout was placed between the foundation block and the strong floor to ensure good contact which was necessary for load distribution (post-tensioning load, axial load, and reserved cyclic lateral load). The use of the hydrostone layer also helped to increase the friction force between the foundation block and the strong floor, minimizing the sliding between them during testing.

After placing the hydrostone layer, the 1-1/4 in. (32 mm) diameter high-strength post-tensioning anchor bars, i.e., Dywidag threaded rods, which passed through holes created by PVC tubes embedded into the foundation block and then connected to couplers embedded into the strong

floor, were post-tensioned to anchor the wall specimen to the strong floor. Bolts and steel bearing plates with the dimensions of $7 \times 6 \times 1.5$ in. ($178 \times 152 \times 38$ mm) were used to spread the post-tensioning force over the foundation block (Figure 4-5). For all test specimens, each anchor bar was post-tensioned to approximately 100 kips, or around 55% of its ultimate capacity. In order to increase the number of anchors between the specimen and the strong floor, two double channel sections ($2C15 \times 33.9$) were positioned on top of the foundation block (Figure 4-1). Post-tensioning anchor bars were passed through the gap between two channel sections and anchored to the strong floor. As a result, a total of twelve anchor bars were used to anchor each test specimen to the strong floor. Details of anchorage of wall specimens to the strong floor, including elevation and side view, are presented in Figure 4-3, whereas Figure 4-4 shows a photograph of wall specimen anchorage. Figure 4-5 describes the post-tensioning of a typical anchor bar.

In order to increase the shear strength of the foundation block, and to help avoid bearing failures associated with the plates supporting the Dywidag bars anchoring the test specimen to the strong floor, four 1 in. (25 mm) diameter high-strength post-tensioning bars were used. The bars were placed within PVC tubes within the foundation block parallel to the strong floor and two 1 in. (25 mm) thick steel plates were used at each end of the foundation block (Figure 4-4).

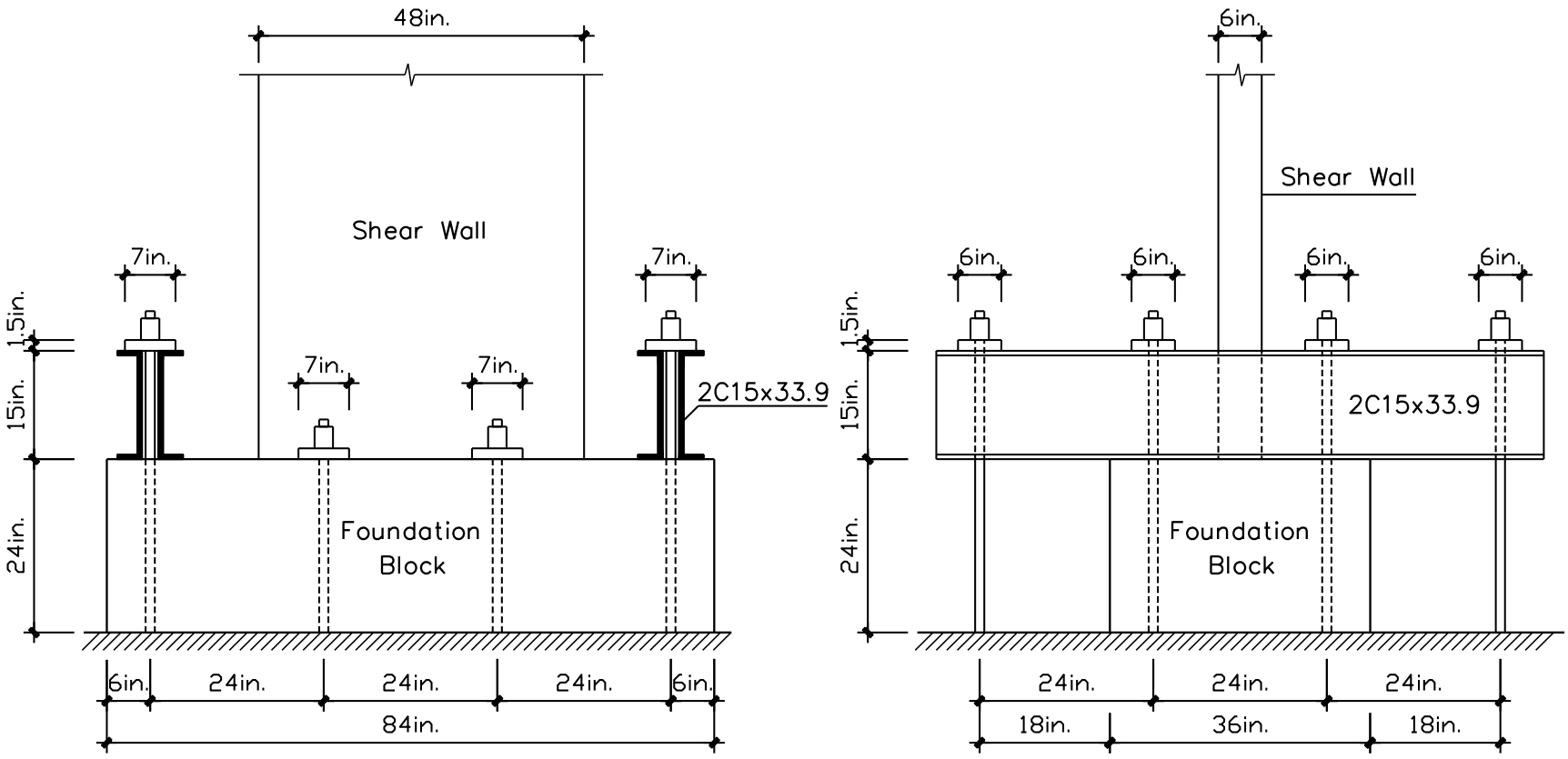

(a) Elevation

(b) Side view

Figure 4-3 Anchorage of wall specimens to the strong floor

Figure 4-4 Photograph of wall specimen anchorage and post-tensioning at side faces of the foundation block

Figure 4-5 Post-tensioning a typical anchor bar

4.2 Lateral Load Application

The lateral load was applied to the wall specimens by a 200 kip (890 kN) hydraulic actuator fitted with a load cell (Figure 4-6). The transfer of lateral load from the hydraulic actuator to the wall was performed through a specially fabricated steel load transfer assembly. This lateral load assembly included two 1.5 in. thick steel plates, one on either wall face along with through-wall post-tensioning bars. Eight 1-1/2 in. (38 mm) diameter Fatigue-Proof steel threaded rods were used as post-tensioning bars for each specimens. Details and a photograph of the lateral load transfer assembly are shown in Figures 4-7 and 4-8, respectively. The applied tension load for each post-tensioning bar was around 100 kips, or approximately 50% of its ultimate capacity. The actuator was attached to the lateral load transfer assembly at one end and to the reaction wall at the other end. The horizontal load was transferred to the wall through a friction mechanism to spread the lateral load uniformly across the top of the wall (Figure 4-9). The reversed cyclic lateral load was transmitted to the wall at a very slow rate. The reaction wall consisted of several blocks of concrete post-tensioned vertically with 1-1/4 in. (32 mm) diameter high-strength post-tensioning anchor bars (see Figure 4-6).

For specimen RW-A20-P10-S38 (Test 1), a layer of hydrostone was used to fill the 3/8 in. (9.5 mm) gap between the wall and the 1.5 in. (38 mm) thick steel plate of the lateral load transfer assembly before post-tensioning the high-strength bars. Although no problems were encountered with the application of reversed cyclic lateral load for Test 1, i.e., no sliding between the steel plate and the wall was observed, filling the gap required a lot of work. Therefore, for the specimen RW-A20-P10-S63 (Test 2), in an attempt to speed up the test setup process, two thin

steel plates were welded to the inside faces of the two 1.5 in. (38 mm) thick steel plates to fill the gaps. The lateral load was transferred through a friction force on a direct contact surface between the wall and the steel plate. The test showed that this method also worked very well without any sliding between the steel plate and the wall; therefore, it was applied for the remainder of the tests

Figure 4-6 Hydraulic actuator and reaction wall

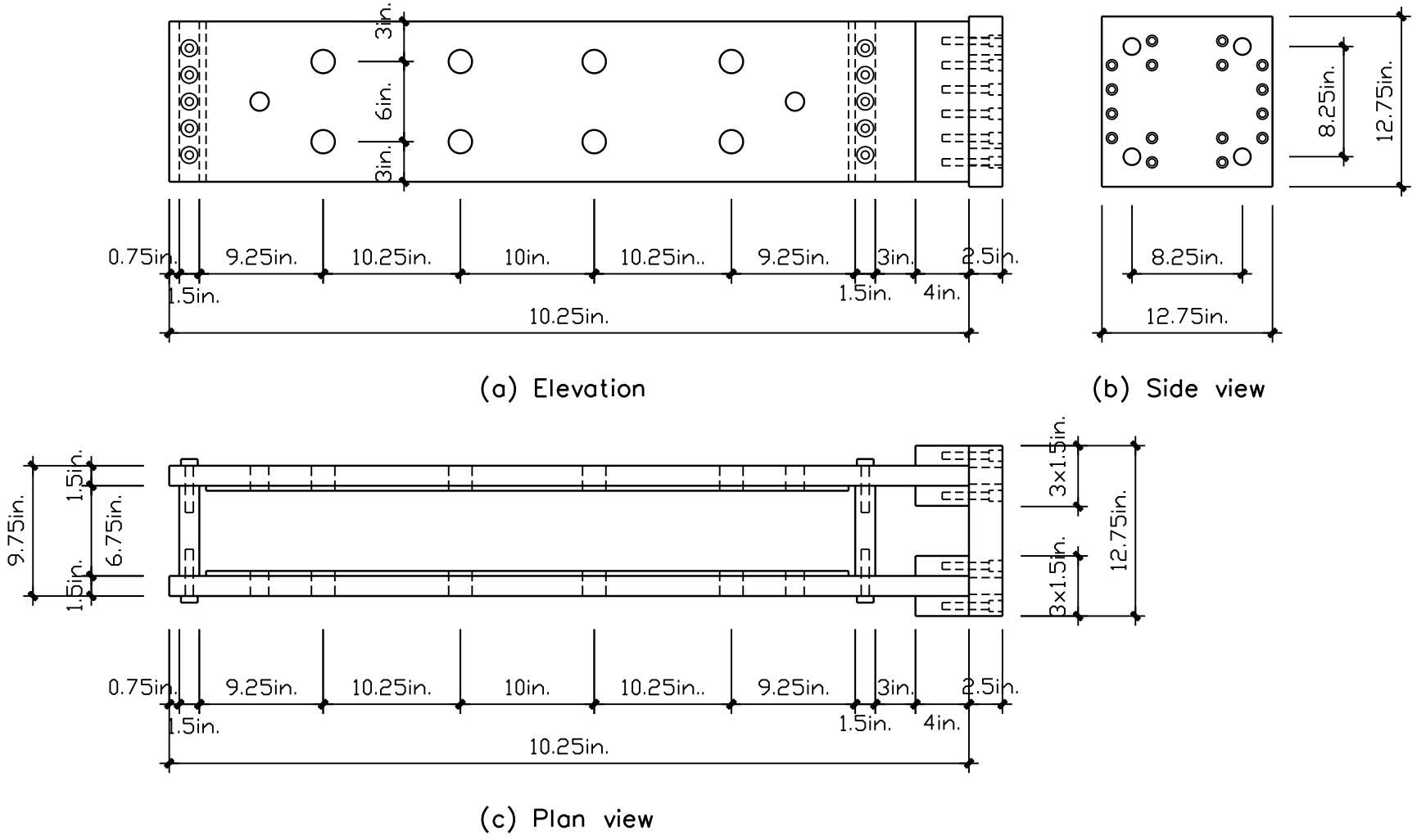

Figure 4-7 Details of lateral load transfer assembly

Figure 4-8 Photograph of lateral load transfer assembly

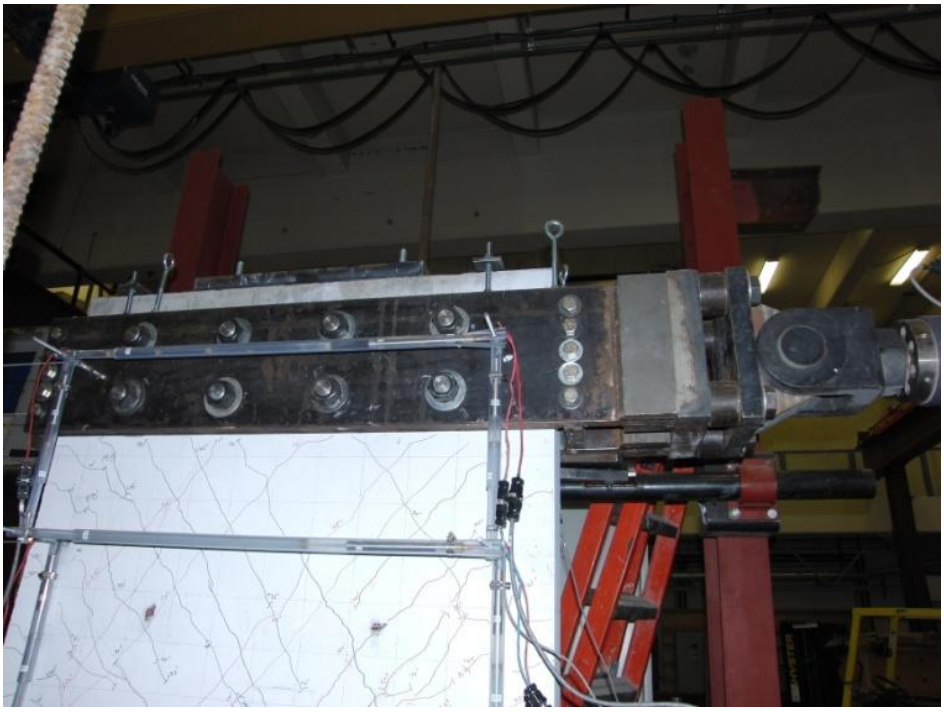

Figure 4-9 Transfer of lateral load to the top of the wall

4.3 Vertical Load Application

The vertical load was applied to the specimens by two 100 ton (224 kip) Enerpac hollow plunger cylinders mounted on a 8 ft. (2.44 m) long, back-to-back channel assembly mounted on the top of the wall (Figure 4-10). Each hollow plunger cylinder post-tensioned a 1-1/4 in. (32 mm) diameter high-strength post-tensioning bar, which was anchored to the strong floor through using a spreader beam. Each spreader beam, consisted of a 3 ft. (914 mm) long back-to-back channels ($2C10\times25$) with each end supported on a 1 ft. (305 mm) long hollow structural section ($HSS8\times4\times1/2$) steel beam anchored to the strong floor by two Dywidag rods (Figure 4-11). A photograph of this anchorage system is shown in Figure 4-12.

In order to measure the axial load applied to the specimen, two strain gauges were installed on opposite faces of each vertical Dywidag rod used for the axial load assembly. Axial load was then applied to the specimen, at various magnitude levels, to determine the calibration factor for this "axial load cell". In order to increase the accuracy of this calibration factor, both loading and unloading cycles were recorded. As well, the axial load applied to perform calibration varied from zero up to the maximum design axial load for test specimens, which was 144 kips (641 kN), or $0.10A_g f_c^{'}$.

During the test, the axial load changed slightly due to the deformation of the wall specimen under the reversed cyclic loading. The axial load was adjusted by adding or releasing pressure to the two hydraulic jacks through the use of an Enerpac hand pump. Two vertical rods used to transfer axial load to the top of the wall specimen rotated during testing due to the lateral

displacement of the top of the specimen. In this case, the projection of axial load on the horizontal cancelled out part of the applied lateral load. However, calculations indicated that the projection of axial load on the horizontal was negligible, compared with the lateral load; therefore, it was considered acceptable in this study.

Figure 4-10 Vertical load application

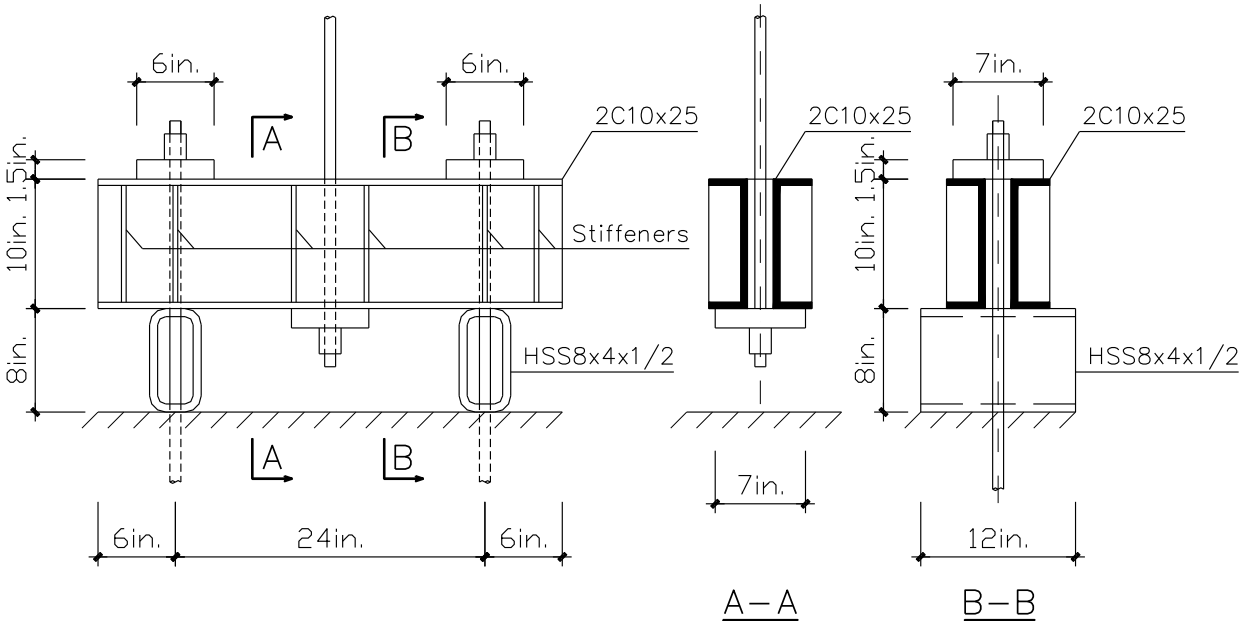

Figure 4-11 Anchorage system for axial load application

Figure 4-12 Photograph of anchorage system for axial load application

4.4 Out-of-plane Support Frame

An out-of-plane support system was designed and built to prevent wall twisting during application of web in-plane lateral loading. The out-of-plane support system consisted of a planar truss and two vertical frames. The planar truss included structural steel channels and an angle section with bolted connections. One end of the truss was attached to the top of the wall at two locations, while the other end of the truss was welded to a long structural steel pipe section, also at two locations. This long pipe section could slide between two short sections of larger diameter pipe sections affixed to vertical columns as shown in Figure 4-13. Each vertical frame consisted of a vertical W section ($W12 \times 26$) along with a diagonal tube brace ($HSS5 \times 3 \times 1/4$), both affixed to the strong floor at one end. Before each test, the contact surface between the outer and inner tubes was greased to minimize the friction between them.

Figure 4-13 Out-of-plane support system

4.5 Design of the Foundation Blocks

Design of the foundation block was accomplished using a strut and tie model according to the provisions of ACI 318-11 Appendix A, since traditional beam theory does not strictly apply. A typical strut-and-tie model is described in Figure 4-14. Although struts have bottle-shape as described in Figure 4-15, they are usually idealized as prismatic compression members for simplification in design. To simplify the design and avoid any possible mistakes during construction, the foundation block corresponding to the critical load combination was designed and used for all five wall specimens. The final design of the foundation block is presented in Figure 4-16. The reinforcement in the foundation block included #8 (25.4 mm) longitudinal bars, #4 (12.7 mm) horizontal bars, #4 hoops, #4 and #3 (9.5 mm) cross-ties; all were A615 Grade 60 and deformed bars.

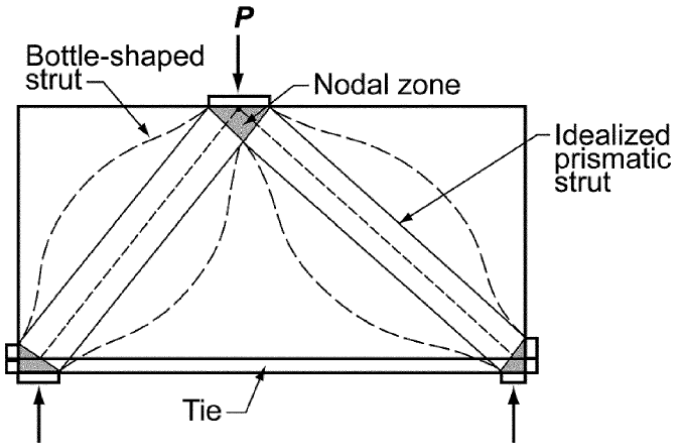

Figure 4-14 Description of strut-and-tie model (ACI 318-11)

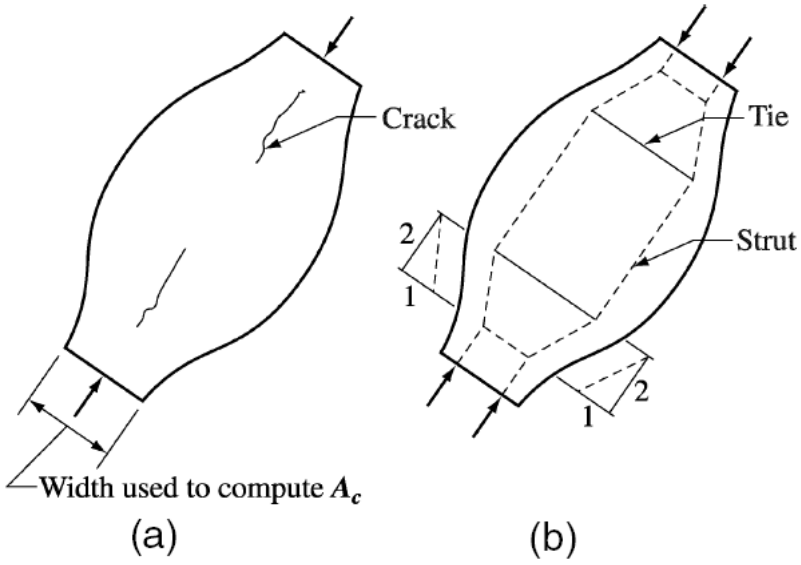

Figure 4-15 Bottle-shaped strut (ACI 318-11)

(a) Cracking of a bottle-shaped strut (b) Strut-and-tie model of a bottle-shaped strut

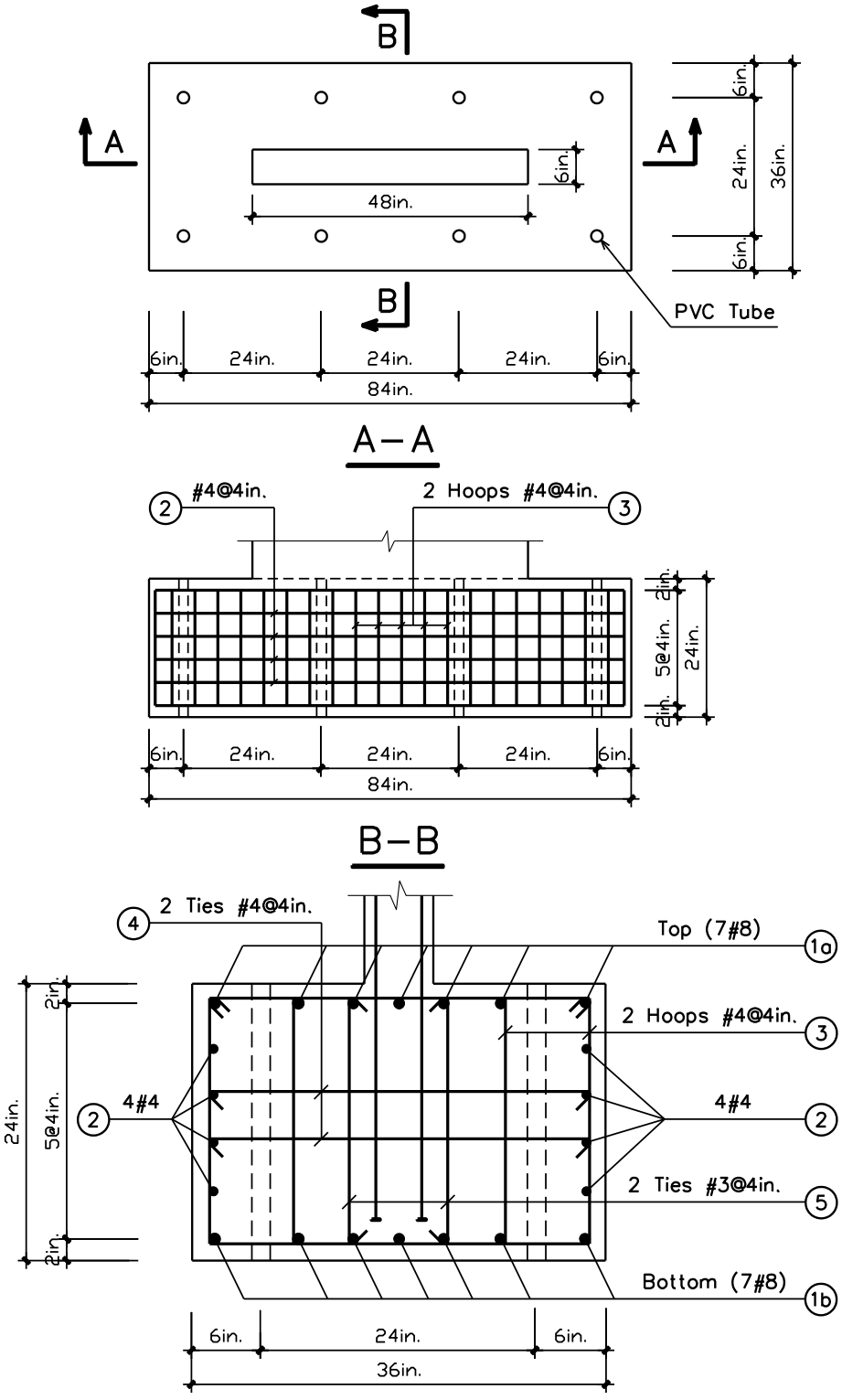

Figure 4-16 Reinforcement details for the foundation block

CHAPTER 5 EXPERIMENTAL PROGRAM

This chapter provides details of the instrumentation and data acquisition system for the tests. As well, testing protocols and procedures to construct five wall specimens are described. Mechanical properties of construction materials, i.e., concrete and reinforcing steel, are also provided.

5.1 Instrumentation and Data Acquisition

Wall specimens were heavily instrumented to obtain detailed response data. LVDTs (Linear Variable Differential Transformers) were used to measure displacements between specified locations. The layout and a photograph of LVDTs for 2.0 aspect ratio wall specimens are presented in Figures 5-1 and 5-2, respectively. These LVDT configurations allowed determination of wall foundation sliding and uplift, lateral wall displacements at various height levels, including flexural, shear, and sliding shear components, and wall average concrete strains over specified gauge lengths (e.g., to enable calculation of wall curvature).

Among LVDTs used for the specimens, only five sensors, numbered from 63 to 67, were AC-LVDTs (Alternating current excited LVDTs), whereas the remainder of sensors were DC-LVDTs (Direct current excited LVDTs). AC-LVDTs had the stroke of 20 in. ($\pm$ 10 in.; $\pm$ 254 mm), while DC-LVDTs were Trans-Tek models 0243-0000, 0244-0000, 0245-0000, and 0246-0000 with various strokes of 1 in. ($\pm$ 0.5 in., $\pm$ 12.7 mm), 2 in. ($\pm$ 1 in., $\pm$ 25.4 mm), 4 in. ($\pm$ 2 in., $\pm$ 50.8 mm), and 6 in. ($\pm$ 3 in., $\pm$ 76.2 mm), respectively. The locations of specific stroke

LVDTs depended on the anticipated strains, with longer strokes used at locations where larger strains or longer gauge lengths were used.

For reference, LVDTs were numbered according to their functional group and their location; therefore, a sequential (continuous) numbering system was not used. A rigid steel reference frame was fixed to the strong floor to provide a rigid reference frame to connect external horizontal LVDTs used to measure lateral displacements over the wall height (sensors from 63 to 67). Sensors 63, 64, and 65 were connected to the wall at the mid points along the wall thickness (edge), whereas sensors 66 and 67 were connected to a 3/8 in. (9.5 mm) diameter rod, which was embedded to the wall during concrete placement, at both faces of the wall. Two vertical sensors attached to the foundation block, i.e., sensors 61 and 62, were used to determine the rotation of the base block.

Two lines of vertical LVDTs near wall edges (sensors 1, 3, 5, 7, 9, 11, 13, 15 and 2, 4, 6, 8, 10, 12, 14, 16, see Figure 5-1) were used to determine average vertical strains and wall curvature profiles over the wall height. The other two series of vertical LVDTs, sensors 21, 23, 25, 27 and 22, 24. 26, 28, were used to provide more detailed data for determination of wall average vertical strains and curvature over the assumed wall plastic hinge length, taken as $l_w/2$. Furthermore, four vertical sensors located at the wall-foundation block interface, sensors 1, 2, 21, 22, were used to measure the contribution of slip and extension of boundary longitudinal reinforcement in the foundation block to the total displacement. In addition, series of vertical sensors at the same height, e.g., sensors 3, 4, 23, 24, gave information on vertical strain profile over the wall length.

Two other vertical LVDTs at the wall sides, sensors 29 and 30, were redundant sensors, used as backup LVDTs.

Two horizontal sensors, sensors 41 and 42, were placed at the wall-foundation interface on two faces of the wall to measure sliding deformations. Horizontal sensors over the wall length, i.e., sensors from 31 to 37, were applied to obtain the average horizontal strain profile over the wall height. Diagonal sensors, i.e., sensors from 43 to 54, installed in pairs for various wall sections, together with other vertical sensors, were used to determine wall shear deformations over the wall height.

The LVDT layout for 1.5 aspect ratio wall specimens is given in Figure 5-3. This configuration of LVDTs is very similar to that for 2.0 aspect ratio walls, except that vertical sensors 15 and 16, horizontal sensor 37, and diagonal sensors 53 and 54 were not used.

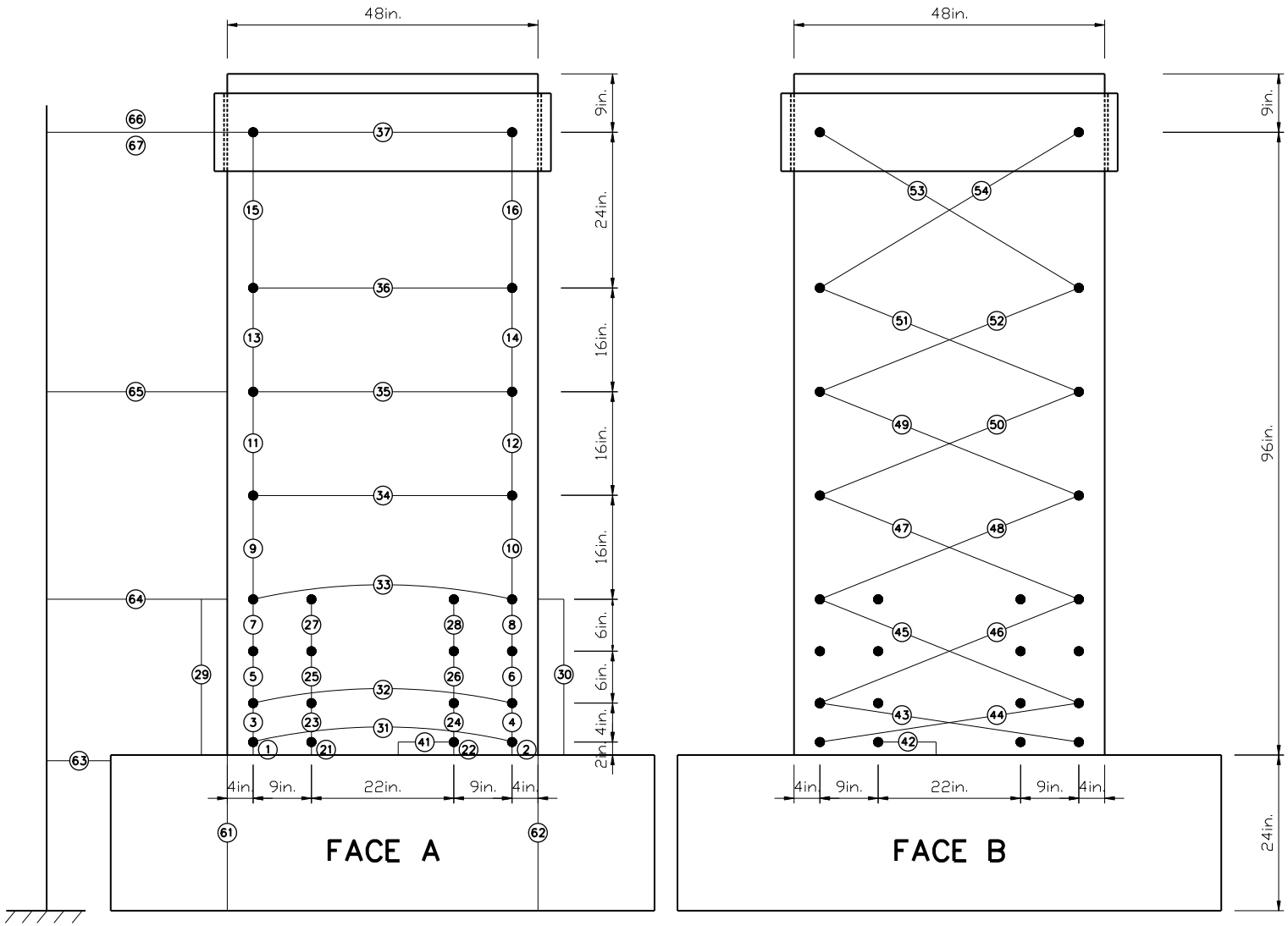

Figure 5-1 LVDT layout for specimens with aspect ratio 2.0

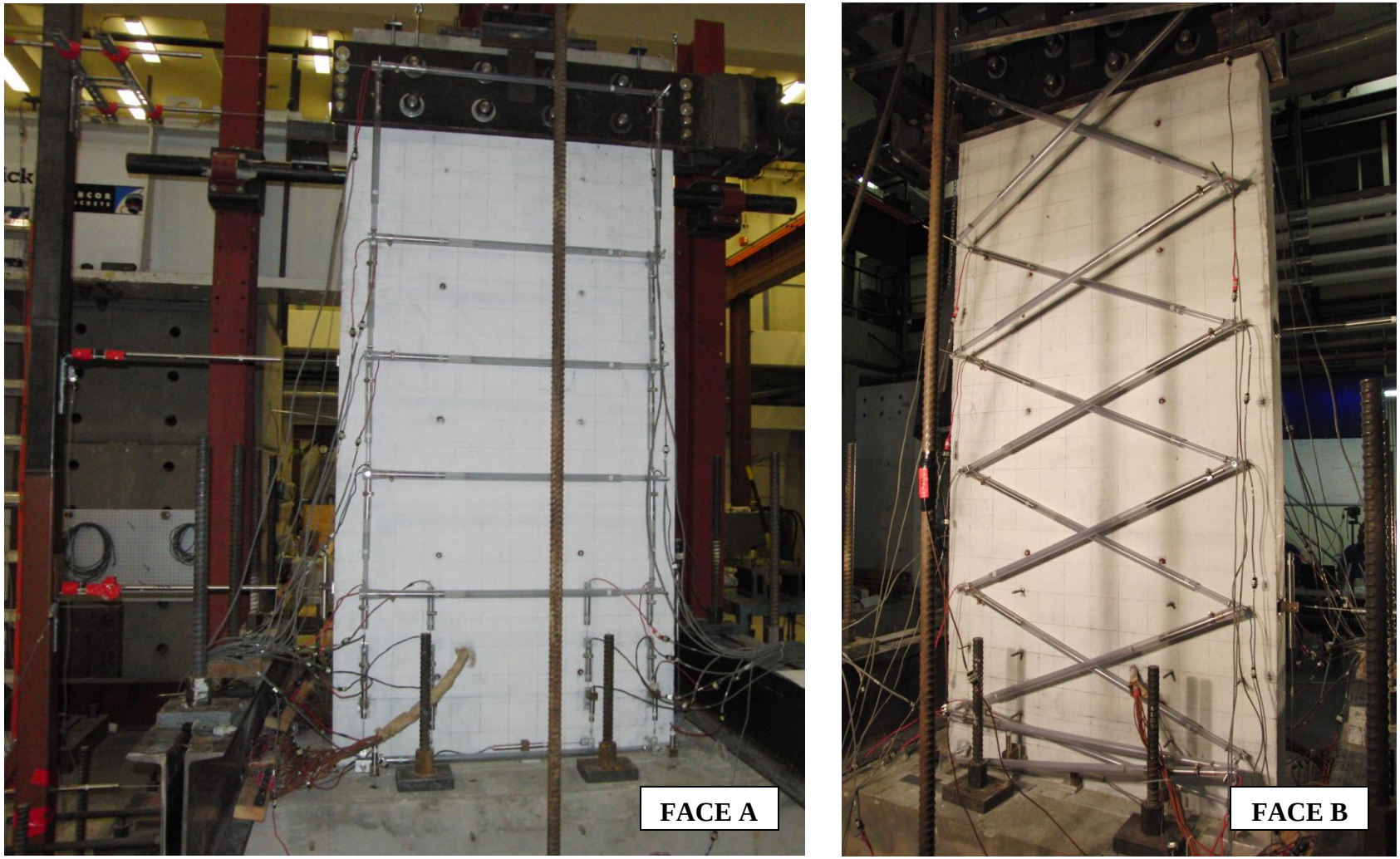

Figure 5-2 Photograph of LVDT configuration for specimens with aspect ratio 2.0

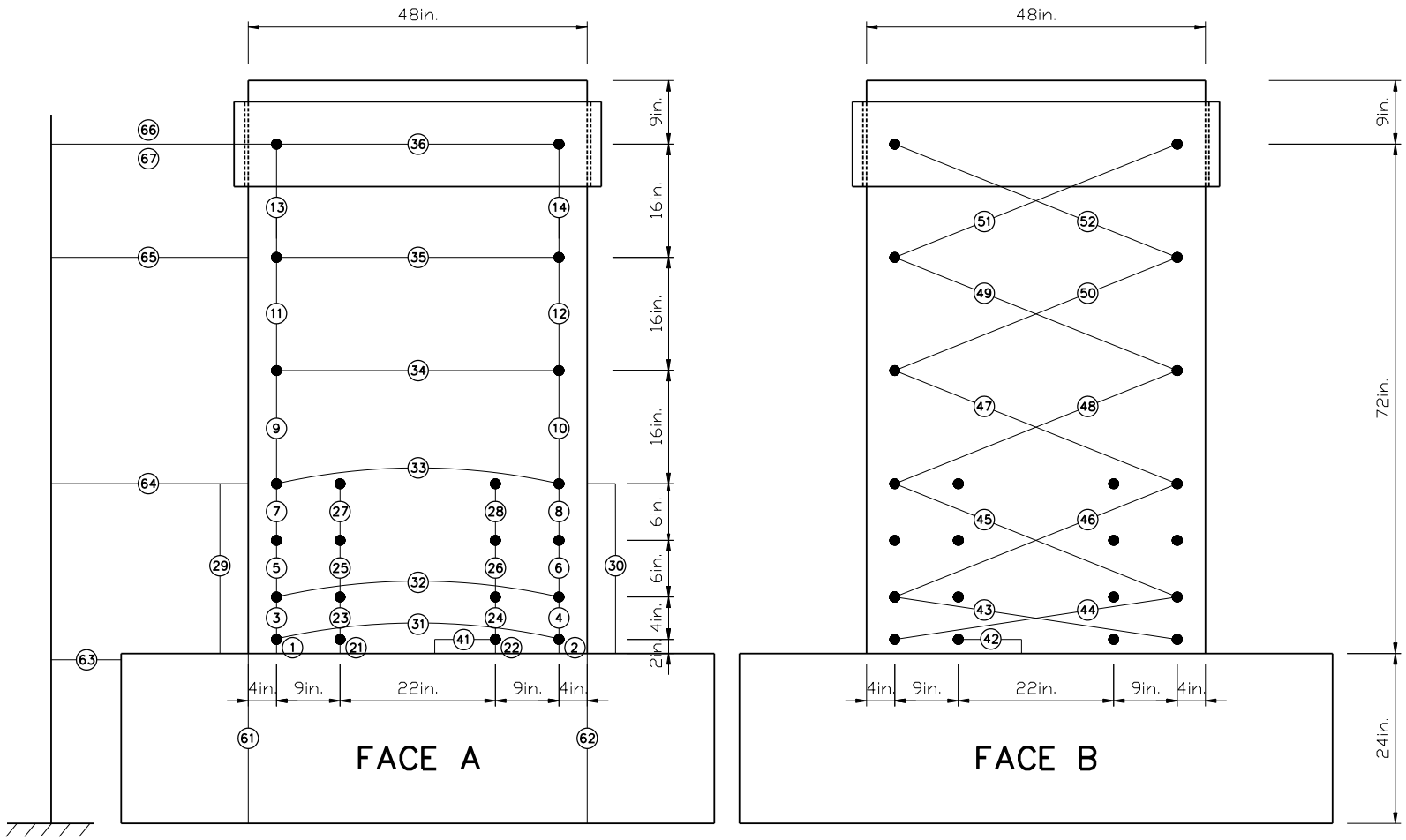

Figure 5-3 LVDT layout for specimens with aspect ratio 1.5

Reinforcement strains were measured at 30 locations using strain gauges affixed to boundary longitudinal and transverse reinforcement, and web vertical and horizontal reinforcement, over the height of about $l_w/2$ from the wall-foundation block interface. The strain gauges were Texas Measurements models YEFLA-2 and YEFLA-5, with gauge lengths of 2 mm (0.079 in.) and 5 mm (0.20 in.), respectively. YEFLA-2 strain gauges were used for #2, D6a, and D6b bars, whereas YEFLA-5 strain gauges were applied for #3, #4, #5, and #6 bars. Figure 5-4 shows the strain gauge layout on boundary longitudinal reinforcement, web vertical and horizontal reinforcement, whereas Figure 5-5 describes the strain gauge layout on boundary transverse reinforcement (hoops and cross-ties).

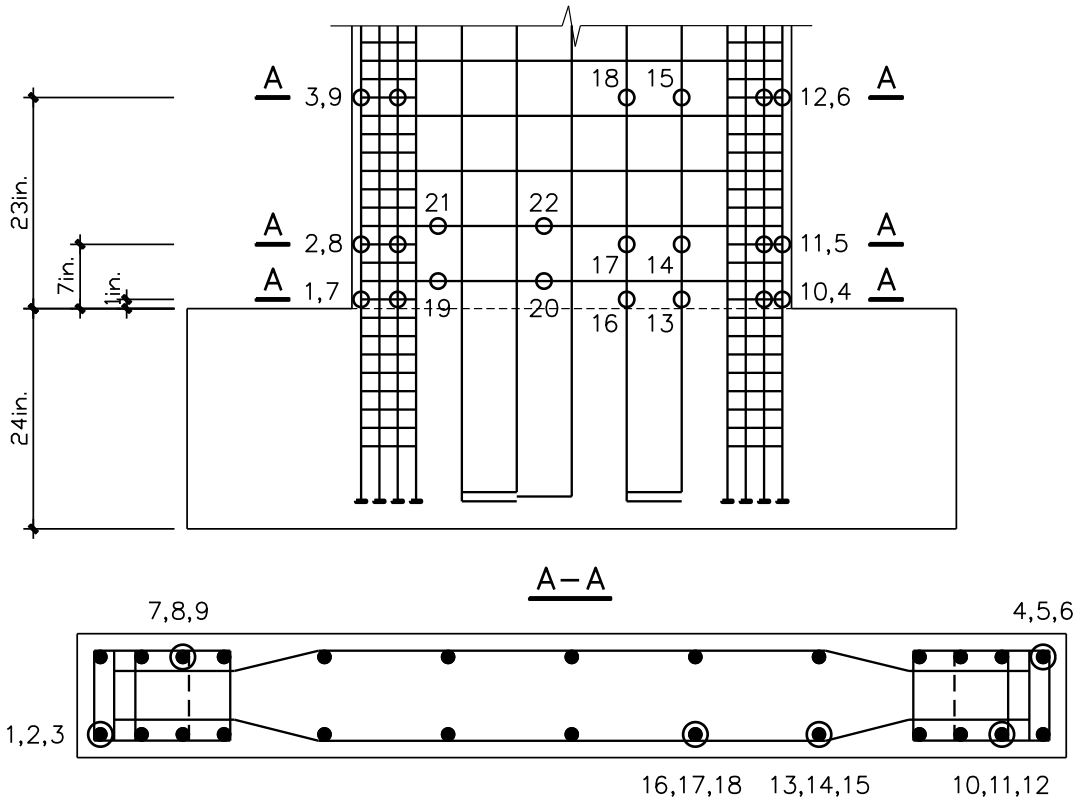

Figure 5-4 Strain gauge layout on boundary longitudinal reinforcement, web vertical and horizontal reinforcement

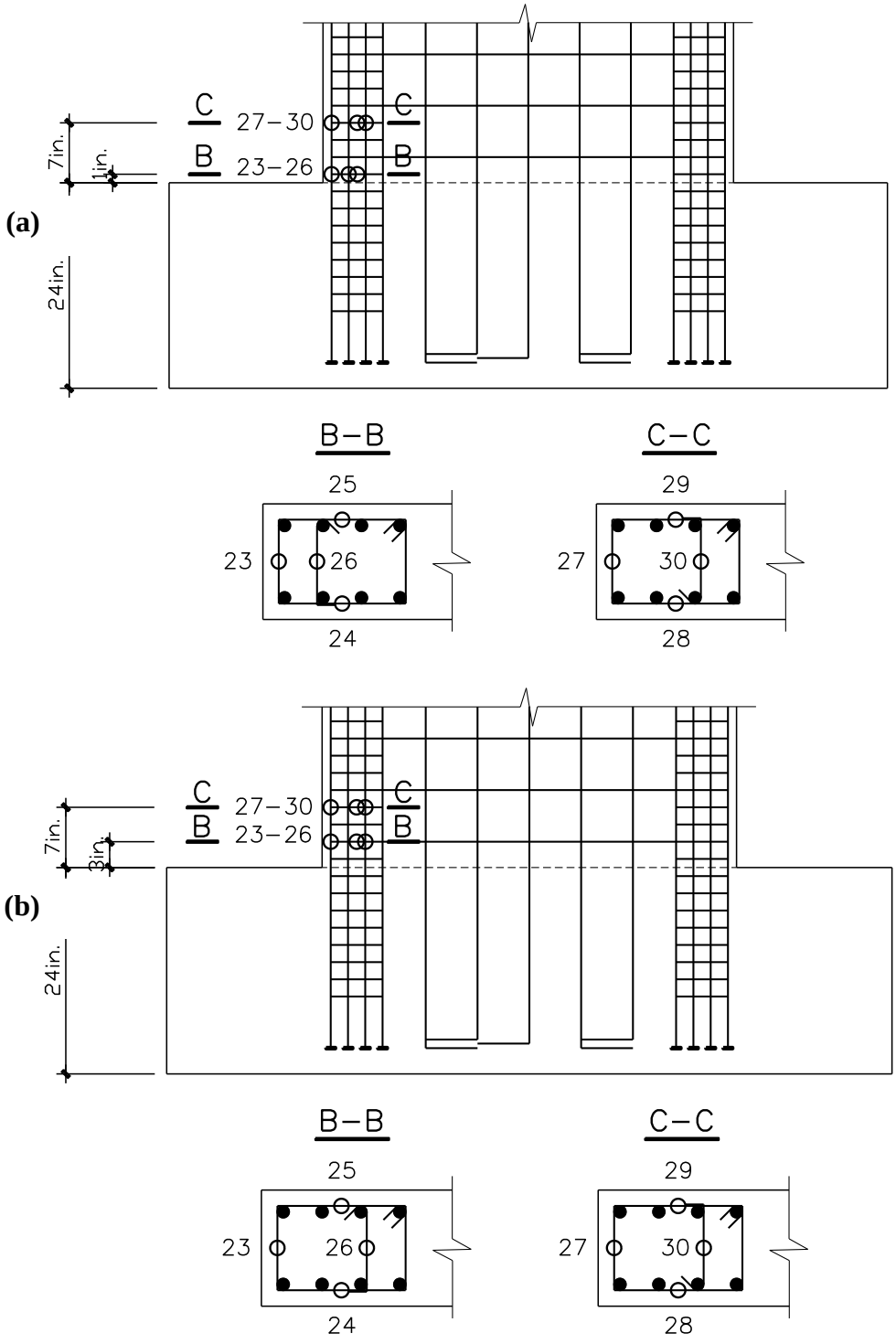

Figure 5-5 Strain gauge layout on boundary transverse reinforcement

(a) For Tests 1 and 3 (b) For Tests 2, 4, and 5

Based on observation of the first three tests, more damage occurred at the right (south) wall boundary than the left (north) wall boundary. Therefore, for Tests 4 and 5, i.e., specimens RW-A15-P10-S78 and RW-A15-P2.5-S64, the orientation of the wall was changed to be opposite to the direction in Figures 5-4 and 5-5, so that the wall boundary with strain gauges attached to the transverse reinforcement was oriented on the right (south).

Lateral load was applied by a hydraulic actuator and measured with a 300 kip capacity Lebow load cell. An external Temposonic transducer was installed along the actuator to enable displacement control. Axial load was applied to the specimens by two 100 ton (224 kip) Enerpac hollow plunger cylinders with an Enerpac hand pump. The magnitude of the wall axial load was recorded by four strain gauges mounted on two vertical Dywidag rods, as mentioned in Section 4.3.

Data from all strain gauges, DC-LVDTs, AC-LVDTs, load cell, and the Temposonic transducer were collected by a data acquisition system (DAQ). This DAQ system included a National Instruments (NI) PXI-1011 chassis, which integrated a NI PXI-8108 controller with seven or eight SCXI modules (seven SCXI modules were used for Tests 1, 2, and 3, whereas eight modules were used for Tests 4 and 5). The NI PXI-8108 was a high-performance Intel Core 2 Duo T9400-based embedded controller, with 2.53 GHz dual-core processor and 2 GB 800 MHz DDR2 RAM. Eight SCXI modules included four or five 8-channel SCXI-1520 modules (four SCXI-1520 modules were used for Tests 1, 2, and 3, whereas five modules were used for Tests 4 and 5), two 32-channel SCXI-1100 modules, and one 8-channel SCXI-1540 module. The SCXI-1520 universal strain/bridge modules, connected with SCXI-1314

terminal blocks, were used for all of the strain gauges, including four strain gages affixed to two vertical high-strength rods to measure axial load. The SCXI-1100 modules, connected with SCXI-1300 terminal blocks, were used for all of the DC-LVDTs, and for the load cell and Temposonic transducer affixed to the horizontal hydraulic actuator, with 10 volts excitation from an external power source. The SCXI-1540 module, connected with SCXI-1315 terminal blocks, were used for all of the AC-LVDTs; all were set with 3 volts excitation at a frequency of 7 kHz.

A LabVIEW script was used to read and plot data from all of the sensors in real-time. The LabVIEW script also allowed real-time monitoring of important responses of the wall specimen, e.g., lateral load versus top displacement, moment versus curvature, moment versus rotation due to extension/slip, moment versus shear sliding, lateral load versus shear strain, in order to ensure that the test was progressing as expected and to assess the reliability of the measurements.

5.2 Testing Protocols

The testing protocol consisted of load-controlled and displacement-controlled cycles (Figure 5-6). Load-controlled cycles were performed generally at 1/8, 1/4, 1/2, and 3/4 of the expected yield force $V_y = M_y / h_w$. Load-controlled cycles were applied at $V_y/6$, $V_y/3$, and $2V_y/3$ for RW-A20-P10-S38 and RW-A20-P10-S63 (Tests 1 and 2), and at $V_y/6$, $V_y/4$, $V_y/2$, and $2V_y/3$ for RW-A15-P10-S51 (Test 3). The expected yield forces were 75, 130,

108, 160, and 140 kips (334, 578, 480, 712, and 623 kN) for Tests 1 to 5, respectively. Three cycles were applied for each load increment during load-controlled stage.

After force-controlled cycles, the testing protocol was switched to displacement-controlled cycles for the rest of the test. Displacement-controlled cycles were performed typically at drift ratios of 0.5%, 0.75%, 1.0%, 1.5%, 2.0%, 3.0%, and 4.0%. For RW-A15-P10-S51 (Test 3), 0.375% was the first drift level used for the displacement-controlled cycles. Due to a cable problem which affected the accuracy of the calibration factor of one LVDT, the actual drift levels for RW-A20-P10-S38 were 0.28%, 0.38%, 0.56%, 0.75%, 1.1%, 1.5%, 2.3%, and 3.1%. Three cycles were applied for each drift ratio increment during displacement-controlled testing up to 2.0%, which is approximately the allowable collapse prevention (CP) limit state for primary components from ASCE 41-06. Two cycles were applied at top drift ratio exceeding 2.0%.

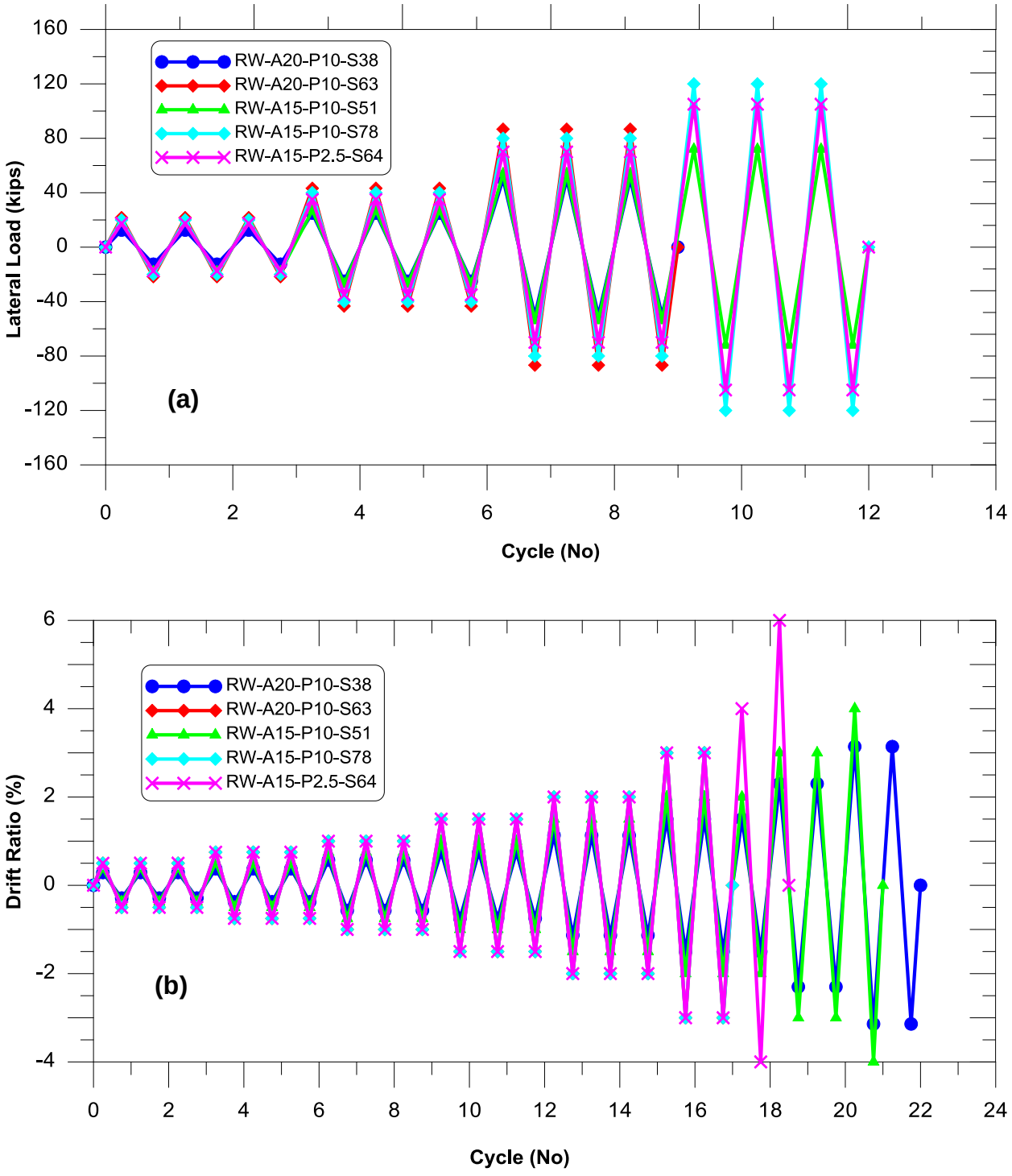

Figure 5-6 Loading protocol

(a) Load-controlled history (b) Displacement-controlled history

5.3 Construction Procedures

The five wall specimens were constructed and tested at the UCLA Structural/Earthquake Engineering Research Laboratory. The first step of the construction process involved cutting, bending, and fabricating reinforcing bars to make reinforcement cages for the foundation blocks (Figure 5-7). Reinforcement cages were then placed in the formwork made from 2×4 in. (51×102 mm) wooden bars and 3/4 in. (19 mm) plywood. Eight pieces of 2 in. (51 mm) diameter PVC pipe were placed vertically in the foundation to allow 1-1/4 in. (32 mm) diameter high-strength post-tensioning Dywidag rods to pass through to the strong floor. Four pieces of 1-1/2 in. (38 mm) diameter PVC pipe were also placed horizontally within the foundation block to allow 1 in. (25 mm) diameter post-tensioning rods to pass through. Four #5 (15.9 mm) hooks, which were used for lifting specimens during construction and test setup, were made and mounted on each reinforcement cage.

The next step of the construction process was to affix strain gauges (Figure 5-8) on boundary longitudinal and transverse reinforcement, and web vertical and horizontal reinforcement, at specified locations (see Figures 5-4 and 5-5). A grinder was used to prepare the rebar surface for application of the strain gauges. The rebar surface was then further prepared using sandpaper and then cleaned. After that, strain gauges with pre-attached lead wires were attached to the reinforcement using adhesive under slight compression. The strain gauges were then covered by coatings and black tape for protection against moisture and damage during concrete placement. Finally, extension lead wires, labeled to identify gauge locations, were connected to the lead wires.

Boundary longitudinal reinforcement and web vertical reinforcement were mounted on guides attached to 2×4 in. (51×102 mm) members. The wooden frames for various walls were connected together to increase their stiffness during concrete placement. Figure 5-9 shows foundation formwork, wooden frames, and vertical bars just prior to concrete placement for the base blocks. Test specimens after pouring the concrete for the foundations are shown in Figure 5-10.

About one week after concrete placement for the foundation blocks, web horizontal reinforcement and boundary transverse reinforcement were fabricated with vertical bars (Figures 5-11 and 5-12). Complete reinforcement in the wall section of a typical specimen is shown in Figures 5-13 and 5-14. Formwork for the wall section were then set up for all five specimens (Figure 5-15) and concrete placement was took place. Figure 5-16 shows specimens after removing the formwork.

The concrete for foundation blocks and shear wall sections was supplied by a commercial ready mix plant in Los Angeles, California. When concrete was delivered to the Laboratory, several slump tests were performed to determine the actual slump height. More details on concrete design mix and slump test results are presented in Section 5.4.1. Prior to concrete placement, four 6×12 in. (152×305 mm) concrete cylinders were prepared for each specimen. After the concrete was poured, either for the foundation blocks or shear wall sections, the specimens were covered by wet burlap and polythene sheets for one week to prevent moisture loss (shrinkage cracking). Afterwards, test specimens remained uncovered until the day of testing.

The wall specimens were painted with white color and 10×10 in. (100×100 mm) grids were drawn onto the surface so that cracks were easily observed during the test. For specimens RW-A20-P10-S38 (Test 1), this work was done after filling the gap between lateral load transfer assembly and the wall with hydrostone grout. For the remainder of the tests, this work was typically performed prior to moving the specimen into place for testing.

Figure 5-7 Making reinforcement cages for the foundation blocks

Figure 5-8 Assembling strain gauges on rebars

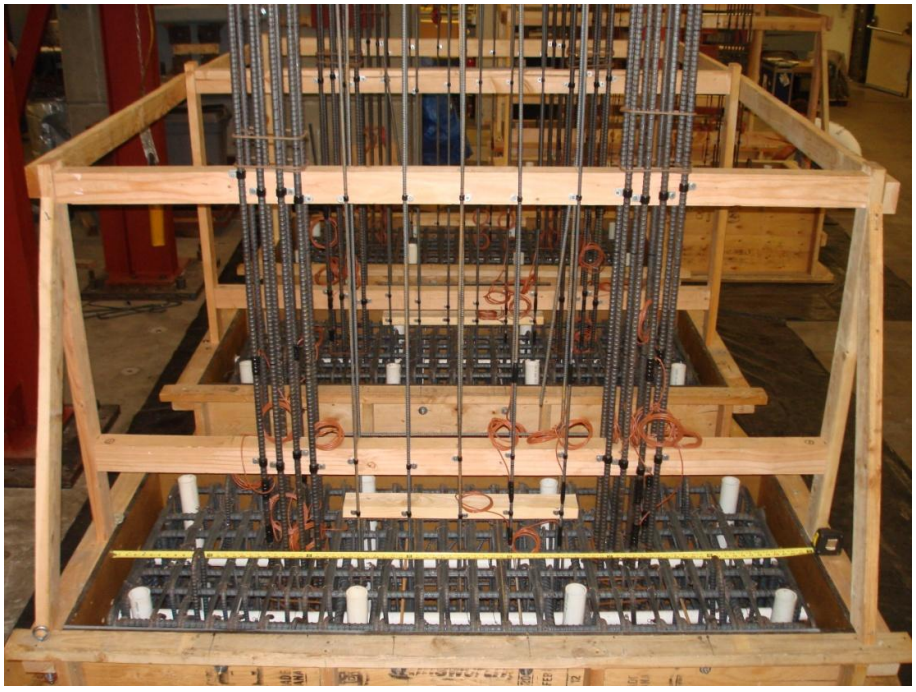

Figure 5-9 Fabricating boundary longitudinal and web vertical reinforcement

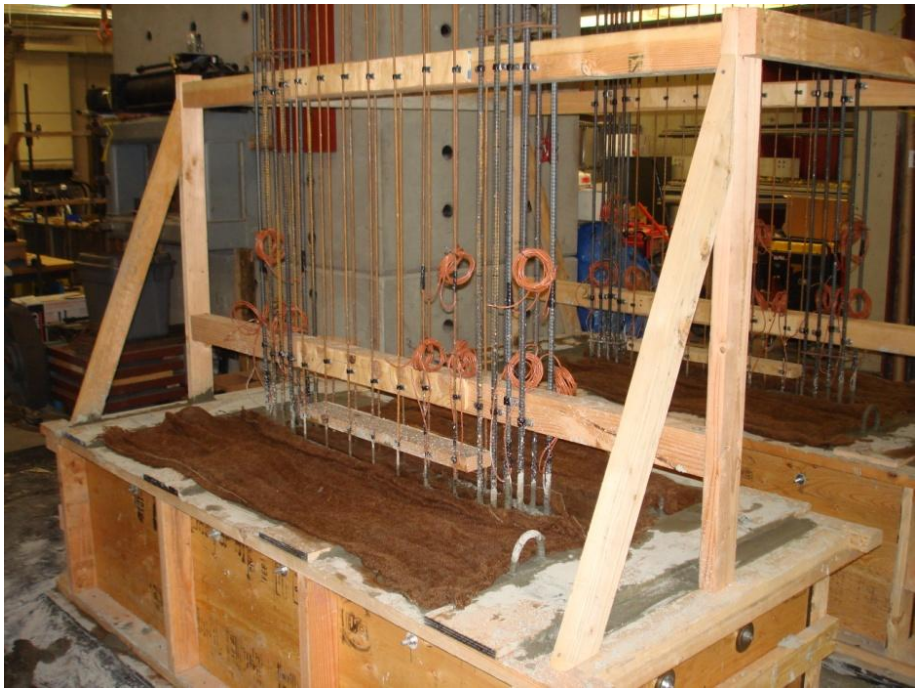

Figure 5-10 Pouring and curing the concrete for the foundation blocks

Figure 5-11 Fabricating boundary transverse and web horizontal reinforcement

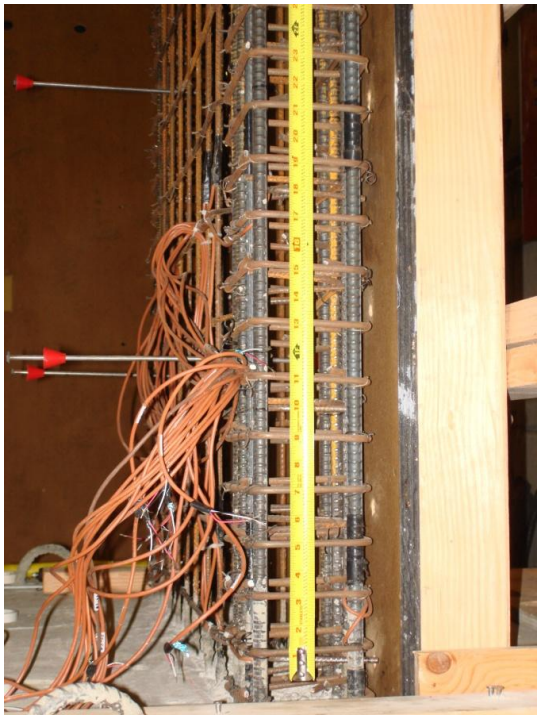

Figure 5-12 Checking spacing of boundary transverse reinforcement

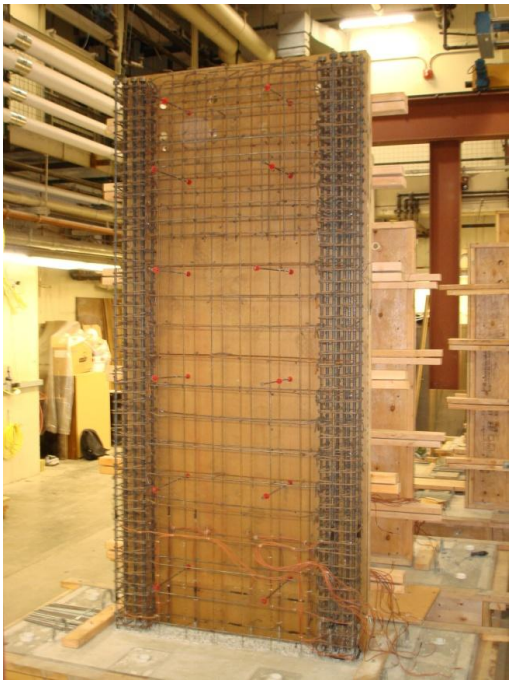

Figure 5-13 Typical wall section

Figure 5-14 Inside the wall specimens: A view from the top

Figure 5-15 Formwork and shoring for specimens

Figure 5-16 Specimens after formwork removal

5.4 Material Properties

Stress-strain relations of concrete and reinforcing steel obtained from testing concrete cylinders and rebar samples are given in Appendix C. This section summarizes main mechanical properties of these construction materials used in the test specimens.

5.4.1 Concrete

Concrete, with a maximum aggregate size of 3/8 in. (9.5 mm), was supplied by a commercial ready mix plant in Los Angeles, California. The concrete mix for foundation blocks of specimens was designed to have a specified concrete compressive strength of 5,000 psi (34.5 MPa) and 5 ± 1 in. (127 ± 25 mm) slump. When concrete was delivered to the UCLA Structural/Earthquake Engineering Laboratory, several slump tests were performed to measure the actual slump height, which ensured the workability and consistency of concrete. The concrete slump tests for the foundation blocks showed that the slump height was 5.5 in. (140 mm), which was in the specified range.

The mix design of concrete for shear wall sections also gave a specified compressive strength of 5,000 ksi (34.5 MPa), but 7 ± 1 in. (178 ± 25 mm) slump. Higher slump was necessary for shear wall section since concrete was placed in a 6 in. (152 mm) thick, heavily-reinforced, shear walls up to a height of 8.75 ft. (2.67 m). The higher slump was obtained by adding super plasticizers to the concrete mix. Actual slump height of 7.5 in. (191 mm) was measured for concrete used in the shear wall.

Concrete placement for the foundation blocks took place on July 26th, 2010, while concrete for the wall sections was poured on December 7th, 2010. For each wall specimen, three $6\times$ 12 in. (152×305 mm) concrete cylinders were tested at the UCLA material testing laboratory at or closed to the test day. Average compressive strength of concrete and strain at the peak stress at test date, as well as wall test date and cylinder test date for all five specimens are given in Table 5-1. More details on mix design of concrete for the foundation blocks and shear walls are given in Appendix C.1, whereas Appendix C.2 provides detailed test results of all concrete cylinders.

Table 5-1 Average compressive strength of concrete at the day of testing

No	Specimen	Wall test date	Cylinder test date	Cylinder maturity days	Compressive strength ksi (MPa)	Strain at peak stress ($x10^3$)
Test 1	RW-A20-P10-S38	07/11/2011 to 07/12/2011	07/06/2011	216	6.83 (47.1)	2.317
Test 2	RW-A20-P10-S64	07/27/2011 to 08/04/2011	08/10/2011	232	7.05 (48.6)	2.014
Test 3	RW-A15-P10-S51	08/19/2011	08/23/2011	255	7.07 (48.8)	2.202
Test 4	RW-A15-P10-S78	10/07/2011	10/10/2011	304	8.09 (55.8)	2.371
Test 5	RW-A15-P2.5-S65	10/24/2011	10/26/2011	321	8.34 (57.5)	2.912

5.4.2 Reinforcing steel

Rebar samples with the length of 24 in. (610 mm) were tested in tension. At least three samples were tested for each type of reinforcement, i.e., D6a, D6b, #2, and #3 bars. For headed bars, consisting of #4, #5, and #6, mill certificates were available and no extra bars were left; therefore, reinforcing steel strengths were specified without testing. Yield and ultimate strengths, together with diameter and cross-sectional area, of all reinforcement are summarized in Table 5-2. Stress-strain curves of reinforcement can be seen in Appendix C.3.

Table 5-2 Yield and ultimate strengths of reinforcement

Bar	#2	#3	#4	#5	#6	D6a	D6b
Diameter, in. (mm)	0.25 (6.4)	0.375 (9.5)	0.5 (12.7)	0.625 (15.9)	0.75 (19.1)	0.236 (6.0)	0.236 (6.0)
Cross-sectional area, $in.^2$ (mm^2)	0.049 (31.7)	0.11 (71.3)	0.20 (126.7)	0.31 (197.9)	0.44 (285.0)	0.044 (28.3)	0.044 (28.3)
Yield strength, ksi (MPa)	61.4 (423)	64.2 (443)	68.4 (472)	68.7 (474)	69.2 (477)	65.3 (450)	74.9 (516)
Ultimate strength, ksi (MPa)	71.3 (492)	102.6 (707)	88.9 (613)	89.9 (620)	92.4 (637)	95.9 (661)	84.2 (580)

CHAPTER 6 EXPERIMENTAL RESULTS

This chapter presents a detailed description and a comprehensive investigation of the experimental results for all five wall specimens. The experimental results include: summary of test results, experimentally observed damage and behavior, lateral load versus top total displacement responses, profiles of total displacement over the wall height, average horizontal strain, and wall vertical growth.

6.1 Summary of Test Results

Test results for all five specimens are summarized in Table 6-1, including lateral load and top displacement under both positive and negative loading at concrete cracking, boundary longitudinal reinforcement yielding, peak loading, and at significant loss of lateral strength. Significant loss of lateral strength is defined as a 20% drop from the peak value.

Table 6-1 Test result summary

Test No.	Wall code	Loading direction	Cracking		Yielding		Peak load		Strength loss	
			F, kN (kips)	Δ^{top}, mm (in.)	F, kN (kips)	Δ^{top}, mm (in.)	F, kN (kips)	Δ^{top}, mm (in.)	F, kN (kips)	Δ^{top}, mm (in.)
1	RW-A20-P10-S38	Positive	148 (33.3)	2.0 (0.079)	379 (85.28)	13 (0.53)	481 (108.03)	56 (2.20)	445 (100.12)	76 (3.01)
		Negative	-143 (-32.2)	-1.8 (-0.069)	-374 (-84.12)	-14 (-0.54)	-436 (-97.98)	-36 (-1.42)	-413 (-92.77)	-75 (-2.96)
2	RW-A20-P10-S63	Positive	169 (38.0)	2.1 (0.084)	630 (141.57)	16 (0.63)	742 (166.91)	69 (2.72)	734 (165.00)	73 (2.88)
		Negative	-165 (-37.1)	-2.0 (-0.080)	-597 (-134.26)	-15 (-0.59)	-717 (-161.14)	-69 (-2.72)	-699 (-157.08)	-73 (-2.88)
3	RW-A15-P10-S51	Positive	190 (42.8)	1.3 (0.051)	527 (118.46)	10 (0.40)	603 (135.45)	52 (2.05)	485 (108.93)	60 (2.38)
		Negative	-189 (-42.6)	-1.1 (-0.045)	-506 (-113.69)	-9 (-0.37)	-575 (-129.31)	-50 (-1.97)	-567 (-127.52)	-55 (-2.16)
4	RW-A15-P10-S78	Positive	201 (45.2)	1.5 (0.060)	776 (174.38)	12 (0.48)	859 (193.15)	27 (1.08)	791 (177.87)	55 (2.16)
		Negative	-198 (-44.5)	-1.1 (-0.044)	-727 (-163.48)	-11 (-0.42)	-823 (-184.91)	-27 (-1.06)	-739 (-166.15)	-55 (-2.16)
5	RW-A15-P2.5-S64	Positive	142 (31.9)	1.3 (0.052)	627 (140.97)	11 (0.44)	670 (150.62)	27 (1.06)	543 (121.98)	55 (2.16)
		Negative	-141 (-31.7)	-1.1 (-0.044)	-588 (-132.28)	-10 (-0.40)	-660 (-148.30)	-27 (-1.07)	-364 (-81.80)	-55 (-2.16)

6.2 Experimentally Observed Damage and Behavior

Observed damage and behavior of each test specimen are presented. Numerous photographs are provided to illustrate damage progression under the prescribed loading protocol which included constant axial load and reverse, cyclic lateral loading to increasing displacement amplitudes. Two types of crack widths are also described in this section, consisting of crack widths measured at peak load (load-controlled cycles) or peak lateral displacement (displacement-controlled cycles), and residual crack widths measured at zero lateral load. In the following sections, these crack widths are referred to as "peak" and "residual" crack widths. More details on crack development are given in Appendices A.1 and A.2, which show crack patterns and summarize maximum and residual crack widths of typical horizontal flexural and diagonal shear (or flexure-shear) cracks, respectively, for all specimens at each force or drift level.

6.2.1 Specimen RW-A20-P10-S38

This wall had horizontal and vertical web reinforcement ratios of 0.0027, which are slightly greater than ACI 318-11 Section 21.9.2 minimum requirements for special structural walls of 0.0025. Initial cracking occurred during the first cycle of the third force-controlled level ($2V_y/3$; 222 kN or 50 kips). These cracks were on the lower portion of the wall, over a 1.0 m (40 in.) height, and consisted of horizontal flexural cracks at wall edges, around 125 mm (5 in.) apart and three major inclined (shear) cracks on each side of the wall which initiated from the boundary zone toward the wall center (Figure A-1). During subsequent displacement-controlled cycles, new flexural and shear cracks tended to form closer to the top of the wall and appeared over

three-quarters of the wall height prior to reaching the yield load. Diagonal cracks were steeper and shorter near the top of the wall.

Data from strain gauges affixed to boundary longitudinal reinforcement indicated that first yielding occurred when the top of the wall was displaced to +13 and -14 mm (0.53 and -0.54 in., or 0.55% and -0.56% drift ratios) at lateral loads of +379 and -374 kN (85.3 and -84.1 kips). At first yielding, peak crack widths were 0.15 mm (0.0059 in.) for horizontal (flexural) cracks and 0.5 mm (0.020 in.) for diagonal (shear) cracks. At zero lateral load, residual crack widths for both horizontal and inclined cracks were 0.1 mm (0.0039 in.). After yielding, the flexural cracks at wall boundaries became denser while the number of major shear cracks was almost unchanged. The flexural cracks also began to join with shear cracks and the width of all cracks grew substantially. Diagonal cracks continued to develop down to the opposite boundary column with increased inclination. The density of cracking was higher in the lower half of the wall. Figure 6-1 shows crack patterns of this wall specimen at drift ratios of 0.56%, 1.5%, and at the end of the test. More details on crack development of specimen RW-A20-P10-S38 over various lateral load or drift levels can be seen in Figures A-1 to A-4 in Appendix A.1.

Slip and extension (or yield penetration) of longitudinal boundary reinforcement increased significantly at 0.75% drift, resulting in a noticeable crack along the wall-foundation block interface. At a drift ratio of 1.1%, vertical cracks were observed at the wall boundaries, followed by minor spalling of cover concrete at both wall ends adjacent to the wall-foundation block interface (Figures 6-2 and 6-3).

As can be seen from Figures 6-4 and 6-5, spalling of cover concrete at both wall ends adjacent to the wall-foundation block interface became more significant during cycles to drift ratios of 1.5% and 2.3%. During the first cycle to 3.1% drift, cover concrete at wall boundaries from the wall-foundation interface to a height of about 175 mm (7 in.) had completely spalled and flexural and shear cracks had maximum residual widths of 1.0 and 1.25 mm (0.039 and 0.049 in.), respectively (Figure 6-6). Minor lateral strength degradation, a drop of approximately 5% from the peak load, was observed in both directions during this cycle.

During the second cycle to 3.1% drift, concrete in the core of the right (south) wall boundary crushed and boundary longitudinal reinforcement buckled under positive loading. Immediately following boundary bar buckling, a sudden diagonal tension failure occurred, with fracture of horizontal web bars along the diagonal crack (see Figure 6-1); lateral strength dropped to 30% of the value at peak load. Photographs of two boundary zones of RW-A20-P10-S38 at the end of the test are shown in Figure 6-7.

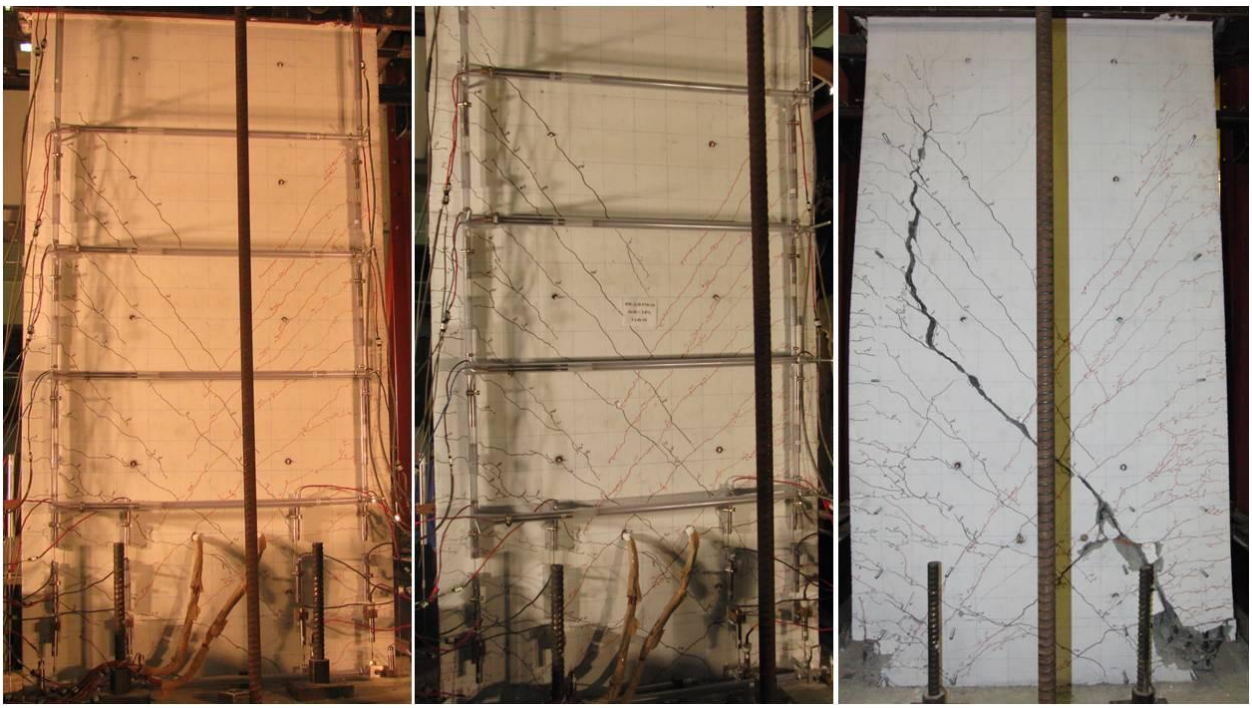

Figure 6-1 RW-A20-P10-S38: Crack patterns at drifts of 0.56%, 1.5%, and at end of test

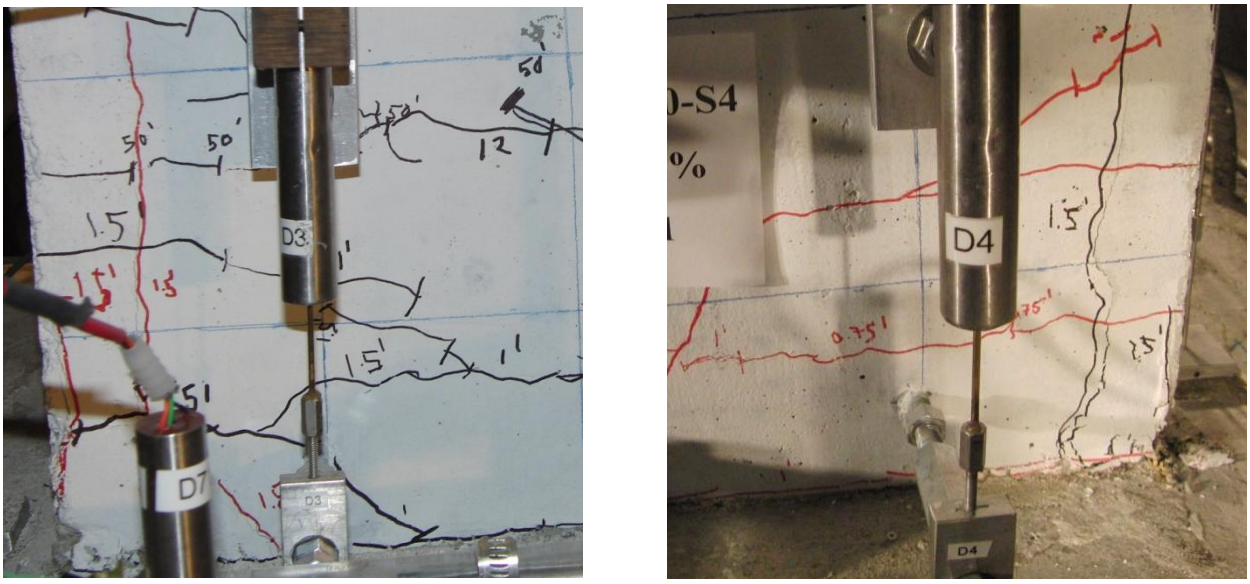

Figure 6-2 RW-A20-P10-S38: North (left) and south (right) wall boundaries at 1.1% drift after first cycle

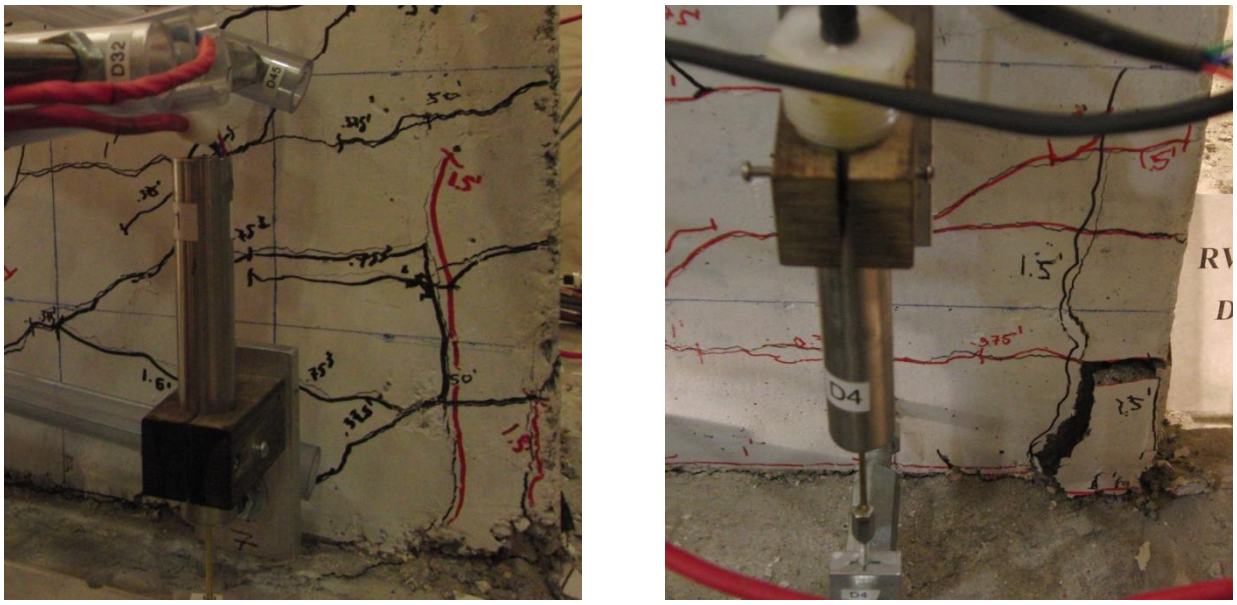

Figure 6-3 RW-A20-P10-S38: North and south wall boundaries at 1.1% drift after third cycle

Figure 6-4 RW-A20-P10-S38: North and south wall boundaries at 1.5% drift after third cycle

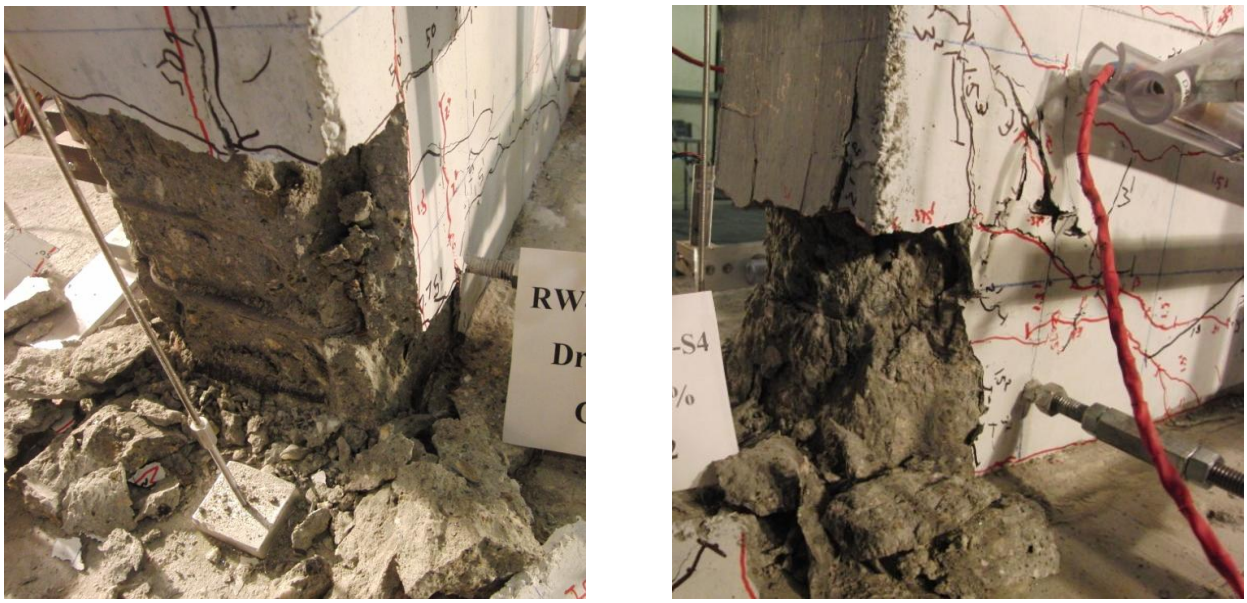

Figure 6-5 RW-A20-P10-S38: North and south wall boundaries at 2.3% drift after second cycle

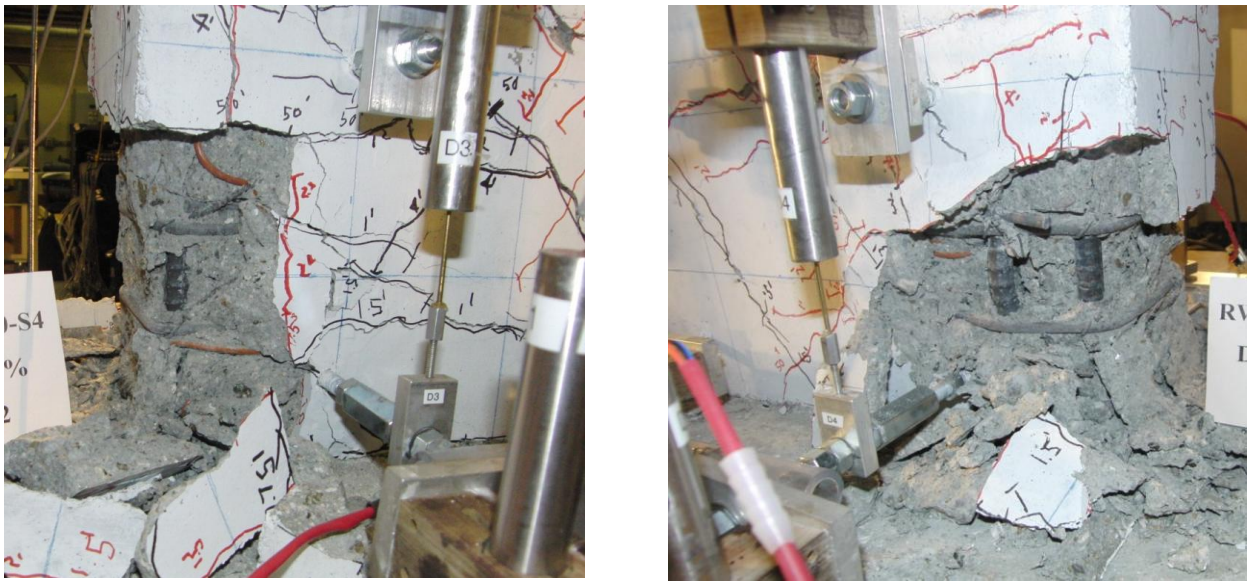

Figure 6-6 RW-A20-P10-S38: North and south wall boundaries at 3.1% drift after first cycle

Figure 6-7 RW-A20-P10-S38: North and south wall boundaries at end of test

6.2.2 Specimen RW-A20-P10-S63

The second test specimen had the same aspect ratio and axial load ratio as the first test specimen, but a higher average shear stress ($6.1\sqrt{f_c'}$ versus $3.6\sqrt{f_c'}$ psi; $0.51\sqrt{f_c'}$ versus $0.30\sqrt{f_c'}$ MPa). The higher shear demand was achieved by approximately doubling the boundary longitudinal reinforcement; web reinforcement also was approximately doubled due to the higher shear demands. Ideally, it might have been preferable to make the two test specimens identical and change the application (resultant) of lateral load to achieve the test objective (change in moment-to-shear span ratio); however, this was not possible within the test budget.

First cracking in RW-A20-P10-S63 was observed during the first cycle of the second force-controlled level ($V_y/3$; 93 kN or 43.3 kips), including one or two major inclined (shear) cracks

on each side of the wall between the wall-foundation interface and a height of around $0.25l_w$ (Figure A-5). With increasing applied lateral load (force-controlled levels) or lateral displacement (displacement-controlled levels), horizontal flexural cracks occurred at the boundaries and new inclined cracks formed. The crack pattern in this wall was very similar to that of RW-A20-P10-S38; however, diagonal cracks formed up to the top of the wall before yielding of longitudinal boundary reinforcement was noted. The inclination of inclined cracks in this specimen also was steeper and the frequency of inclined cracks was denser than those observed in RW-A20-P10-S38.

Crack patterns at drift ratios of 0.5%, 1.5%, and at the end of the test are shown in Figure 6-8. More details on crack development of specimen RW-A20-P10-S63 at various lateral load or drift ratio levels are provided in Figures A-5 through A-8 in Appendix A.1.

First yielding of boundary longitudinal reinforcement occurred at lateral loads of +630 and -597 kN (142 and -134 kips) at wall top displacements of +16 and -15 mm (0.63 and -0.59 in., or 0.66% and -0.61% drift ratios). A horizontal crack at the wall-foundation block interface and a few 100 mm (4 in.) - length vertical cracks at wall boundaries formed during cycles to 1.0% drift ratio (Figure 6-9). Up to this drift levels, peak horizontal and diagonal cracks widths did not exceed 0.8mm (0.031 in.), while residual crack widths did not exceed 0.5 mm (0.020 in.) for horizontal cracks and 0.2 mm (0.0079 in.) for diagonal cracks. Wider and longer vertical cracks were observed at these locations during subsequent cycles to higher drift levels. Spalling of

cover concrete at each wall boundary was noted at 1.5% and 2.0% drift levels (Figures 6-10 and 6-11).

During the first cycle to 3.0% drift, cover concrete spalling at the wall boundaries extended up to approximately 110 mm (4.5 in.) from the wall-foundation interface (Figure 6-12). During the 3.0% lateral drift cycles, diagonal crack widths as large as 3.5 mm (0.14 in.) and horizontal (flexural) crack widths as large as 1.5 mm (0.059 in.) were measured; maximum residual crack widths were 1.0 and 0.6 mm (0.039 and 0.024 in.) for diagonal and horizontal cracks, respectively.

A substantial decrease in wall lateral strength occurred under negative loading during the second cycle to 3.0% drift, due to crushing of concrete and buckling of vertical boundary and some vertical web reinforcement at the north wall boundary. When the loading was reversed, a similar failure mode was observed at the south wall boundary. Due to safety concerns, the test was stopped at drift ratio of 2.4% when the residual lateral strength was only approximately 20% of the peak lateral load. Photographs of two boundary zones of RW-A20-P10-S63 at the end of the test are shown in Figure 6-13. It is noted that, unlike the first test (RW-A20-P10-S38), loss of lateral strength was associated with lateral instability of the boundary zone.

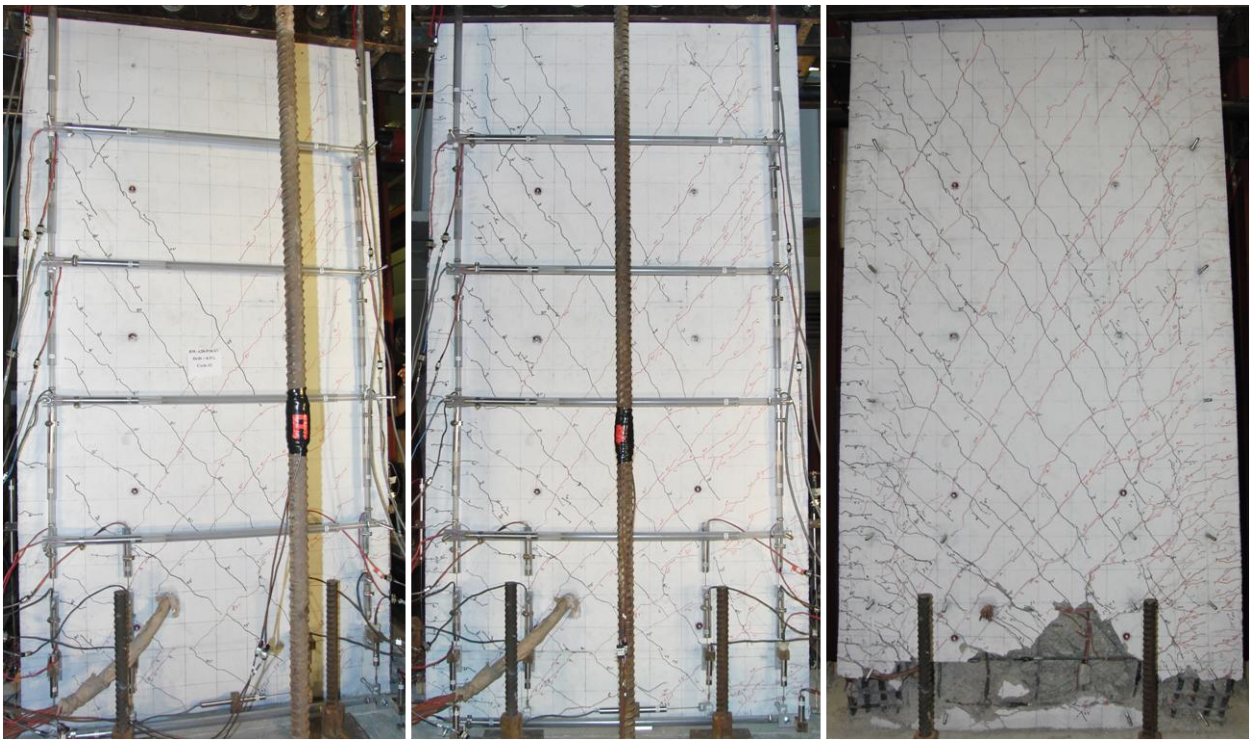

Figure 6-8 RW-A20-P10-S63: Crack patterns at drifts of 0.5%, 1.5%, and at end of test

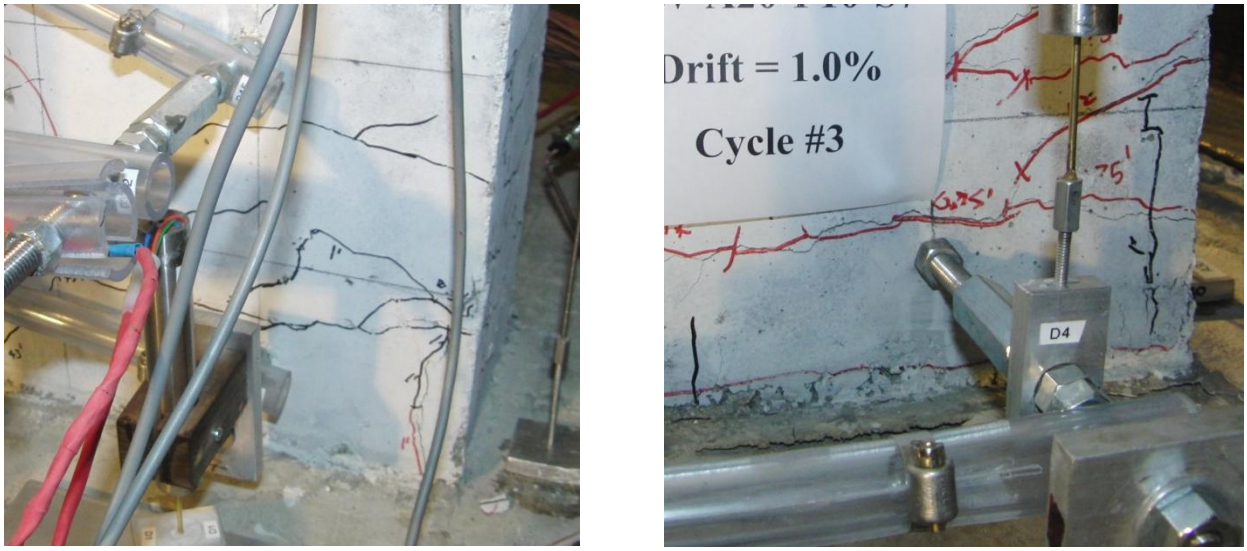

Figure 6-9 RW-A20-P10-S63: North (left) and south (right) wall boundaries at 1.0% drift after third cycle

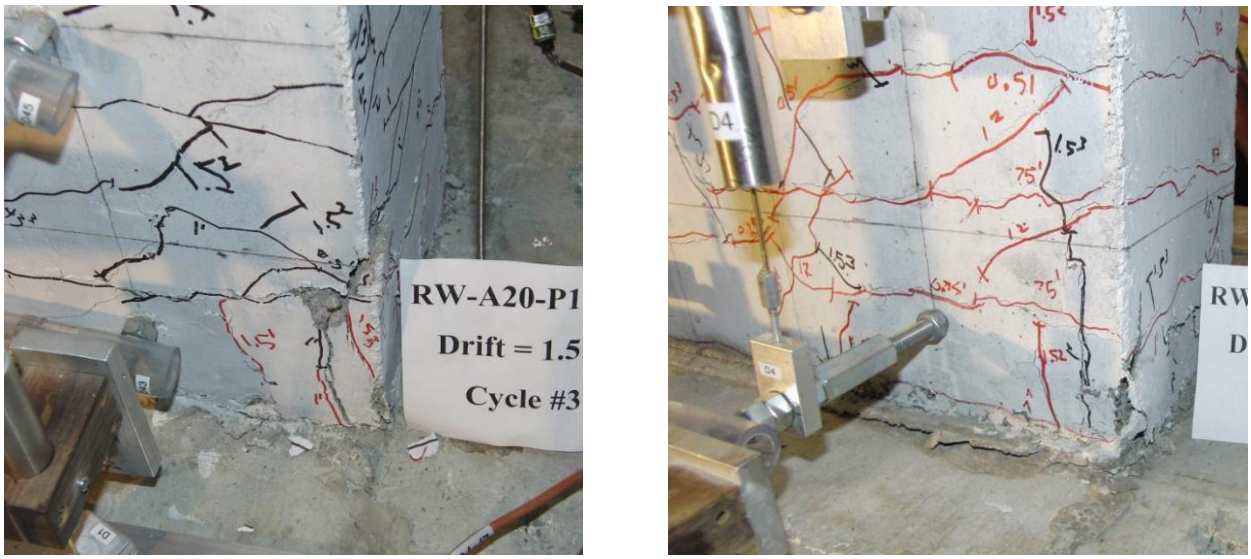

Figure 6-10 RW-A20-P10-S63: North and south wall boundaries at 1.5% drift after third cycle

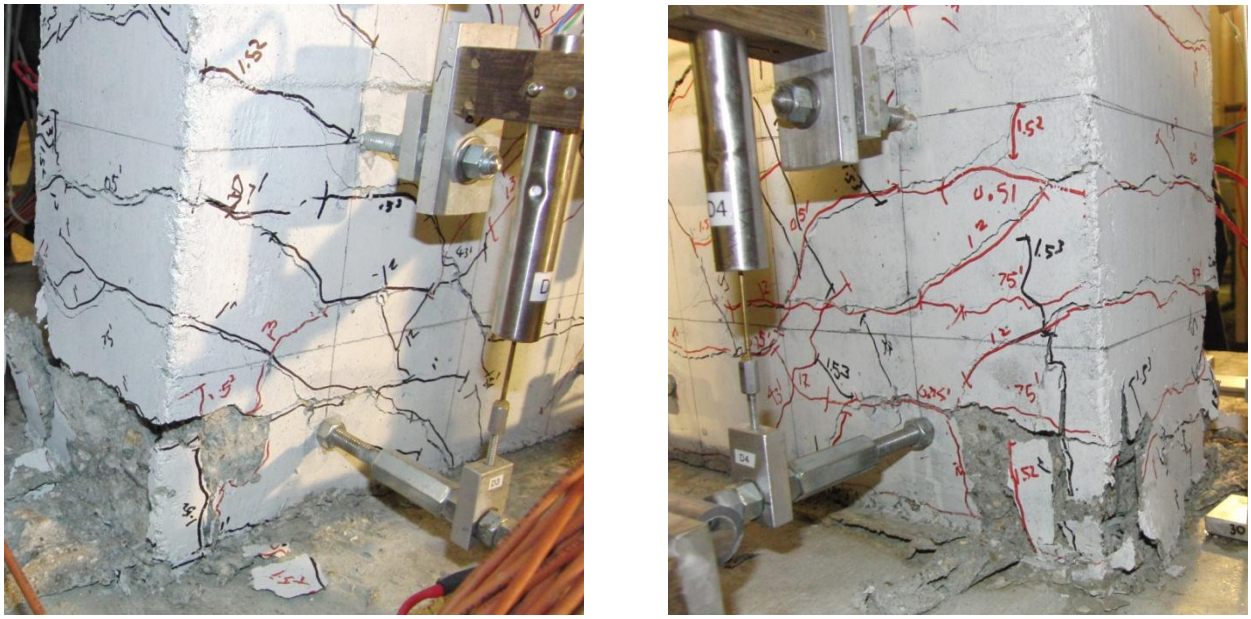

Figure 6-11 RW-A20-P10-S63: North and south wall boundaries at 2.0% drift after third cycle

Figure 6-12 RW-A20-P10-S63: North and south wall boundaries at 3.0% drift after first cycle

Figure 6-13 RW-A20-P10-S63: North and south wall boundaries at end of test

6.2.3 Specimen RW-A15-P10-S51

The third wall specimen had the same longitudinal boundary reinforcement and axial load ratios as the first wall specimen, but a lower aspect ratio (1.5 versus 2.0) and a slightly higher web reinforcement ratio (0.0032 versus 0.0027) because the lateral load corresponding to the nominal moment capacity was larger, leading to a higher design shear stress than for RW-A20-P10-S38.

First cracks in specimen RW-A15-P10-S51 formed during the first cycle of the third force-controlled level ($2V_y/3$; 240 kN or 54 kips) and were located in the lower portion of the wall, from the wall-foundation interface up to the height of approximately $0.5l_w$ above the interface. These cracks consisted of several horizontal flexural cracks along the wall boundaries and three major diagonal (shear) cracks on each side of the wall propagating from the boundaries toward the wall center. The propagation of cracks was observed to develop from the bottom to the top of the wall. Crack patterns at drift ratios of 0.5%, 1.5%, and at the end of the test are shown in Figure 6-14. More details on crack development of specimen RW-A15-P10-S51 over various lateral load or drift ratio levels are provided in Figures A-9 to A-13 in Appendix A.1.

First yielding at boundary longitudinal reinforcement occurred at a drift ratios of +0.55% and -0.51% at lateral loads of +527 and -506 kN (118.5 and -113.7 kips). After yielding, several new flexural cracks formed along the edges of the wall while the quantity of shear cracks remained quite stable. Existing inclined cracks continued to extend closer to the other wall boundary. The inclination of shear cracks ranged from approximately 35 to 63 degrees to the horizontal, with higher values for cracks forming at higher levels of the wall.

At a drift ratio of 1.0%, peak crack widths for horizontal and inclined cracks did not exceed 1.25 and 1.0 mm (0.049 and 0.039 in.), respectively; the maximum residual crack widths were 0.2 mm (0.0079 in.) for flexural cracks and 0.1 mm (0.0039 in.) for shear cracks. A few vertical cracks were observed at wall-foundation interface at wall boundaries at 0.75% drift. Minor spalling of concrete cover occurred at 1.0% drift (Figure 6-15) and extensive spalling of concrete cover was observed at drift ratio of 1.5% and 2.0% (see Figures 6-16, 6-17, and 6-18).

Peak lateral capacities were reached during the first cycle to 3.0% drift. Signs of deterioration of core concrete and buckling of boundary longitudinal reinforcement at the right (south) wall boundary were noted in the subsequent cycle (Figure 6-19). Peak crack widths at 3.0% drift reached 2.0 mm (0.079 in.) for horizontal cracks and 3.0 mm (0.12 in.) for diagonal cracks, whereas maximum residual widths for both types of cracks were 0.8 mm (0.031 in.).

When the wall was loaded in positive direction to 4.0% drift, crushing of core concrete of the south wall boundary and buckling of vertical boundary reinforcement occurred, which initiated diagonal tension failure along a major crack with an angle of about 40 degrees with the horizontal at the wall base (crack ∗ in Figure 6-14), with fracture of several horizontal web bars crossing the diagonal crack. As a result, the wall was able to resist only 41% of the peak strength at 4.0% drift. When reserved loading was applied, fracture of two longitudinal bars at the south wall boundary was observed, along with concrete crushing and buckling of longitudinal reinforcement at the north wall boundary, and the lateral load dropped to only 10% of the peak load. Photographs of two boundary zones of RW-A15-P10-S51 at the end of the test are shown in Figure 6-20.

Figure 6-14 RW-A15-P10-S51: Crack patterns at drifts of 0.5%, 1.5%, and at end of test

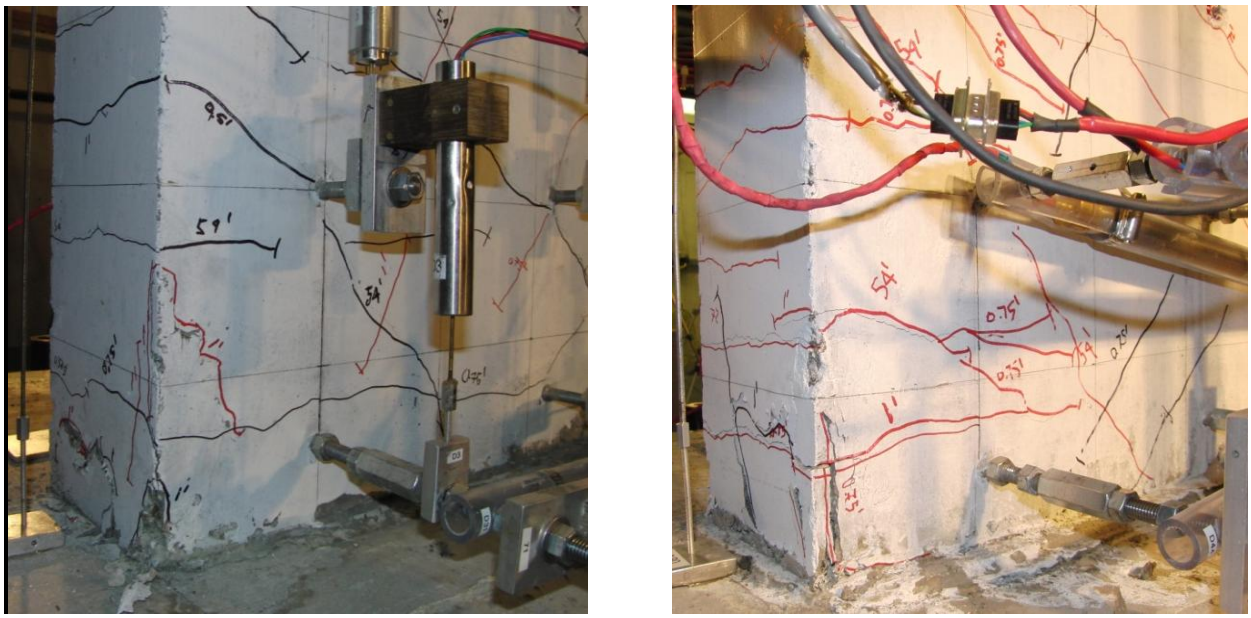

Figure 6-15 RW-A15-P10-S51: North (left) and south (right) wall boundaries at 1.0% drift after third cycle

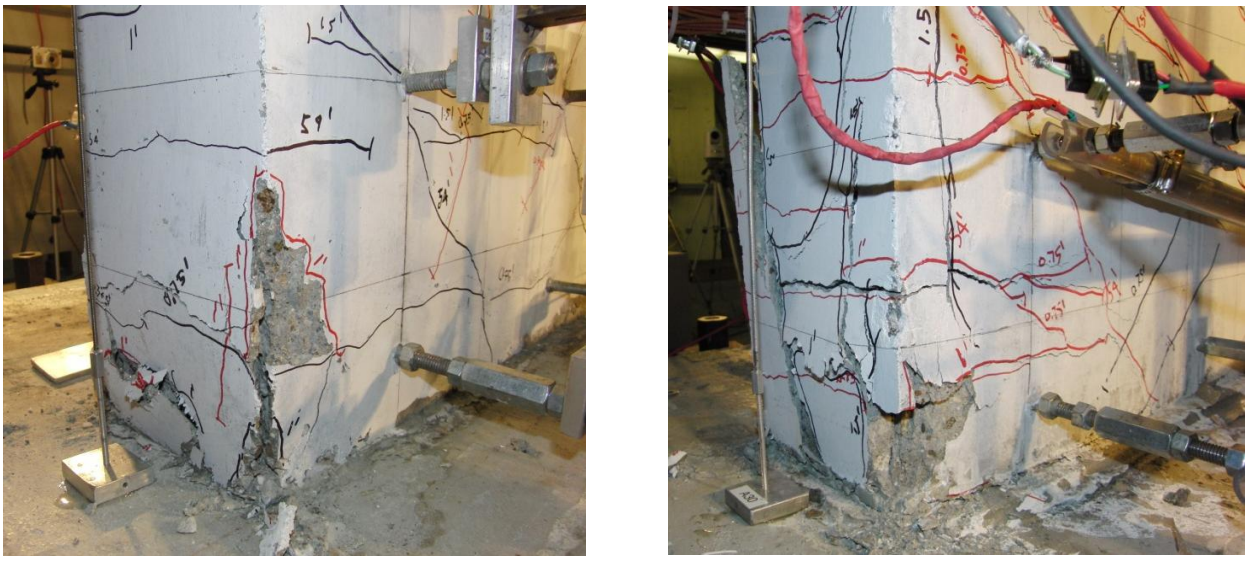

Figure 6-16 RW-A15-P10-S51: North and south wall boundaries at 1.5% drift after first cycle

Figure 6-17 RW-A15-P10-S51: North and south wall boundaries at 1.5% drift after third cycle

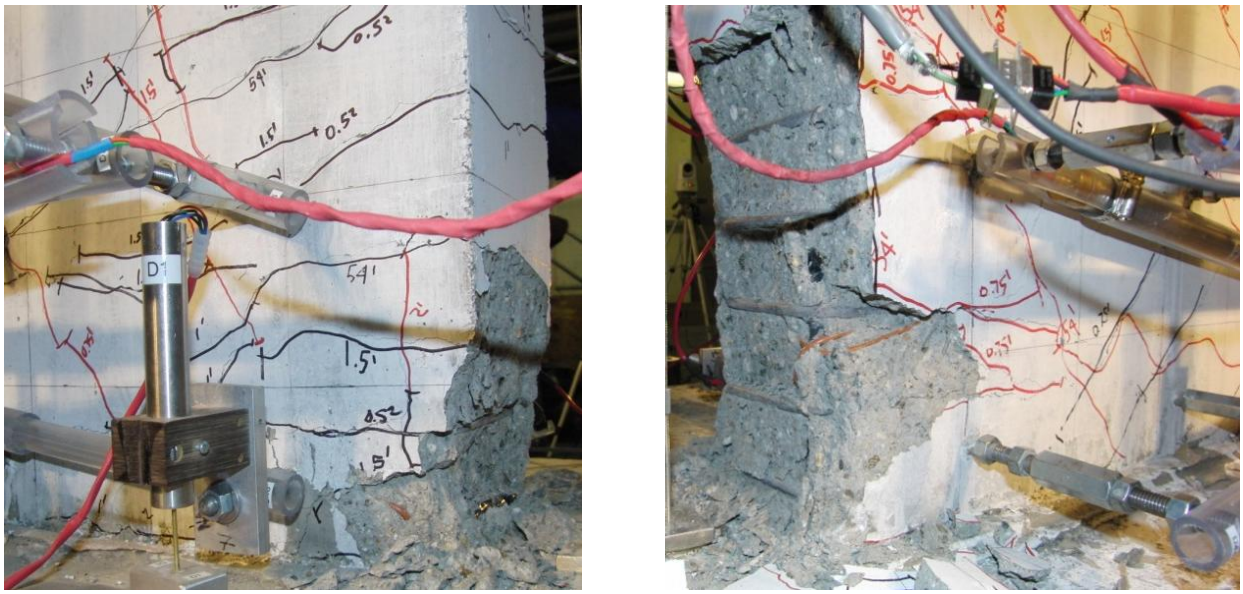

Figure 6-18 RW-A15-P10-S51: North and south wall boundaries at 2.0% drift after third cycle

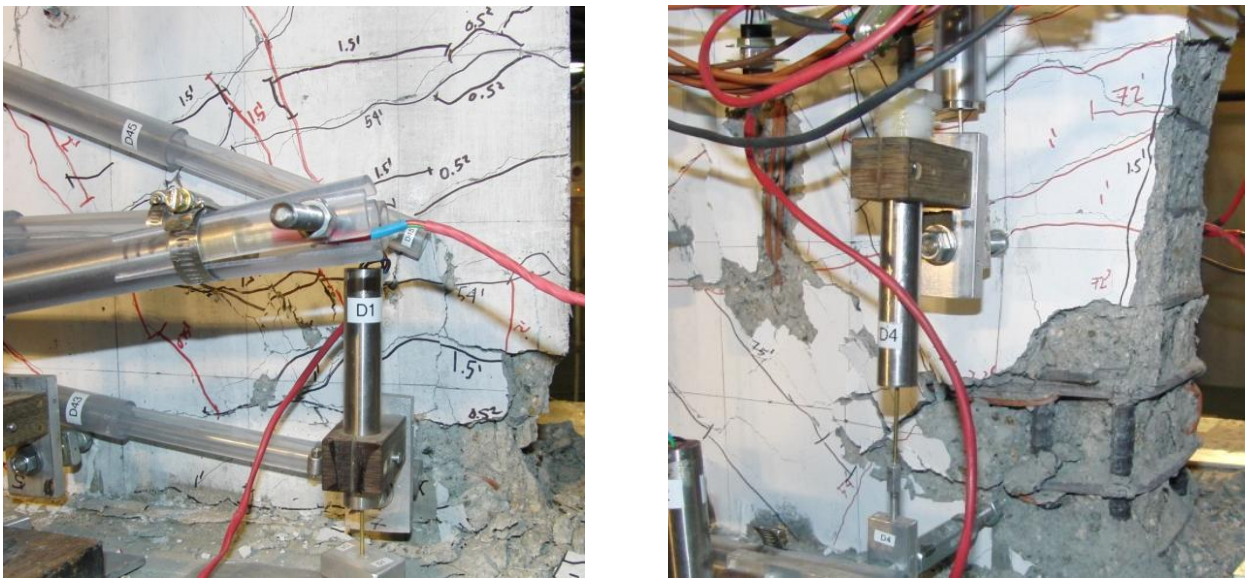

Figure 6-19 RW-A15-P10-S51: North and south wall boundaries at 3.0% drift after second cycle

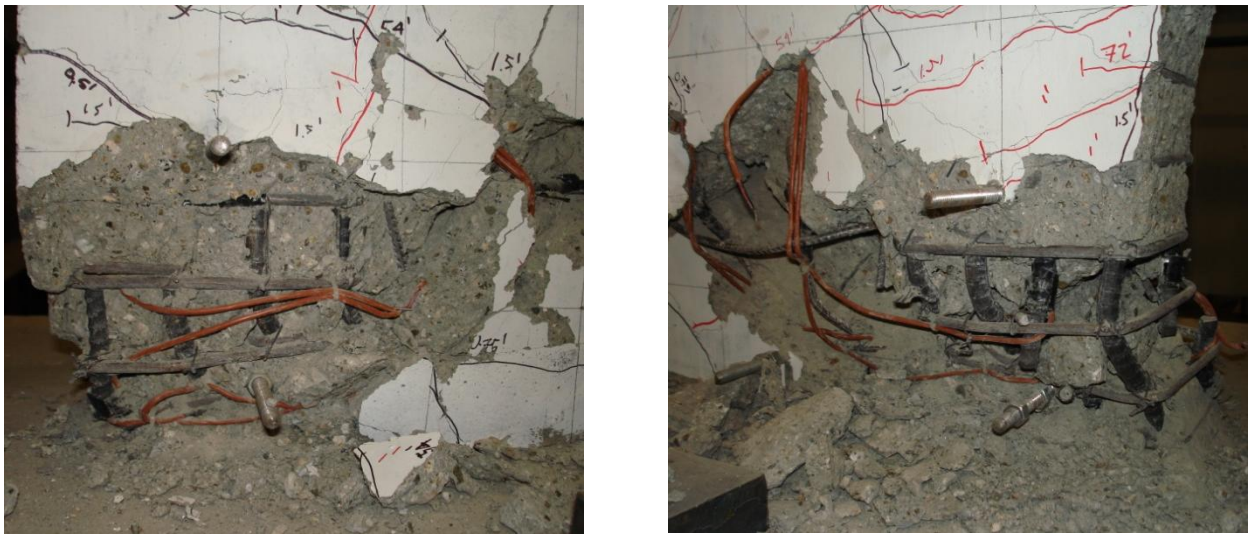

Figure 6-20 RW-A15-P10-S51: North and south wall boundaries at end of test

6.2.4 Specimen RW-A15-P10-S78

This wall had the same aspect ratio and axial load level as RW-A15-P10-S51; however, the actual average shear stress for this specimen is much higher ($7.0\sqrt{f_c'}$ versus $4.9\sqrt{f_c'}$ psi or $0.58\sqrt{f_c'}$ versus $0.41\sqrt{f_c'}$ MPa).

First cracking in RW-A15-P10-S78 was observed during the first cycle of the third force-controlled level ($V_y/2$; 356 kN or 80 kips), including horizontal (flexural) cracks between the wall-foundation interface to a height of approximately l_w (1.22m or 48 in.) at wall edges and three major diagonal (shear) cracks on each side of the wall (Figure A-14). Although the pattern and development of cracks in this wall was similar to that of RW-A15-P10-S51, the propagation of inclined cracks was more extensive in RW-A15-P10-S78. Crack patterns at drift ratios of 0.5%, 1.5%, and at the end of the test are shown in Figure 6-21. More details on crack

development of specimen RW-A15-P10-S78 over various lateral load or drift ratio levels are provided in Figures A-14 to A-17 in Appendix A.1.

First yielding of vertical boundary reinforcement was observed at drift ratios of +0.67% and -0.58%, which were slightly larger than those from RW-A15-P10-S51. At 1.0% drift, a noticeable crack crossing the wall-foundation block interface appeared and two approximately 100 mm (4 in.) - length vertical cracks formed at the south wall boundary (Figure 6-22). Horizontal peak crack widths as large as 1.0 mm (0.039 in.) and inclined peak crack widths as large as 0.8 mm (0.031 in.) were measured; maximum residual crack widths were 0.4 and 0.2 mm (0.016 and 0.0079 in.) for horizontal and inclined cracks, respectively. Cover concrete spalling was observed over lengths of nearly 25 mm (1 in.) at 1.5% drift (Figure 6-23) and about 75 mm (3 in.) at 2.0% drift (Figure 6-24).

Peak lateral loads were observed at 1.5% lateral drift for both directions. Maximum horizontal peak crack width grew modestly to 1.25 mm (0.049 in.), whereas maximum inclined peak crack width increased quickly to 1.5 mm (0.059 in.); residual crack widths for these two types of cracks reached 0.5 and 0.6 mm (0.020 and 0.024 in.), respectively.

During the first cycle to 3.0% drift, modest spalling of cover concrete was observed along diagonal compressive concrete struts near the wall-foundation block interface at the wall boundaries. Accordingly, the lateral strength of the wall decreased to 92% and 90% of the peak load in positive and negative directions, respectively. At this drift level, maximum peak crack widths were 2.0 and 3.0 mm (0.079 and 0.12 in.), and maximum residual crack widths were 1.0

and 1.25 mm (0.039 and 0.049 in.), for horizontal and inclined cracks, respectively. Damage of two wall boundaries at 3.0% drift after the first cycle was shown in Figure 6-25.

As the wall was loaded in the positive direction during the second cycle to 3.0% drift, shear sliding was observed, followed by out-of-plane buckling at the south wall boundary. As a result, the wall lost about two-thirds of its peak lateral strength. When loading was reversed, out-of-plane buckling occurred at the north wall boundary, and the lateral load capacity dropped down to only 20% of the peak lateral load. Photographs of two boundary zones of RW-A15-P10-S78 at the end of the test are shown in Figure 6-26. Failure mechanism in RW-A15-P10-S78 is shown in Figure 6-27.

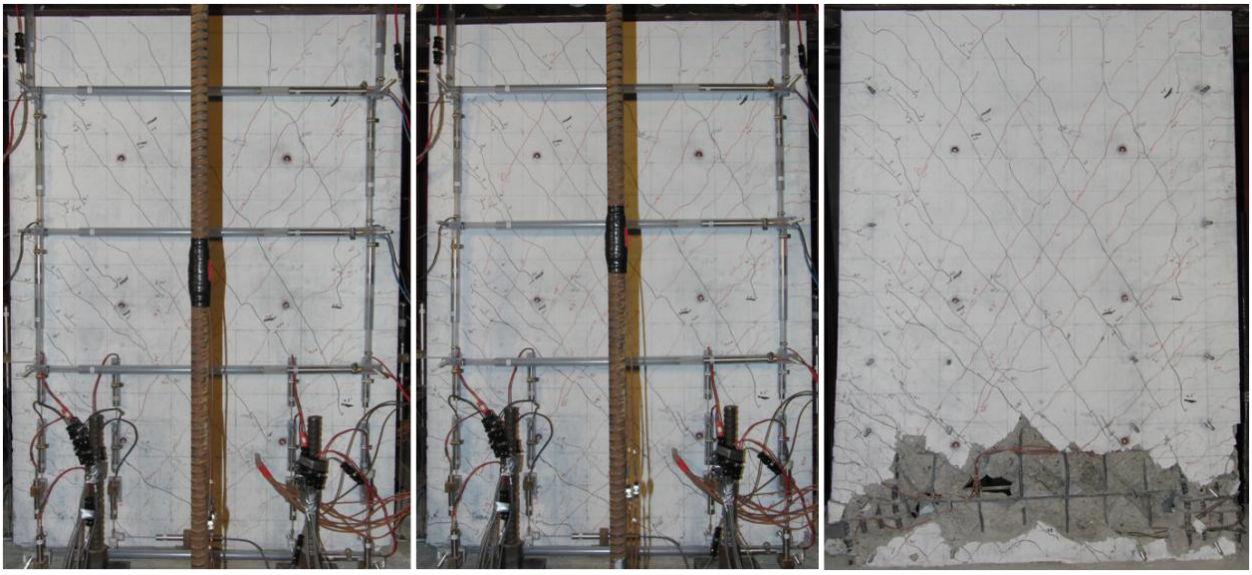

Figure 6-21 RW-A15-P10-S78: Crack patterns at drifts of 0.5%, 1.5%, and at end of test

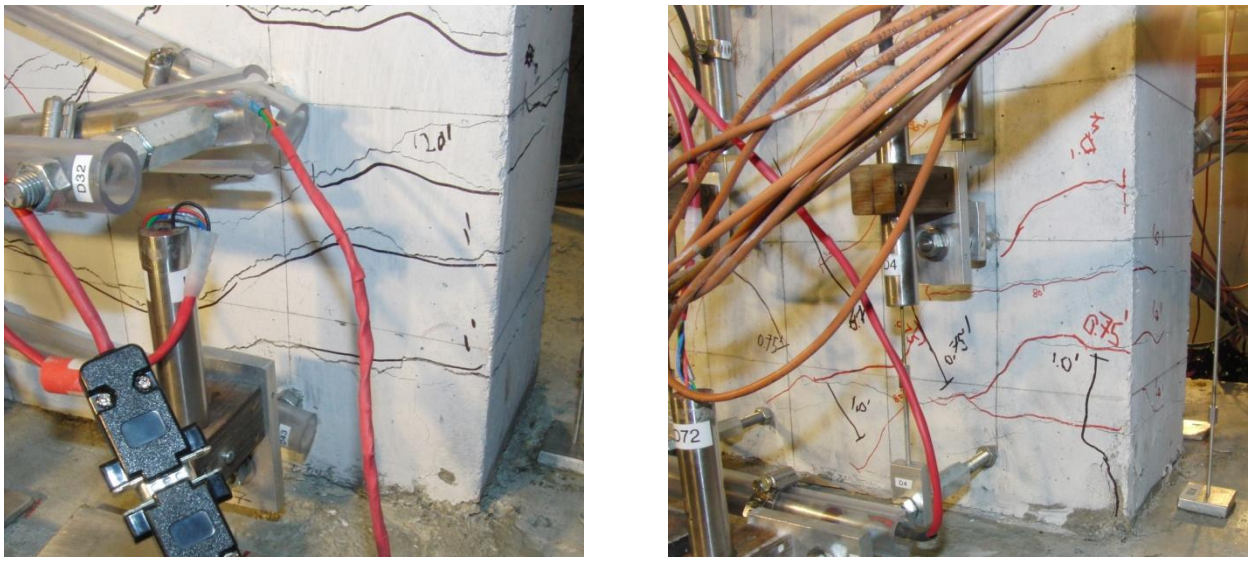

Figure 6-22 RW-A15-P10-S78: North (left) and south (right) wall boundaries at 1.0% drift after third cycle

Figure 6-23 RW-A15-P10-S78: North and south wall boundaries at 1.5% drift after third cycle

Figure 6-24 RW-A15-P10-S78: North and south wall boundaries at 2.0% drift after third cycle

Figure 6-25 RW-A15-P10-S78: North and south wall boundaries at 3.0% drift after first cycle

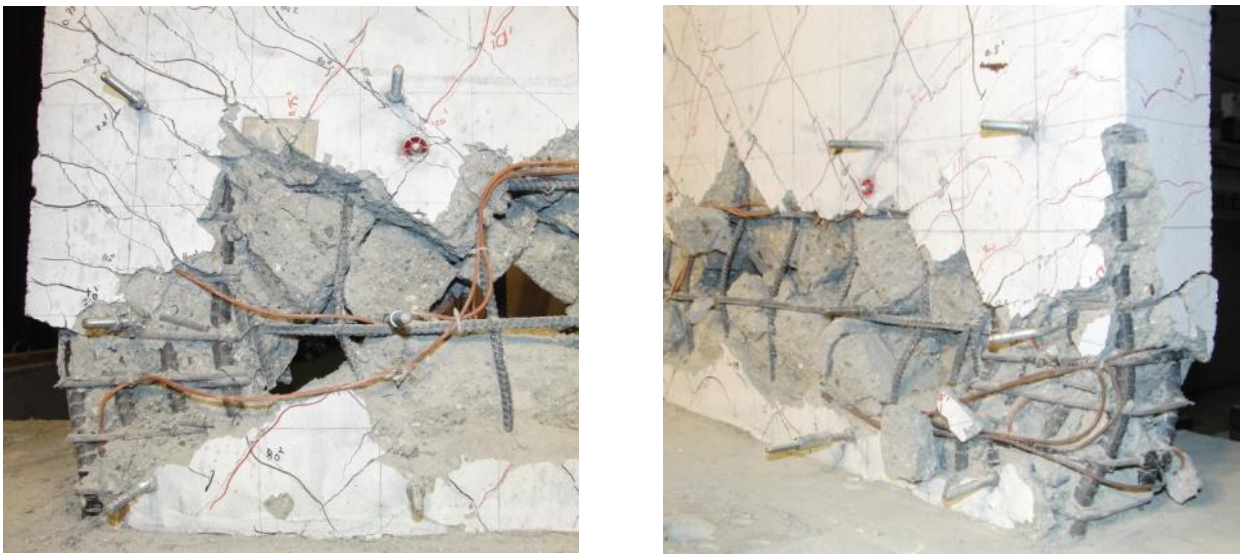

Figure 6-26 RW-A15-P10-S78: North and south wall boundaries at end of test

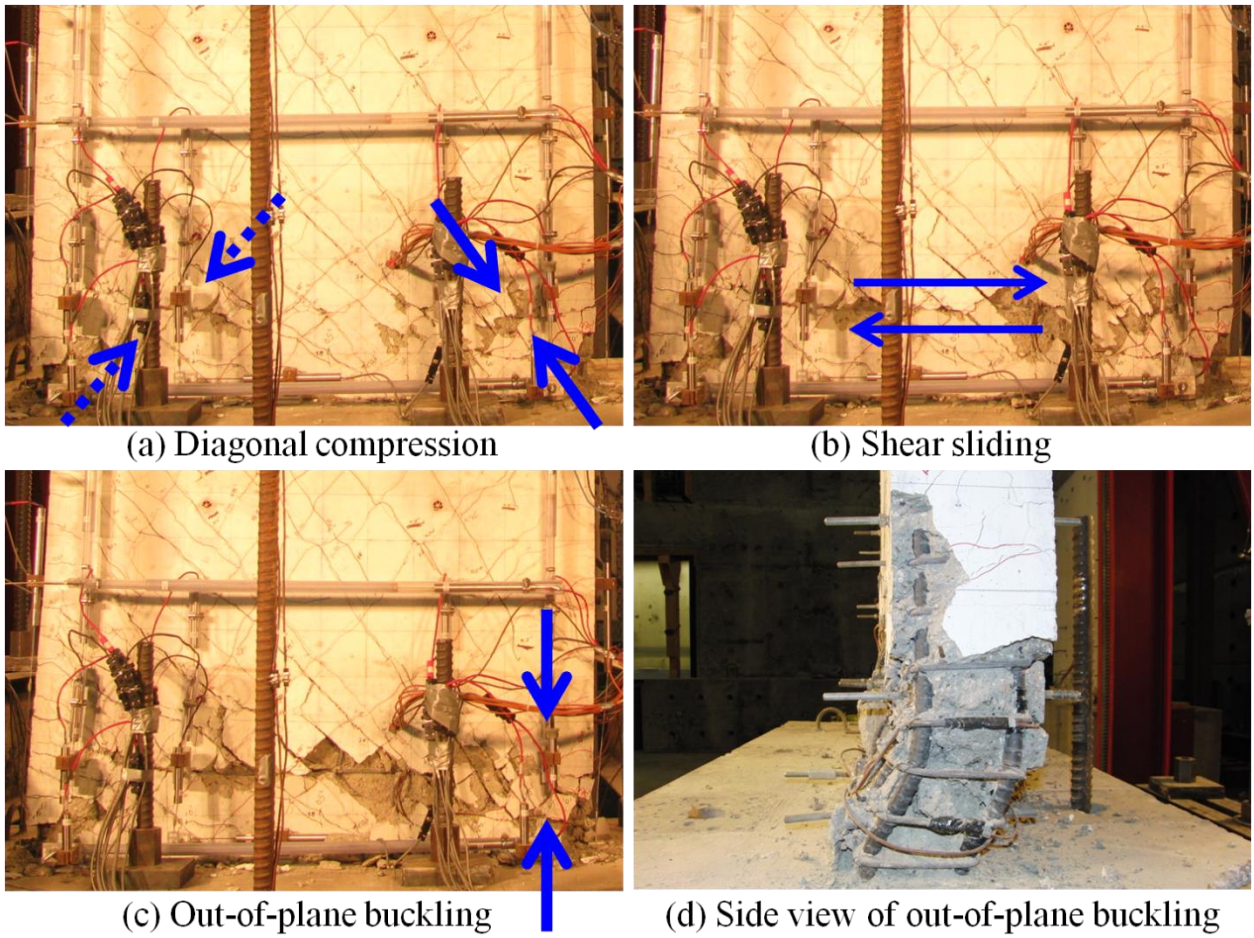

Figure 6-27 Failure mechanism in RW-A15-P10-S78

6.2.5 Specimen RW-A15-P2.5-S64

This test specimen had the same reinforcement configuration as specimen RW-A15-P10-S78, except a slightly smaller web reinforcement ratio. The main difference between these two walls was the axial load ratio $P/A_g f_c^{'}$, i.e., the axial load ratio of RW-A15-P2.5-S64 was only one-fourth of that of RW-A15-P10-S78 (0.016 versus 0.064).

First cracking in RW-A15-P2.5-S64 formed during the first cycle of the second force-controlled level ($V_y/4$; 156 kN or 35 kips), and consisted of one or two short diagonal (shear) cracks on each side of the wall (Figure A-18). The propagation of cracks in this wall was similar to that of RW-A15-P10-S78; however, the angle of inclined cracks was shallower in RW-A15-P2.5-S64. The inclination of shear cracks increased when they became closer to the opposite boundary zone. Due to the lower axial load ratio, diagonal cracks in this specimen were wider than those in RW-A15-P10-S78. Maximum peak inclined crack widths in RW-A15-P2.5-S64 were 2.0 and 3.0 mm (0.079 and 0.12 in.) at 1.5% and 2.0% drift, respectively, whereas those in wall RW-A15-P10-S78 were only 1.5 and 2.0 mm (0.059 and 0.079 in.). Crack patterns at drift ratios of 0.5%, 1.5%, and at the end of the test are shown in Figure 6-28. More details on crack development of specimen RW-A15-P2.5-S64 for various lateral load or drift ratio levels are provided in Figures A-18 to A-22 in Appendix A.1.

First yielding of boundary longitudinal reinforcement was observed at drift ratios of +0.61% and -0.56%, which were slightly less than those from RW-A15-P10-S78. Slip and extension of vertical reinforcement at the wall-foundation interface became significant at 0.75% drift, leading to the appearance of a noticeable horizontal crack at the wall-foundation block interface. Vertical cracks were observed at the wall-foundation block interface at the wall boundaries at 1.0% drift, indicating initial concrete cover spalling (Figure 6-29). Slight spalling of cover concrete occurred at 1.5% drift, with spalling extending up to about 75 mm (3 in.) above the foundation block at the south wall boundary at 2.0% drift (Figures 6-30 and 6-31). The wall reached its maximum

lateral capacities at a drift ratio of 1.5% for both positive and negative loadings, which also was the case for RW-A15-P10-S78.

Similar to RW-A15-P10-S78, during the first cycle to 3.0% drift, modest spalling of cover concrete was observed along diagonal compressive concrete struts near the wall-foundation interface at the wall boundaries, leading to a relatively significant strength degradation in both loading directions. Shear sliding was observed during the subsequent cycle, causing a substantial reduction of the wall lateral strength. Boundary longitudinal reinforcement buckled in the direction of the applied load (in-plane, Figure 6-32), versus the out-of-plane instability that was observed in RW-A15-P10-S78, with higher axial load. When loading was continued to 4.0% and 6.0% drift, the lateral strength progressively degraded with substantial shear sliding and in-plane buckling of boundary longitudinal bars, without loss of axial load capacity. Photographs of two boundary zones of RW-A15-P2.5-S64 at the end of the test are shown in Figure 6-32.

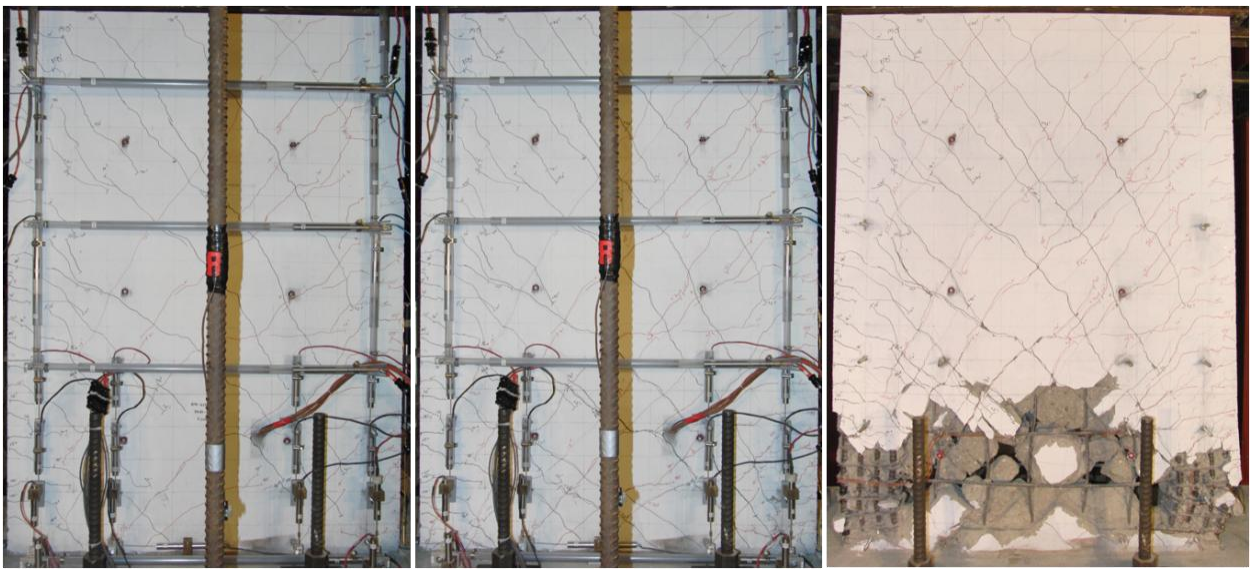

Figure 6-28 RW-A15-P2.5-S64: Crack patterns at drifts of 0.5%, 1.5%, and at end of test

Figure 6-29 RW-A15-P10-S64: North (left) and south (right) wall boundaries at 1.0% drift after third cycle

Figure 6-30 RW-A15-P10-S64: North and south wall boundaries at 1.5% drift after third cycle

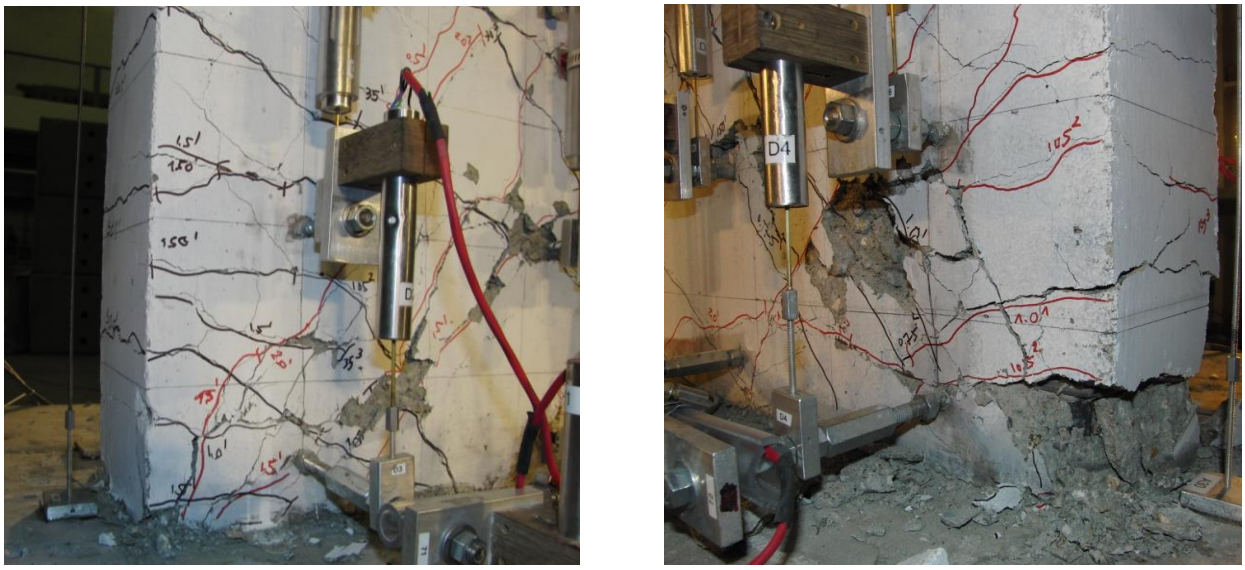

Figure 6-31 RW-A15-P10-S64: North and south wall boundaries at 2.0% drift after third cycle

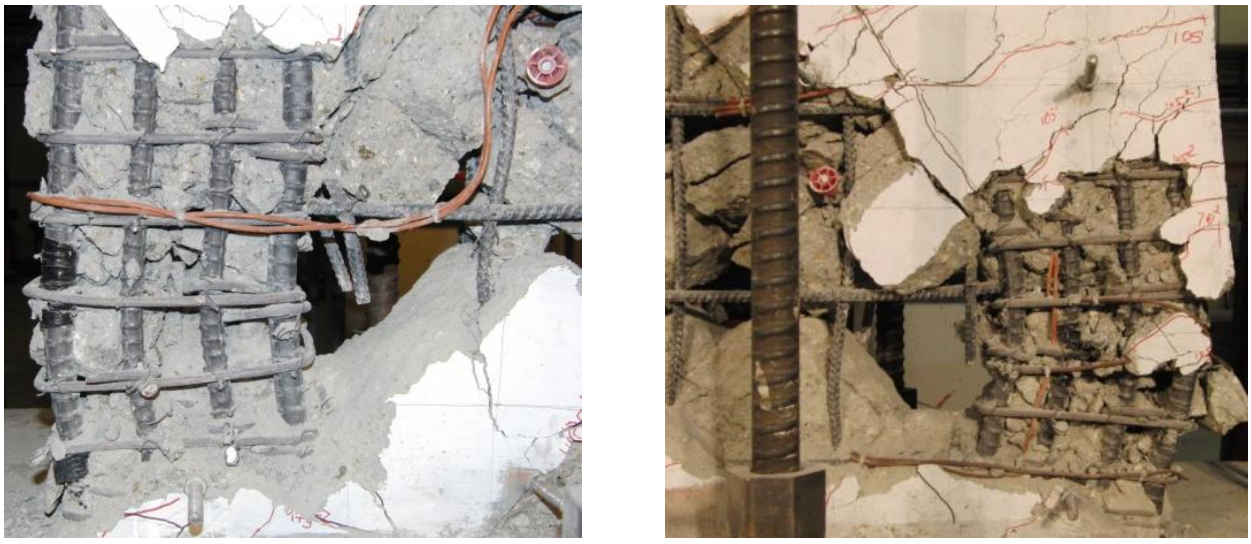

Figure 6-32 RW-A15-P10-S64: North and south wall boundaries at end of test

6.3 Lateral Load versus Top Lateral Displacement Relations

The lateral displacement at the top of wall specimens was determined by subtracting the measured top lateral displacement to the lateral displacements due to sliding and rotation of the foundation block, as the following.

$$\Delta_{total}^{top} = \Delta_{avg}^{top} - \Delta_{sld}^{b} - \Delta_{rot}^{b}$$

where Δ_{avg}^{top} is the average displacement obtained from two top horizontal sensors mounted between the test specimen and an external steel reference frame, sensors 66 and 67 (see LVDT layout in Figures 5.1 and 5.3). Two LVDTs were used to measure the top lateral displacement in order to account for any wall twisting during application of web in-plane lateral loading. Δ_{sld}^{b} is the sliding of the base (foundation) block, measured by an external horizontal sensor attached to the top of the foundation block, sensor 63. Δ_{rot}^{b} is the top lateral displacement due to the rotation of the base block based on the assumption that the base block rotated as a rigid body, i.e.:

$$\Delta_{rot}^{b} = \frac{\delta_1 - \delta_2}{L} H$$

where δ_1 and δ_2 are vertical displacements measured from two vertical sensors attached to the foundation block, sensors 61 and 62; L is the distance between these two gages; and H is the height of the wall section, i.e., the distance from the wall-foundation interface to the level where lateral load was applied to the wall. Measurements indicated that twisting of the wall, sliding and rotation of the foundation block were very small throughout all tests.

6.3.1 Walls with aspect ratio of 2.0

The lateral load versus top displacement relation for RW-A20-P10-S38 is shown in Figure 6-33. As can be seen from this figure, the peak lateral load of +481 kN (108.0 kips), which was 27% higher than the load at first yielding due to strain hardening in boundary longitudinal reinforcement and 3% higher than V_n^{ACI}, was reached at 2.3% drift under positive loading. Under negative loading, the peak lateral load was reached at -1.5% drift with the magnitude of -436 kN (-98.0 kips), which was 17% higher than first yielding load and 7% less than V_n^{ACI}. Gradual strength degradation was observed after the specimen reached the peak load. During the first cycle to 3.1% drift, the wall lateral capacity decreased 7% and 5% under positive and negative loadings, respectively. During the second cycle to the same drift ratio, lateral strength dropped sharply from 415 to 147 kN (93.3 to 33.0 kips), or to only 30% of the peak load, due to a diagonal tension failure as described in Section 6.2.1.

The lateral load-displacement response for RW-A20-P10-S63 is shown in Figure 6-34, with peak lateral loads of +742 and -717 kN (166.9 and -161.1 kips) reached at the same drift ratio of 2.8% during the first cycle to 3.0% drift for both positive and negative loading directions. The positive peak lateral load was 18% larger than the first yielding load and 3% higher than V_n^{ACI}, whereas the negative peak lateral load was 20% larger than the first yielding load and equal to V_n^{ACI}. Wall lateral strength dropped drastically to -278 kN (-62.4 kips) or 39% of the peak strength under negative loading during the second cycle to 3.0% drift, due to crushing of concrete and out-of-plane buckling of boundary longitudinal and some web vertical reinforcement at the north

wall boundary. A similar failure mode was observed at the south wall boundary when the wall was loaded in the opposite direction. When the test was stopped at drift ratio of 2.4%, the residual strength was only about 20% of the peak capacity.

The relations of lateral load versus top displacement for RW-A20-P10-S38 and RW-A20-P10-S63 are simultaneously plotted in Figure 6-35. The figure shows that the relations for the aspect ratio 2.0 walls are very similar, even with the variation in shear demand, although the failure modes were quite different.

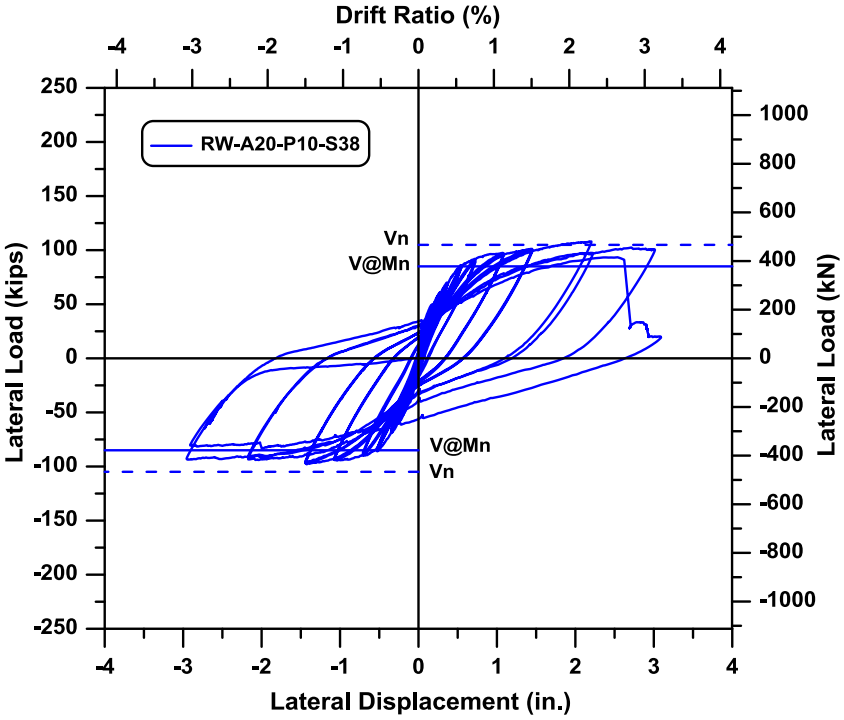

Figure 6-33 Top lateral displacement for RW-A20-P10-S38

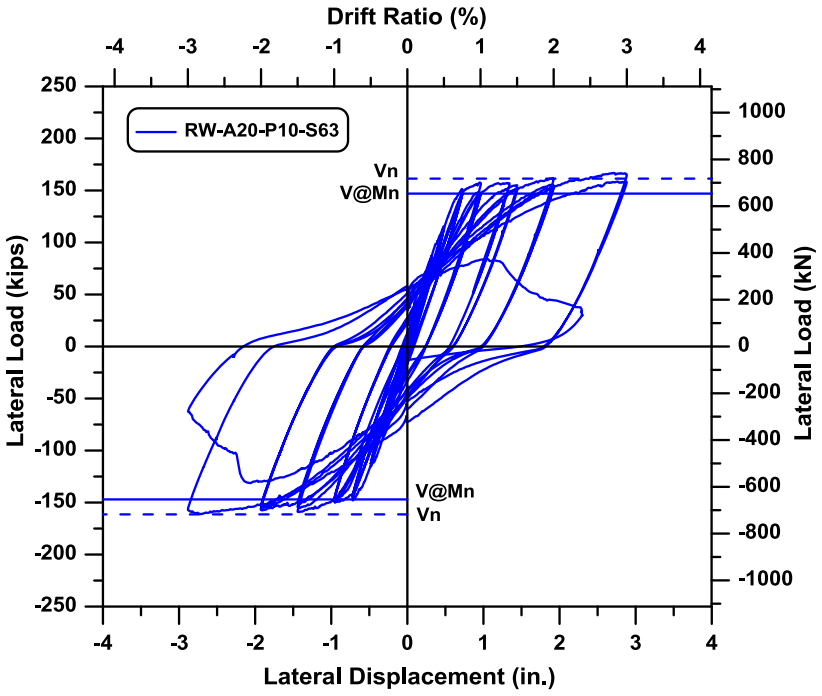

Figure 6-34 Top lateral displacement for RW-A20-P10-S63

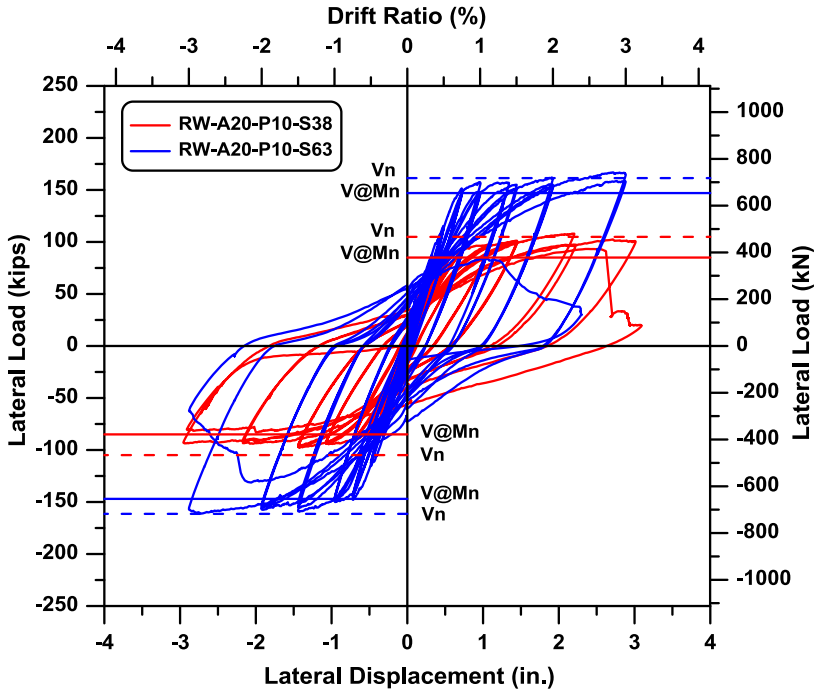

Figure 6-35 Top lateral displacements for RW-A20-P10-S38 and RW-A20-P10-S63

6.3.2 Walls with aspect ratio of 1.5

The measured lateral load-displacement relation for RW-A15-P10-S51 is shown in Figure 6-36. The relation indicates that peak lateral strengths of +603 and -575 kN (135.5 and -129.3 kips) were reached at 2.8% and -2.7%, respectively, during the first cycle to 3.0% drift. These peak loads are equivalent to 95% and 91% of V_n^{ACI}, respectively. Abrupt lateral strength degradation was observed in positive direction to 4.0% drift, with only 245 kN (55.1 kips), or 41% of the peak strength left, due to a diagonal tension failure initiated by crushing of core concrete of the south wall boundary and buckling of boundary longitudinal reinforcement, as mentioned in Section 6.2.3. Under opposite loading, the residual strength dropped to only 10% of the peak load.

The lateral load-displacement relation for RW-A15-P10-S78 is shown in Figure 6-37. The figure shows that peak lateral load of +859 and -823 kN (193.2 and -184.9 kips) were both measured at 1.5% lateral drift for positive and negative loading, or equal to 91% and 87% of V_n^{ACI}, respectively. Gradual strength degradation occurred after the peak capacities during subsequent cycles. During the second cycle to 3.0% drift, significant strength degradation occurred, with the residual strength of only 285 kN (64.0 kips), or 33% of the peak capacity, due to shear sliding and out-of-plane buckling at the south wall boundary. Under opposite loading, lateral strength decreased drastically to only -167 kN (-37.6 kips), or 20% of the peak lateral load.

The lateral load-displacement relation for RW-A15-P2.5-S64 is shown in Figure 6-38. As can be seen from this figure, peak lateral load of +670 and -660 kN (150.6 and -148.3 kips) were both

measured at 1.5% lateral drift for positive and negative loading, or only about 78% and 77% of V_n^{ACI}, respectively. The lateral capacity was almost unchanged during subsequent cycles to 2.0% drift. During the first cycle to 3.0% drift, the wall lateral load decreased to 81% and 55% of the peak loads in positive and negative directions, respectively, due to spalling of concrete as investigated in Section 6.2.5. During the next cycle, wall lateral load dropped sharply to only 36% and 26% of the peak strength for positive and negative loading, respectively. The residual strength was only 21% and 15% of the peak strengths under positive and negative directions at 4.0% drift. At 6.0% drift, the wall still had a residual lateral load capacity of 13% of the peak load for positive loading.

The lateral load-displacement relations for RW-A15-P10-S51 and RW-A15-P10-S78 are simultaneously plotted in Figure 6-39, whereas Figure 6-40 shows the lateral load-displacement relations for RW-A15-P10-S78 and RW-A15-P2.5-S64.

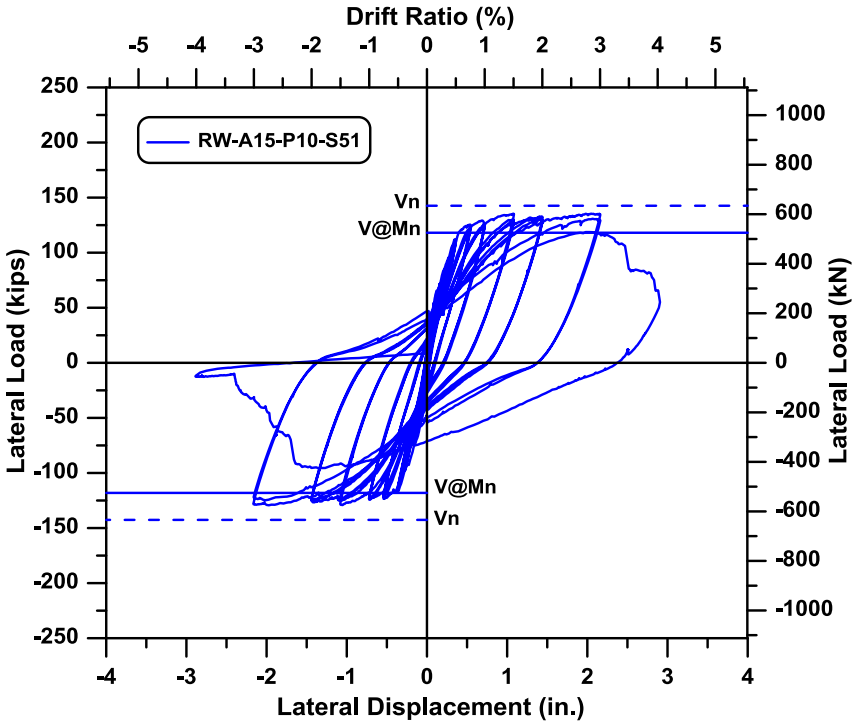

Figure 6-36 Top lateral displacement for RW-A15-P10-S51

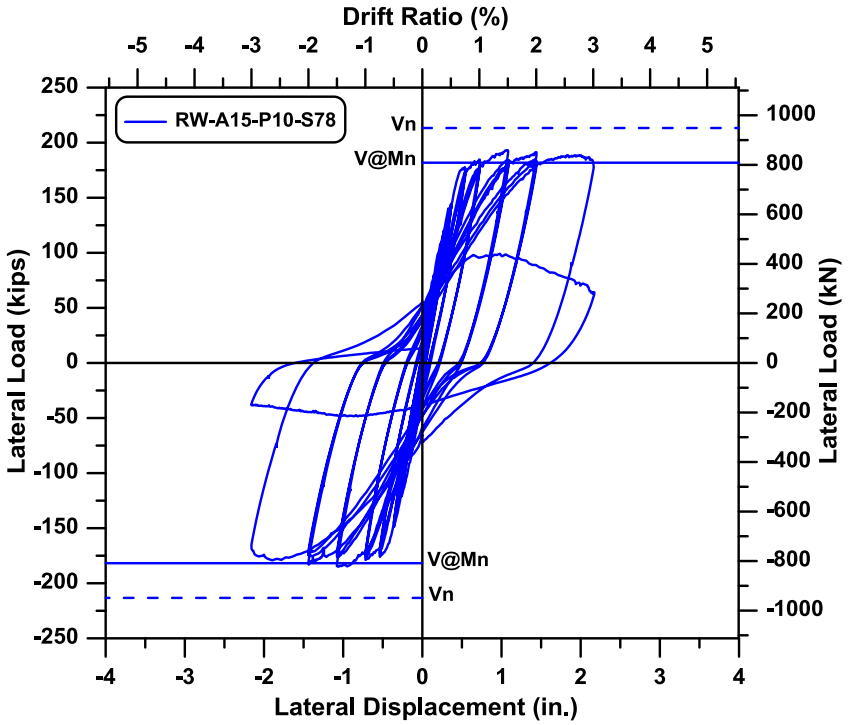

Figure 6-37 Top lateral displacement for RW-A15-P10-S78

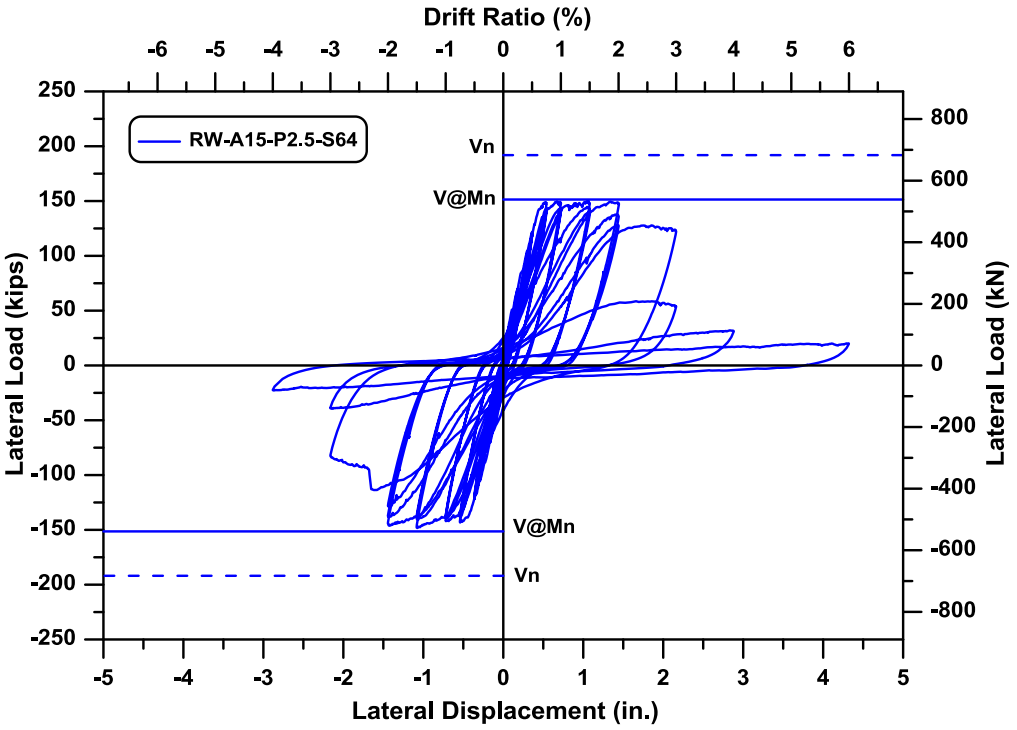

Figure 6-38 Top lateral displacement for RW-A15-P2.5-S64

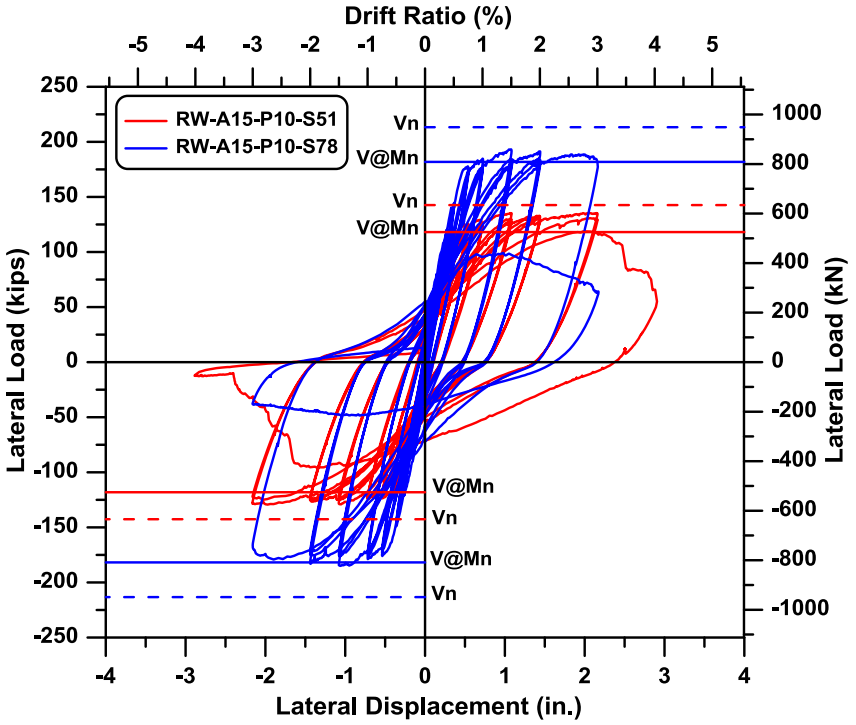

Figure 6-39 Top lateral displacements for RW-A15-P10-S51 and RW-A15-P10-S78

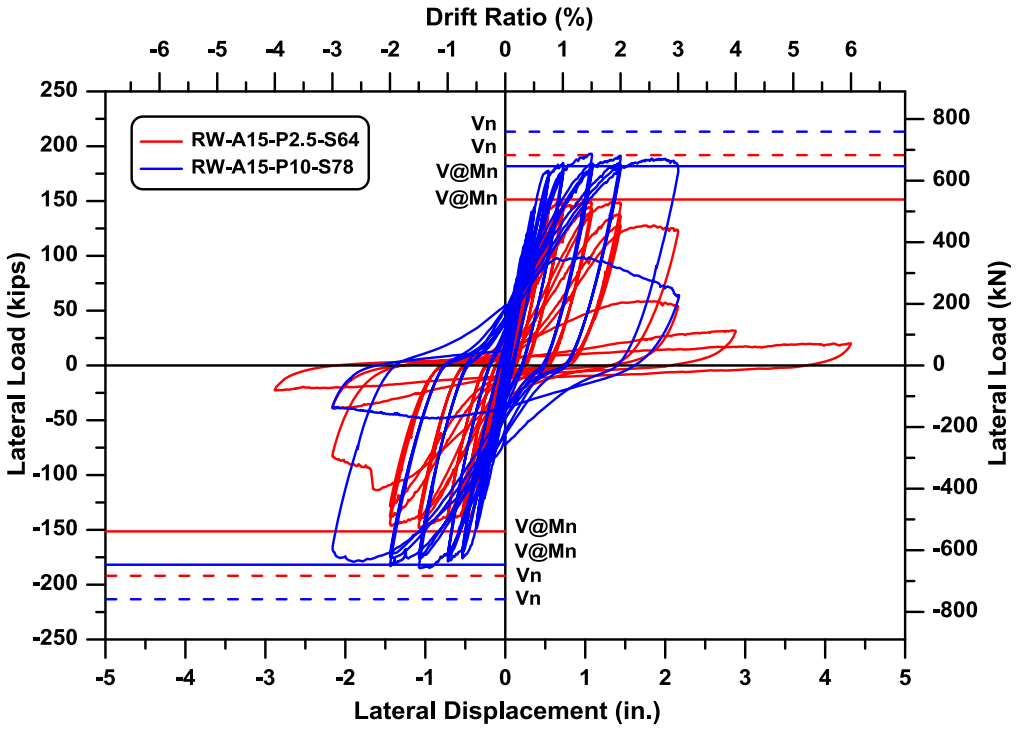

Figure 6-40 Top lateral displacements for RW-A15-P10-S78 and RW-A15-P2.5-S64

6.4 Total Displacement Profiles

Profiles of total lateral displacement over the wall height can be determined using either "external sensors" or "internal sensors". The first method, using external sensors, is the approach used to determine top lateral displacements described in Section 6.3. During the tests, especially after the appearance of diagonal (shear) cracks, wall expansion in the horizontal direction was observed and this deformation was measured by horizontal sensors over the wall length, sensors 31 to 37 on 2.0 aspect ratio walls or sensors 31 to 36 on 1.5 aspect ratio walls. Due to this horizontal expansion, it would be more accurate to measure the total displacement to the vertical center line of the wall, instead of the wall edge, as direct measurements from external sensors were attached to the side face of the wall. The expression calculating the top total lateral

displacement in Section 6.3 can be modified to determine the total displacement at various height levels, taking into account the horizontal expansion of the wall, as the following.

$$\Delta_{total} = \Delta_{ext} - \Delta^{b}_{sld} - \Delta^{b}_{rot} + \Delta_{\exp}$$

where Δ_{ext} is the displacement obtained from the external horizontal sensor mounted on an external steel reference frame at the height considered, sensor 64 or 65; Δ^{b}_{sld} is the sliding of the base (foundation) block, measured by an external horizontal sensor attached to the top of the foundation block, sensor 63; Δ^{b}_{rot} is the top lateral displacement due to the rotation of the base block based on the assumption that the base block rotated as a rigid body, as mentioned in Section 6.3.

$$\Delta^{b}_{rot} = \frac{\delta_1 - \delta_2}{L} H^{*}$$

where δ_1 and δ_2 are vertical displacements measured from two vertical sensors attached to the foundation block, sensors 61 and 62; L is the distance between these two gages; and H^{*} is the vertical distance from the top of the foundation block to the height considered.

$\Delta_{\exp}$ is one-half of the displacement obtained from horizontal sensors over the wall length, sensors 31 to 37 for Tests 1 and 2, or sensors 31 to 36 for Tests 3, 4, and 5. The horizontal expansion at the top of the wall was negligible due to the post-tensioning of the lateral load transfer assembly to the wall concrete to create the friction resistance necessary for load transfer. The negligible expansion at the top of the wall was confirmed from test measurements.

Therefore, the top lateral displacement can be determined without accounting for Δ_{exp}, as presented in Section 6.3.

The second method, method of using internal sensors installed with "X" configuration to find total displacement, is summarized as follows (Figure 6-41).

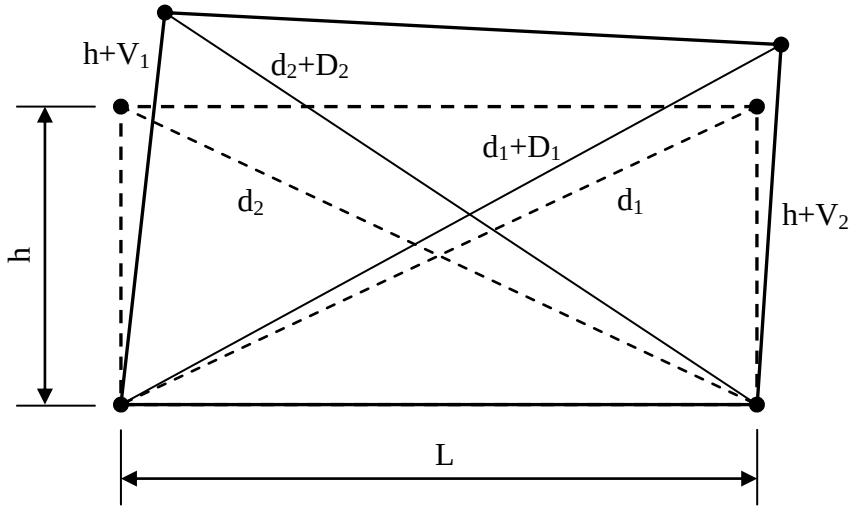

Figure 6-41 Deformation of a wall section

The total lateral displacement of the wall section is determined as

$$\Delta_{total}^{\sec} = \frac{\sqrt{(d_1 + D_1)^2 - (h + V_2)^2} - \sqrt{(d_2 + D_2)^2 - (h + V_1)^2}}{2}$$

where d_1 and d_2 are original lengths of the two diagonal sensors, D_1 and D_2 are displacements measured from these diagonal sensors, h is the height of the wall section, V_1 and V_2 are displacements measured from vertical sensors.

In this study, both of these methods were used to determine the total displacements. Although the comparison indicated that the results from these two methods were consistent (similar), external sensor approach was used as a primary method because it was not dependent on the accuracy of sensor gauge length measurements. Therefore, external sensor method was applied to find total displacement profiles. Internal diagonal sensors were installed to provide backup data and used to find total displacements for locations where external sensors were not available.

Profiles of total displacement over the wall height for Tests 1 to 5 are presented in Figures 6-42 to 6-46, respectively. In these profiles, total displacements were determined at maximum lateral load (for force-controlled cycles) or maximum displacement (for displacement-controlled cycles) during the first cycle under both positive and negative loadings. In the five figures, continuous lines represent positive loading, whereas the dashed lines represent negative loading. Total displacements were obtained at height levels of 24 in. (610 mm), 40 in. (1016 mm), 56 in. (1422 mm), 72 in. (1829 mm), and 96 in. (2438 mm).

As can be seen from these figures, profiles for walls with moderate shear stress levels, RW-A20-P10-S38 (Test 1) and RW-A15-P10-S51 (Test 3), are almost linear over the height at all drift ratios. For the remaining, i.e., walls with higher shear stress levels, larger total displacements were measured at the height of $l_w/2$ for drift ratios of 1.5% or 2.0%. The total displacements tend to be largest in RW-A15-P2.5-S64 (Test 5) where the axial load is the lowest one among five specimens, only $0.016A_g f_c^{'}$.

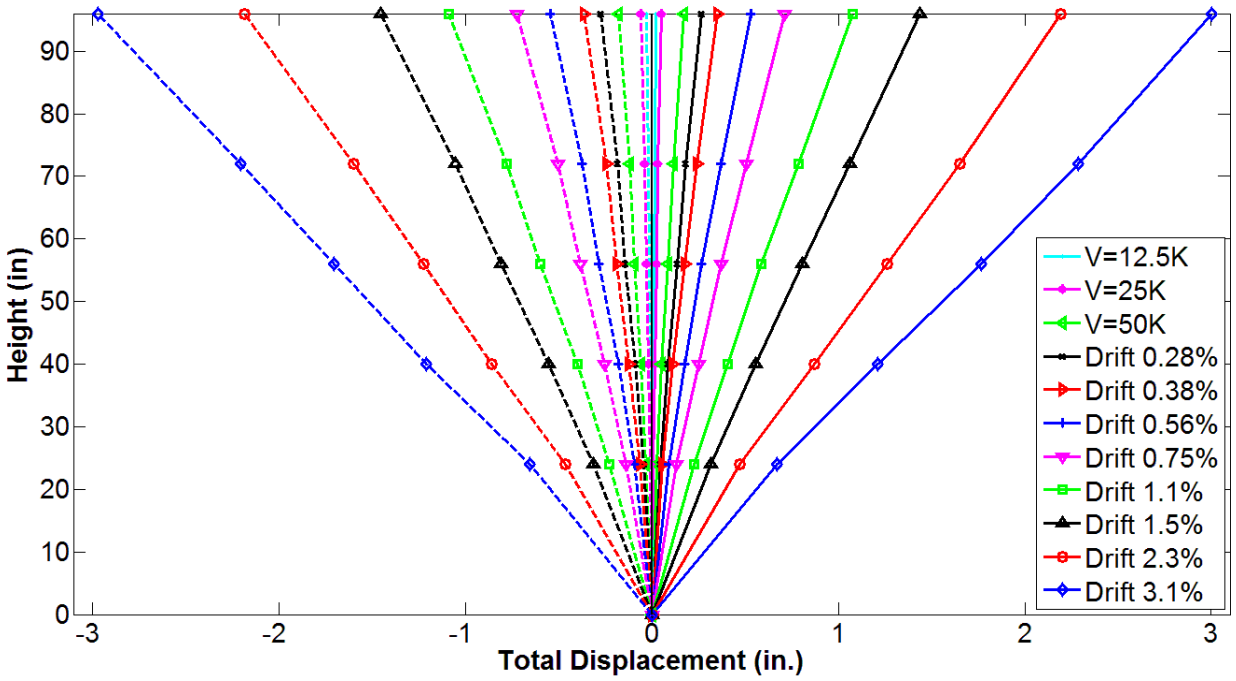

Figure 6-42 Total displacement profile for Test 1, RW-A20-P10-S38

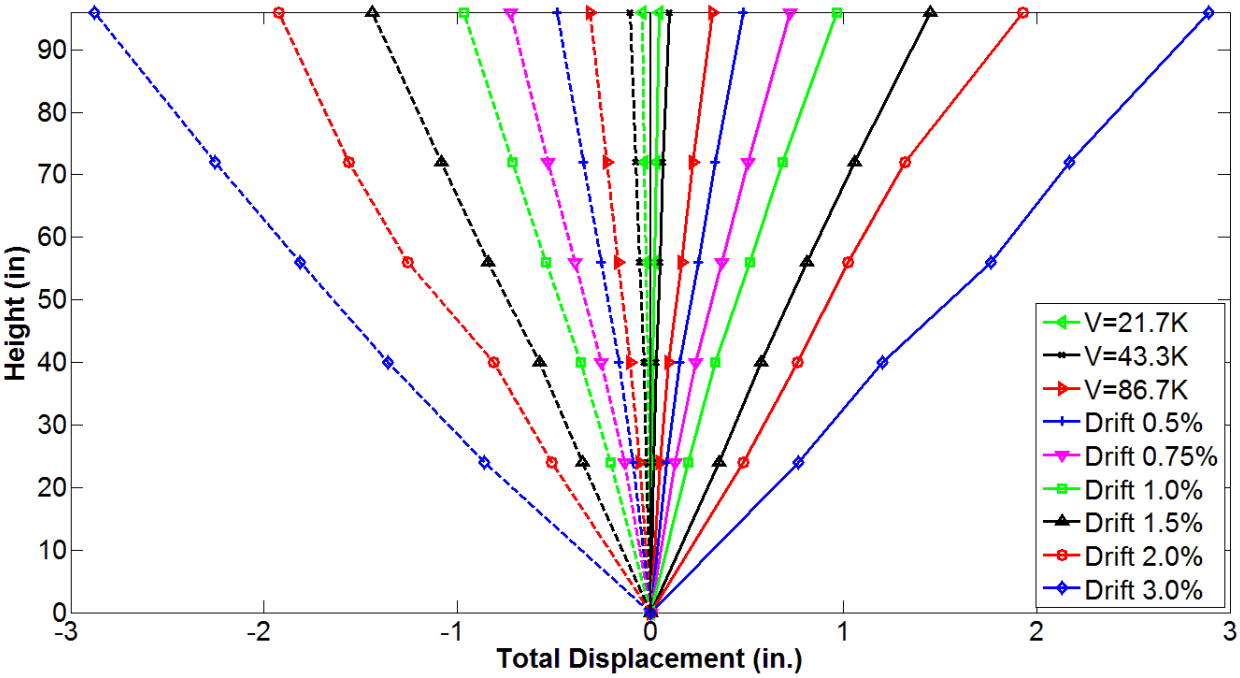

Figure 6-43 Total displacement profile for Test 2, RW-A20-P10-S63

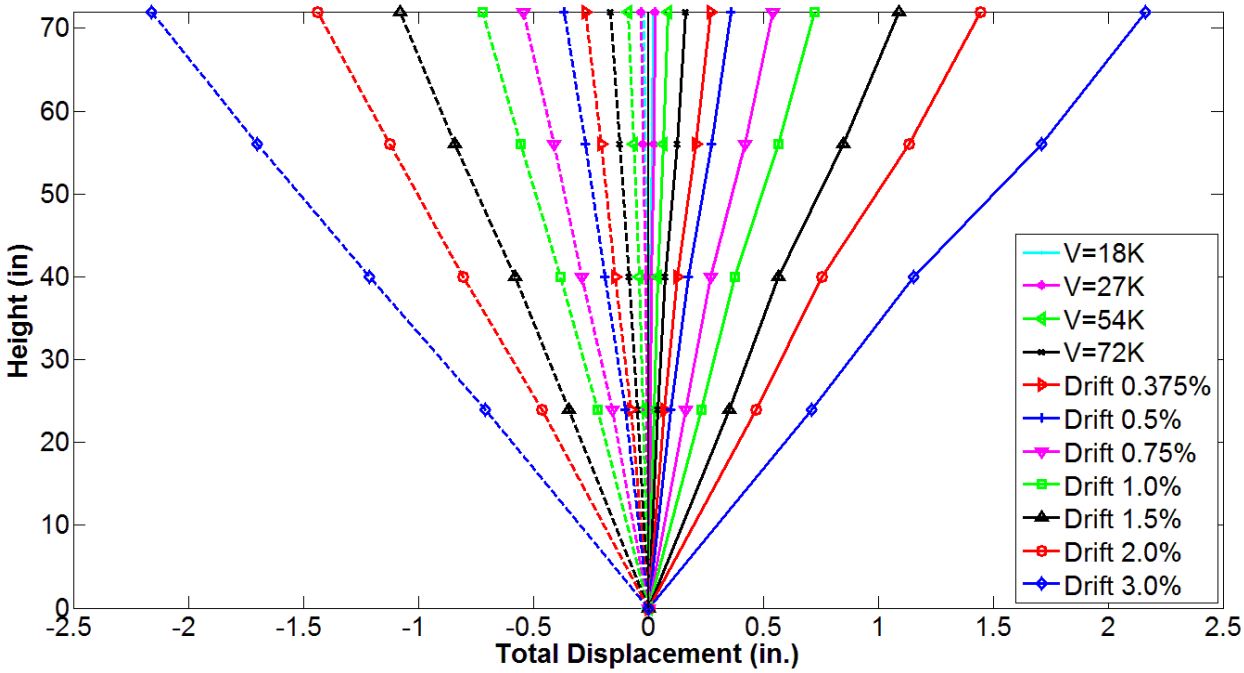

Figure 6-44 Total displacement profile for Test 3, RW-A15-P10-S51

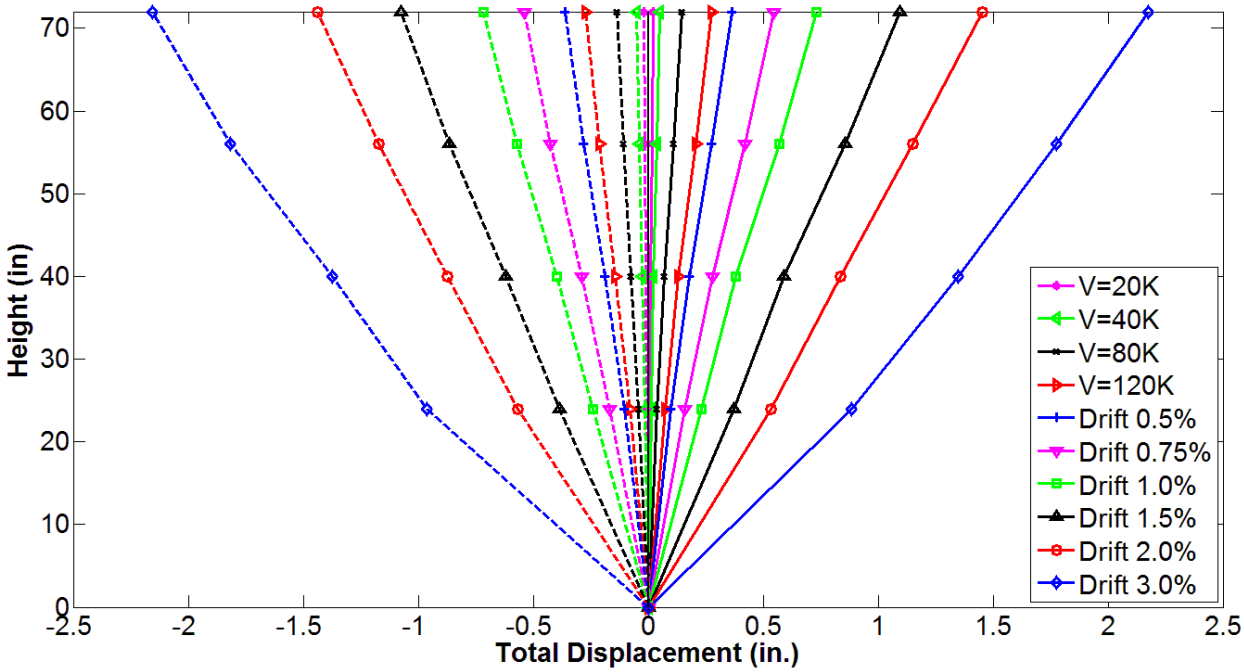

Figure 6-45 Total displacement profile for Test 4, RW-A15-P10-S78

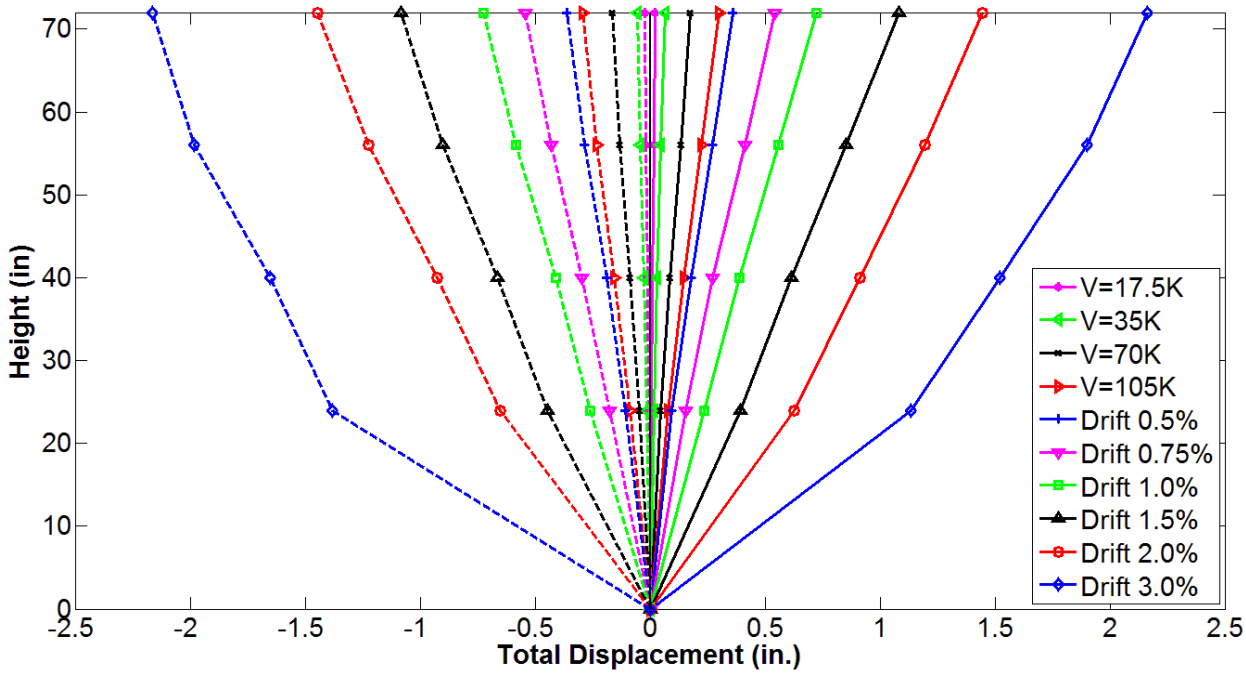

Figure 6-46 Total displacement profile for Test 5, RW-A15-P2.5-S64

6.5 Average Horizontal Strain Profiles

The average horizontal strain distributions were measured by sensors installed horizontally over the wall height at seven levels for the 2.0 aspect ratio walls (see Figure 5.1) and at six levels for 1.5 aspect ratio walls (see Figure 5.3). The sensors were mounted horizontally 2 in. (51 mm), 8 in. (203 mm), 24 in. (610 mm), 40 in. (1016 mm), 56 in. (1422 mm), 72 in. (1829 mm), for all wall specimens, and 96 in. (2438 mm) for 2.0 aspect ratio walls, above the wall-foundation block interface.

6.5.1 Average horizontal strain profiles for positive and negative loading

Profiles of average horizontal strain for positive and negative loading for Tests 1 to 5 are shown in Figures 6-47 through 6-51, respectively. In these profiles, average horizontal strains were determined at maximum lateral load (for force-controlled cycles) or maximum displacement (for displacement-controlled cycles) during the first cycle under positive and negative loading.

The figures indicate that average horizontal strain profiles were almost identical under both positive and negative loading. The profiles also show that at drift ratios equal to or less than 2.0%, average horizontal strains in test specimens were low near the bottom and the top of the wall, due to the restraint provided by the foundation block and the lateral load application device, and reached maximum values at a height of either 24 in. (610 mm) or 40 in. (1016 mm), which is lower than wall mid-height.

Comparison of horizontal strain profiles for RW-A15-P10-S51 and RW-A15-P10-S78 (Tests 3 and 4) for drift levels equal to or less than 2.0% reveals that maximum average horizontal strains in these two specimens are very similar, irrespective of the significant discrepancy in their shear stress levels, i.e., the nominal shear stress $V@M_n/A_{cv}\sqrt{f_c'}$ was 4.9 and 7.0 for Tests 3 and 4, respectively. These observations also apply to Tests 1 and 2, which had very different nominal shear stress, i.e., 3.6 versus 6.1, respectively, but very similar average shear strains. The results indicate that average shear strain was almost independent on average shear stress level. Actually, average horizontal strains were dependent on the amount of horizontal web reinforcement. The ratios $V_y^{Test4}/V_y^{Test3}=1.5$ and $V_{\max}^{Test4}/V_{\max}^{Test3}=1.4$ whereas $\rho_t^{Test4}/\rho_t^{Test3}=1.9$, indicating that

horizontal web reinforcement in Test 4 resisted horizontal deformations more effectively than that in Test 3, leading to smaller average horizontal strains.

During cycles before significant strength loss, i.e., cycles at drift levels of 2.0% and 3.0%, the peak values of horizontal strain developed appeared to depend primarily on wall failure modes. Maximum horizontal strain occurred at the height of $l_w/2$ above the foundation block for Tests 1 and 3 which had diagonal tension failure, and at the height of $l_w/6$ for Tests 2, 4, and 5, where significant shear sliding was observed.

Comparison of profiles for RW-A15-P10-S78 and RW-A15-P2.5-S64 (Tests 4 and 5) indicate that average horizontal strains for Test 5 were much larger than those of Test 4, despite that the average shear stress for Test 5 of $V@M_n/A_{cv}f_c^{'}$ was smaller than that for Test 4, i.e., 5.8 versus 7.0, and $V_y^{Test5}/V_y^{Test4} = V_{\max}^{Test5}/V_{\max}^{Test4} = 0.8$ whereas $\rho_t^{Test5}/\rho_t^{Test4} = 0.84$. The results indicate that axial load level had the greatest impact on the magnitude of average horizontal strain, i.e., average horizontal strain increased when axial load level decreased.

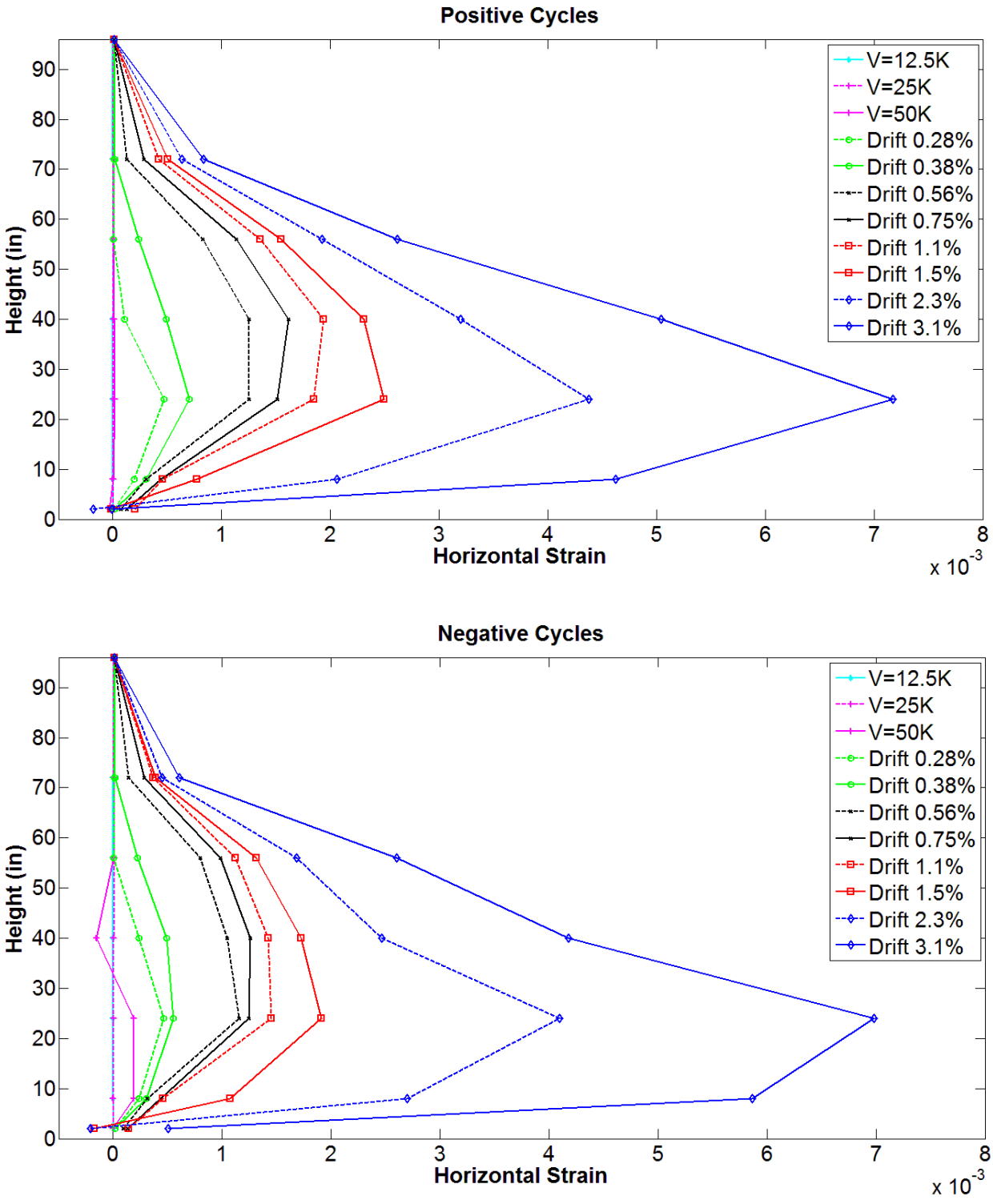

Figure 6-47 Average horizontal strain for Test 1, RW-A20-P10-S38

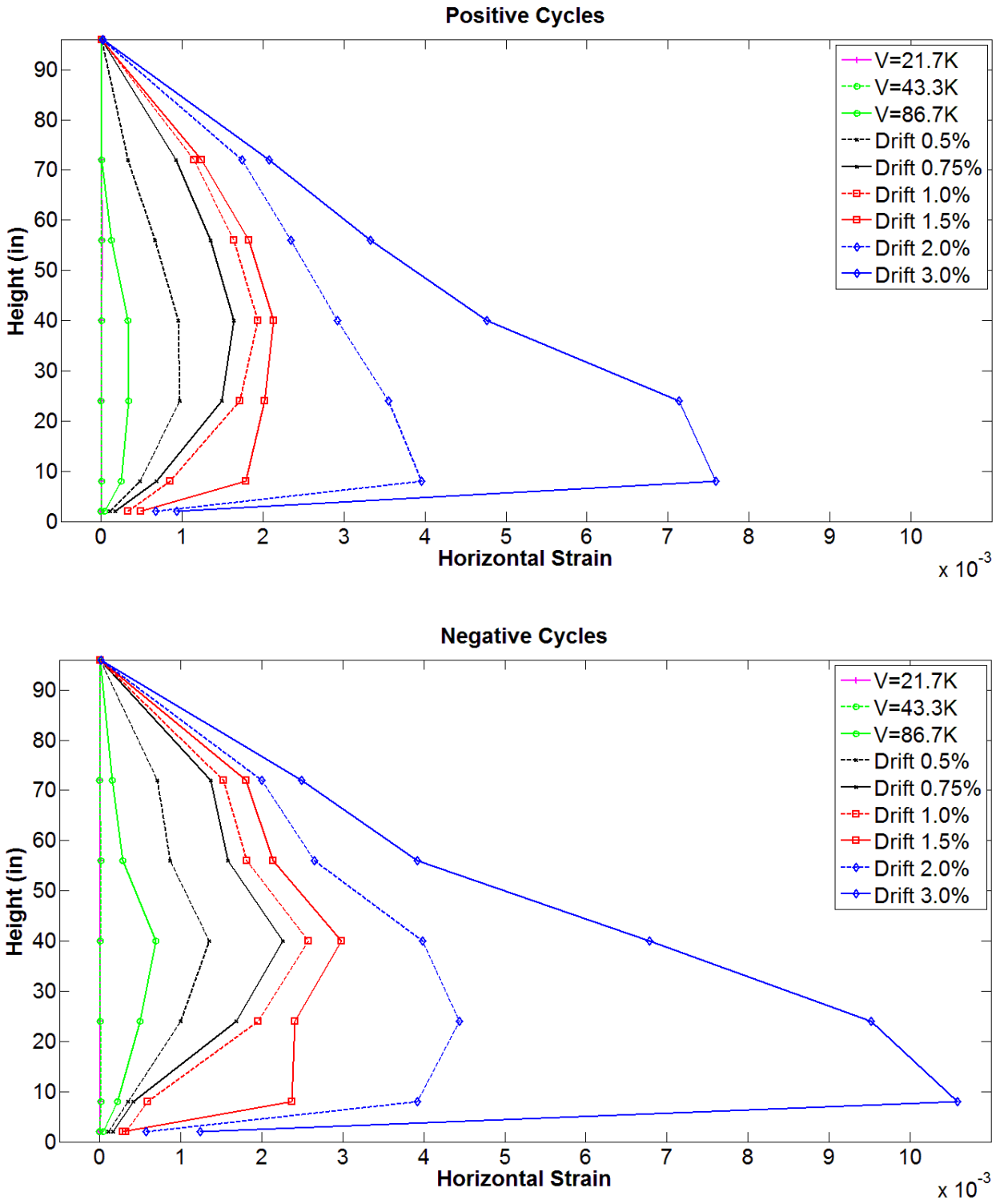

Figure 6-48 Average horizontal strain for Test 2, RW-A20-P10-S63

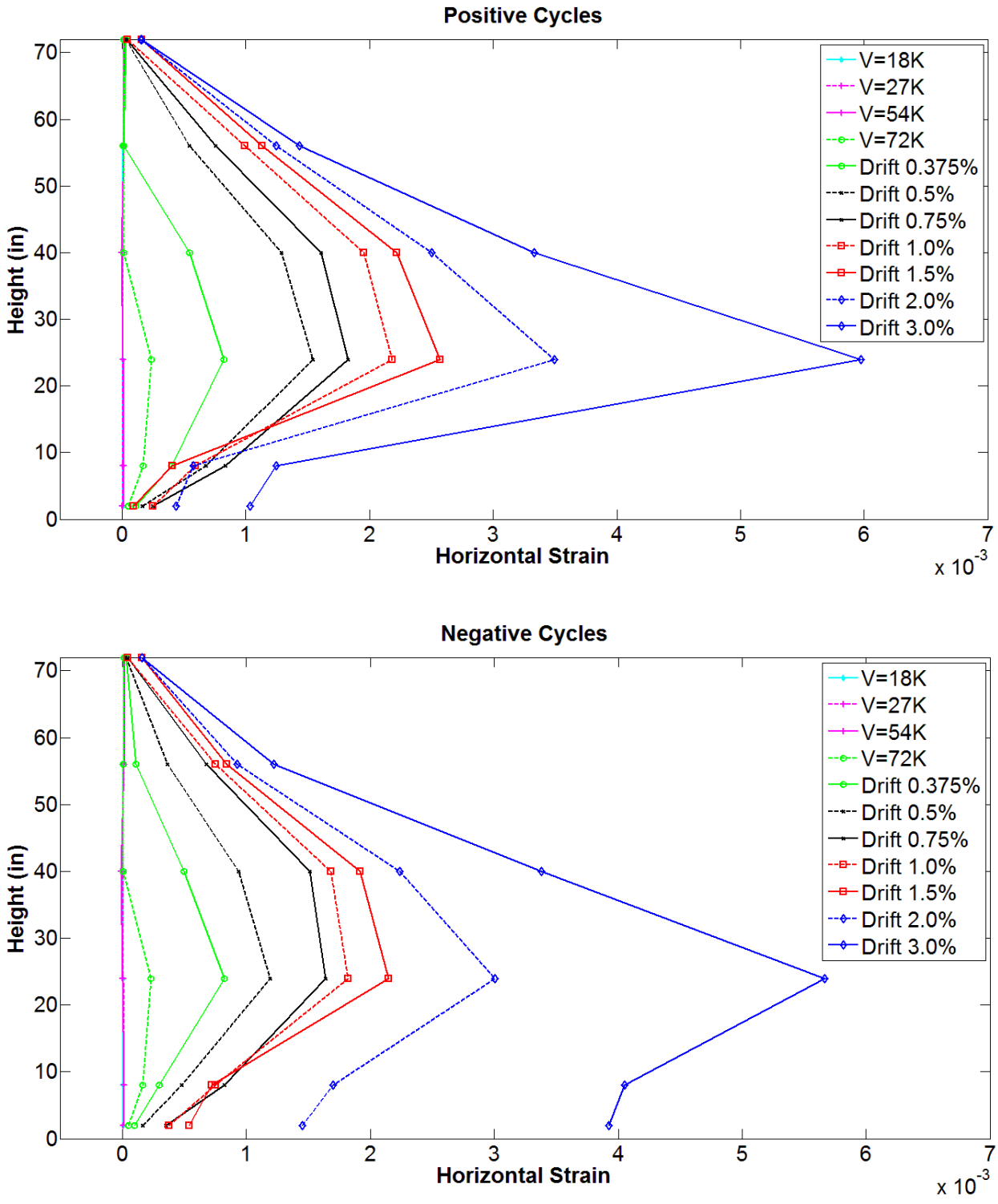

Figure 6-49 Average horizontal strain for Test 3, RW-A15-P10-S51

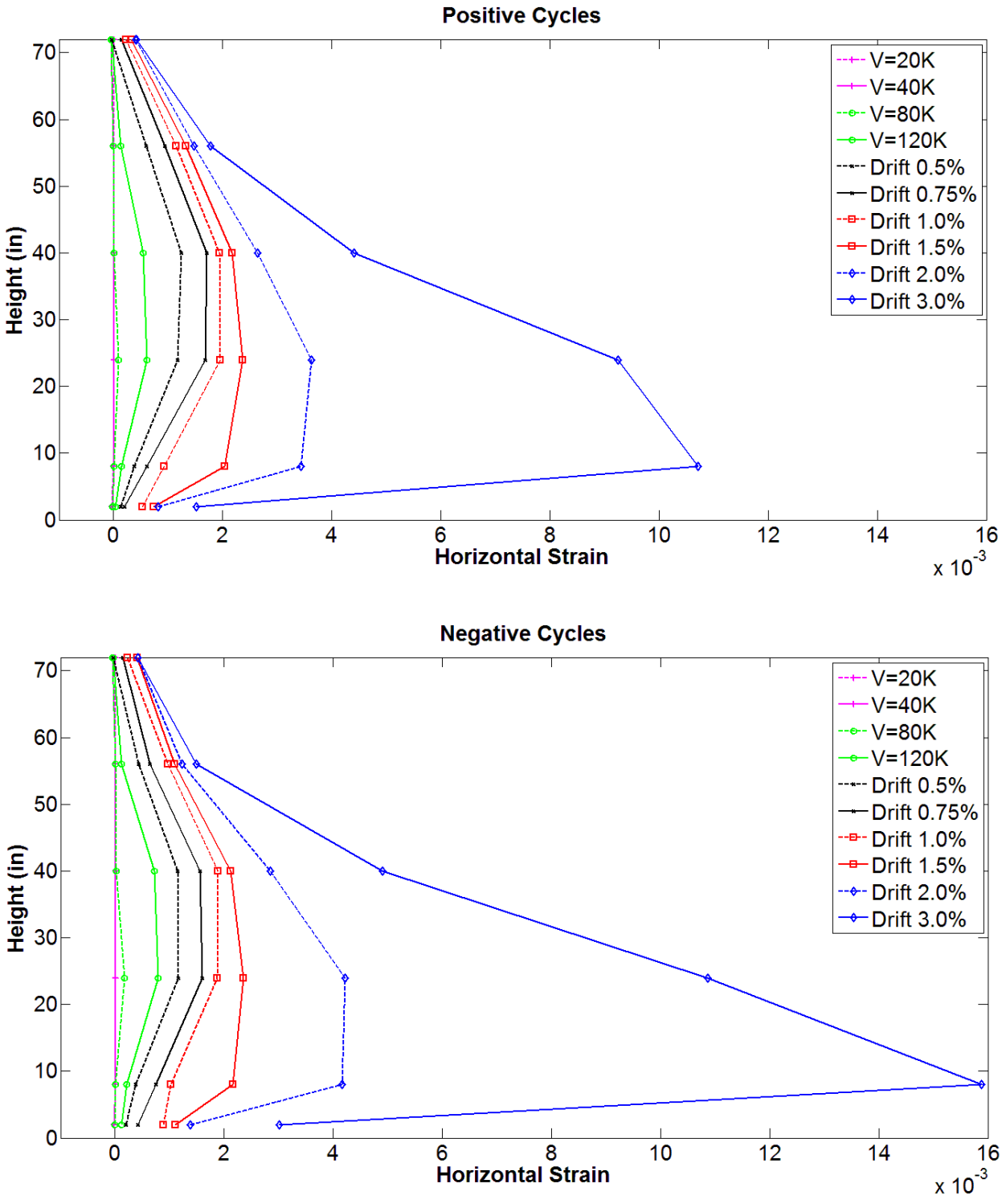

Figure 6-50 Average horizontal strain for Test 4, RW-A15-P10-S78

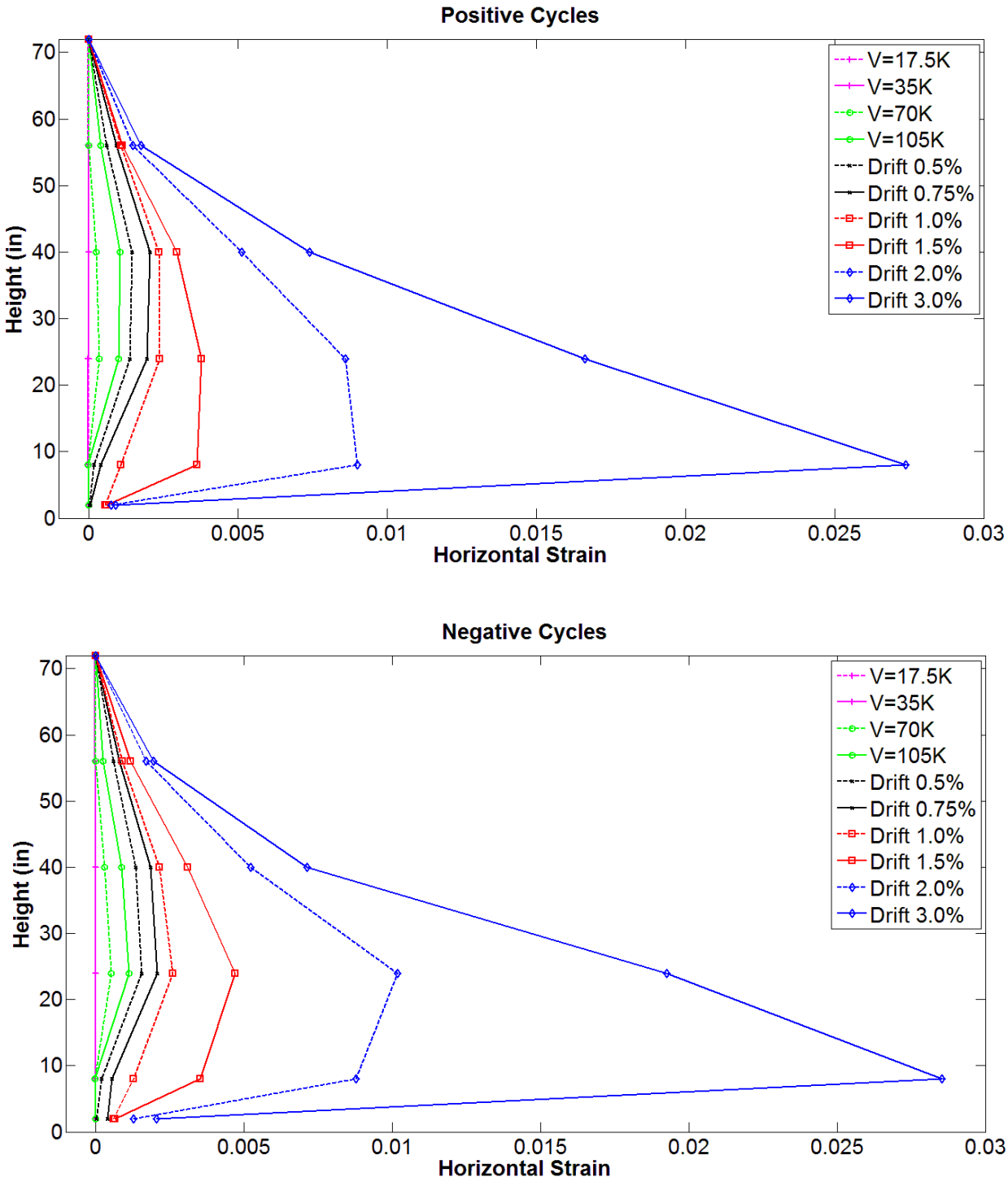

Figure 6-51 Average horizontal strain for Test 5, RW-A15-P2.5-S64

6.5.2 Residual and maximum average horizontal strain profiles

Profiles of residual and maximum average horizontal strains for five wall specimens are shown in Figures 6-52 to 6-56. The maximum average horizontal strains are essentially a combination of average horizontal strain profiles for positive and negative cycles, which are given in Section 6.5.1, and are presented here to enable comparisons with residual (minimum) average horizontal strains.

The figures show that residual strains in Tests 1 to 4 are quite similar, with the maximum magnitudes ranging from approximately 0.002 to 0.003 at 2.0% drift, and about 0.004 to 0.005 at 3.0% drift. The residual strains in Test 5 were much larger than those in the other walls, equal to around 0.005 at 2.0% drift and 0.014 at 3.0% drift.

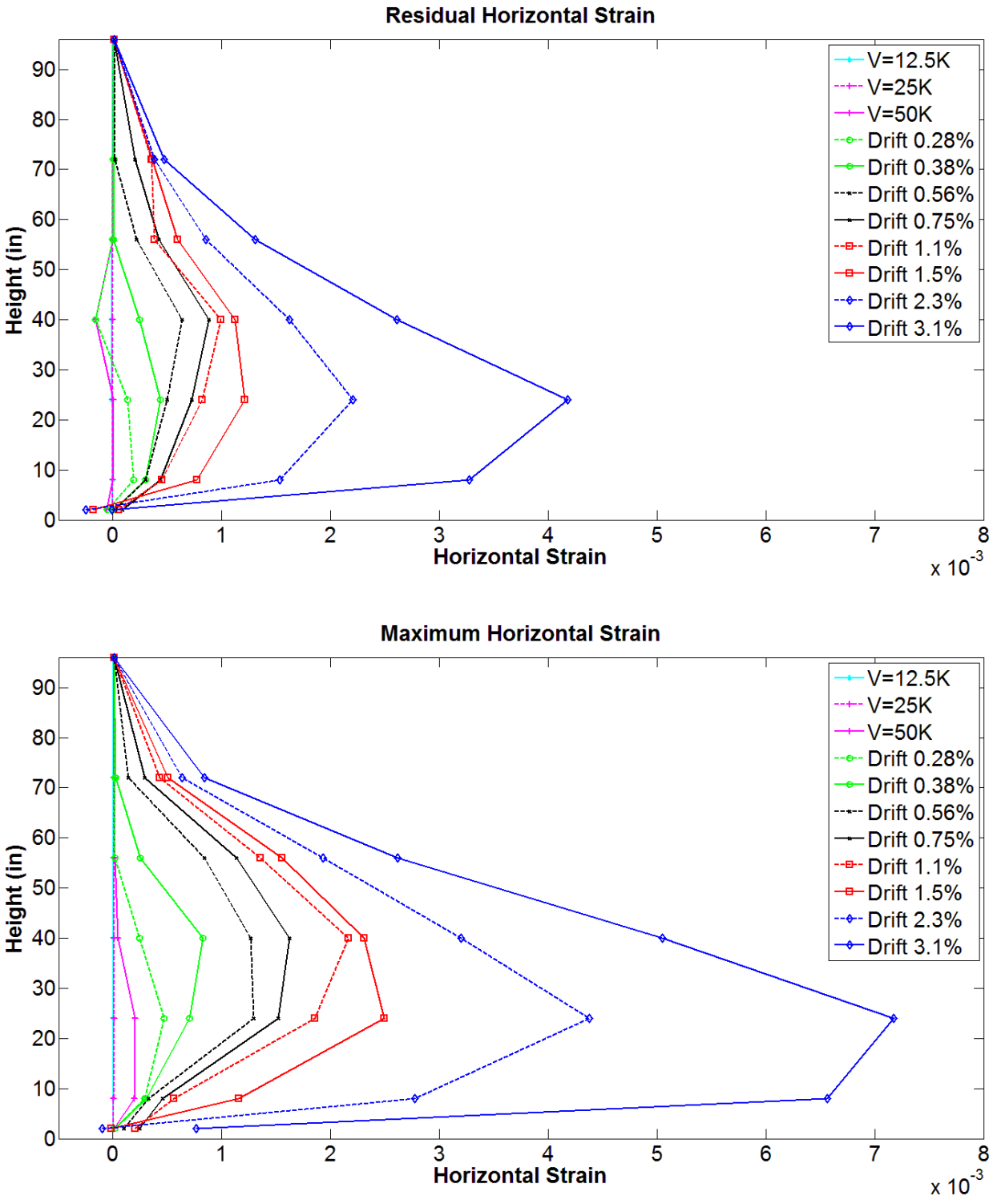

Figure 6-52 Residual and maximum average horizontal strains for RW-A20-P10-S38

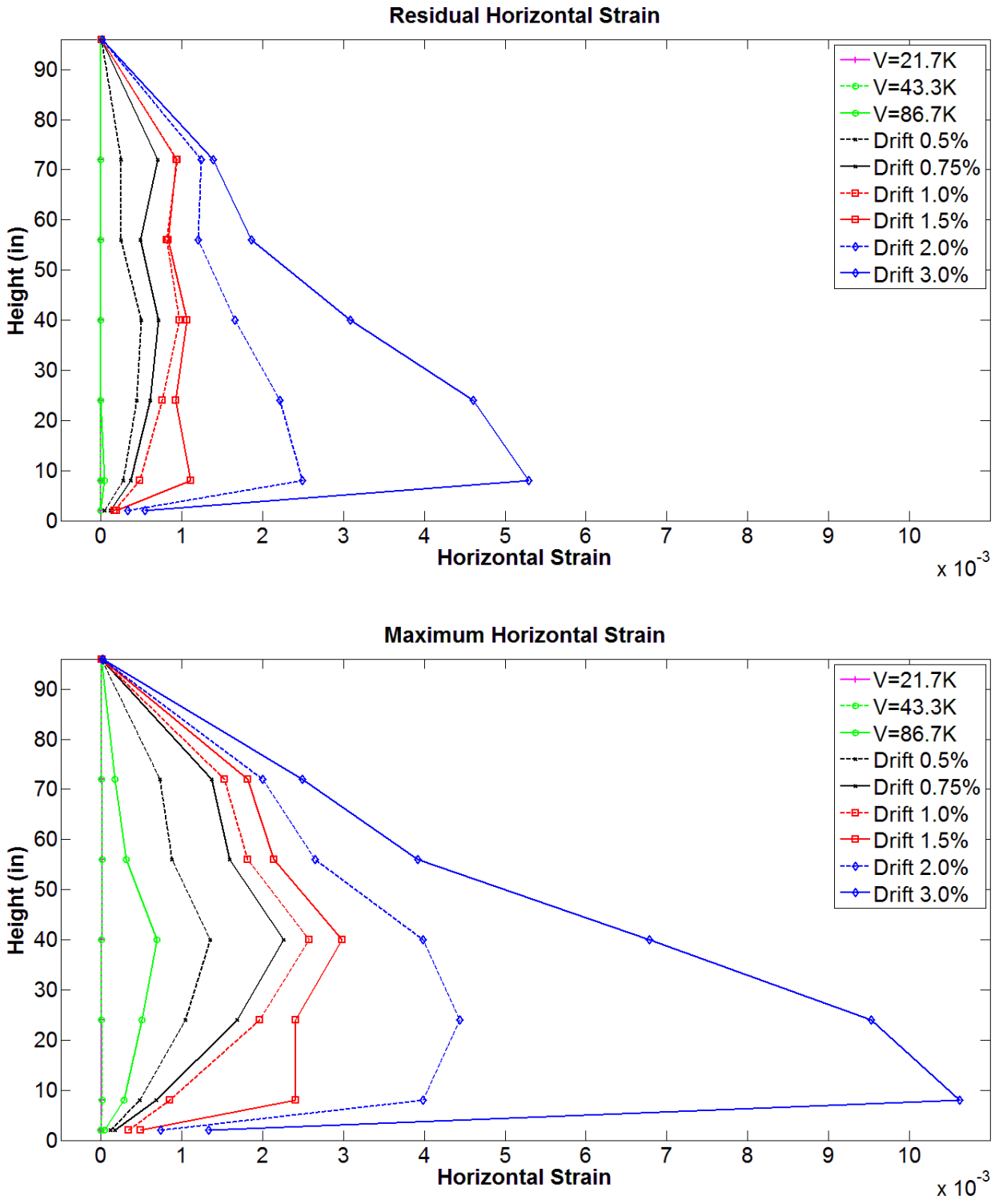

Figure 6-53 Residual and maximum average horizontal strains for RW-A20-P10-S63

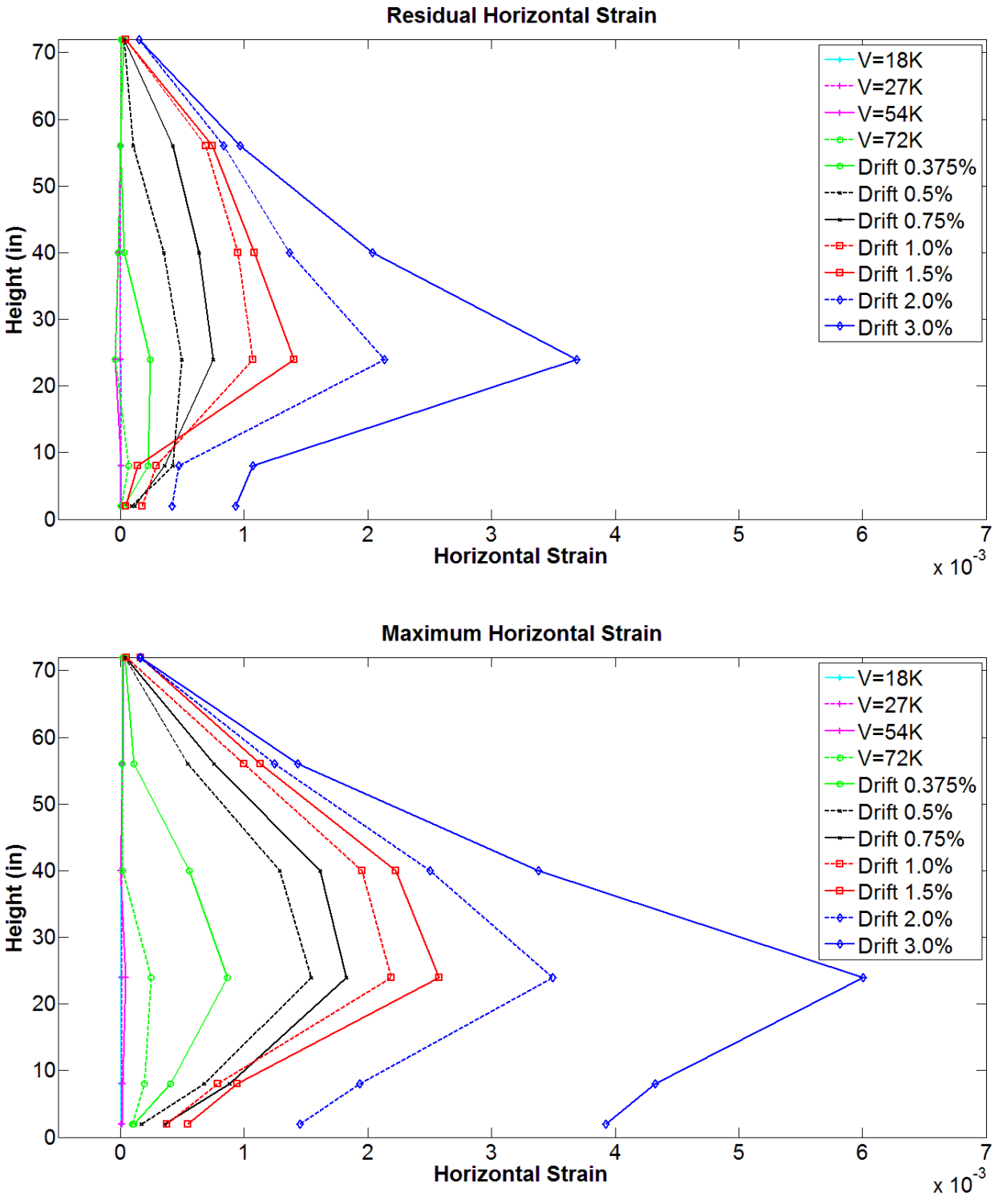

Figure 6-54 Residual and maximum average horizontal strains for RW-A15-P10-S51

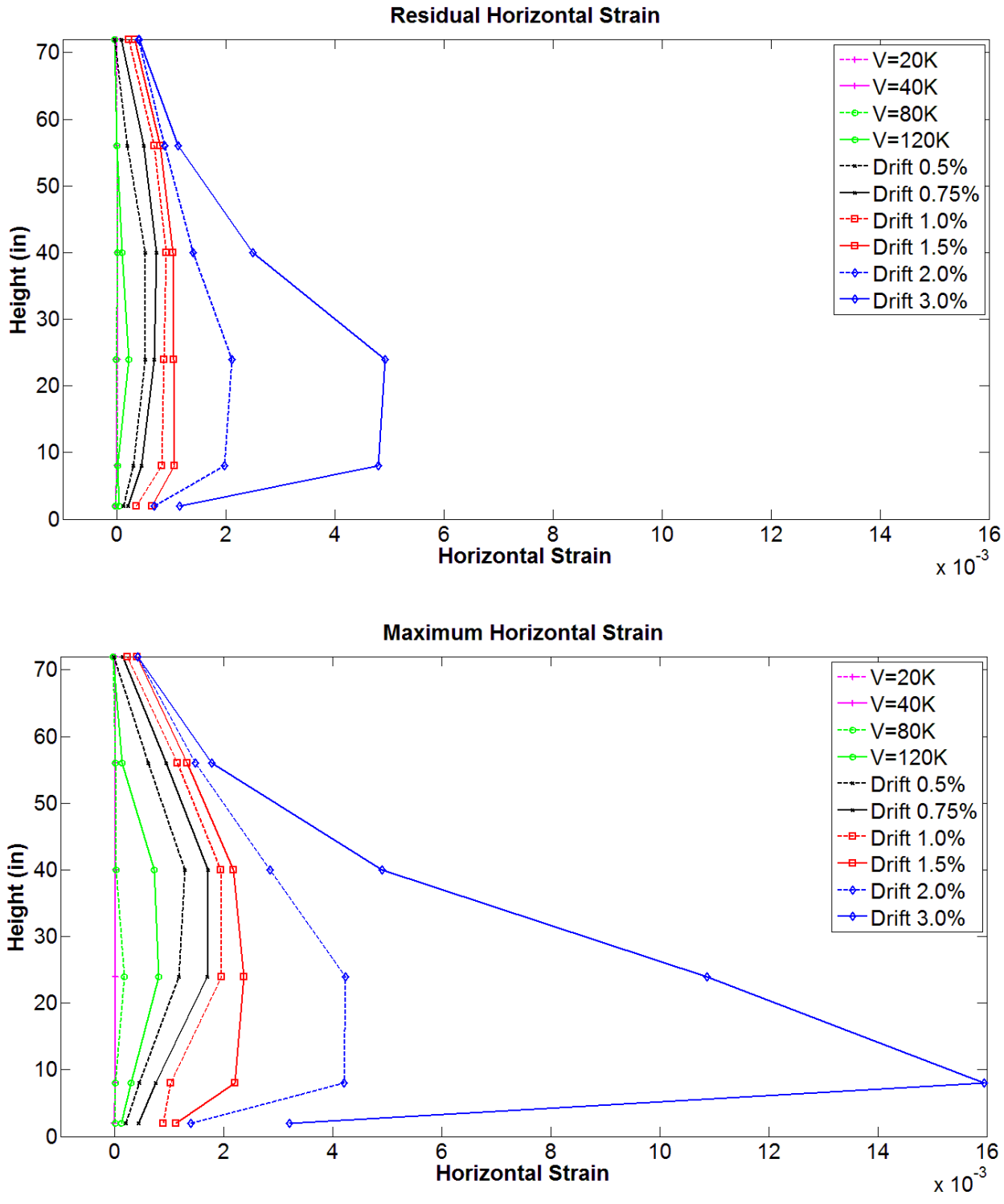

Figure 6-55 Residual and maximum average horizontal strains for RW-A15-P10-S78

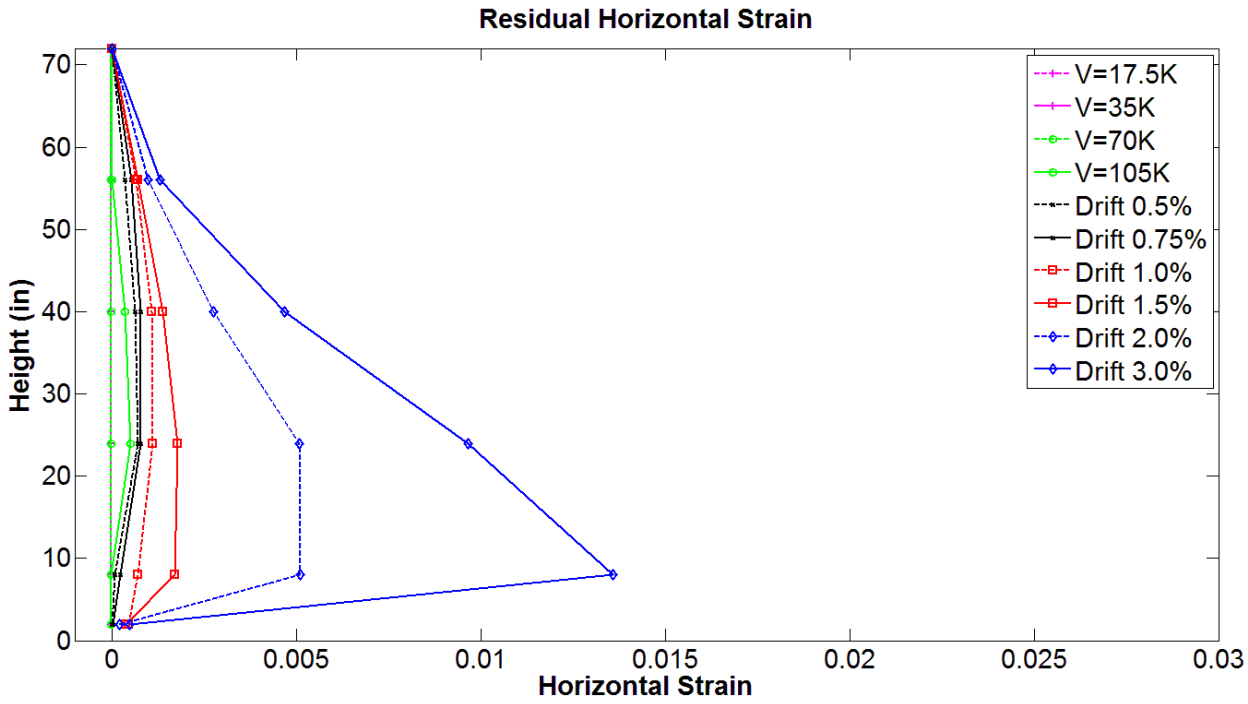

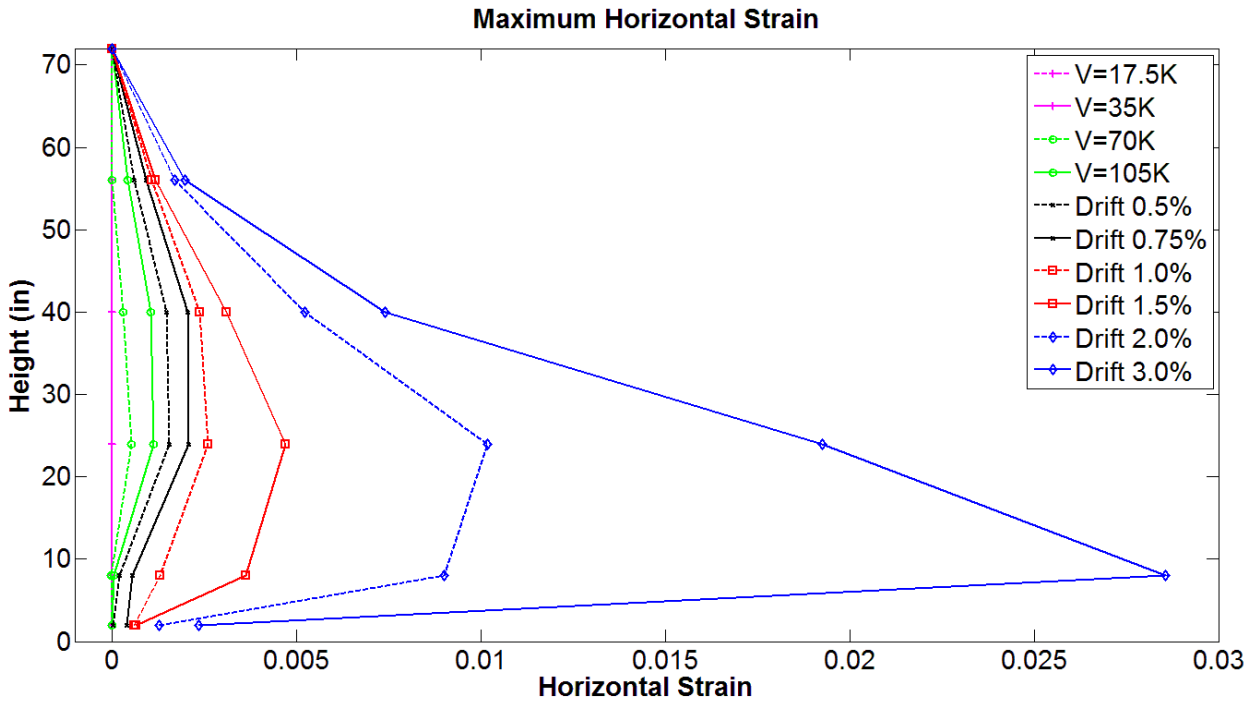

Figure 6-56 Residual and maximum average horizontal strains for RW-A15-P2.5-S64

6.6 Wall Vertical Growth

6.6.1 Vertical growth versus top lateral displacement relations

The vertical growth-lateral displacement relations for Tests 1 to 5 are shown in Figures 6-57 to 6-61, respectively. The relations indicate that the vertical growths of Tests 1 to 4, which had the same design axial load of $0.1A_g f_c^{'}$, were very similar during cycles up to 2.0% drift. At drift ratio larger than 2.0%, the increase in vertical growth of RW-A15-P10-S78 (Test 4) was slower than that in the other walls, likely due to significant out-of-plane buckling of boundary longitudinal reinforcement occurring in this specimen.

The profiles also reveal that vertical growth of the wall with low axial load ratio, RW-A15-P2.5-S64, was larger than that of the other walls during cycles up to 2.0% drift. However, during subsequent cycles at 3.0% drift ratio, wall vertical growth was almost unchanged, due to substantial in-plane buckling of boundary longitudinal reinforcement at both wall boundaries.

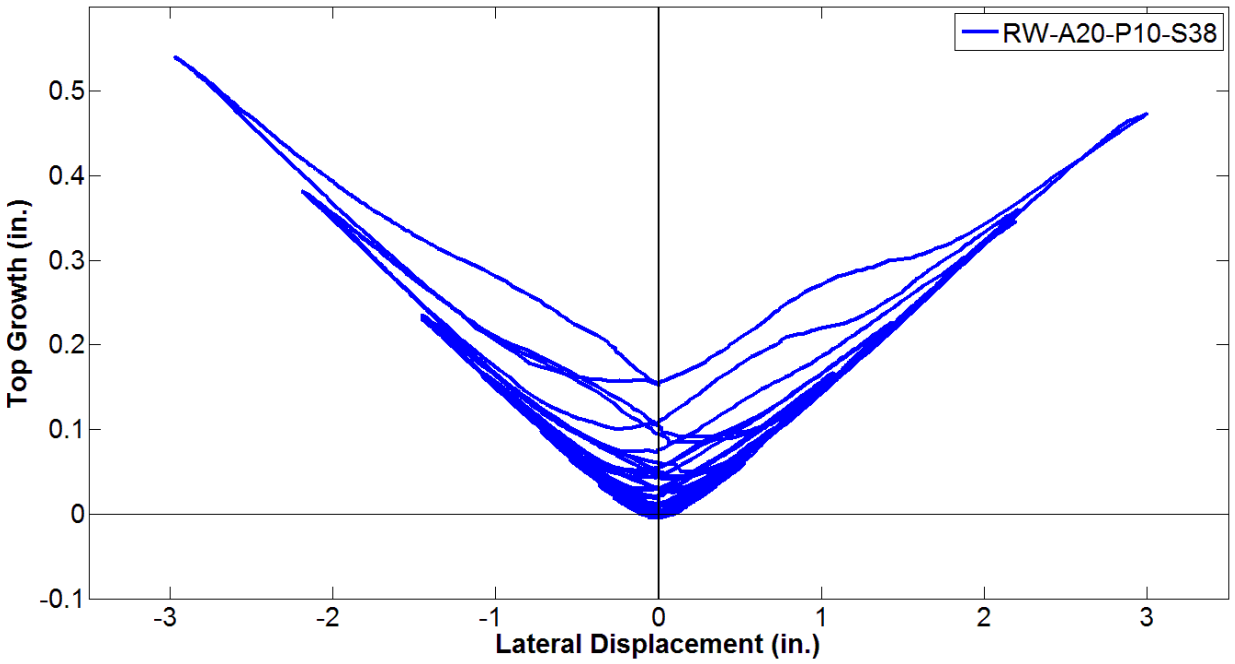

Figure 6-57 Vertical growth versus lateral displacement for RW-A20-P10-S38

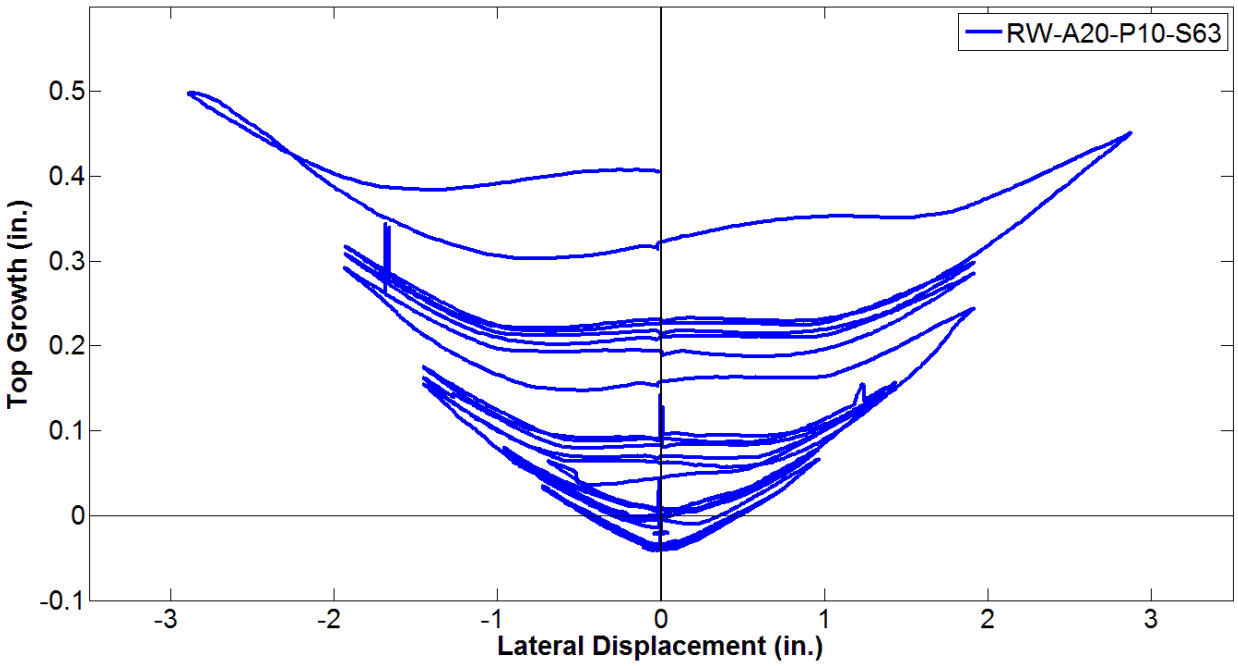

Figure 6-58 Vertical growth versus lateral displacement for RW-A20-P10-S63

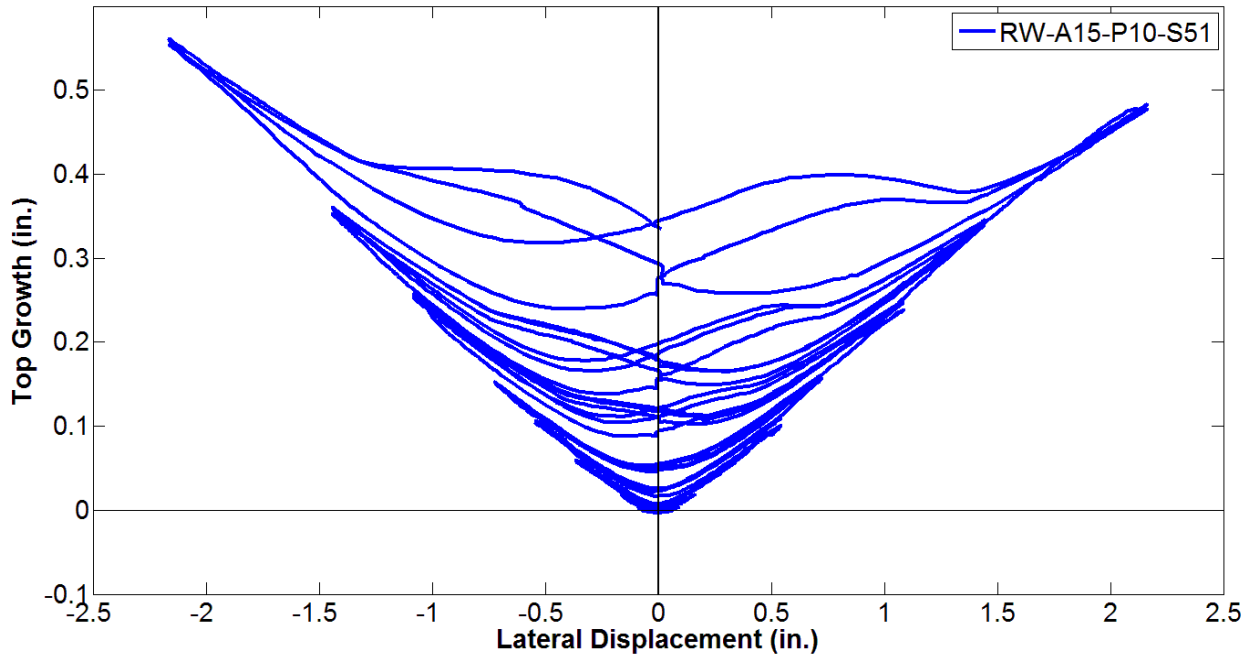

Figure 6-59 Vertical growth versus lateral displacement for RW-A15-P10-S51

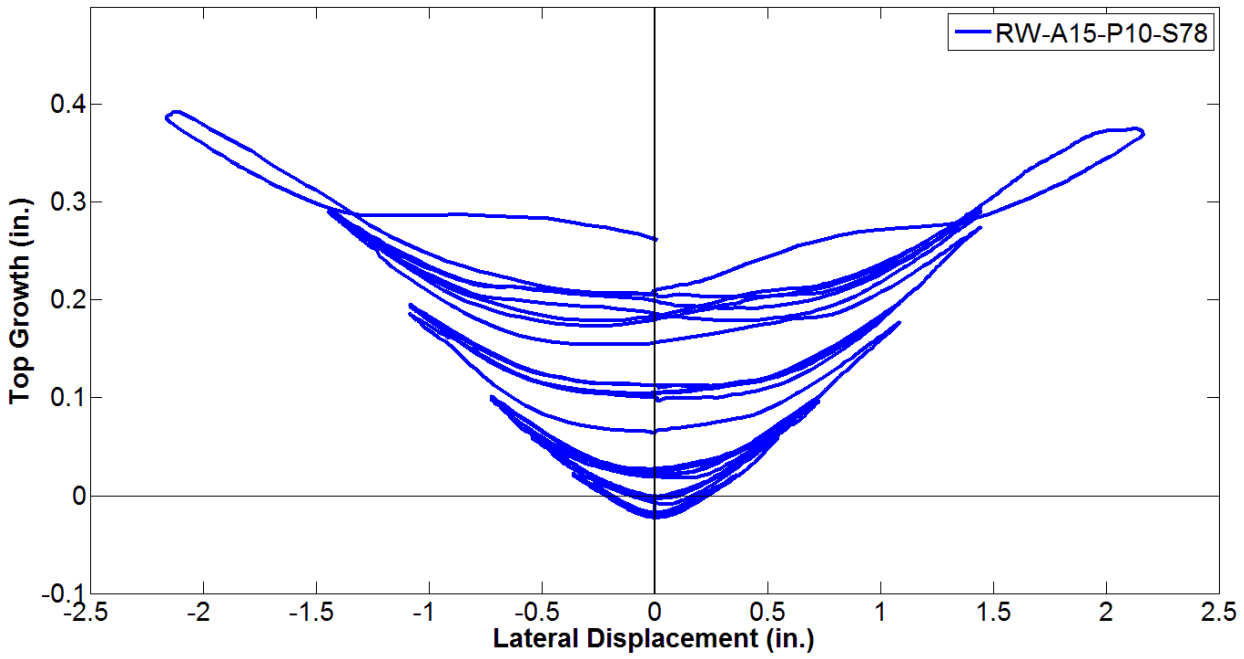

Figure 6-60 Vertical growth versus lateral displacement for RW-A15-P10-S78

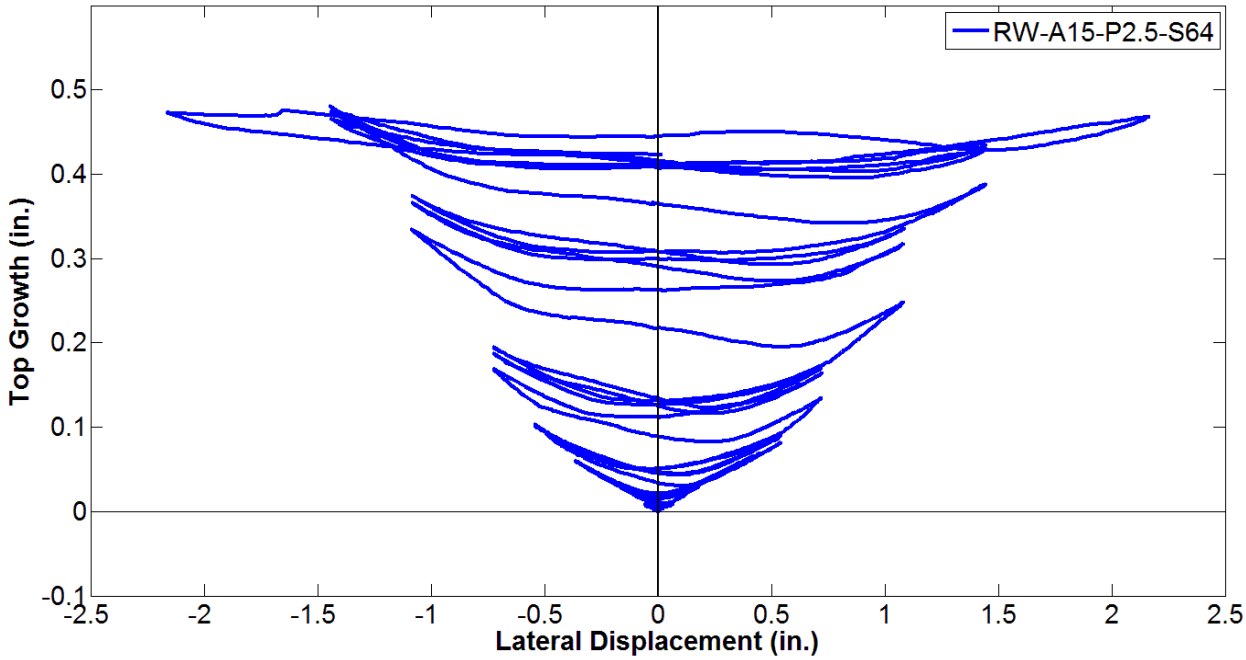

Figure 6-61 Vertical growth versus lateral displacement for RW-A15-P2.5-S64

6.6.2 Vertical growth profiles

Profiles of vertical growth over the wall height for Tests 1 to 5 are presented in Figures 6-62 to 6-66, respectively. In these profiles, vertical growth was determined at maximum lateral load (for force-controlled cycles) or maximum displacement (for displacement-controlled cycles) during the first cycle under both positive and negative loading. In the five figures, continuous lines represent positive loading, whereas the dashed lines represent negative loading. Vertical growth was obtained at the height levels of 24 in. (610 mm), 40 in. (1016 mm), 56 in. (1422 mm), 72 in. (1829 mm), and 96 in. (2438 mm) above the wall-foundation interface.

The figures show that the distributions of vertical growth were almost linear at low drift levels. After yielding in boundary longitudinal reinforcement, vertical growth profiles are nonlinear,

with a large contribution coming from the deformation over a wall height of $l_w/2$ from the wall-foundation interface; this distance is commonly used as an estimate of the wall plastic hinge length.

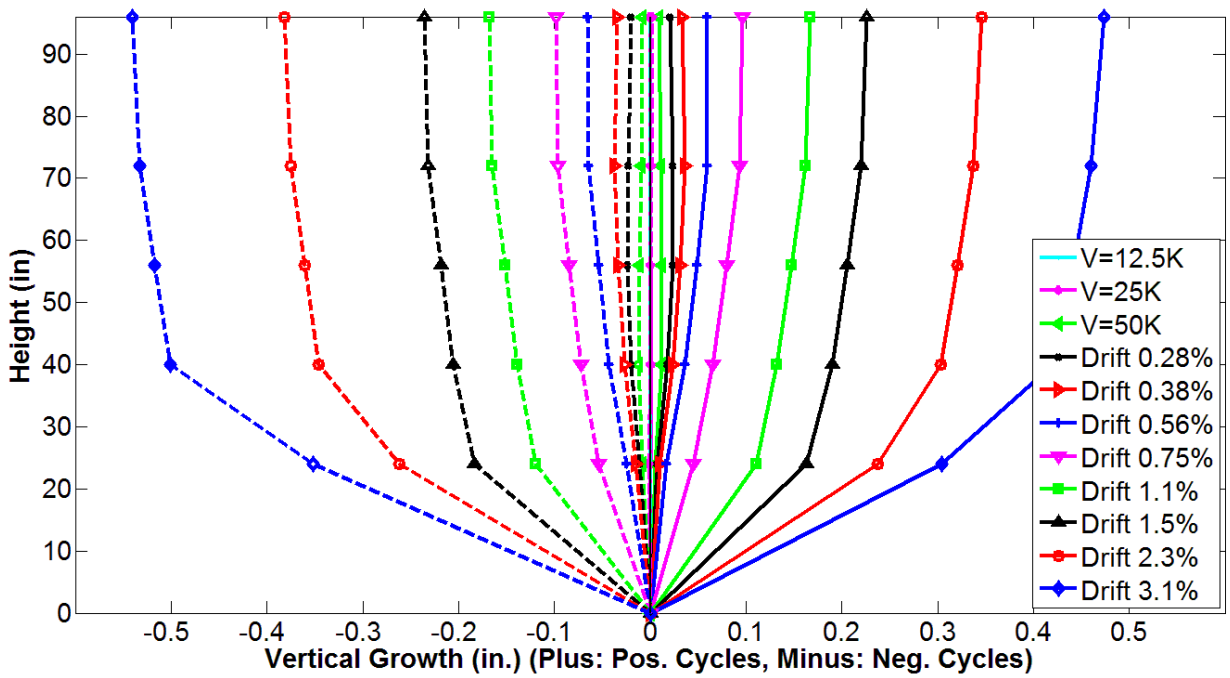

Figure 6-62 Vertical growth profile for RW-A20-P10-S38

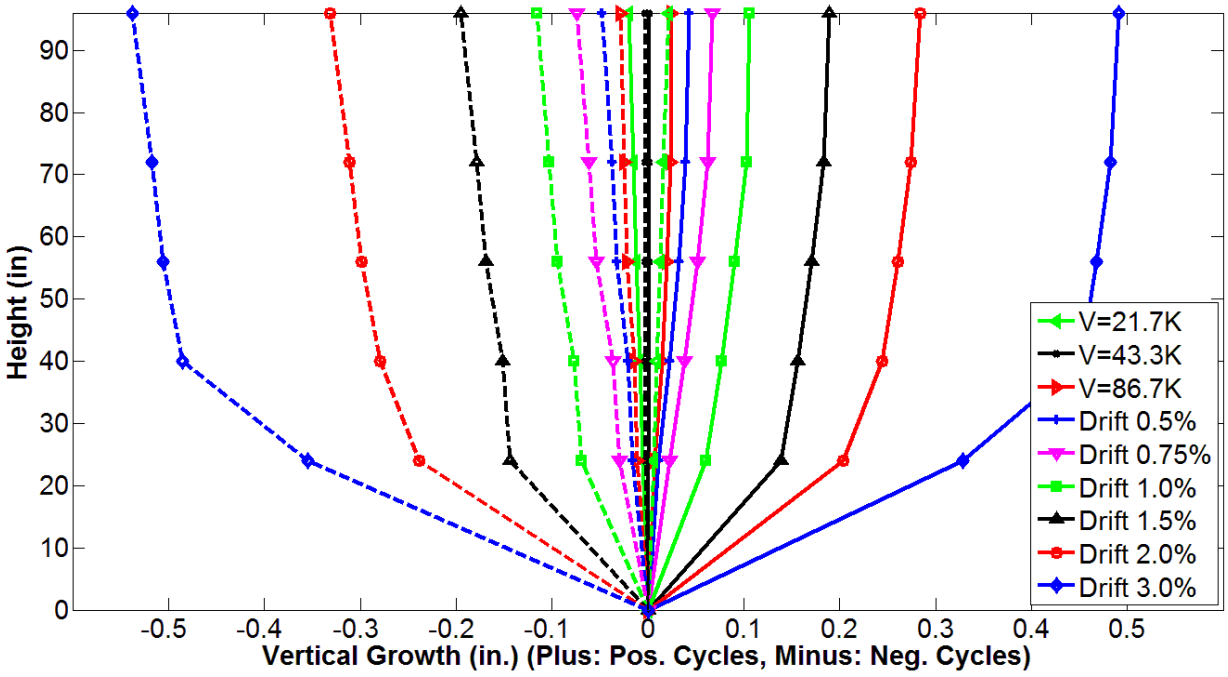

Figure 6-63 Vertical growth profile for RW-A20-P10-S63

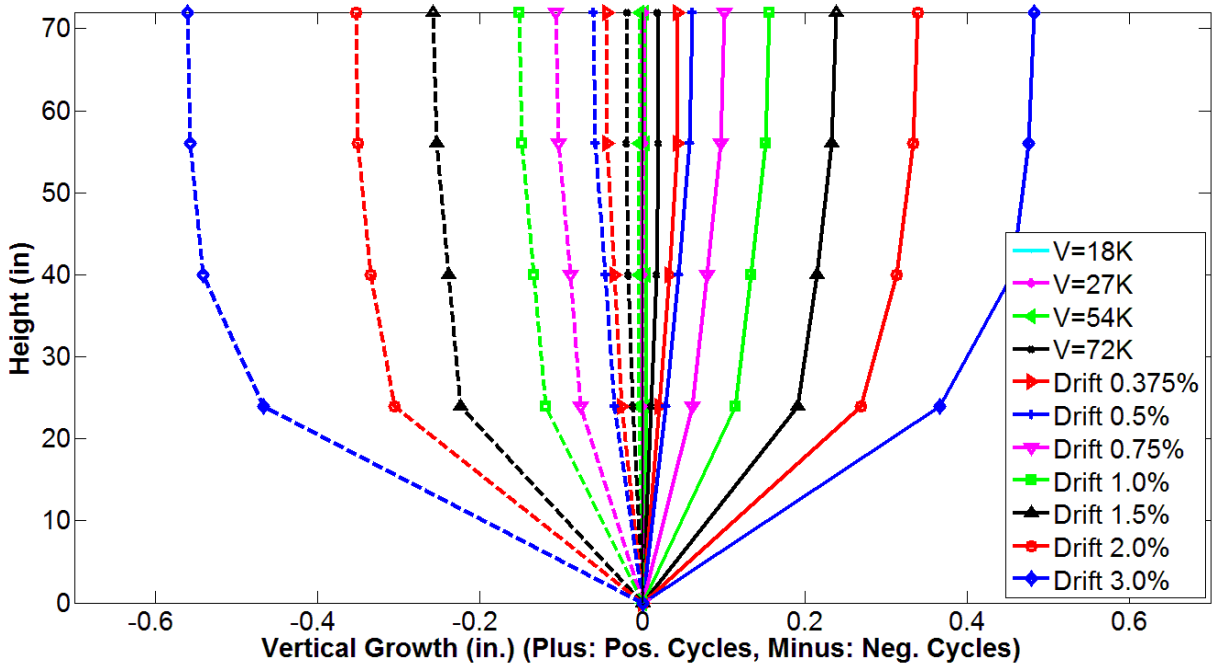

Figure 6-64 Vertical growth profile for RW-A15-P10-S51

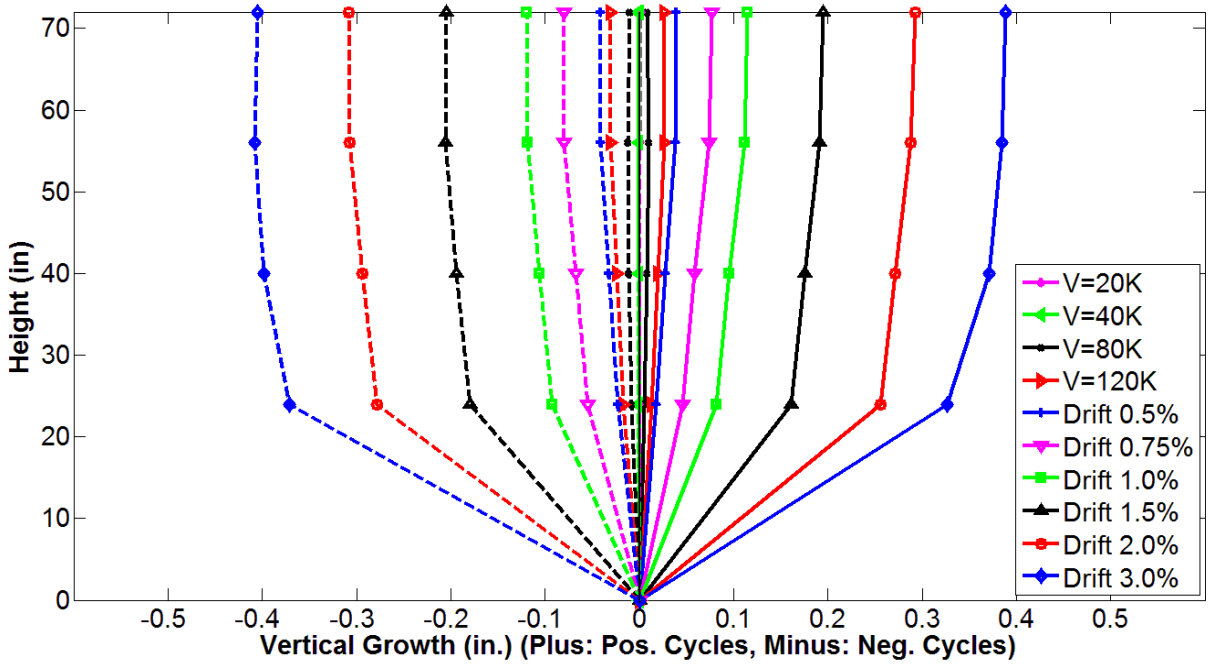

Figure 6-65 Vertical growth profile for RW-A15-P10-S78

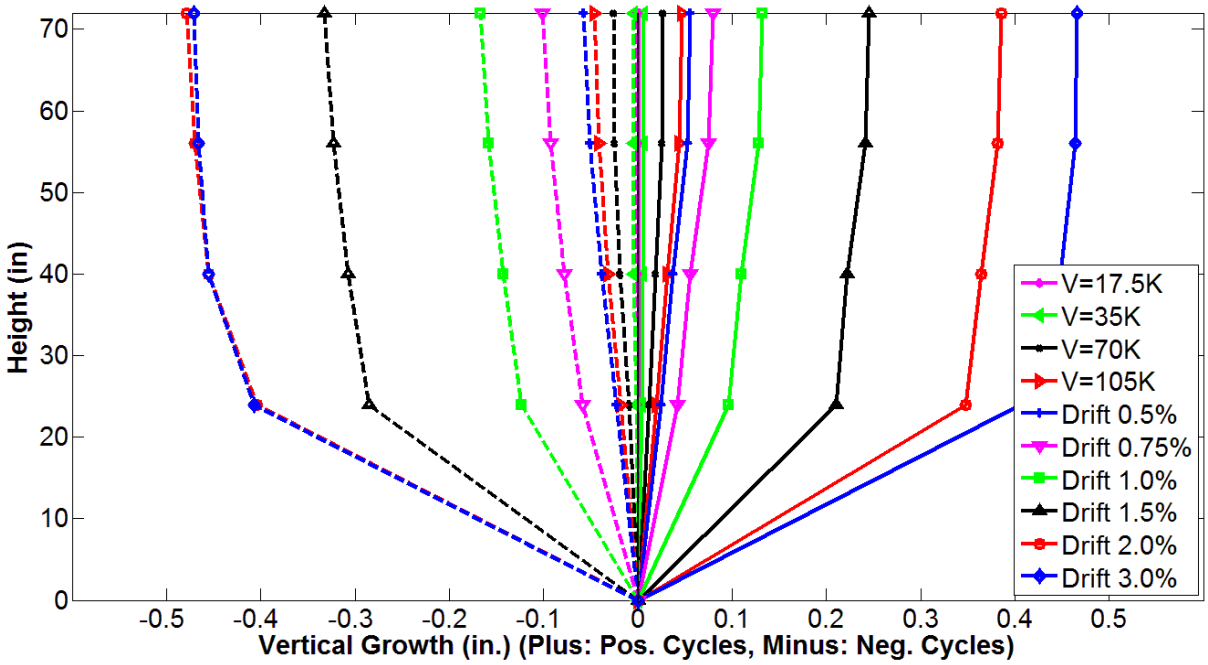

Figure 6-66 Vertical growth profile for RW-A15-P2.5-S64

CHAPTER 7 COMPONENTS OF LATERAL DISPLACEMENT

This chapter presents approaches used to determine various components of wall lateral displacement from flexural, shear, and sliding shear deformations. Lateral displacement due to slip and extension of boundary longitudinal reinforcement also is calculated. Contributions of each component to the total displacement are obtained at each lateral load or drift level for all five test specimens. Based on these results, an evaluation of deformation capacities of moderate aspect ratio walls is provided.

7.1 Flexural Component of Lateral Displacement

Flexural displacement of a wall section is computed as the following.

$$\Delta_f = \alpha\theta h$$

where Δ_f is the flexural lateral displacement at the top of the wall section, α is the relative distance from the top of the wall section to the centroid of the curvature diagram, h is the height of the wall section, θ is the rotation at the top of the wall section. This equation can be easily derived from the definition of the location of the center of the curvature distribution (see Figure 7-1).

$$\alpha h = \frac{\int_0^h \Phi x dx}{\int_0^h \Phi dx} = \frac{\Delta_f}{\theta}$$

$$\Rightarrow \Delta_f = \alpha\theta h$$

where αh is the absolute distance from the top of the wall section to the centroid of the curvature diagram, $\Phi = \Phi(x)$ is the curvature of the wall at section x.

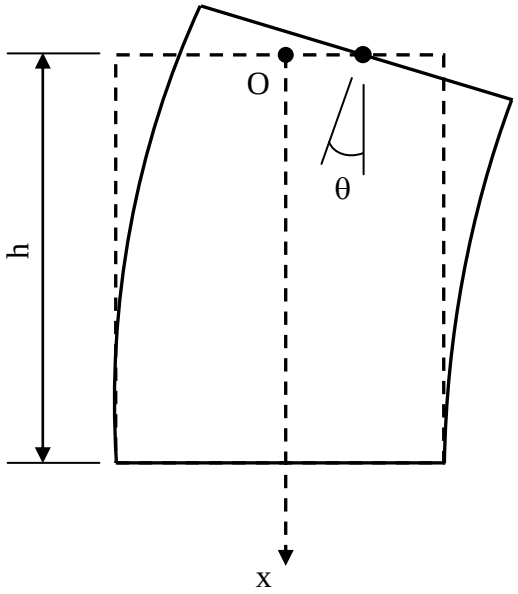

Figure 7-1 Calculation of flexural deformation for a wall section

The rotation θ at the top of the wall was obtained as

$$\theta = \frac{V_1 - V_2}{L}$$

where V_1 and V_2 are vertical displacements measured from two lines of vertical sensors near wall edges and L is the horizontal distance between the sensors.

The wall specimens were divided into several sections where at least one pair of vertical displacement transducers was installed. Figures 7-2a and 7-2b show the number and height of wall sections used for walls with aspect ratios of 2.0 and 1.5, respectively. The bottom section, section A, had the height of $l_w/2$, which was equal to the anticipated plastic hinge length of the

wall. Several previous studies have indicated that yielding was primarily limited to this region; therefore, more than one pair of sensors were installed in this region to obtain a sufficiently detailed estimate of the wall curvature distribution. Massone and Wallace (2004) suggested that four to six pairs of displacement sensors at each wall boundary would be sufficient to accurately determine centroid of the nonlinear curvature distribution over the plastic hinge length, and thus the contribution of flexural deformations to wall top lateral displacement; four pairs of vertical LVDTs were used in this study. For the remaining of wall sections, which are above the assumed plastic hinge region, only one pair of vertical sensors was used to measure average curvature. More details on LVDT layout can be seen in Figures 5.1 and 5.3 in Chapter 5.

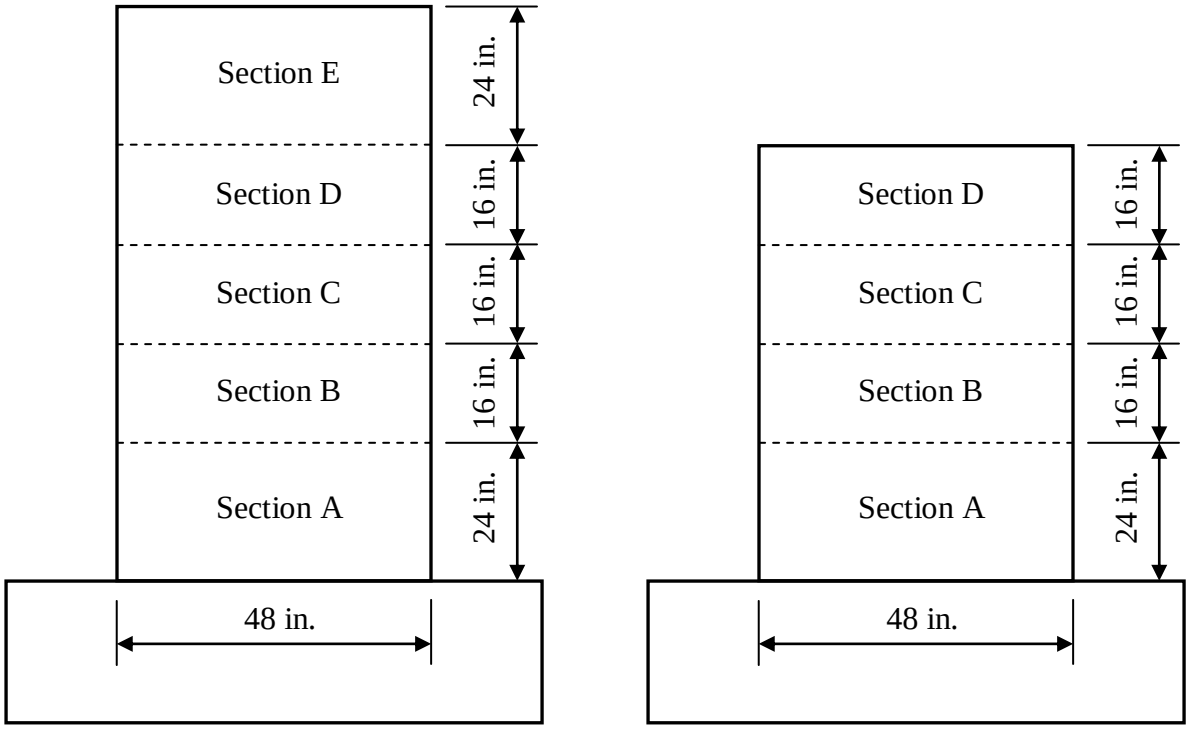

(a) 2.0 aspect ratio walls (b) 1.5 aspect ratio walls

Figure 7-2 Sections in wall specimens with 2.0 and 1.5 aspect ratios

Coefficient α gives the location of the centroid of the curvature distribution over the wall section. In section A, α was determined using four values of curvature obtained from the four pairs of vertical sensors. In the other sections, the calculation of α was performed with the assumption that the wall flexural stiffness, EI, was constant throughout the regions; therefore, the curvature Φ was linearly proportional to the applied moment, based on the relation $M = EI\Phi$. The moment diagram of a cantilever wall was triangular; hence, the curvature diagrams in the other wall sections are assumed to be trapezoidal, except for the top section, which is triangular. As a result, α was determined to be 25/48, 19/36, 13/24, and 2/3 for sections B, C, D, and E in 2.0 aspect ratio walls, respectively. Similarly, for walls with aspect ratio of 1.5, the values of α were 8/15, 5/9, and 2/3 for sections B, C, and D, respectively.

7.1.1 Lateral load versus flexural displacement relations

7.1.1.1 Walls with aspect ratio of 2.0

The relations of lateral load versus flexural displacement at the top of the wall for specimens RW-A20-P10-S38 and RW-A20-P10-S63 are shown in Figures 7-3 and 7-4, respectively, whereas Figure 7-5 plots both relations. The figures show that the load-flexural displacement relations for these two specimens resemble the shape of their load-total displacement diagrams, which were given in Section 6.3.1. The main difference between the two load-flexural displacement responses is that flexural deformations in RW-A20-P10-S63 (Test 2) were much smaller than those in RW-A20-P10-S38 (Test 1) at large drift ratios, although both of these two specimens reached about the same drift levels prior to significant loss of lateral strength. Comparison between the relations for Tests 1 and 2 also indicates that the wall with higher shear

has less pinching. This is probably because of the larger compression and deeper compression zone, which would lead to more pullout in the wall with lower shear.

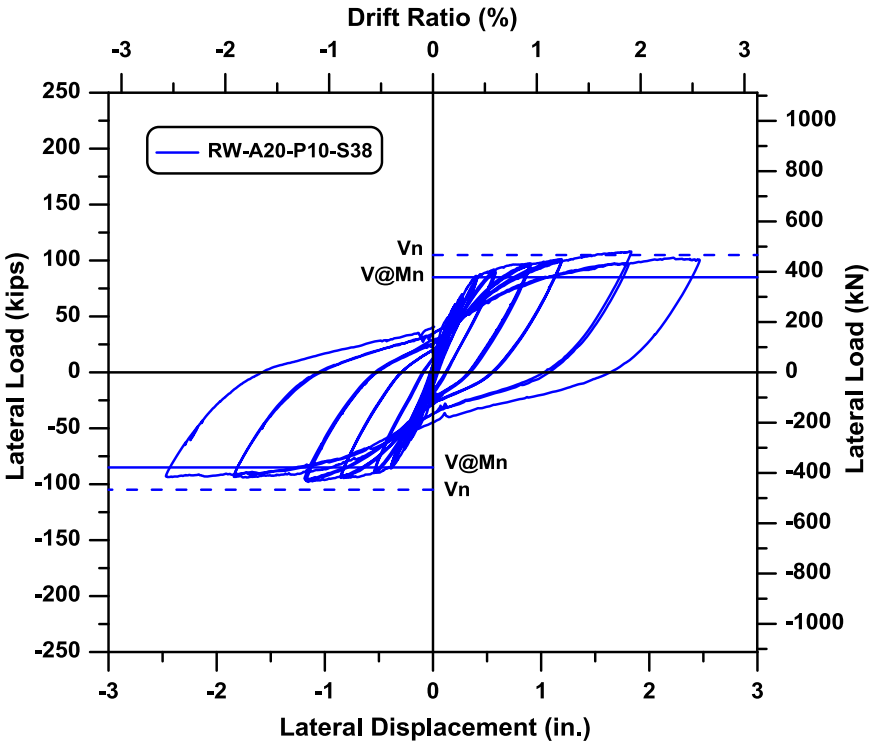

Figure 7-3 Top flexural displacement for RW-A20-P10-S38

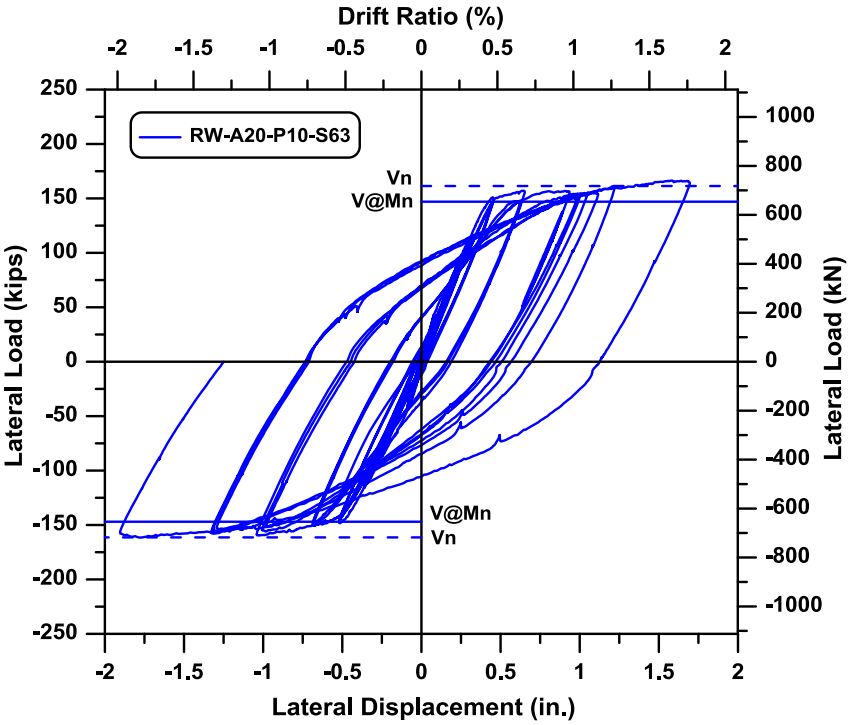

Figure 7-4 Top flexural displacement for RW-A20-P10-S63

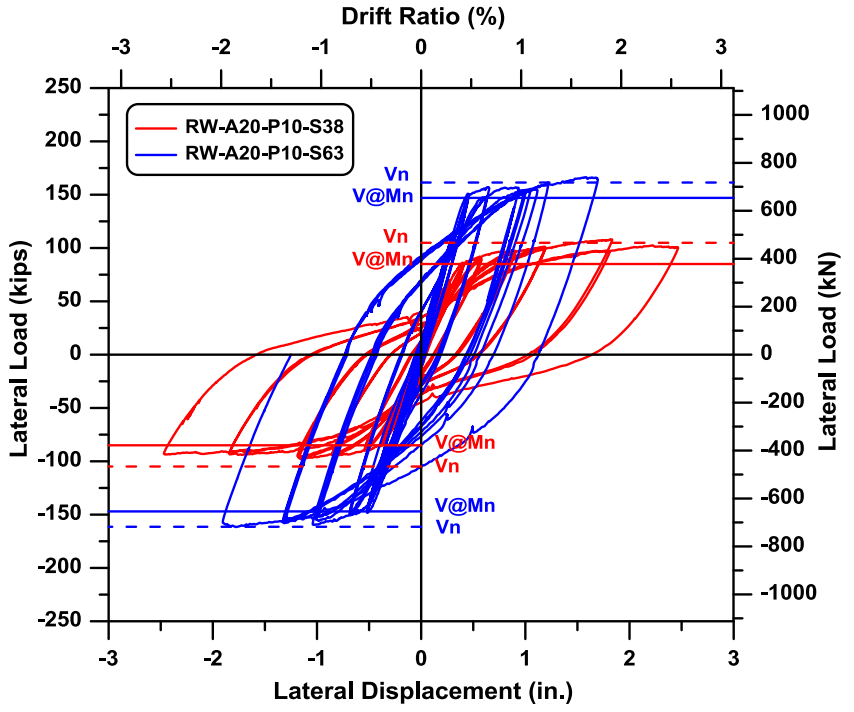

Figure 7-5 Top flexural displacements for RW-A20-P10-S38 and RW-A20-P10-S63

7.1.1.2 Walls with aspect ratio of 1.5

Lateral load versus top flexural displacement relations for specimens RW-A15-P10-S51 (Test 3), RW-A15-P10-S78 (Test 4), and RW-A15-P2.5-S64 (Test 5) are given in Figures 7-6, 7-7, and 7-8, respectively. Both relations for Tests 3 and 4 are plotted in Figure 7-9, whereas Figure 7-10 shows responses for Tests 4 and 5.

The figures indicate that the load-flexural displacement responses for Tests 3 and 4 are quite similar to their total displacement responses, although flexural displacements of Test 4 tend to be smaller than those of Test 3 during cycles at large drift levels, probably for the same reasons noted in the comparison of Tests 1 and 2. For Test 5 with relatively low axial load level, flexural deformations are much lower than those of Test 4 after yielding in boundary longitudinal reinforcement. Top flexural displacements in Test 5 decrease slightly under positive loading and substantially under negative loading at a drift ratio of 3.0%, compared to flexural displacements at 2.0% drift, due to significant shear sliding behavior at 3.0% drift.

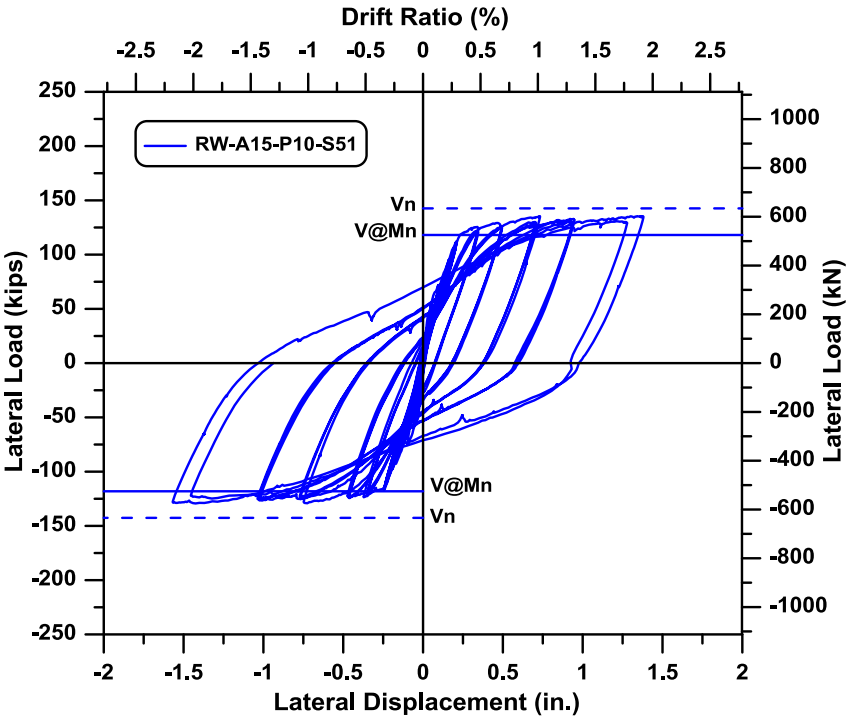

Figure 7-6 Top flexural displacement for RW-A15-P10-S51

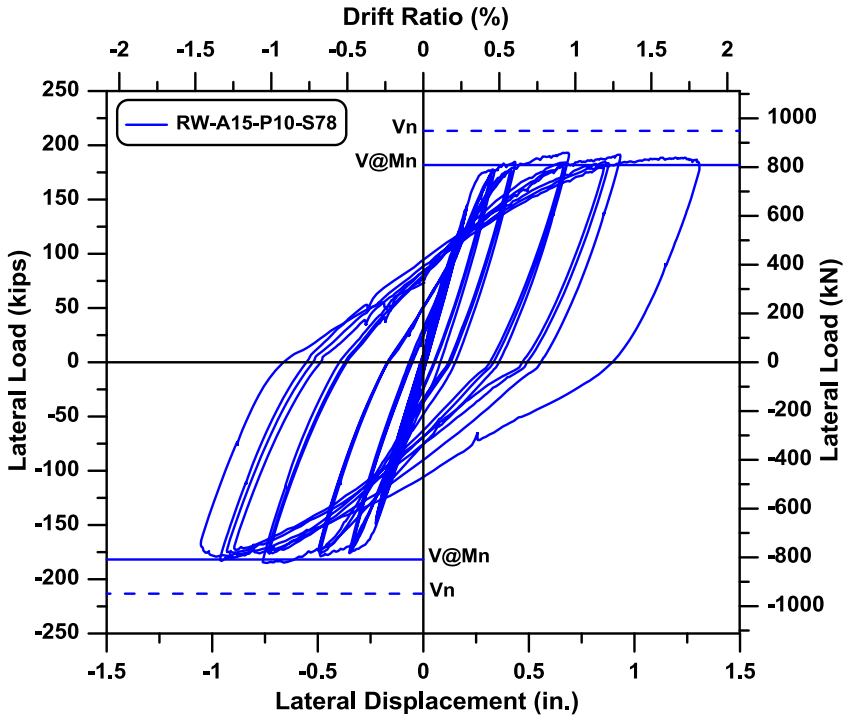

Figure 7-7 Top flexural displacement for RW-A15-P10-S78

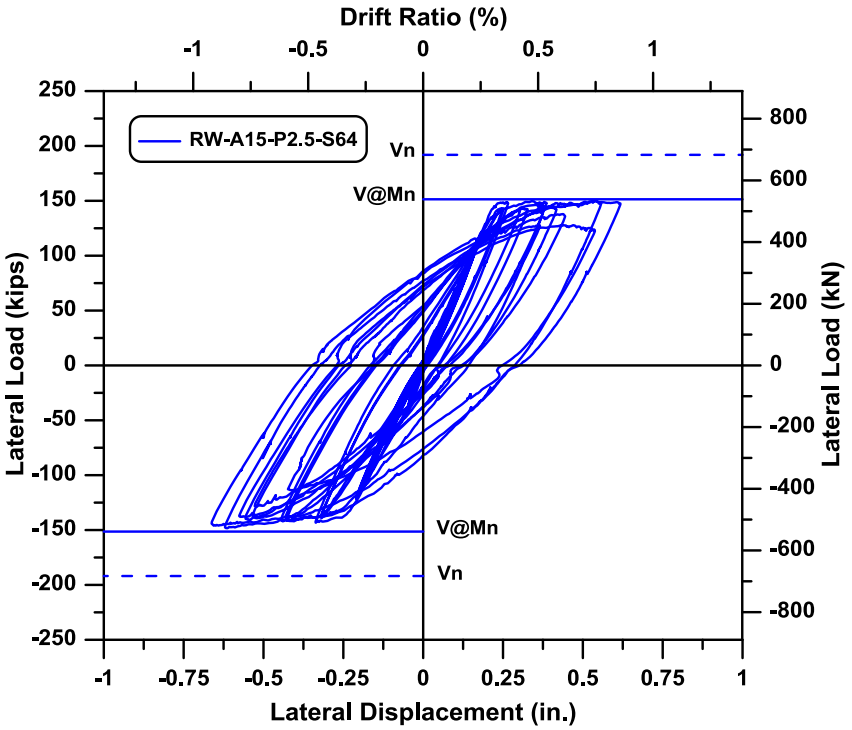

Figure 7-8 Top flexural displacement for RW-A15-P2.5-S64

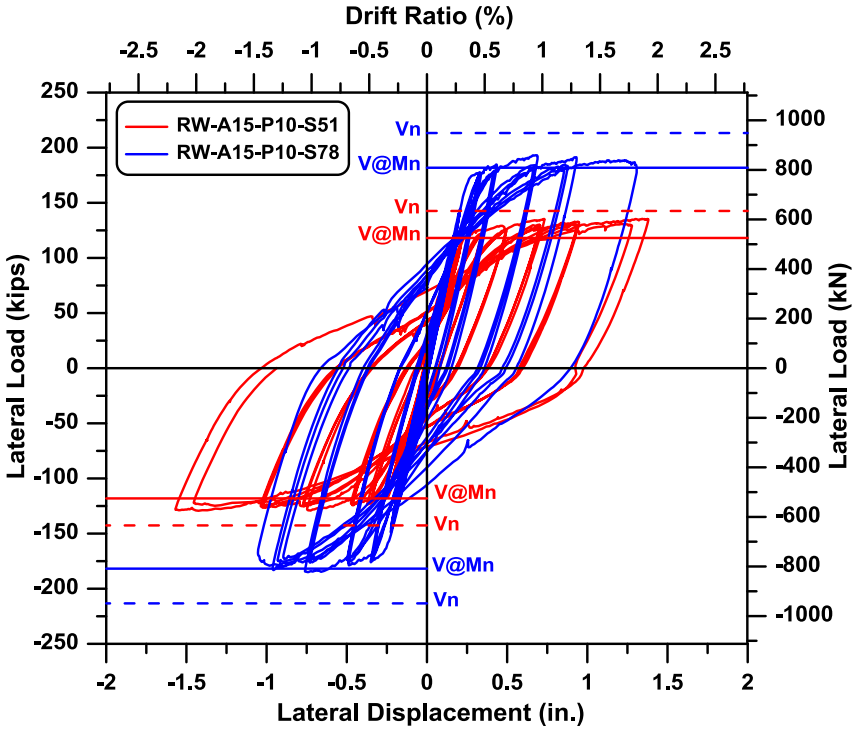

Figure 7-9 Top flexural displacement for RW-A15-P10-S51 and RW-A15-P10-S78

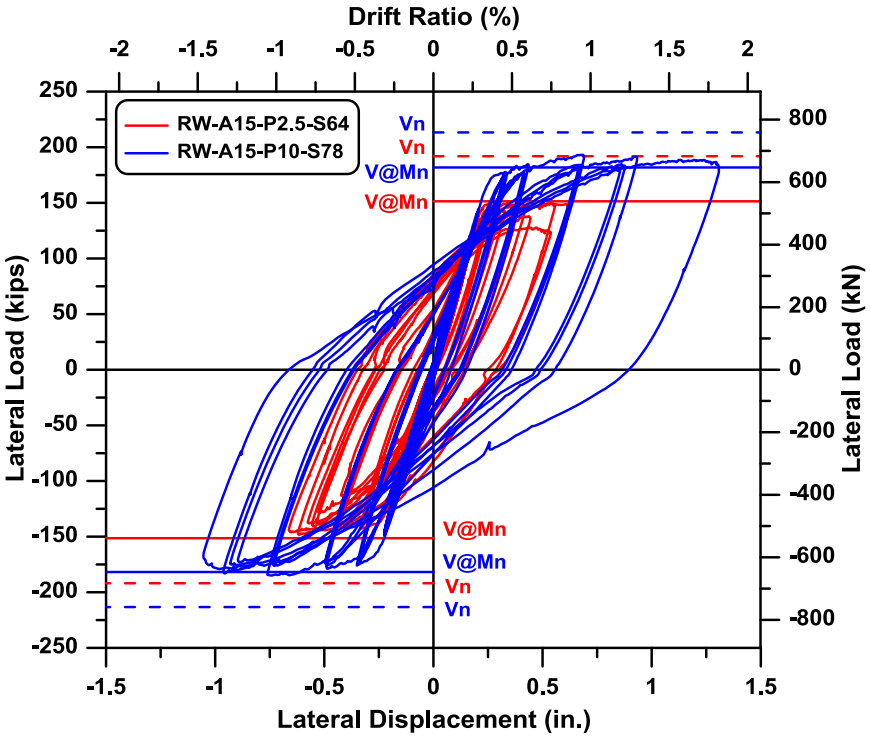

Figure 7-10 Top flexural displacement for RW-A15-P10-S78 and RW-A15-P2.5-S64

7.1.2 Flexural displacement profiles

Profiles of flexural displacement over the wall height for Tests 1 to 5 are presented in Figures 7-11 to 7-15, respectively. In these profiles, flexural displacements were determined at maximum lateral load (for force-controlled cycles) or maximum displacement (for displacement-controlled cycles) during the first cycle under both positive and negative loadings. In the five figures, continuous lines represent positive loading, whereas the dashed line represent negative loading. Flexural displacements were obtained 24 in. (610 mm), 40 in. (1016 mm), 56 in. (1422 mm), 72 in. (1829 mm), and 96 in. (2438 mm) above the wall-foundation block interface.

As can be seen in these figures, the profiles of flexural displacements of all five specimens are nonlinear within the bottom region, section A, with the height of $l_w/2$. It is also observed that the contribution to top flexural displacement from section A becomes more significant at larger drift ratios, indicating that the plastic deformations were mostly concentrated in this region. For wall sections above section A, the flexural displacement profiles are relatively linear, indicating that nonlinear flexural deformations were likely relatively small at these locations.

The decrease in flexural displacements in RW-A15-P2.5-S64 (Test 5) at 3.0% drift compared to 2.0% drift can be clearly seen in Figure 7-15. Furthermore, there is only a very slight increase in flexural deformations for this wall between 1.5% and 2.0% drift, likely an indicator that significant sliding deformations were likely initiating between these drift levels.

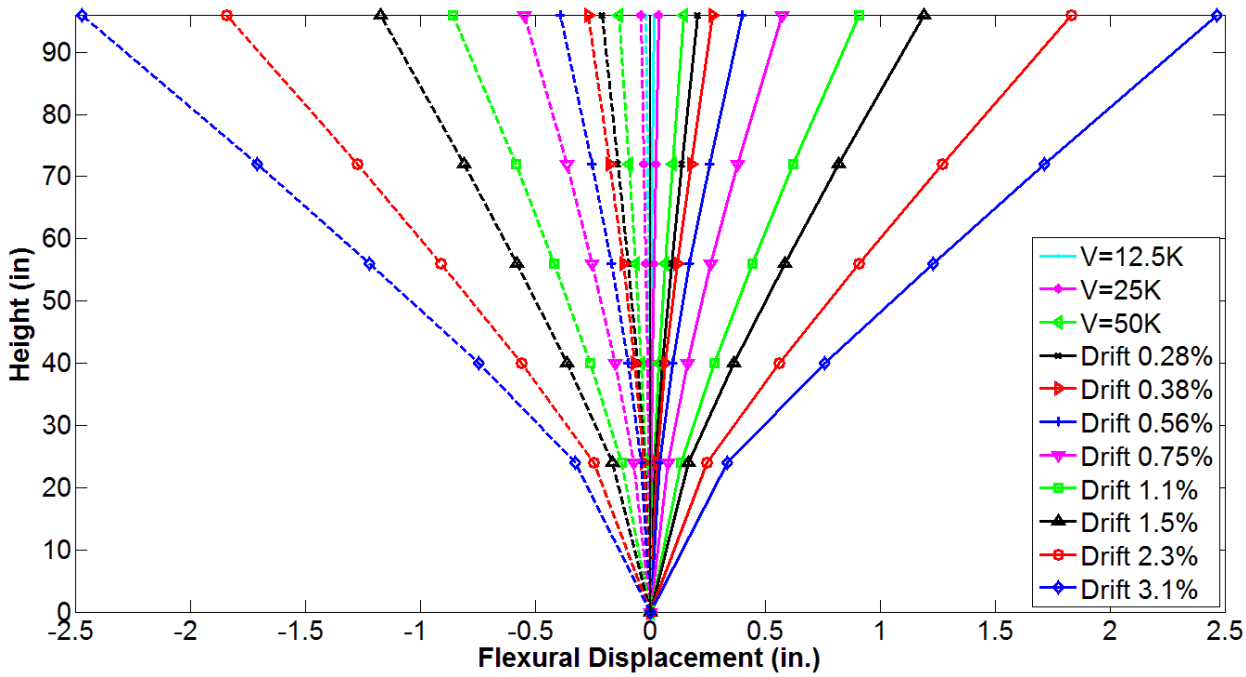

Figure 7-11 Flexural displacement profile for Test 1, RW-A20-P10-S38

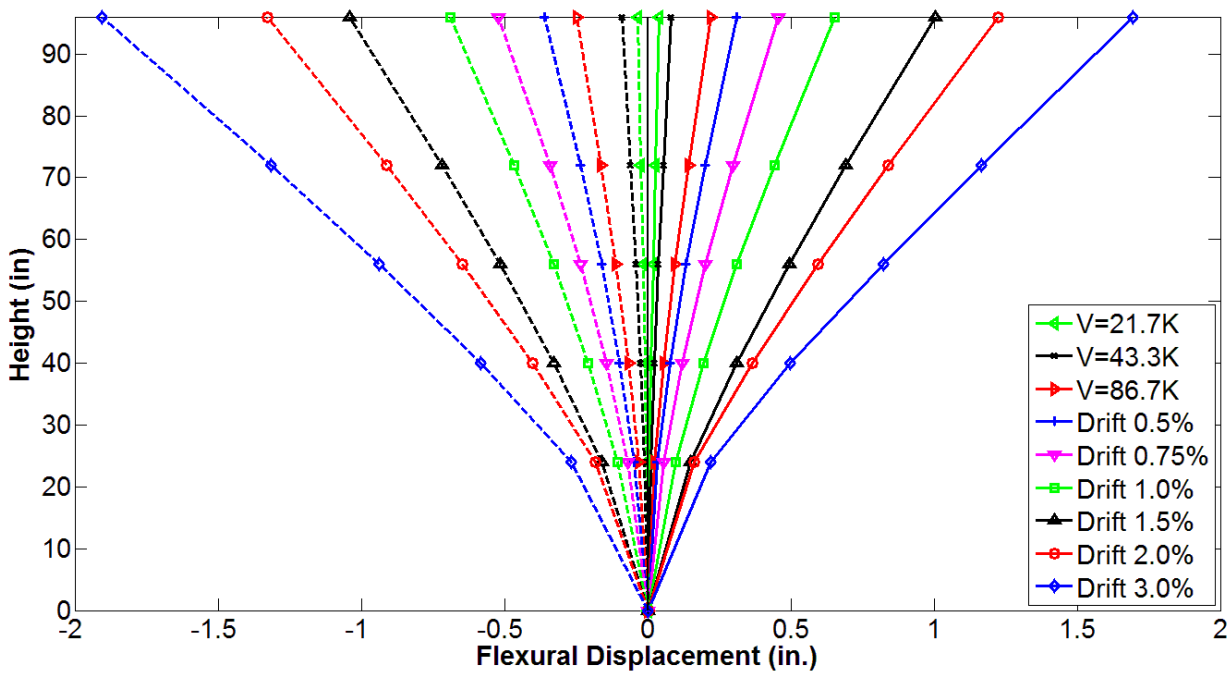

Figure 7-12 Flexural displacement profile for Test 2, RW-A20-P10-S63

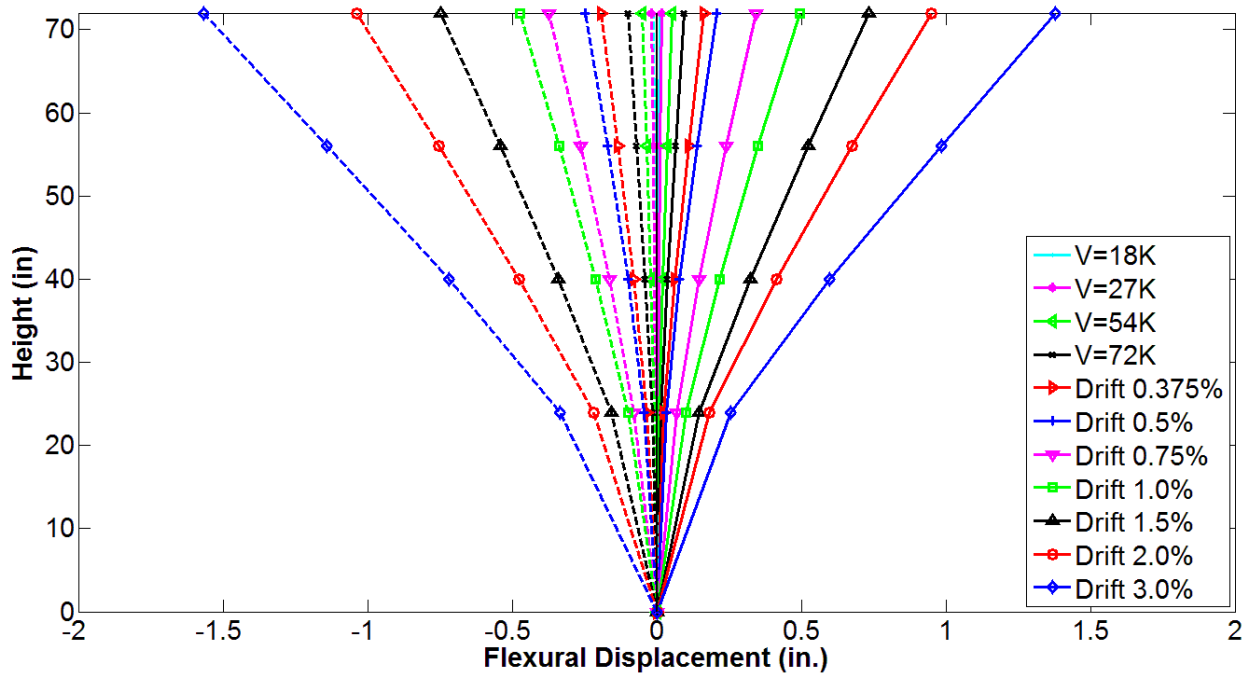

Figure 7-13 Flexural displacement profile for Test 3, RW-A15-P10-S51

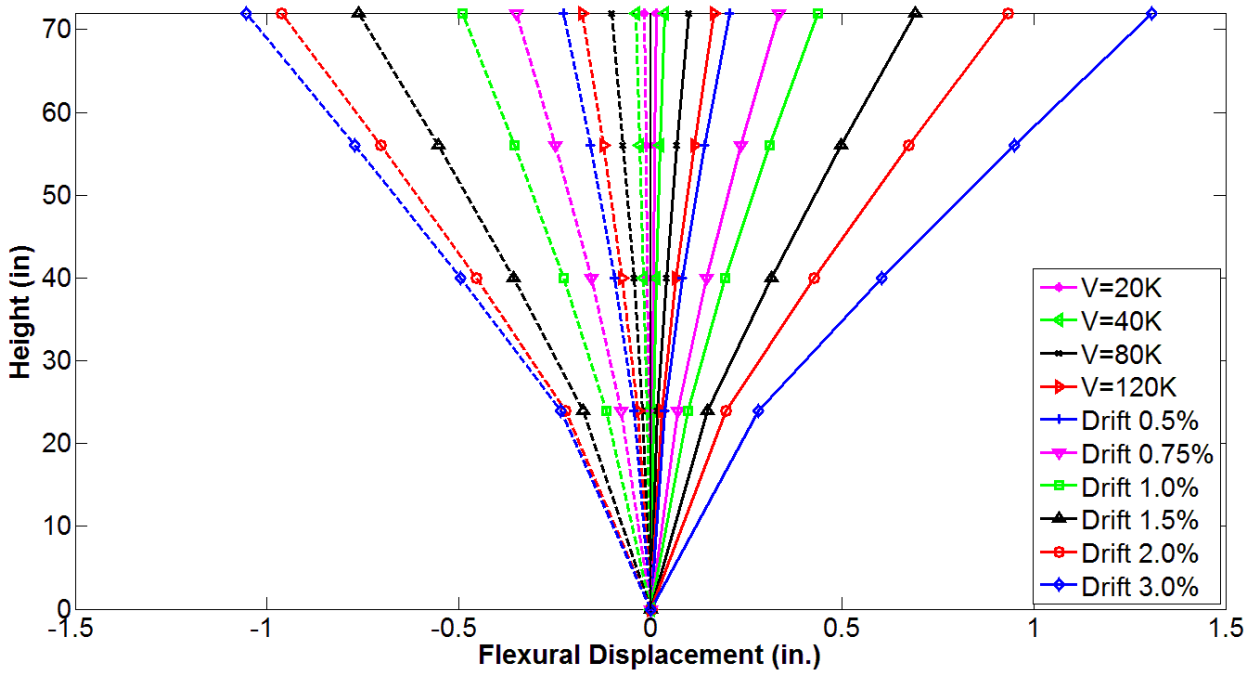

Figure 7-14 Flexural displacement profile for Test 4, RW-A15-P10-S78

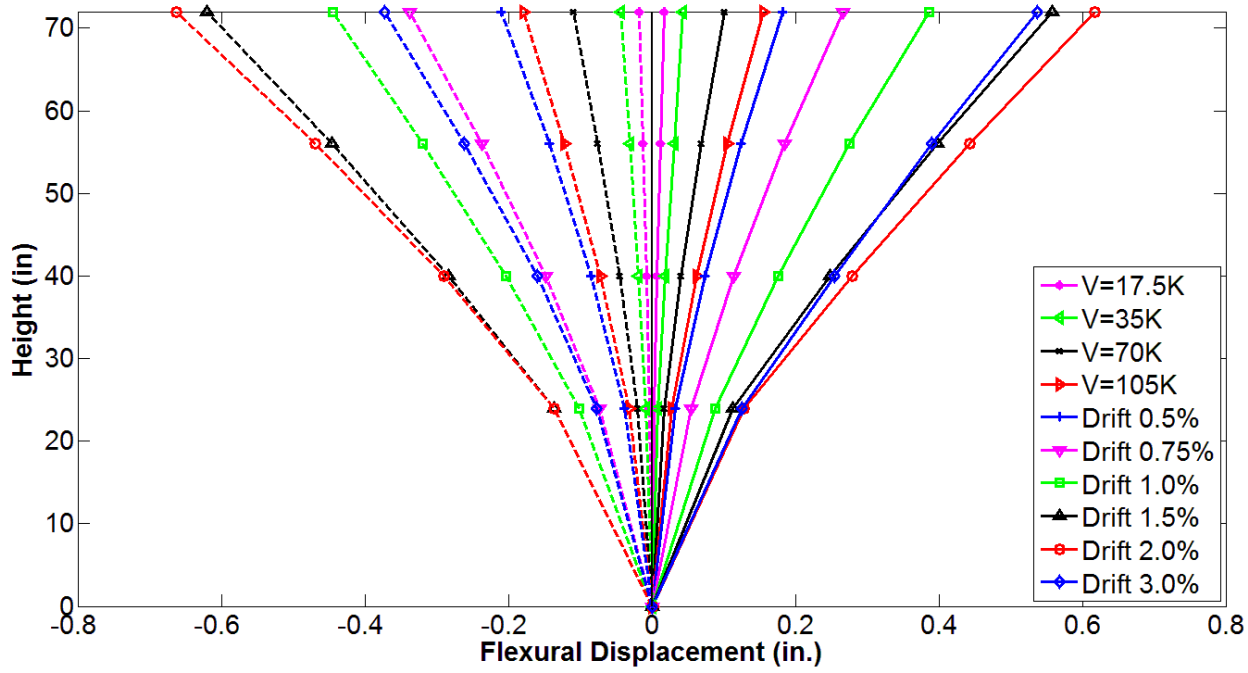

Figure 7-15 Flexural displacement profile for Test 5, RW-A15-P2.5-S64

7.1.3 Slip and extension of boundary longitudinal reinforcement

Vertical deformation due to slip and extension of boundary longitudinal reinforcement in the foundation block was measured using two vertical sensors located at the wall-foundation block interface and near the wall edges, sensors 1 and 2 (see Figures 5.1 and 5.3 in Chapter 5). Although installed with a small gage length, 2 in. (51 mm) for the nominal length, the measurement from these two sensors included some flexural deformations, i.e., the portion of flexural deformation due to the curvature of the wall over the short gage length. In an attempt to obtain the deformation from slip and extension only, this part of flexural deformation must be estimated and subtracted from the measured deformations of sensors 1 and 2. With the assumption that the curvature of this 2 in. (51 mm) height wall region was equal to that of the next wall section above, the 6 in. (152 mm) height wall region with the curvature measured from sensors 3 and 4 (see Figures 5.1 and 5.3), the rotation due to only slip and extension can be computed as

$$\theta_{slip/ext} = \frac{\left(D_1 - D_3 \frac{d_1}{d_3}\right) - \left(D_2 - D_4 \frac{d_2}{d_4}\right)}{L}$$

where D_1, D_2, D_3, D_4 are displacements measured from sensors 1, 2, 3, 4, respectively; d_1, d_2, d_3, d_4 are original lengths of sensors 1, 2, 3, 4, respectively; L is the horizontal distance between the gages.

The following figures, Figures 7-16 through 7-20, present the contribution of slip and extension of boundary longitudinal reinforcement in the foundation block to the top flexural lateral

displacement for Tests 1 to 5, respectively. The figures show that the slip and extension made up approximately 10 to 25% of the top flexural displacement for the 2.0 aspect ratio walls. The contribution of slip and extension tends to be larger, from 10 to 40%, for the 1.5 aspect ratio walls. It also is observed that the slip and extension deformations reached local maxima at a drift ratio between 0.75 and 1.0% for Test 2, and at 0.75% drift for the other four specimens. These results are consistent with observations during the tests, i.e., that horizontal cracks along the wall-foundation block interface occurred during cycles at these drift levels.

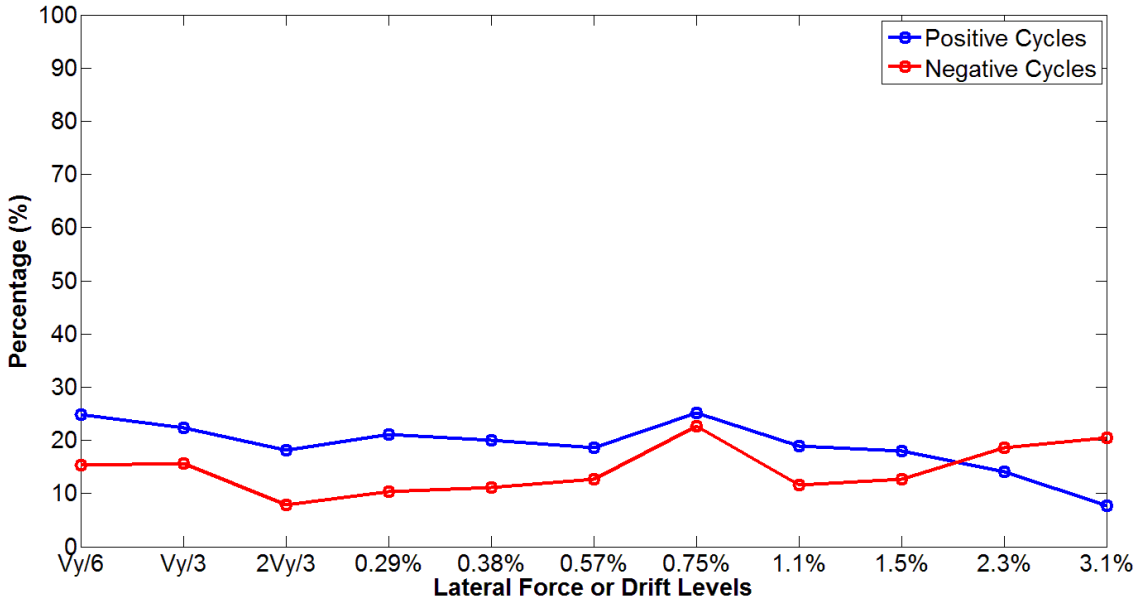

Figure 7-16 Contribution of slip/extension to top flexural displacement for Test 1, RW-A20-P10-S38

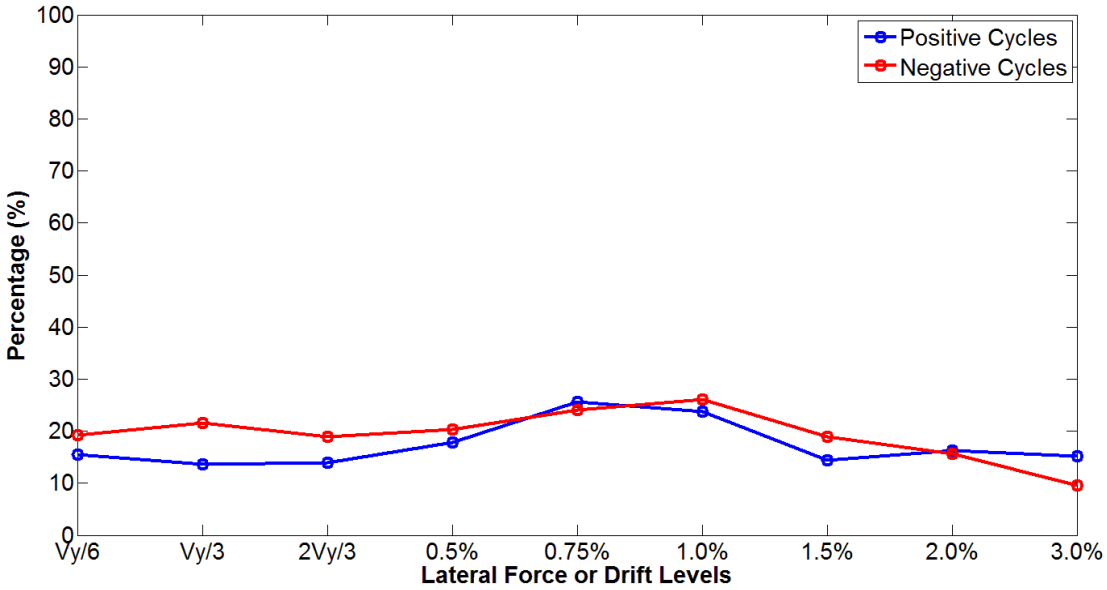

Figure 7-17 Contribution of slip/extension to top flexural displacement for Test 2, RW-A20-P10-S63

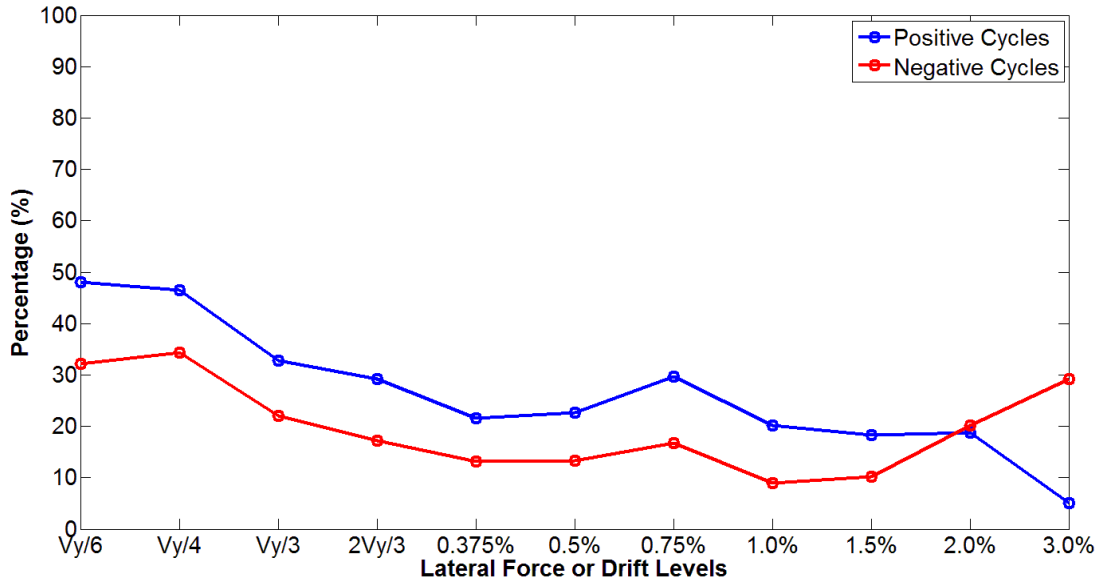

Figure 7-18 Contribution of slip/extension to top flexural displacement for Test 3, RW-A15-P10-S51

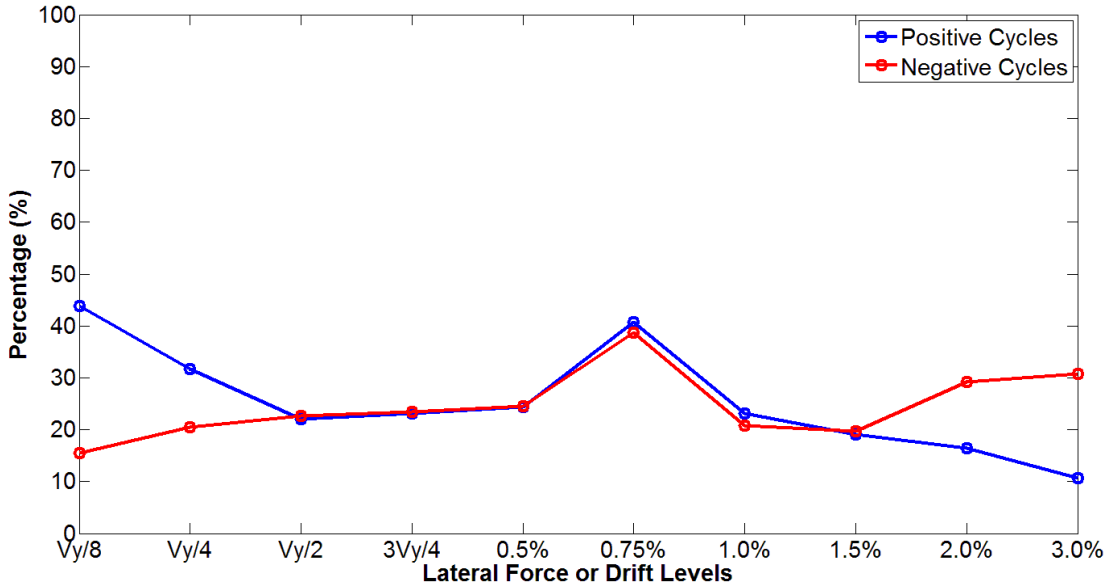

Figure 7-19 Contribution of slip/extension to top flexural displacement for Test 4, RW-A15-P10-S78

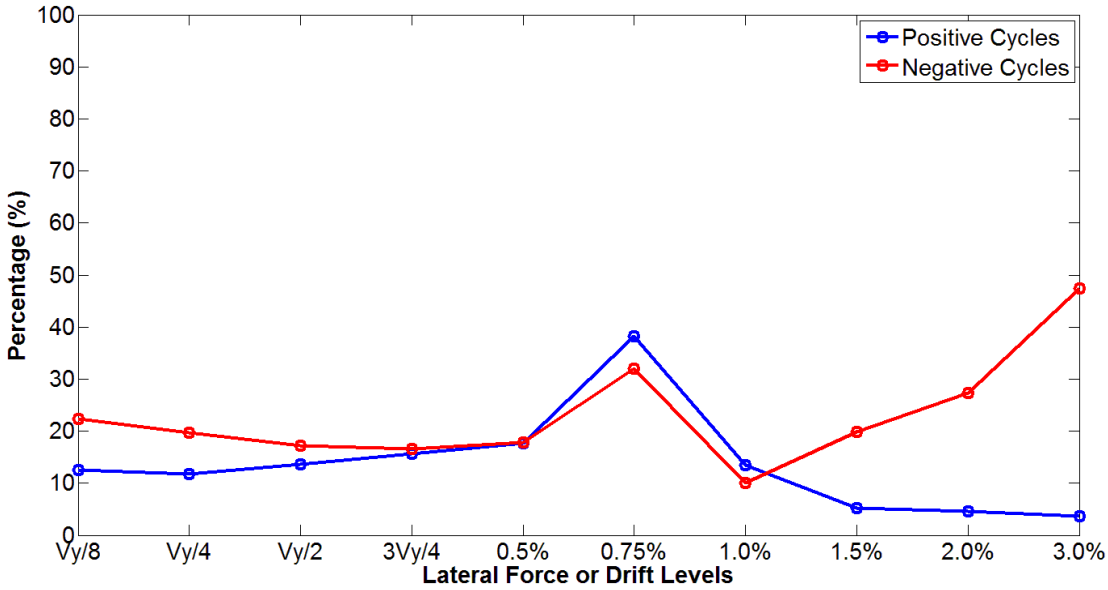

Figure 7-20 Contribution of slip/extension to top flexural displacement for Test 5, RW-A15-P2.5-S64

7.2 Sliding Shear Component of Lateral Displacement

Sliding shear deformation at the wall-foundation block interface was measured during the tests, using two horizontal sensors located on two faces of the wall, sensors 41 and 42 (see Figures 5-1 and 5-3). Two LVDTs were used to eliminate the impact of any wall twisting during testing.

Relations of lateral load versus sliding shear displacement for Tests 1 to 5 are given in Figures 7-21 through 7-25. Figure 7-26 plots simultaneously the load-sliding shear displacement relations for Tests 1 and 2, whereas Figure 7-27 presents relations for Tests 3 and 4, and Figure 7-28 shows relations for Tests 4 and 5. The figures show that the sliding shear displacements were very small compared to the total displacements at the top of the wall. For all five specimens, the maximum sliding shear displacements did not exceed 0.11 in. (2.8 mm), or only $0.001h_w$ for the 96 in. (2.44 m) tall walls. The percentage of sliding shear displacement to the top total displacement at each load or displacement level is presented in more details in Section 7.4.

The figures also indicate that sliding shear deformation was dependent on shear stress level, number of loading cycles applied, and axial stress level. Comparisons of sliding shear displacements between wall specimens with different levels of average shear stress, i.e., Test 1 versus Test 2 on Figure 7-26 and Test 3 versus Test 4 on Figure 7-27, reveal that sliding shear deformations increase when shear stress increases. Figures 7-21 to 7-25 show that sliding shear deformation was influenced by the number of loading cycles; i.e., at the same drift level, the sliding shear deformation increased cycle-to-cycle. As well, Figure 7-28 indicates that sliding shear deformations in the wall with low axial load level, RW-A15-P2.5-S64 or Test 5, were

larger than those in RW-A15-P10-S78, or Test 4, although the shear stress in Test 5 was lower than that in Test 4. This indicates that axial stress had an important impact on sliding shear deformation; i.e., sliding shear displacement increases when axial stress decreases.

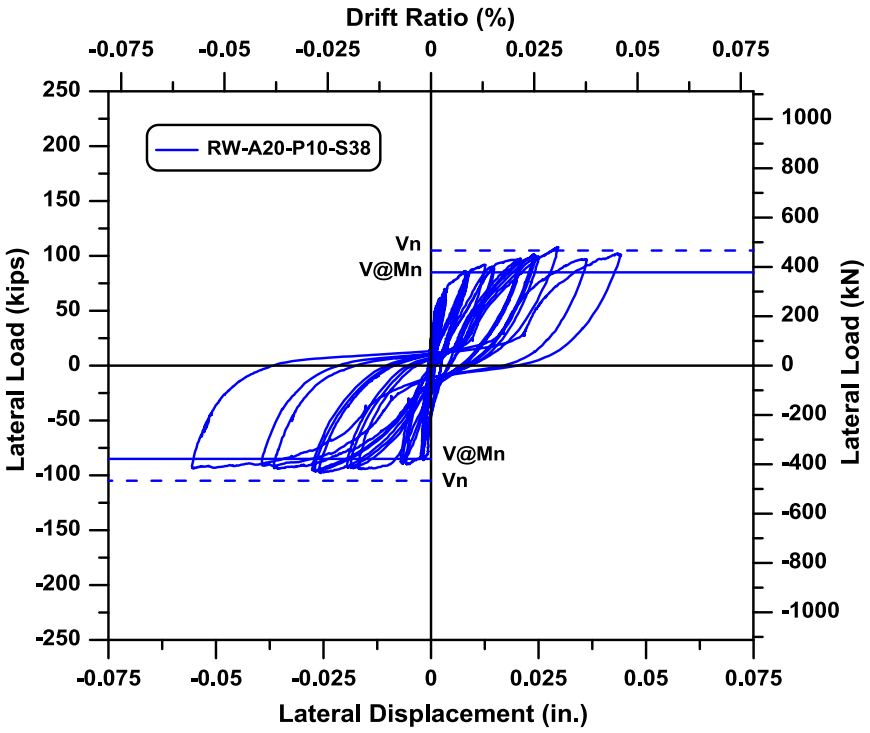

Figure 7-21 Sliding shear displacement for RW-A20-P10-S38

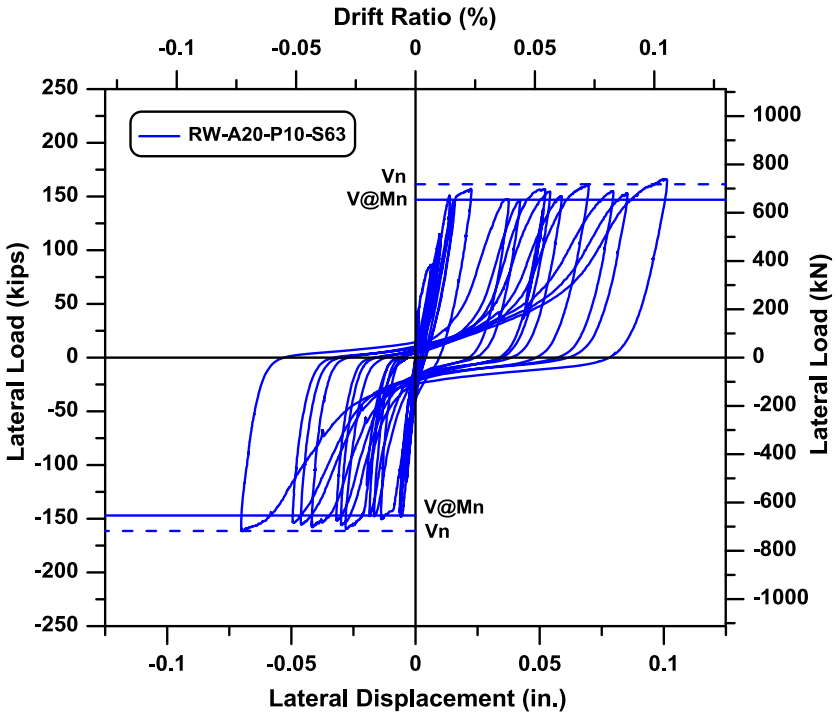

Figure 7-22 Sliding shear displacement for RW-A20-P10-S63

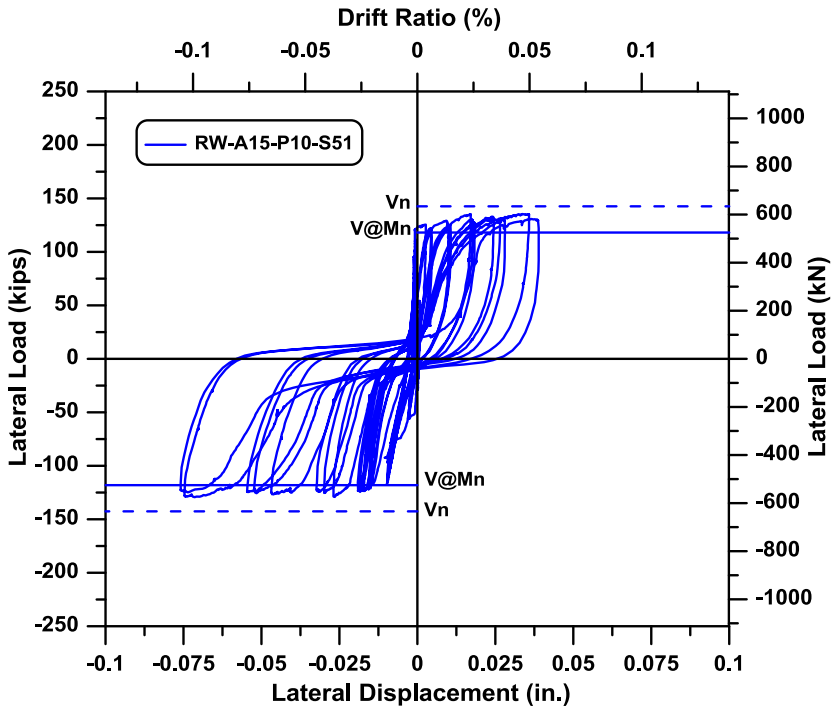

Figure 7-23 Sliding shear displacement for RW-A15-P10-S51

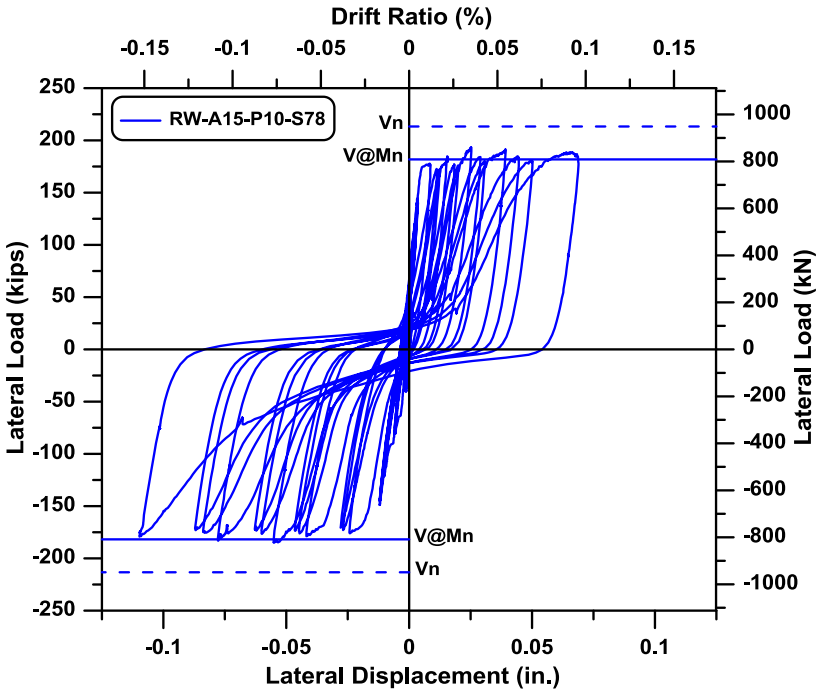

Figure 7-24 Sliding shear displacement for RW-A15-P10-S78

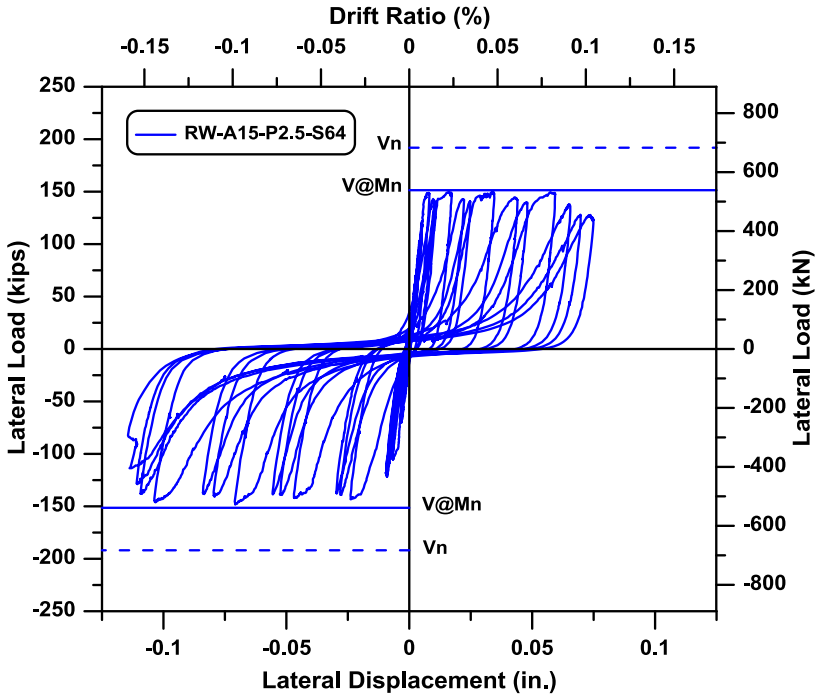

Figure 7-25 Sliding shear displacement for RW-A15-P2.5-S64

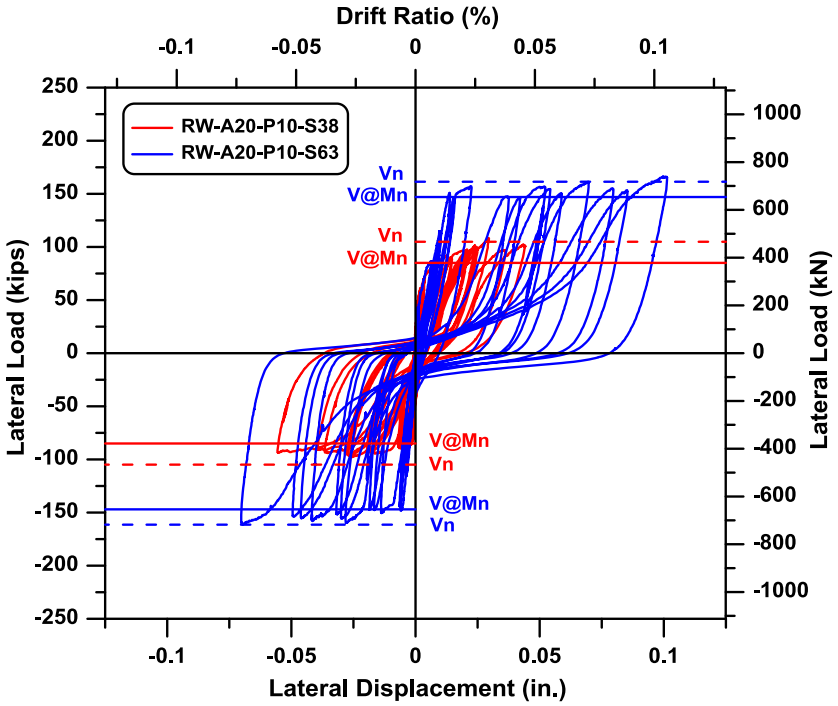

Figure 7-26 Sliding shear displacement for RW-A20-P10-S38 and RW-A20-P10-S63

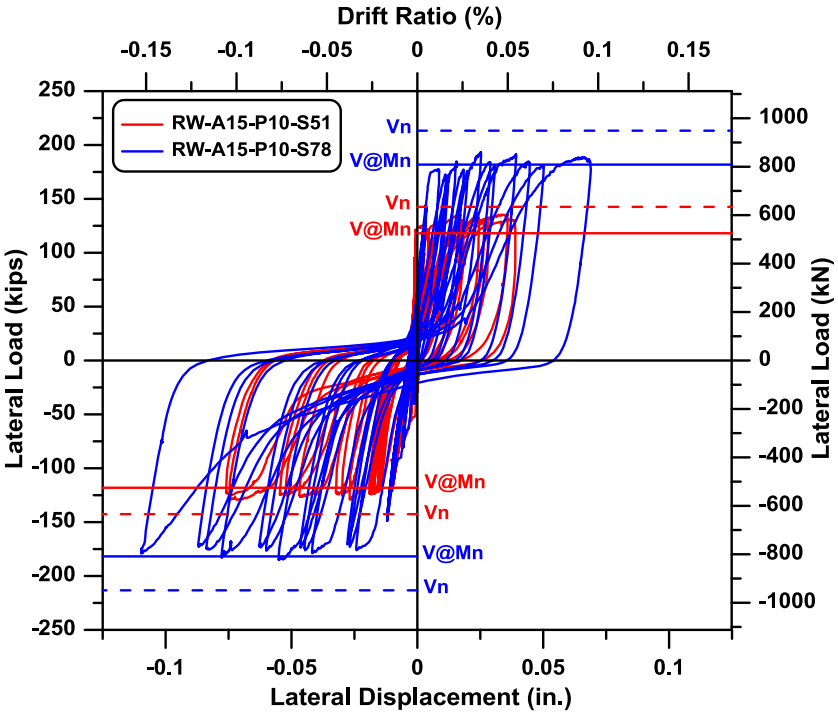

Figure 7-27 Sliding shear displacement for RW-A15-P10-S51 and RW-A15-P10-S78

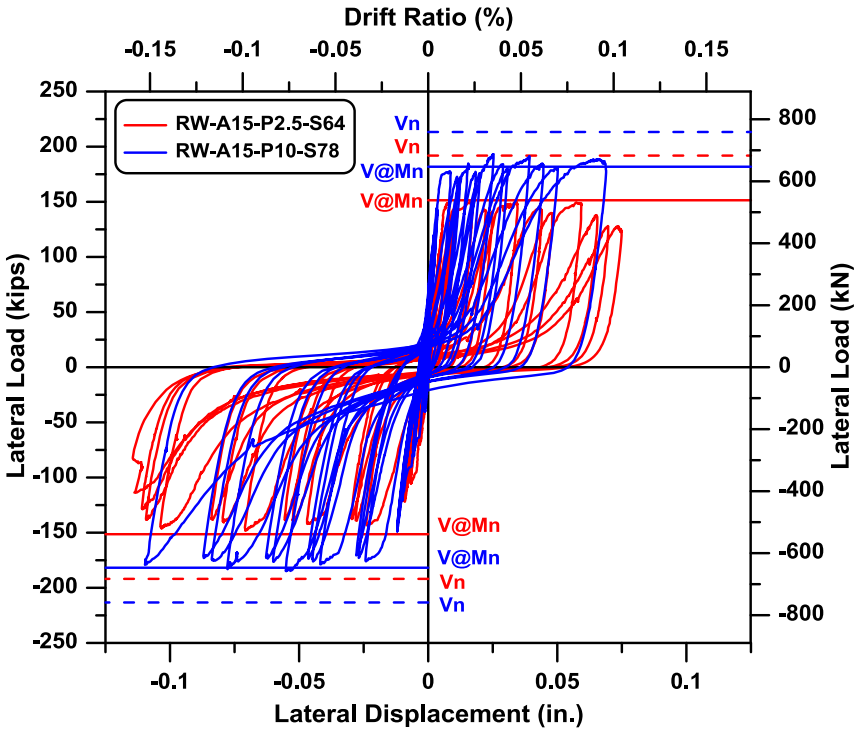

Figure 7-28 Sliding shear displacement for RW-A15-P10-S78 and RW-A15-P2.5-S64

7.3 Shear Component of Lateral Displacement

Shear deformations can be calculated directly from an "X" configuration as shown in Figure 7-29 as:

$$\Delta_s = \frac{1}{2}\left[\sqrt{(d_1 + D_1)^2 - h^2} - \sqrt{(d_2 + D_2)^2 - h^2}\right]$$

where d_1 and d_2 are original lengths of the two diagonal sensors, D_1 and D_2 are displacements measured from these diagonal sensors, h is the height of the wall section.

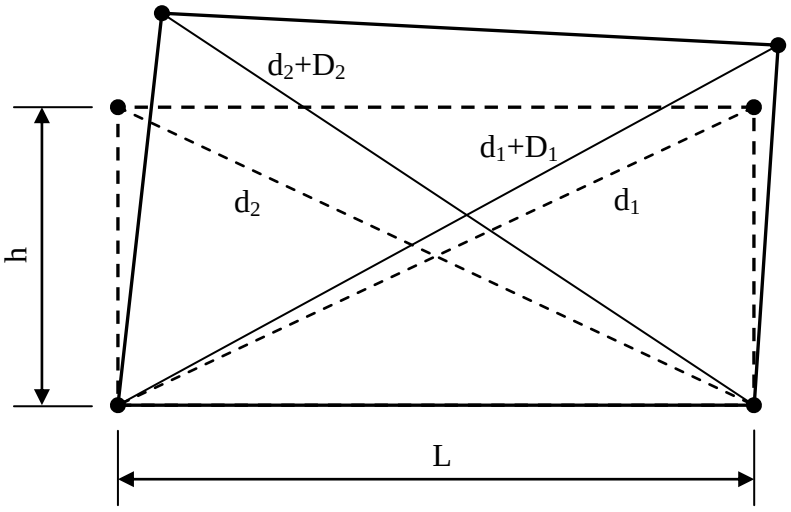

Figure 7-29 Simplified method for determination of shear deformation of a wall section

This approach for determination of shear deformation, without accounting for the impact of curvature distribution of the wall to the shear response, is very simple, but only accurate for the case of $\alpha = 0.5$ (Hiraishi, 1984; Massone and Wallace, 2004). The value of α is usually larger than 0.5, leading to an overestimation of shear distortion. Within the wall yielding region, Massone and Wallace (2004) showed that this simplified method overestimated shear deformations by as much as 30%.

In this study, shear lateral deformation was determined by subtracting the total lateral displacement to the flexural and sliding shear displacements.

$$\Delta_s = \Delta_{total} - \Delta_f - \Delta_{sld}$$

where Δ_{total} and Δ_f are the total and flexural lateral displacements at the height considered, Δ_{sld} is the sliding shear displacement at the wall-foundation block interface. The computation of total

lateral displacement was presented in Sections 6.3 and 6.4, whereas the calculation of flexural and sliding shear deformations were described in Sections 7.1 and 7.2, respectively.

7.3.1 Lateral load versus shear displacement relations

7.3.1.1 Walls with aspect ratio of 2.0

Relations of lateral load versus shear displacement at the top of the wall for specimens RW-A20-P10-S38 (Test 1) and RW-A20-P10-S63 (Test 2) are shown in Figures 7-30 and 7-31, respectively, whereas Figure 7-32 plots both relations simultaneously. These two specimens had the same aspect ratio and almost the same actual axial stress, but were different in shear stress level. The figures show that shear displacements in Test 2 were much larger than those in Test 1, which was consistent with expectations, given the much larger shear stress for Test 2.

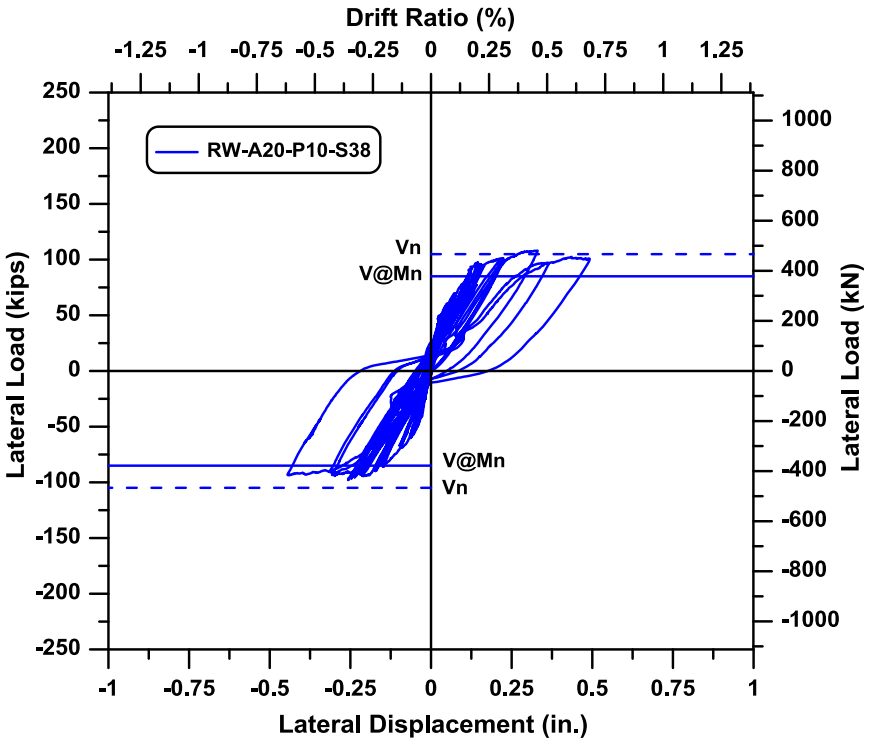

Figure 7-30 Top shear displacement for RW-A20-P10-S38

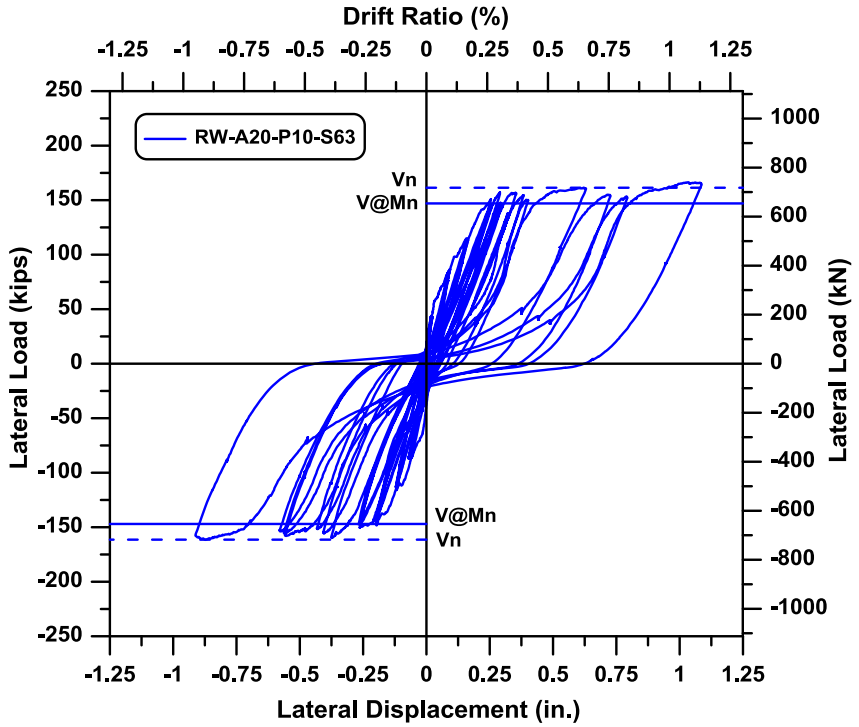

Figure 7-31 Top shear displacement for RW-A20-P10-S63

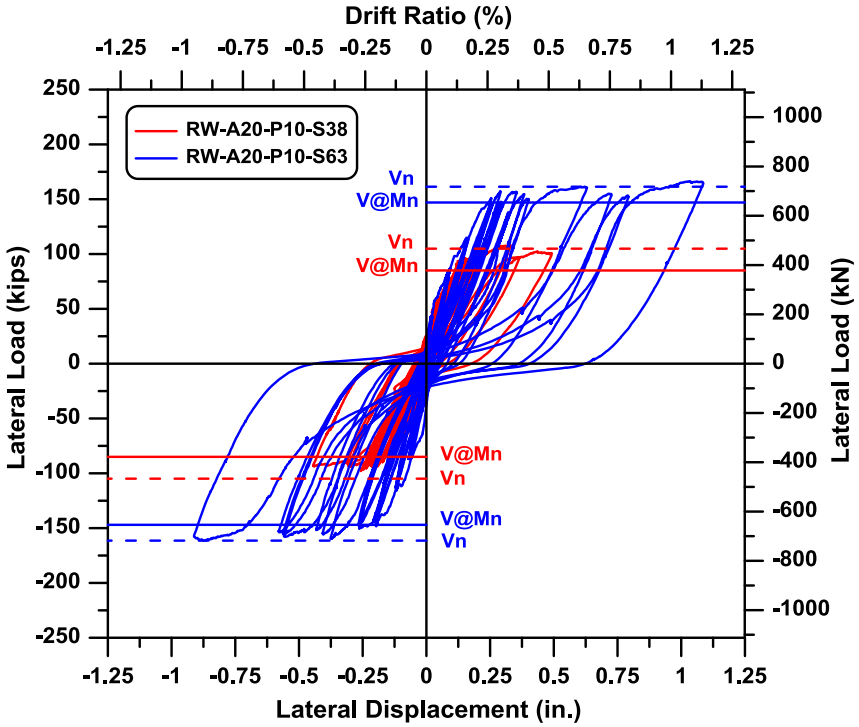

Figure 7-32 Top shear displacement for RW-A20-P10-S38 and RW-A20-P10-S63

7.3.1.2 Walls with aspect ratio of 1.5

Lateral load versus top shear displacement relations for specimens RW-A15-P10-S51 (Test 3), RW-A15-P10-S78 (Test 4), and RW-A15-P2.5-S64 (Test 5) are given in Figures 7-33 to 7-35, respectively. Both relations for Tests 3 and 4 are plotted in Figure 7-36, whereas Figure 7-37 shows simultaneously responses for Tests 4 and 5. The figures show that shear displacements in Test 5 were much larger than those in Tests 3 and 4, indicating that axial stress had a significant impact on the magnitude of the shear displacement, i.e., shear displacements may increase significantly as axial stress decreases. Since many test programs on low- and moderate-aspect ratio walls do not include or vary the level of applied axial stress, this impact has not been widely reported and the data provided here will help with model development and validation.

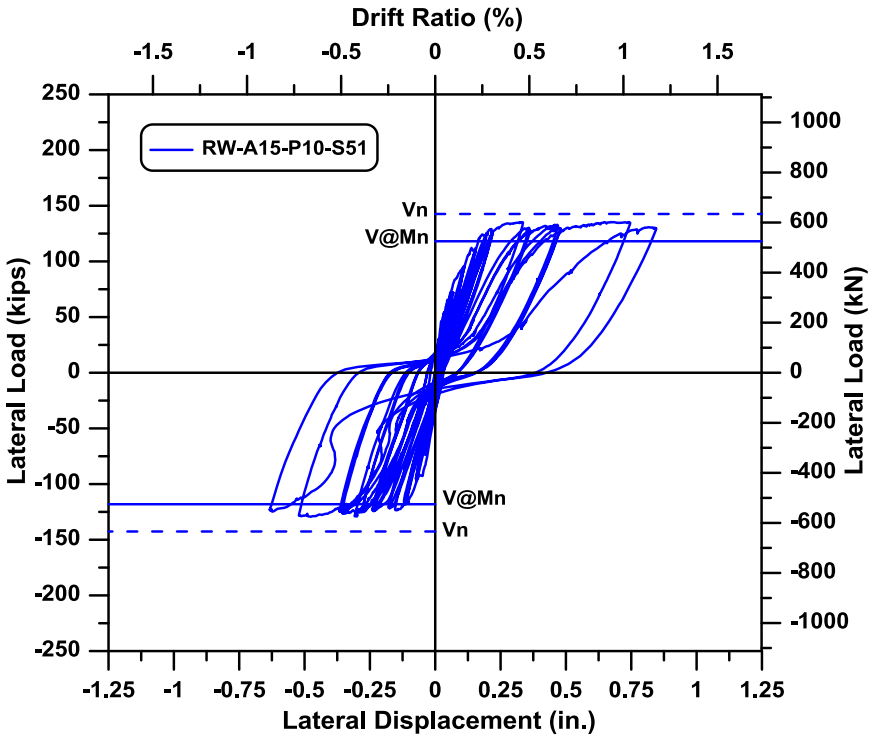

Figure 7-33 Top shear displacement for RW-A15-P10-S51

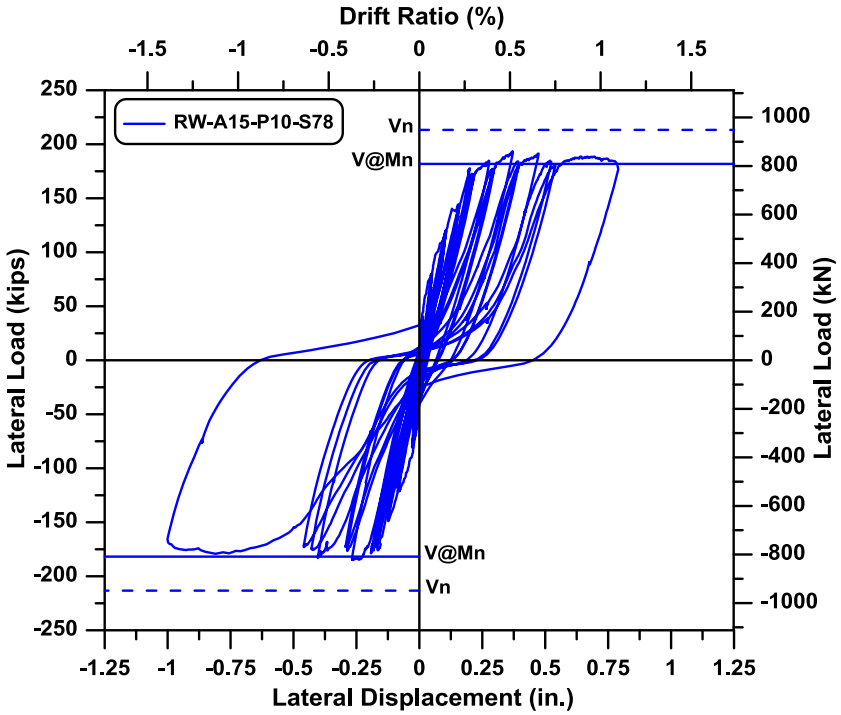

Figure 7-34 Top shear displacement for RW-A15-P10-S78

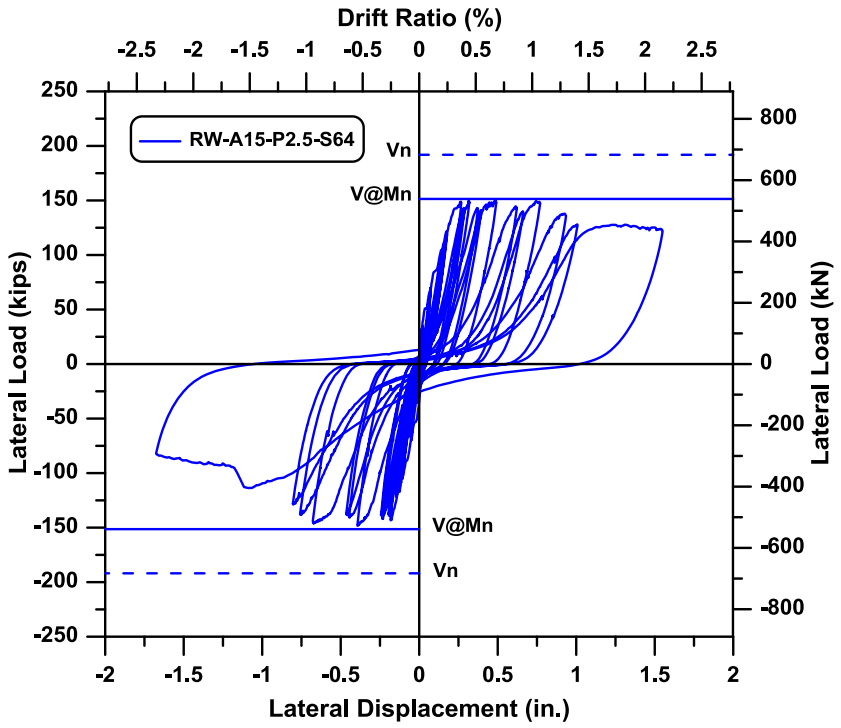

Figure 7-35 Top shear displacement for RW-A15-P2.5-S64

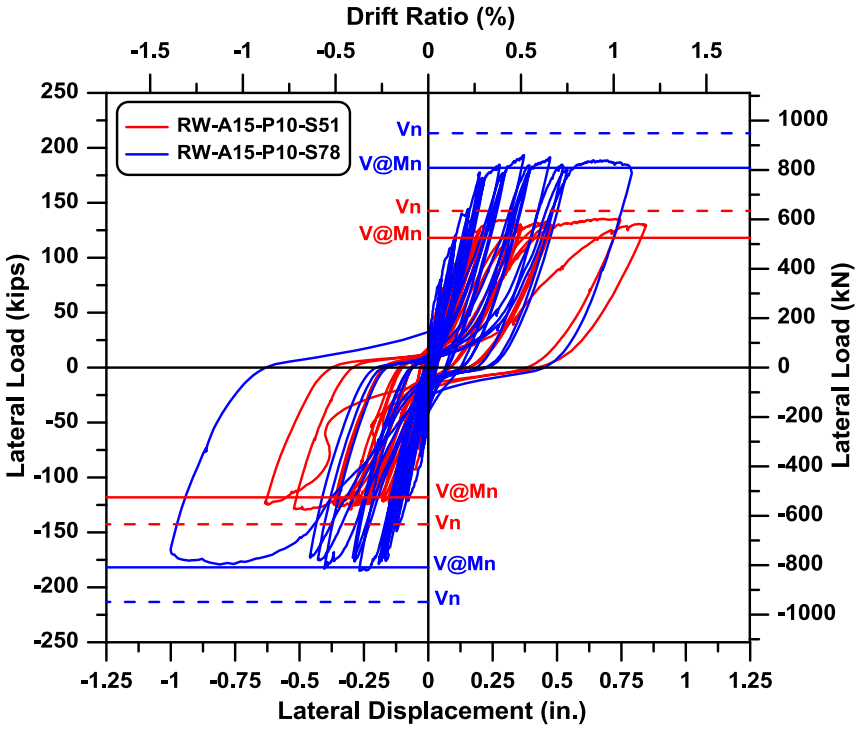

Figure 7-36 Top shear displacement for RW-A15-P10-S51 and RW-A15-P10-S78

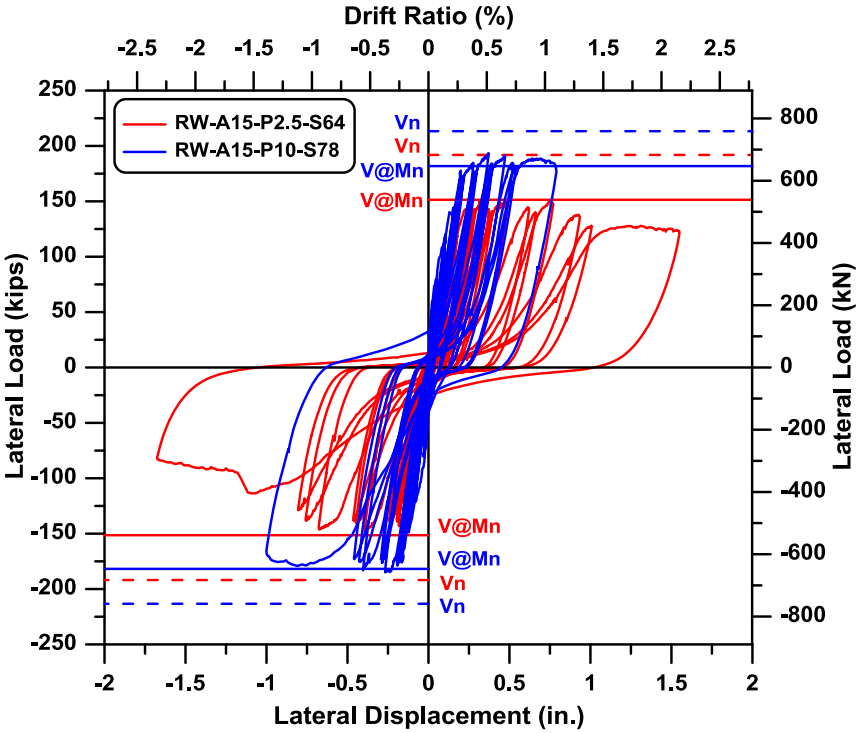

Figure 7-37 Top shear displacement for RW-A15-P10-S78 and RW-A15-P2.5-S64

7.3.2 Shear displacement profiles

Profiles of shear displacement over the wall height for Tests 1 to 5 are presented in Figures 7-38 to 7-42, respectively. Similar to the profiles of total and flexural displacements, in shear displacement profiles, shear displacements were determined at maximum lateral load (for force-controlled cycles) or maximum displacement (for displacement-controlled cycles) during the first cycle under both positive and negative loadings. Continuous lines represent positive loading, whereas the dashed line represent negative loading. As well, shear displacements were obtained 24 in. (610 mm), 40 in. (1016 mm), 56 in. (1422 mm), 72 in. (1829 mm), and 96 in. (2438 mm) above the wall-foundation block interface.

As observed in the figures, shear deformations were concentrated over the plastic hinge. The figures also indicate that nonlinear shear occurred even for walls that yield in flexure (and this has been observed before; Massone and Wallace, 2004; Oesterle et al., 1976 and 1979). Magnitude of shear deformations increases with increasing shear, especially for walls with high shear stress levels, i.e., RW-A20-P10-S63 (Test 2), RW-A15-P10-S78 (Test 4), and RW-A15-P2.5-S64 (Test 5).

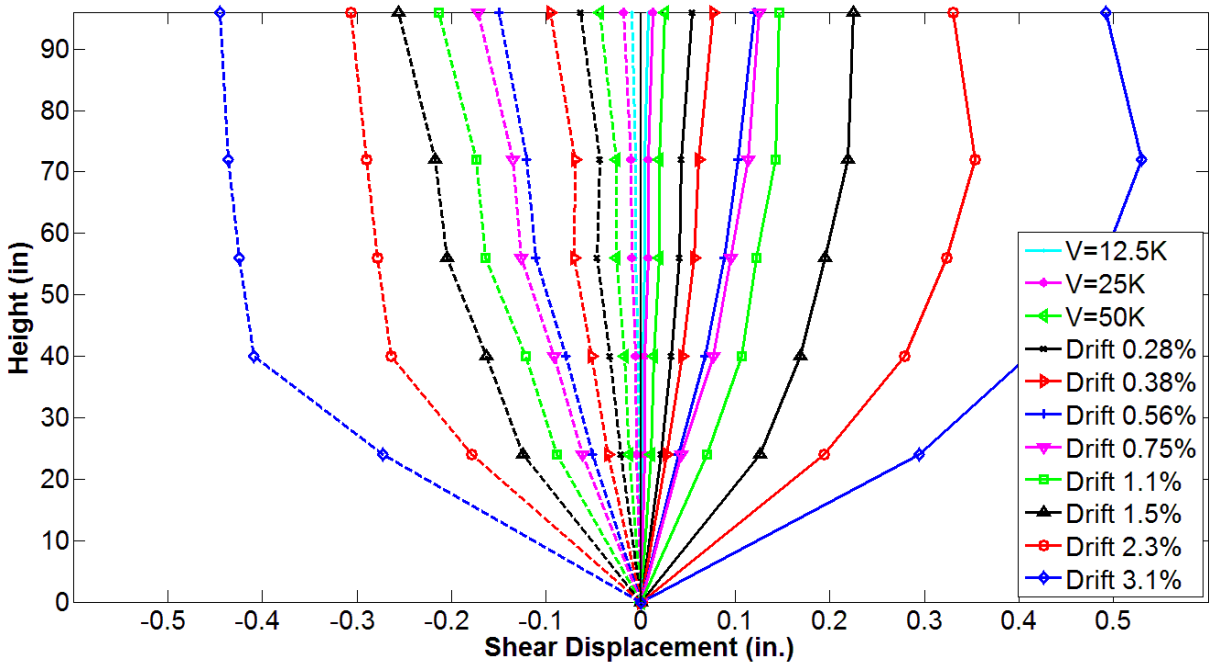

Figure 7-38 Shear displacement profile for Test 1, RW-A20-P10-S38

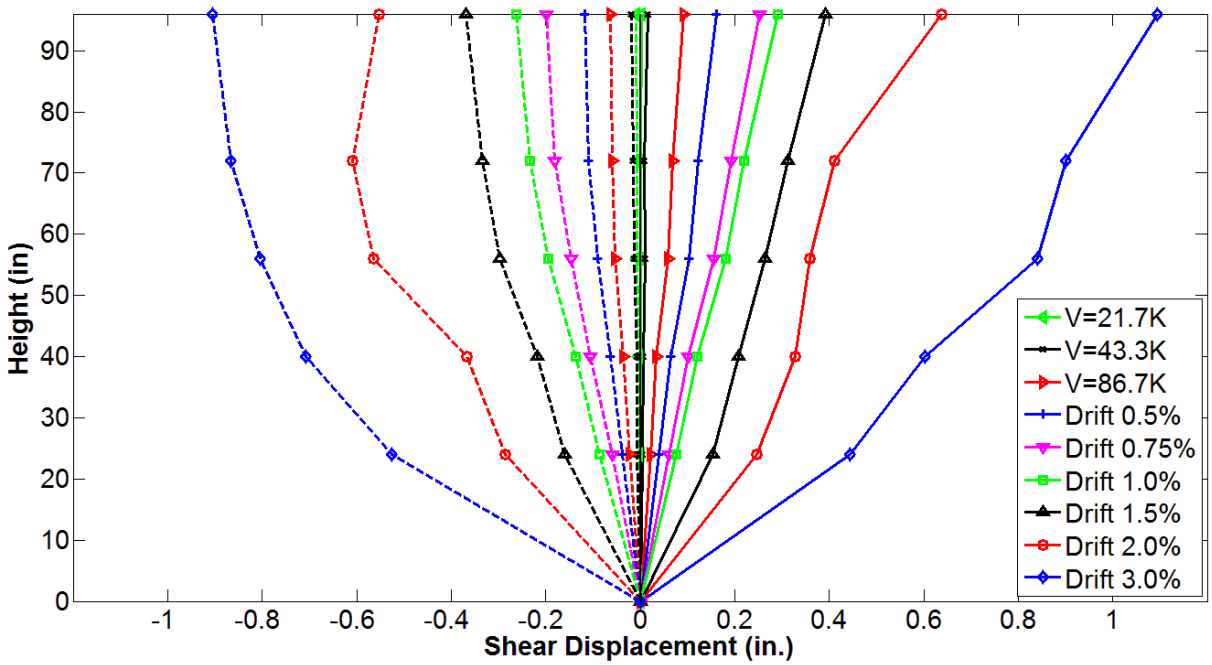

Figure 7-39 Shear displacement profile for Test 2, RW-A20-P10-S63

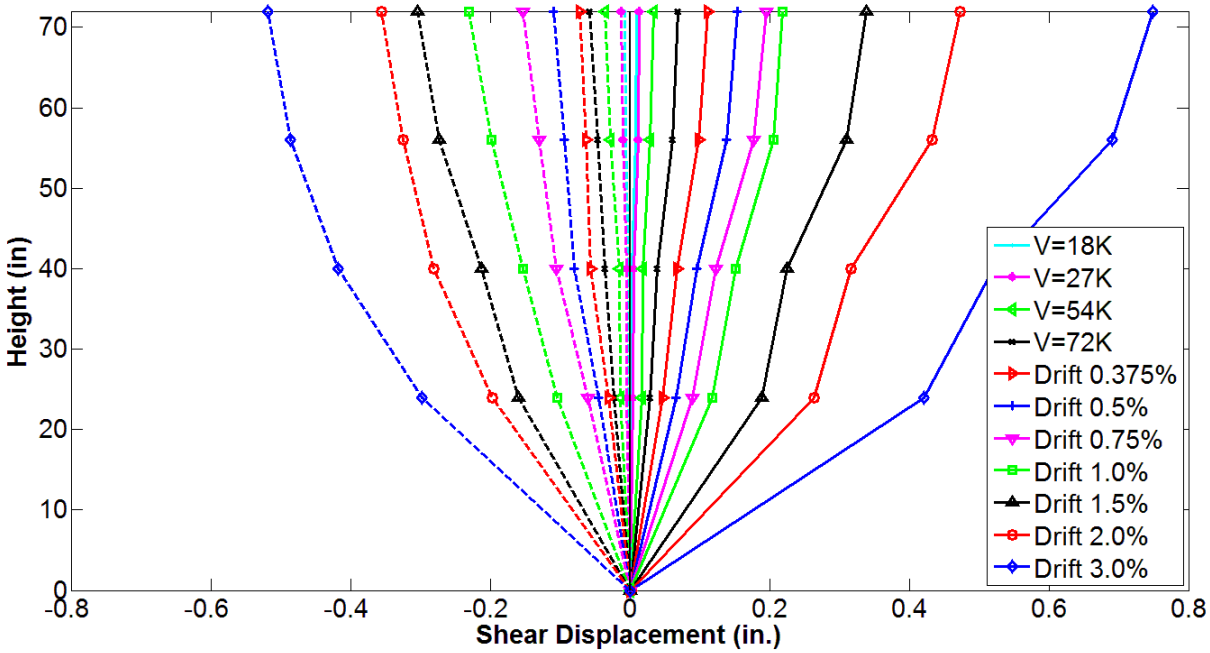

Figure 7-40 Shear displacement profile for Test 3, RW-A15-P10-S51

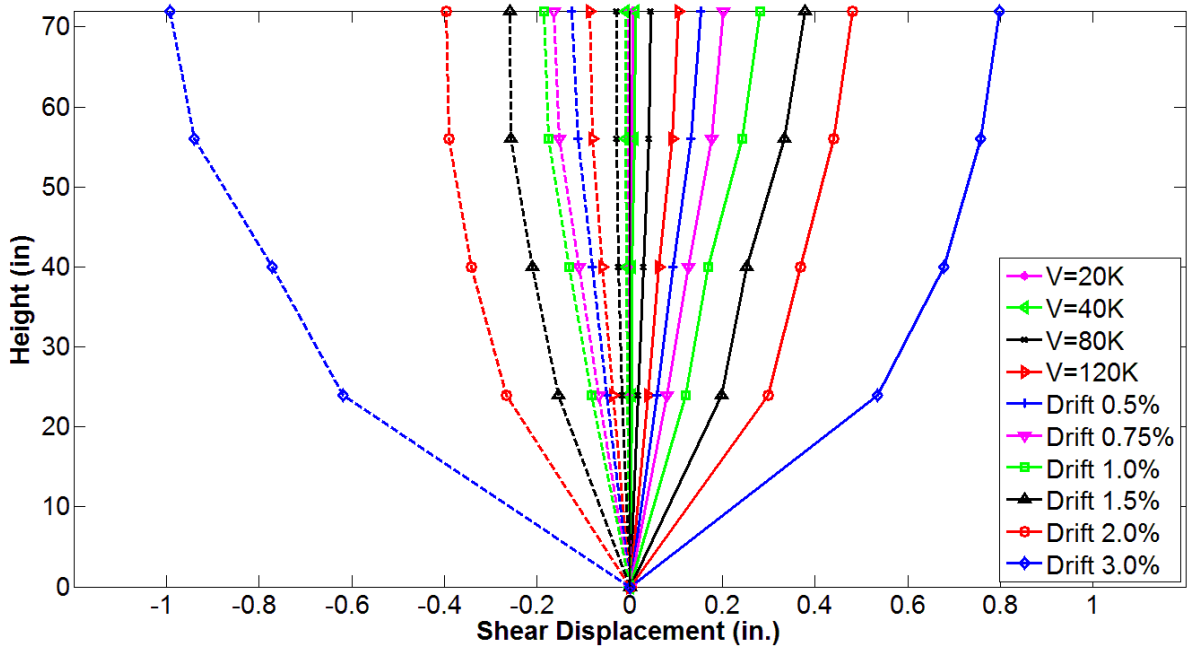

Figure 7-41 Shear displacement profile for Test 4, RW-A15-P10-S78

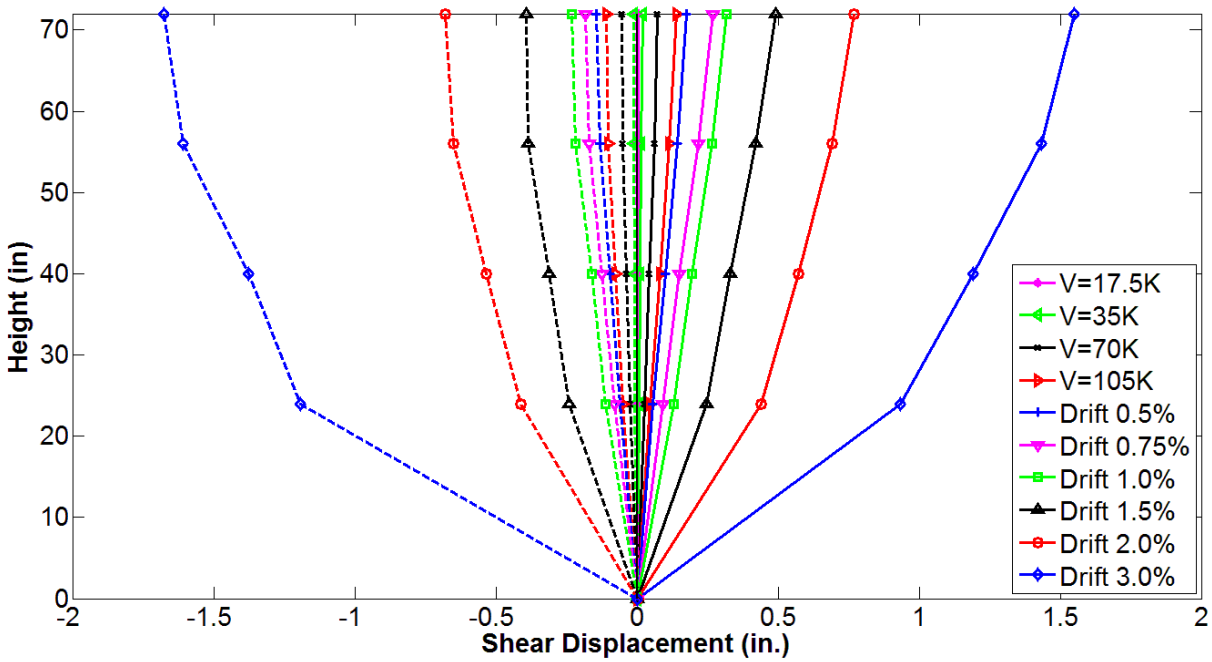

Figure 7-42 Shear displacement profile for Test 5, RW-A15-P2.5-S64

7.4 Contribution of Various Components to Total Lateral Displacement

Contributions of flexural, shear, and sliding shear deformations to top total lateral displacement for Tests 1 to 5 are shown in Figures 7-43 to 7-47, respectively. The contribution of each lateral displacement component was computed at each force or displacement level for the first cycle under both positive and negative loadings. Continuous lines represent positive loading, whereas the dashed lines represent negative loading.

The figures show that sliding shear deformation contributed very little to the top total displacement, with an average percentage of approximately 1%, 2%, 2%, 3%, and 3% for Tests 1 to 5, respectively, for all drift levels. The contribution of sliding shear deformation to the total

lateral displacement tended to be higher during cycles at large drift ratios, and reached maximum values of about 2%, 4%, 4%, 6%, and 7% for Tests 1 to 5, respectively.

The contribution of flexure to total displacement tends to increase slightly from the beginning to the end of the test for walls with moderate shear stress levels, i.e., RW-A20-P10-S38 (Test 1) and RW-A15-P10-S51 (Test 3). In contrast, for the remaining tests, the percentage contribution of flexural displacement tends to decrease, especially once significant lateral strength degradation initiates. Due to the very small contribution of sliding shear deformations, the trend of shear displacement contribution to the total displacement is opposite to the trend of the flexural contribution, e.g., the contribution of shear displacement component generally increases from the beginning of the test until the end of the test for specimens with higher shear stress levels, i.e., RW-A20-P10-S63 (Test 2), RW-A15-P10-S78 (Test 4), and RW-A15-P2.5-S64 (Test 5), where sliding shear failure was part of their failure modes. The average contributions of shear deformations after first flexural yielding of boundary longitudinal reinforcement were approximately 20%, 30%, 30%, 35%, and 50% for Tests 1 to 5, respectively.

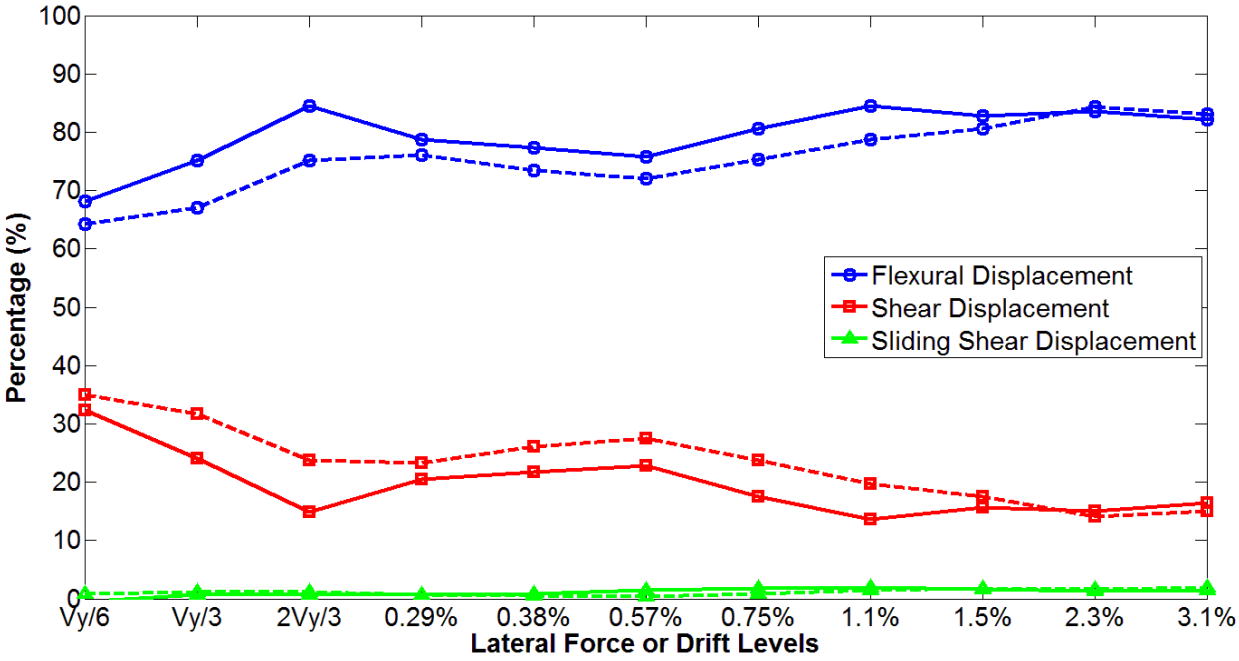

Figure 7-43 Contributions to top lateral displacement for Test 1, RW-A20-P10-S38

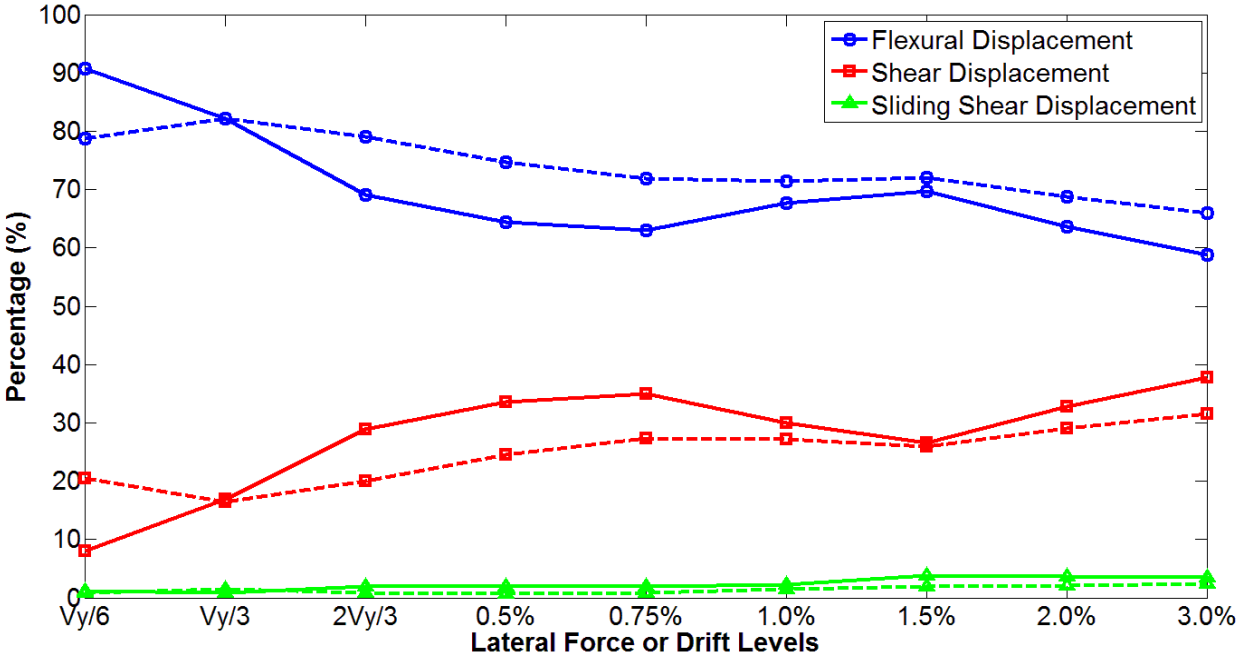

Figure 7-44 Contributions to top lateral displacement for Test 2, RW-A20-P10-S63

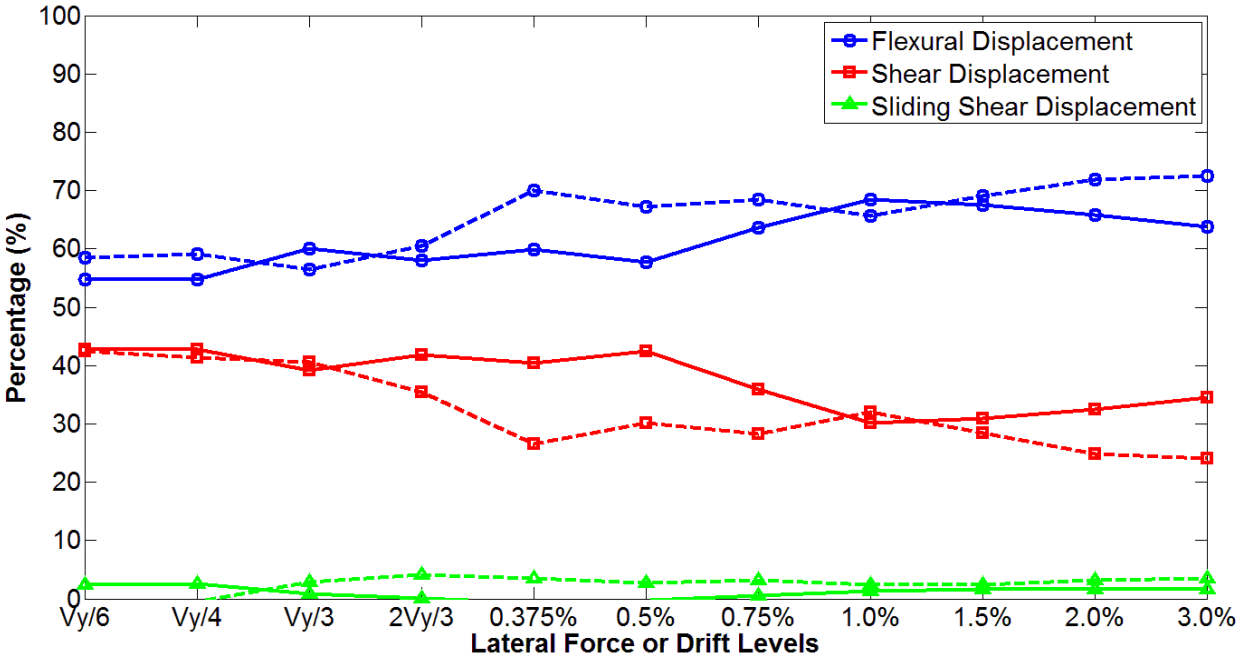

Figure 7-45 Contributions to top lateral displacement for Test 3, RW-A15-P10-S51

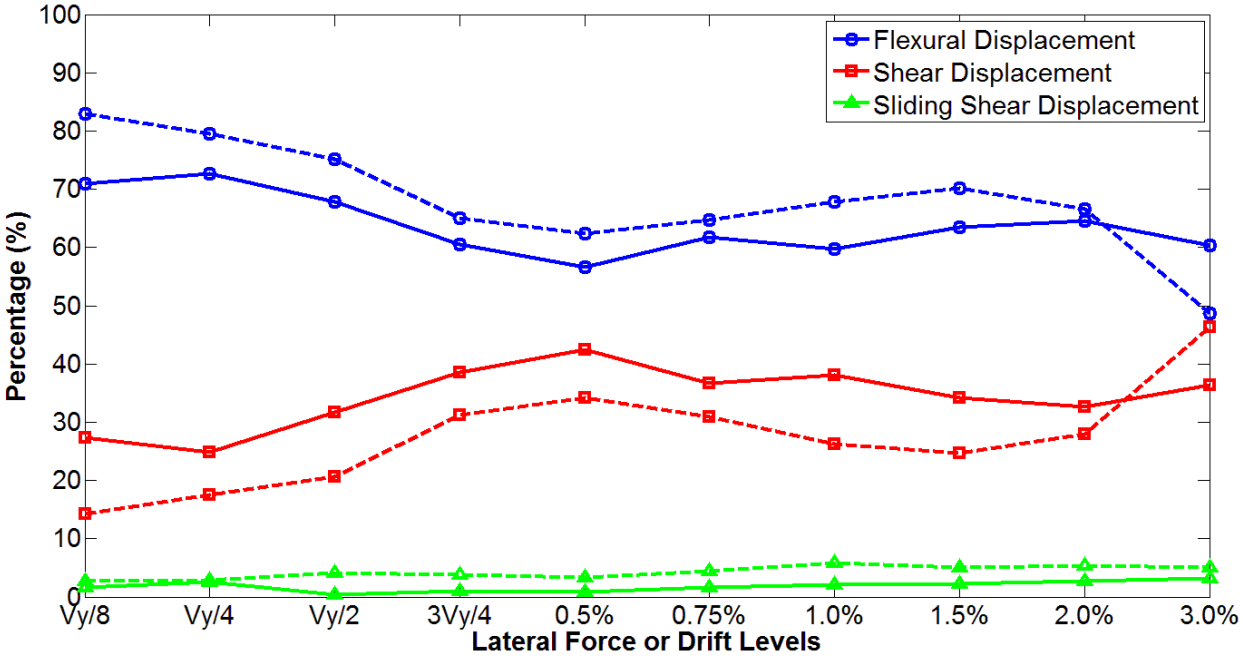

Figure 7-46 Contributions to top lateral displacement for Test 4, RW-A15-P10-S78

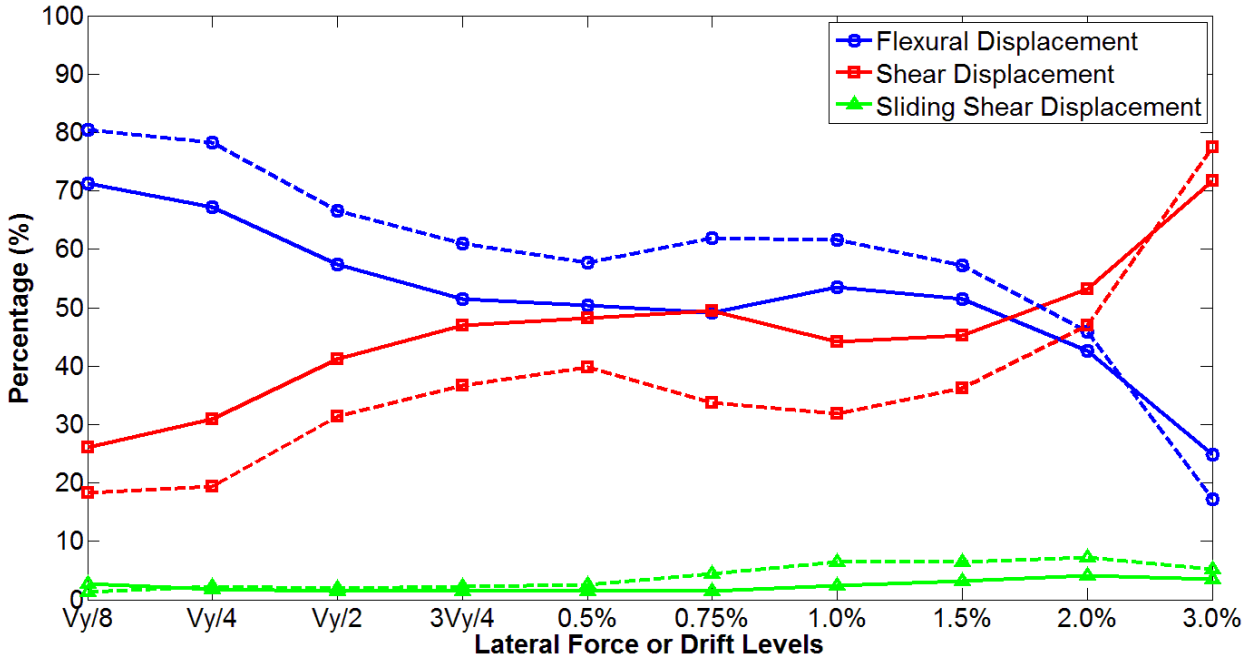

Figure 7-47 Contributions to top lateral displacement for Test 5, RW-A15-P2.5-S64

The following figures, Figures 7-48 through 7-52, provide a comparison of shear displacement contributions to top total displacement at the first and third cycles for Tests 1 to 5, respectively. In these figures, continuous lines represent positive loading, whereas the dashed line represent negative loading. For RW-A20-P10-S38, only two cycles were performed at 2.3% drift ratio; therefore, the shear contribution at the first cycle is compared with that at the second cycle. The figures show the consistency between the results from the first and third cycles for all specimens at all drift levels, except for RW-A15-P10-S64 (Test 5) where significant shear sliding occurred at large drift levels. For Test 5, the contribution to the total displacement from shear component at the third cycle was much larger than that at the first cycle, starting from drift ratio of 1.0%.

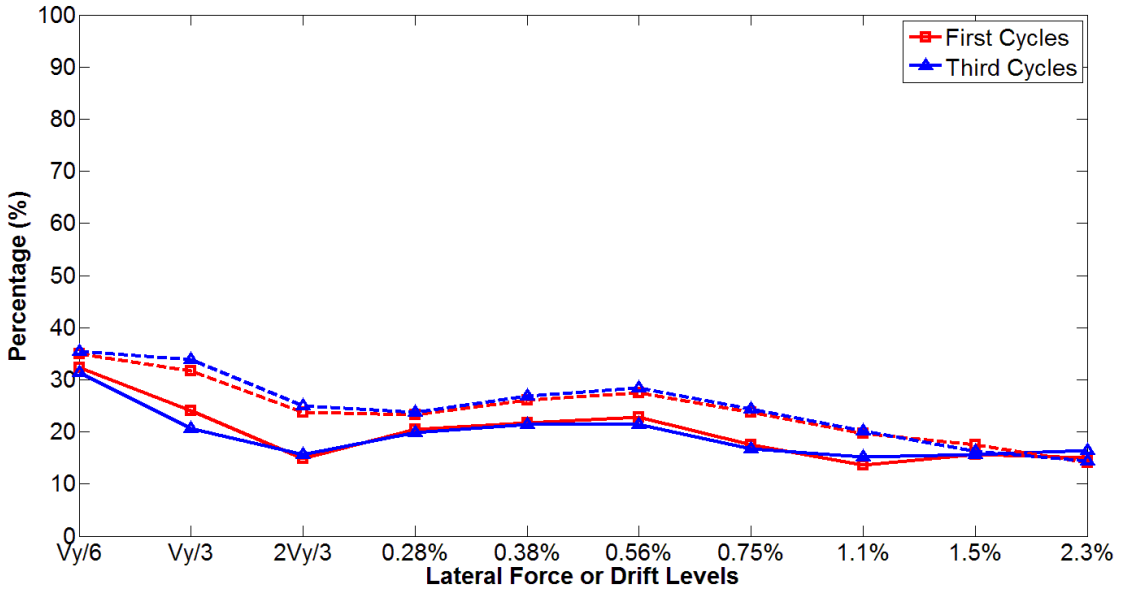

Figure 7-48 Shear contribution to top lateral displacement at first and third cycles for Test 1, RW-A20-P10-S38

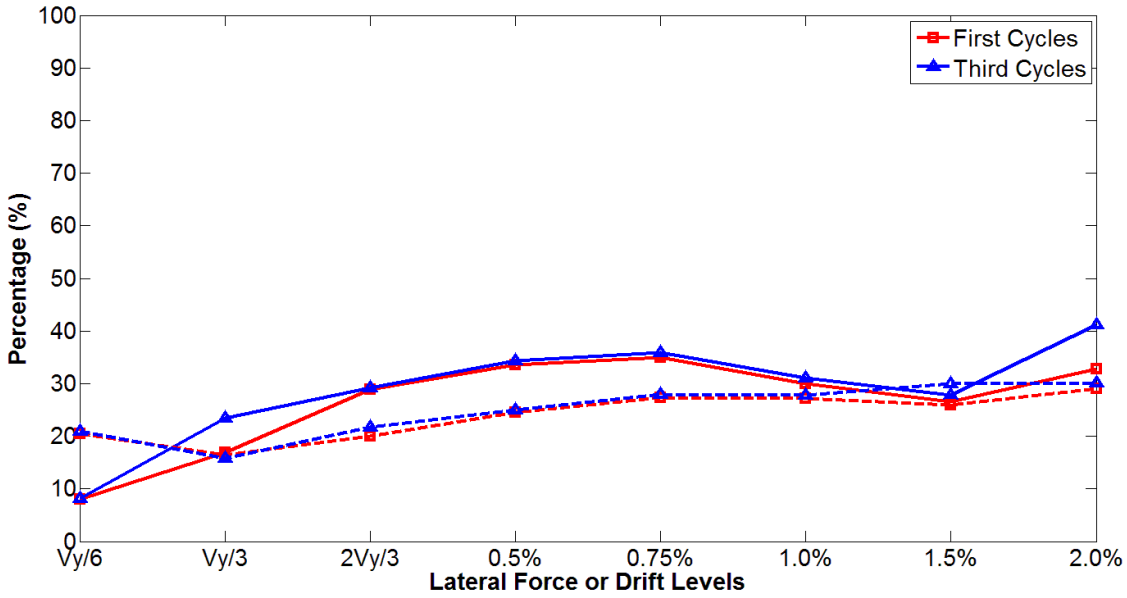

Figure 7-49 Shear contribution to top lateral displacement at first and third cycles for Test 2, RW-A20-P10-S63

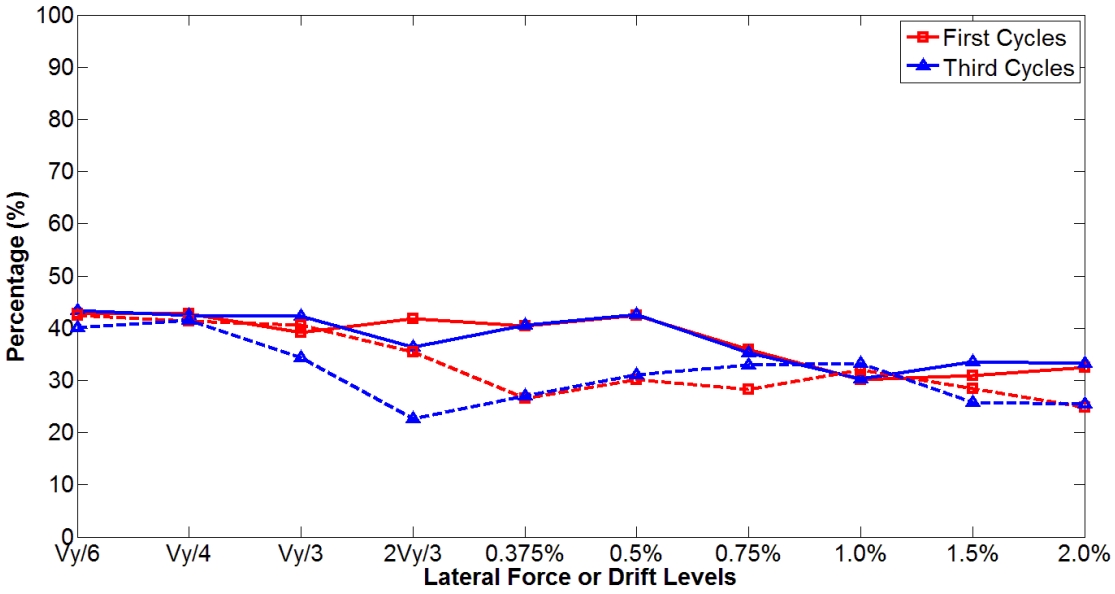

Figure 7-50 Shear contribution to top lateral displacement at first and third cycles for Test 3, RW-A15-P10-S51

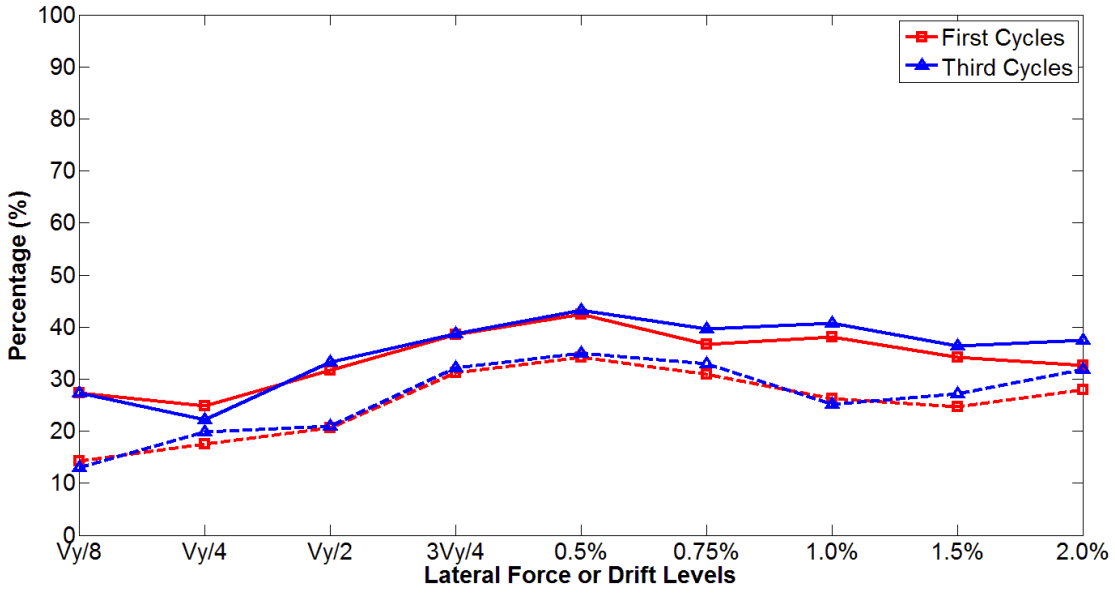

Figure 7-51 Shear contribution to top lateral displacement at first and third cycles for Test 4, RW-A15-P10-S78

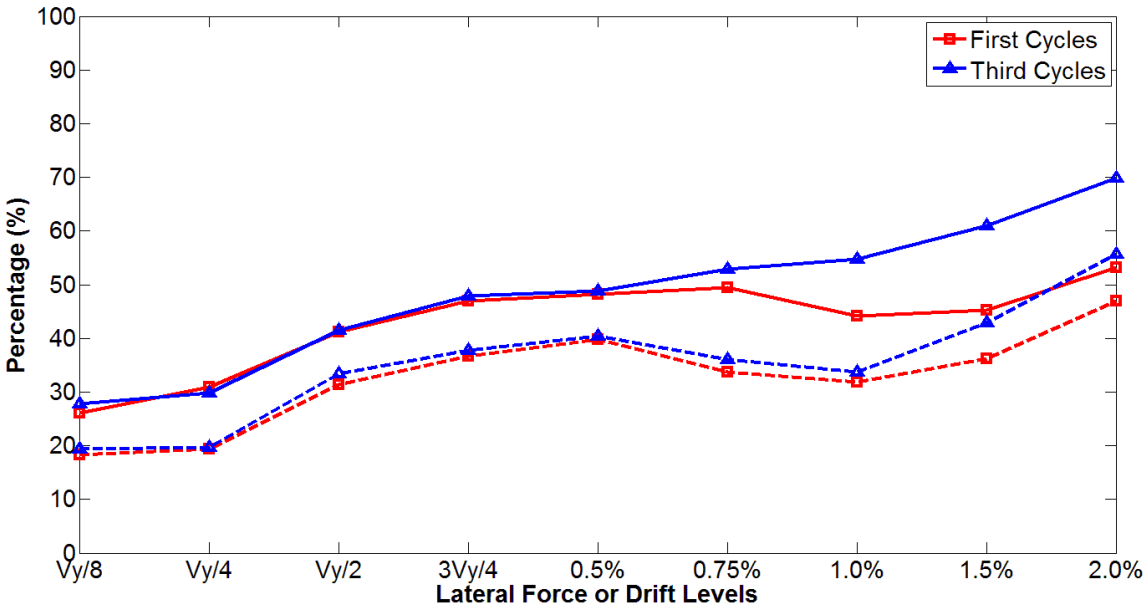

Figure 7-52 Shear contribution to top lateral displacement at first and third cycles for Test 5, RW-A15-P2.5-S64

CHAPTER 8 MODELING

In this chapter, the effective flexural and shear stiffness values of wall specimens are derived from test results and compared with values recommended by ASCE 41-06 and FEMA 356. The backbone curves of all five wall specimens also are constructed and compared with models from ASCE 41-06, including Supplement No.1 (2007). Finally, monotonic modeling results for both an uncoupled (P-M and V independent) and a coupled model are computed and compared with test results.

8.1 Effective Flexural Stiffness

Effective flexural and shear stiffness values are important modeling parameters for linear and nonlinear analysis of buildings that incorporate structural walls for lateral load resistance. Effective flexural stiffness is addressed in this subsection, whereas effective shear stiffness is considered in the next section. ASCE 41-06 including Supplement No.1, Seismic Rehabilitation of Existing Buildings, recommends a flexural rigidity of $0.5E_cI_g$ for cracked walls. FEMA 356, Prestandard for the Seismic Rehabilitation of Buildings, suggests the same value of flexural stiffness for cracked walls, $0.5E_cI_g$, and also recommends a flexural stiffness of $0.8E_cI_g$ for walls that are uncracked on inspection.

Effective secant flexural stiffness values of the wall specimens are derived from the test results, based on the lateral stiffness for a cantilever wall as: $F = k_f \Delta_f$, where $k_f = \frac{3E_cI_{eff}}{h_w^3}$. Therefore,

secant flexural stiffness normalized by the concrete gross section flexural stiffness is determined as

$$\frac{I_{eff}}{I_g} = \frac{E_c I_{eff}}{E_c I_g} = \frac{k_f h_w^3}{3E_c I_g} = \frac{h_w^3}{3E_c I_g}\left(\frac{F}{\Delta_f}\right)$$

where F is the lateral load, Δ_f is the flexural displacement at the top of the wall, E_c is Young's modulus of concrete determined using ACI 318 requirements, and h_w is the height of the wall.

Figures 8-1 and 8-2 present relations of secant flexural stiffness versus drift ratios for all five wall specimens; in Figure 8-1, slip and extension deformations of boundary longitudinal reinforcement are included, whereas these contributions are excluded in the relations plotted in Figure 8-2. The figures indicate that flexural rigidity values for uncracked and cracked walls are approximately $0.65E_cI_g$ and $0.30E_cI_g$, respectively, when anchorage slip and extension deformations are included, and $0.85E_cI_g$ and $0.40E_cI_g$, when slip and extension deformations are excluded, respectively. These values are modestly lower than those recommended by ASCE 41-06 (2007) and FEMA 356 (2000). Flexural rigidities obtained from each test, along with values suggested by ASCE 41-06 and FEMA 356, are summarized in Table 8-1.

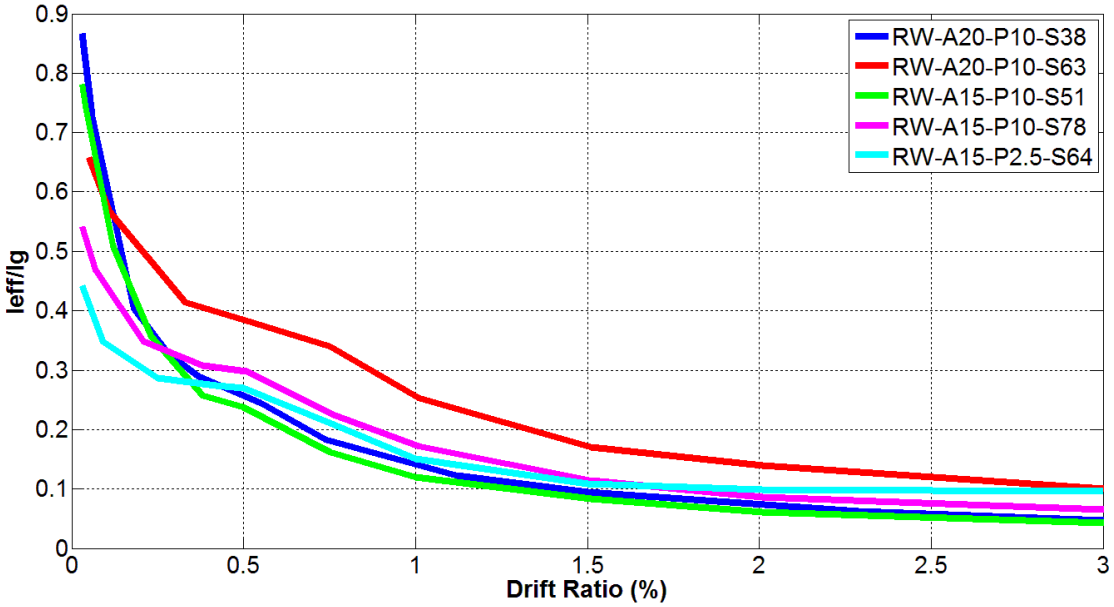

Figure 8-1 Effective secant flexural stiffness values derived from test results including slip/extension deformations

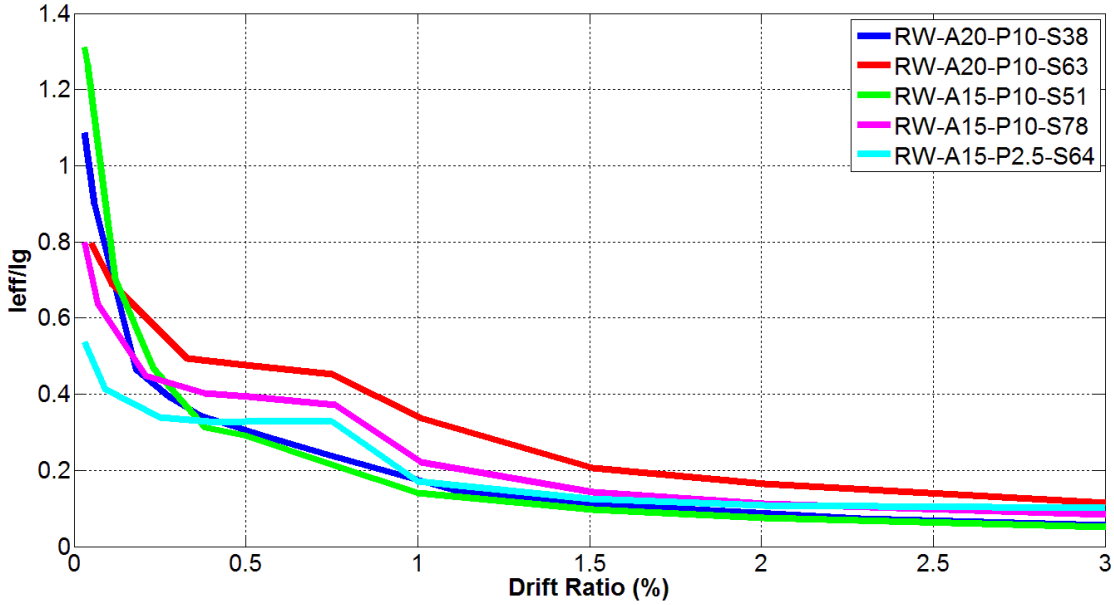

Figure 8-2 Effective secant flexural stiffness values derived from test results excluding slip/extension deformations

8.2 Effective Shear Stiffness

ASCE 41-06 Supplement No.1 recommends a shear rigidity of $0.4E_cA_w$ for cracked walls, whereas FEMA 356 suggests the same value of shear stiffness, $0.4E_cA_w$, for both uncracked and cracked walls. Effective secant shear stiffness of wall specimens, normalized by E_cA_w, is derived from the test results, as follows.

$$\frac{GA_{eff}}{E_cA_w} = \frac{F/\gamma_s}{E_cA_w} = \frac{h_w}{E_cA_w}\left(\frac{F}{\Delta_s}\right)$$

where F is the lateral load, γ_s is the shear strain, Δ_s is the shear displacement at the top of the wall, A_w is the wall cross-section area.

Figure 8-3 presents the relations of secant shear stiffness versus drift ratio for all five wall specimens. The figures show that shear rigidity for uncracked walls is approximately $0.20E_cA_w$, which is about half of the value recommended by ASCE 41 and FEMA 356. The shear stiffness for cracked walls is about $0.10E_cA_w$, which is much lower than the shear rigidity suggested by these two documents. Results are summarized in Table 8-1.

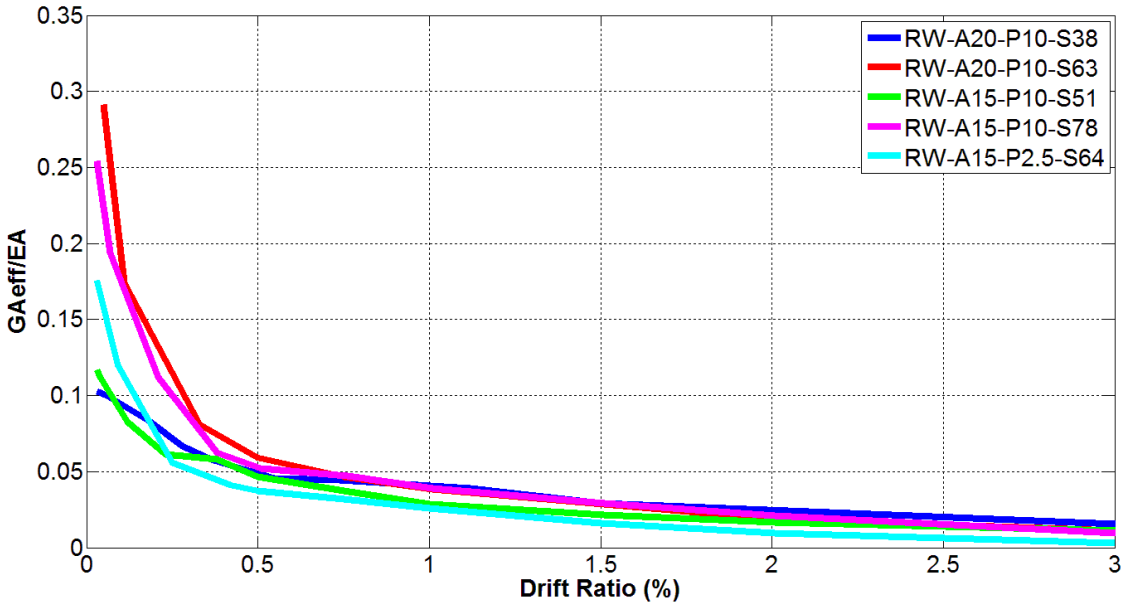

Figure 8-3 Effective secant shear stiffness values derived from test results

Table 8-1 Effective flexural and shear stiffness values

	$E_c I_{eff}[\%E_c I_g]$	$G_c A_{eff}[\%E_c A_w]$
Test Results - With slip/ext - Uncracked walls	65	20
Test Results - Without slip/ext - Uncracked walls	85	
Test Results - With slip/ext - Cracked walls	30	10
Test Results - Without slip/ext - Cracked walls	40	
FEMA 356 - Uncracked walls (On inspection)	80	40
FEMA 356 - Cracked walls	50	40
ASCE 41-06 Supplement No.1 - Cracked walls	50	40

8.3 Load-Deformation Backbone Relations

Backbone (envelop) curves derived from test results for both positive and negative loading directions are shown on Figures 8-5 to 8-9. The test results for all five wall specimens are consistent, with first yielding in boundary longitudinal reinforcement at approximately 0.6% drift and substantial loss of lateral load capacity at 3.0% drift. The peak lateral loads were reached at drift ratios ranging from 1.5% to 2.8% drift.

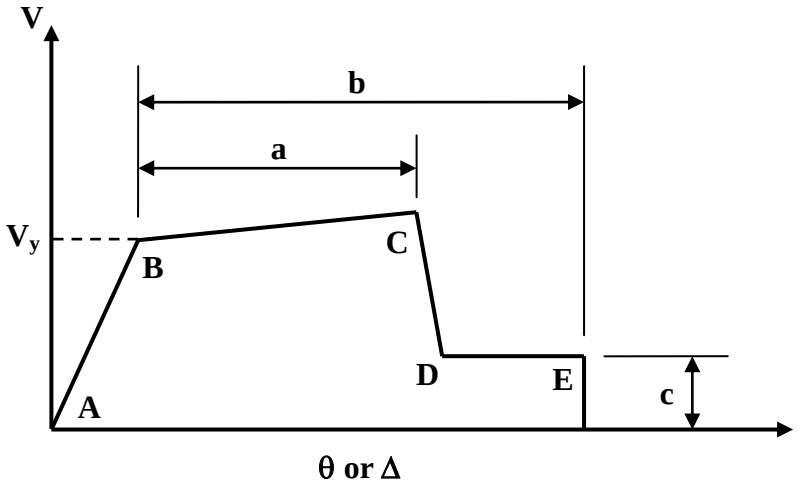

Figure 8-4 Generalized force-deformation relations for concrete elements (ASCE 41-06)

The nonlinear "backbone" relations derived by using the modeling parameters given in ASCE 41-06 (2007) Table 6-18 (Figure 8-4) are also plotted on these figures. The determination of yield displacement for the ASCE 41 backbone relations is based on the recommended rigidity values, $0.5E_cI_g$ for flexural stiffness and $0.4E_cA_w$ for shear stiffness, as discussed in Sections 8.1 and 8.2. The comparisons of test results and ASCE 41 backbone relations show that test

specimens are more flexible at yield than the ASCE 41 backbone curves, as yield displacements obtained from ASCE 41 are only 40 to 65% of those obtained from tests. The results presented also show that test specimens have much higher deformation capacity prior to significant loss of lateral load capacity than the ASCE 41 backbone relations. The ASCE 41 modeling parameter *a*, which defines the plastic rotation from the yielding point to Collapse Prevention (CP) limit state for primary components, varies from 1.0 to 1.5%, which is much lower than corresponding value from test results, ranging from 2.3 to 2.5%.

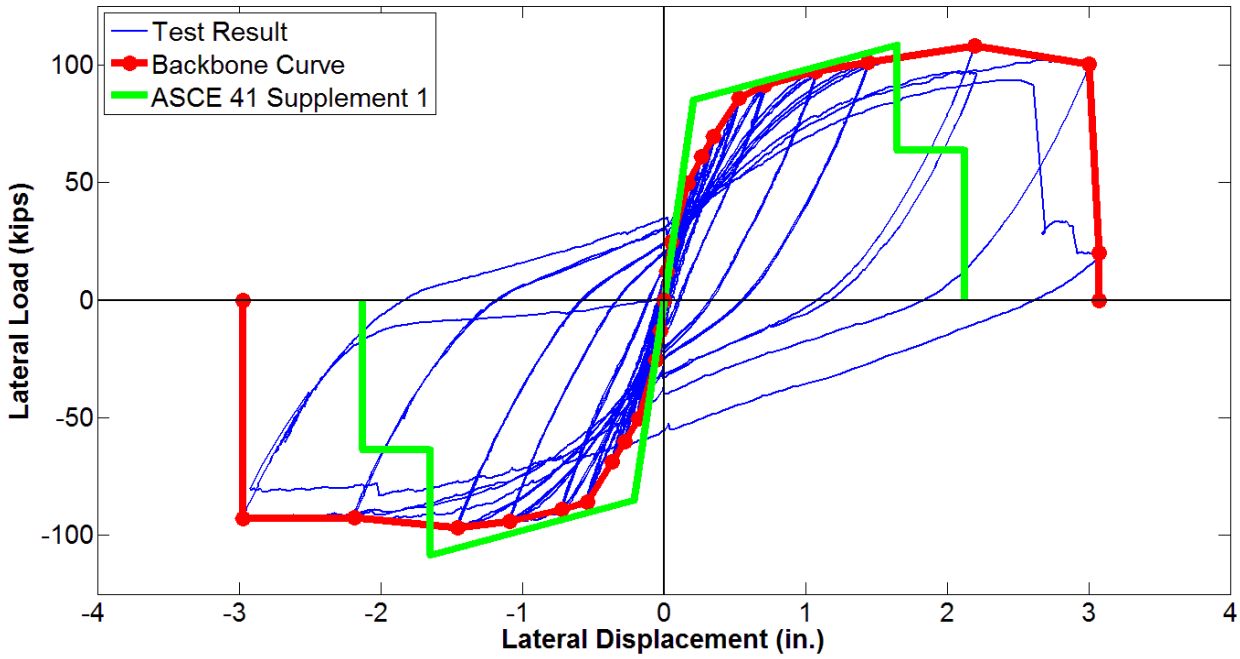

Figure 8-5 Backbone curves for RW-A20-P10-S38 and ASCE 41-06 model

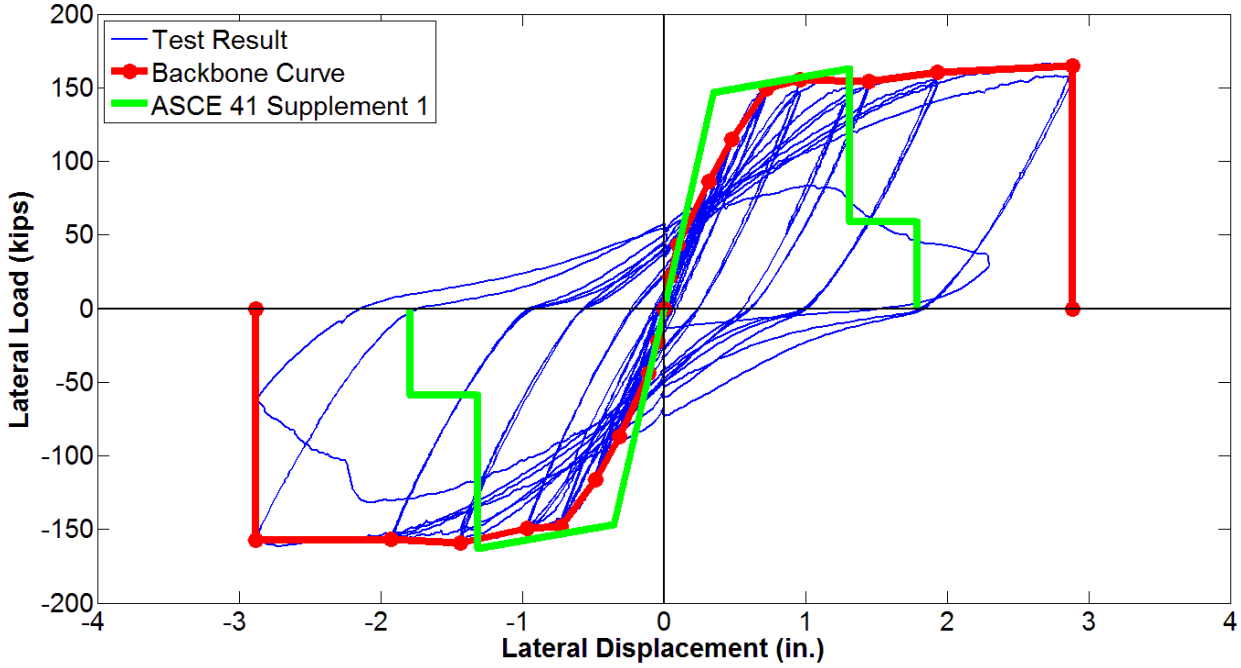

Figure 8-6 Backbone curves for RW-A20-P10-S63 and ASCE 41-06 model

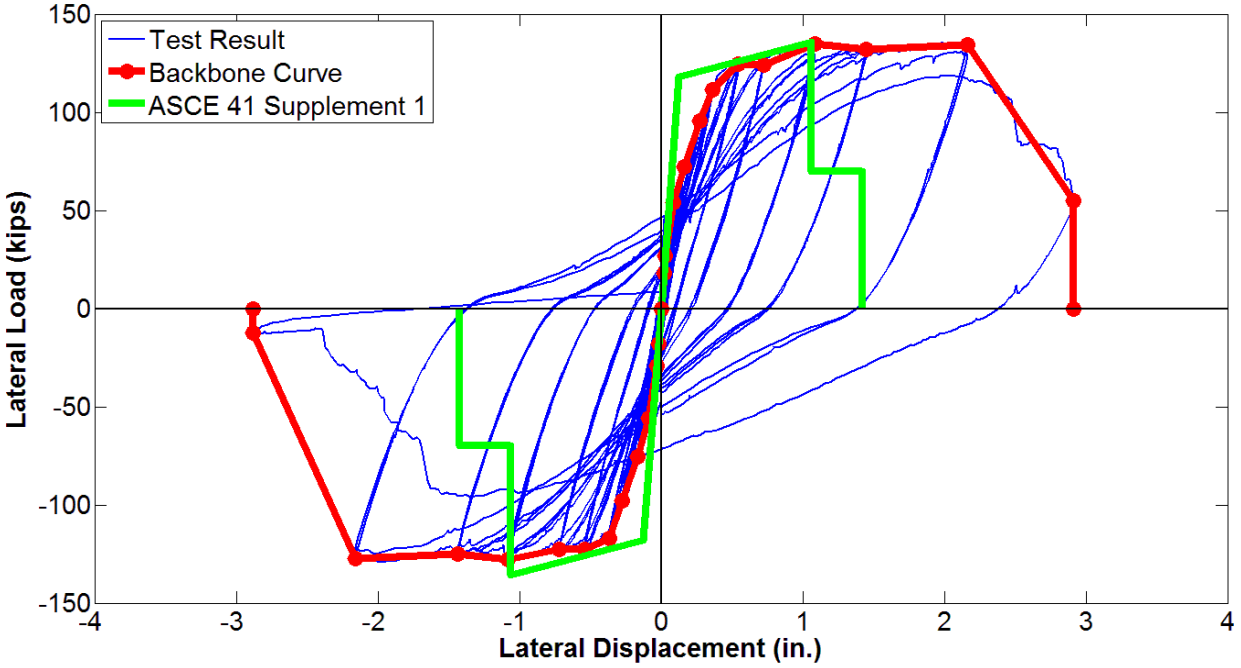

Figure 8-7 Backbone curves for RW-A15-P10-S51 and ASCE 41-06 model

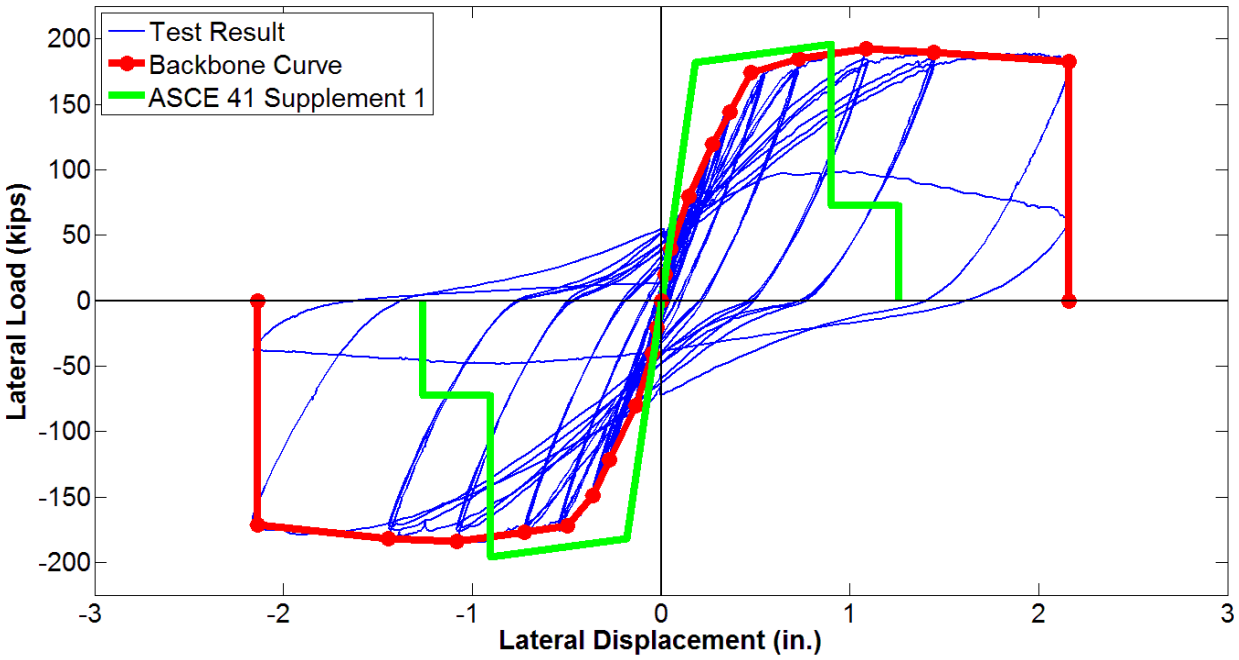

Figure 8-8 Backbone curves for RW-A15-P10-S78 and ASCE 41-06 model

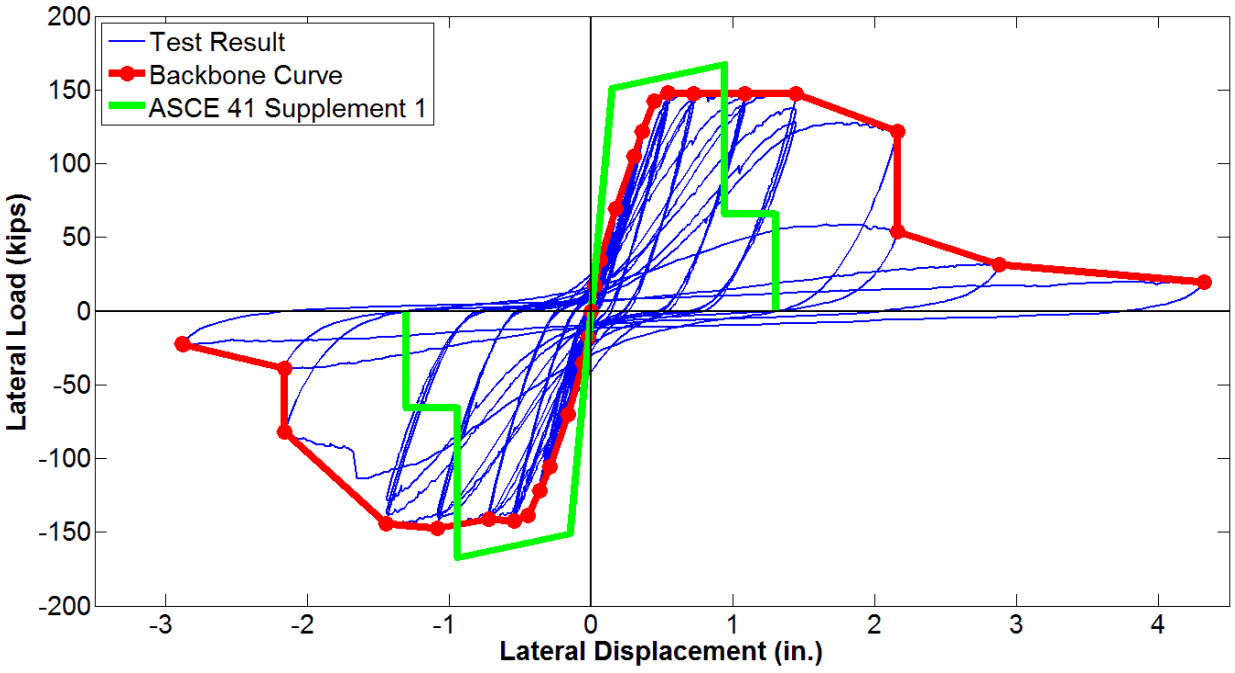

Figure 8-9 Backbone curves for RW-A15-P2.5-S64 and ASCE 41-06 model

8.4 Model versus Test Results

In this section, results of monotonic analysis using both uncoupled (P-M and V independent) and coupled models are compared with the cyclic test results obtained for each wall specimens. The analyses are performed using OpenSees (Open System for Earthquake Engineering Simulation), an open source nonlinear finite element program.

8.4.1 Uncoupled model results

Monotonic analysis with an uncoupled model of flexure and shear responses is performed using Concrere06 and Steel02, two constitutive material laws incorporated into OpenSees for concrete and reinforcing steel, respectively. Concrete06 constructs a uniaxial concrete material object with tensile strength and nonlinear tension stiffening. Concrete compressive behavior is modeled with a constitutive material law defined as the Thorenfeldt-based curve, which is similar to the relation by Popovic (1973). The tensile envelope uses the tension stiffening equation by Belarbi and Hsu (1994) with a general exponent. A stiffness of 7.1% of the initial elastic stiffness, i.e., $0.071E_c$, is used for the unloading path in compression as recommended by Palermo and Vecchio (2003). Steel02 simulates a uniaxial Giuffre-Menegotto-Pinto steel material object with isotropic strain hardening.

The analytical and experimental lateral load versus top displacement relations for RW-A20-P10-S38 (Test 2), RW-A15-P10-S78 (Test 4), and RW-A15-P2.5-S64 (Test 5), are presented in Figures 8-10 to 8-12. The analyses are applied for test specimens with two different shear rigidity values, $0.4E_cA_w$ as recommended in ASCE 41-06 including Supplement No.1 and

$0.1E_cA_w$ as suggested from test results. As can be seen from the figures, the lateral load capacity and lateral stiffness are substantially overestimated for both models for all drift levels. The lateral load-top displacement responses using the recommended effective shear stiffness of $0.1E_cA_w$ give better correlation with test results.

8.4.2 Coupled model results

A model integrating flexure and shear interaction (Massone, 2006; Massone et al., 2006, Orakcal et al., 2006, Massone et al., 2009), implemented in OpenSees, is used to determine lateral load versus top displacement relations for wall specimens. This model incorporates reinforced concrete panel behavior into Multiple Vertical Line Element Model (MVLEM), a two-dimensional macroscopic fiber model, using a rotating-angle approach. Concrere06 and Steel02 also are used to model constitutive laws for concrete and reinforcing steel, respectively.

The analytical lateral load-top displacement responses using the coupled model for RW-A20-P10-S38 (Test 2), RW-A15-P10-S78 (Test 4), and RW-A15-P2.5-S64 (Test 5), are also plotted in Figures 8-10 to 8-12, together with relations obtained from the uncoupled model and the test results. The figures indicate that both the uncoupled and coupled models overestimate both lateral strength and stiffness of test specimens. The failure of the model to incorporate cyclic degradation, especially for the reinforcement (curvature parameter R), is one of the primary reasons that the coupled model does not match the test result (Orakcal et al., 2006). Although the lateral load capacity and lateral stiffness from both uncoupled and coupled models are overestimated, the extent of the discrepancy is different. The overestimation tends to be more

significant for the uncoupled model when the drift level approaches to the first yielding of boundary longitudinal reinforcement, indicating that the interaction of flexural and shear responses becomes more significant at these drift levels.

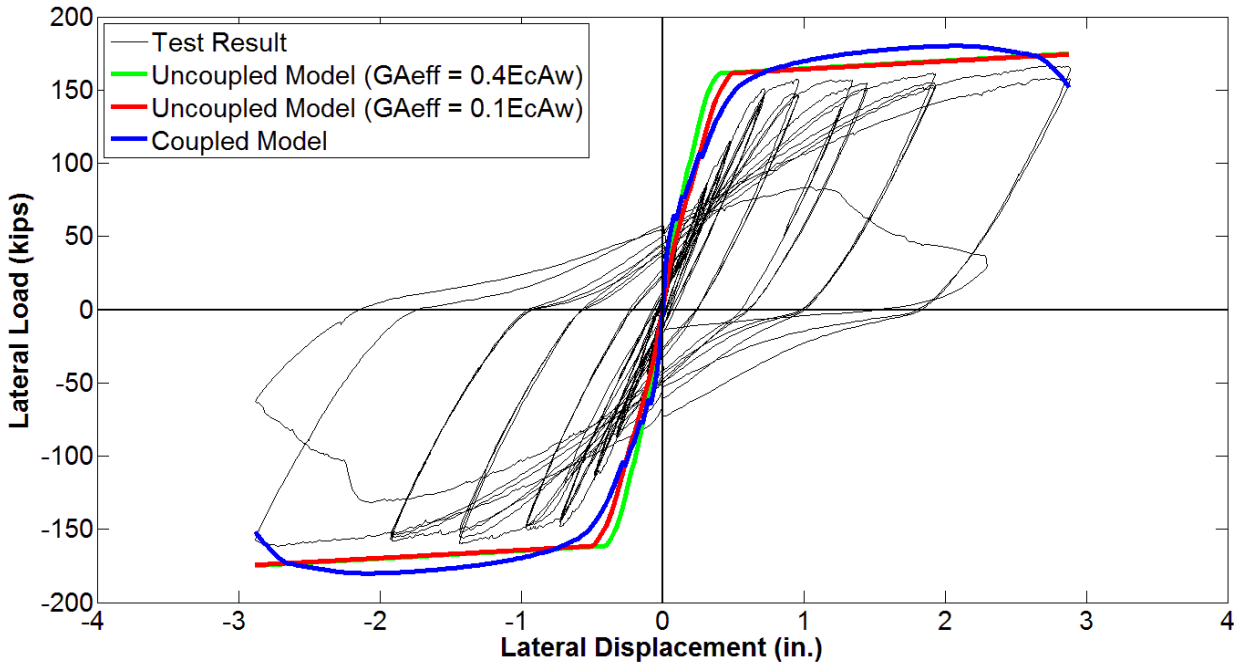

Figure 8-10 Lateral load-top displacement relations for RW-A20-P10-S63

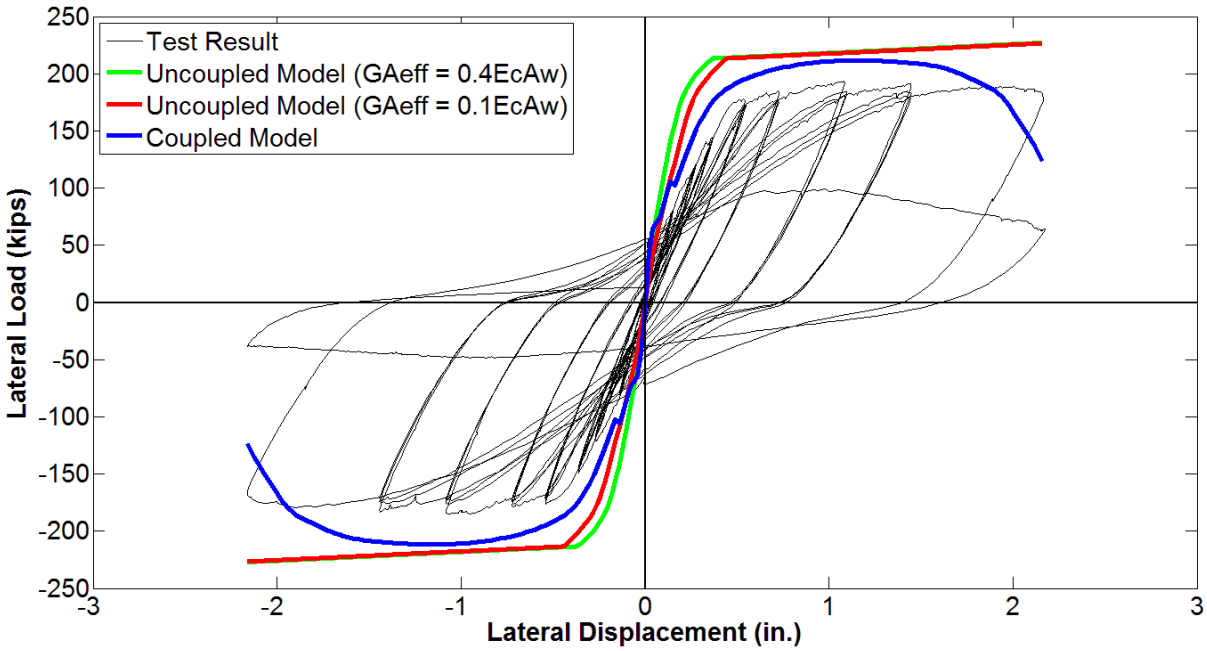

Figure 8-11 Lateral load-top displacement relations for RW-A15-P10-S78

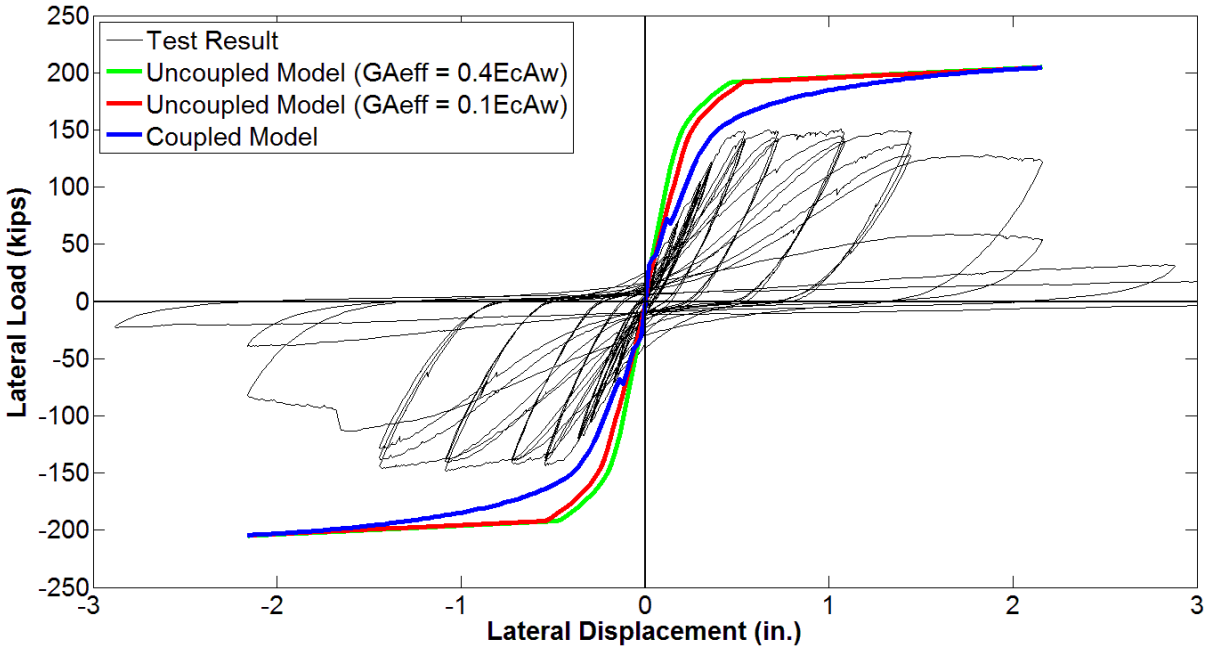

Figure 8-12 Lateral load-top displacement relations for RW-A15-P2.5-S64

CHAPTER 9 SUMMARY AND CONCLUSIONS

This experimental and analytical study was conducted to provide insight into the nonlinear cyclic response of moderate aspect ratio reinforced concrete structural walls. Five large-scale cantilever structural wall specimens, subjected to constant axial load and reversed cyclic lateral loading, were designed and tested. The wall specimens were designed to yield in flexure prior to loss of lateral load capacity. Primary test variables included aspect ratio (1.5 and 2.0), which is equal to the shear-span ratio for these tests, axial load level ($0.025A_g f_c^{'}$ and $0.10A_g f_c^{'}$), and wall shear stress level (between approximately 4 and $8\sqrt{f_c^{'}}\,psi$). The specimens were heavily instrumented to obtain detailed response information. Studies also were carried out to evaluate the ability of both uncoupled and coupled (shear-flexure interaction) models to capture the measured responses. The conclusions from the study are briefly presented in the following paragraphs.

1) Substantial loss of lateral load capacity was observed for a variety of reasons, such as diagonal tension, web crushing, sliding shear, concrete crushing, and buckling of vertical reinforcement. The test results indicated that significant strength loss was impacted by aspect ratio, axial load level, and wall shear stress level. For the walls with moderate shear stress, strength loss was a result of a diagonal tension failure, initiated by concrete crushing and buckling of wall boundary longitudinal reinforcement. For the aspect ratio 2.0 wall with high shear stress, crushing of core concrete at wall boundaries, together with diagonal compression, led to out-of-plane buckling of boundary longitudinal reinforcement and some web vertical reinforcement. For the aspect ratio 1.5 test with

high shear stress and axial load of $0.1A_g f_c^{'}$, strength loss was caused by large diagonal compression leading to shear sliding and significant out-of-plane buckling of wall boundary vertical reinforcement. For the aspect ratio 1.5 test with high shear stress but low axial load, only $0.025A_g f_c^{'}$, large diagonal compression and significant shear sliding were observed, followed by in-plane buckling of boundary longitudinal reinforcement.

2) Although various failure modes were observed for five wall specimens, the deformation capacities for all specimens were essentially the same, with a substantial loss of lateral load capacity at approximately 3.0% drift for all tests. First yielding in boundary longitudinal reinforcement was observed between 0.5 and 0.7% drift for all tests.

3) Sliding shear deformations at the wall-foundation block interface were dependent on shear stress level, number of loading cycles applied, and axial stress level. However, the contributions of sliding at the wall-foundation interface to the top total lateral displacements were small, with the average contributions of 1 to 3% and maximum contributions of 2 to 7% for all five wall specimens.

4) Slip and extension deformations of boundary longitudinal reinforcement accounted for approximately 10 to 25% of the top flexural displacements for 2.0 aspect ratio walls, and tended to be higher, from about 10 to 40% for 1.5 aspect ratio walls. The slip and extension deformations reached their local maxima at drift ratios of 0.75 or 1.0%,

simultaneously with the appearance of the horizontal crack along the wall-foundation block interface.

5) The average contribution of nonlinear shear deformations to wall top lateral displacement are approximately 20%, 30%, 30%, 35%, and 50% for Tests 1 to 5, respectively. For walls with moderate shear stress levels, the contribution of shear to total displacement generally decreased slightly from the beginning to the end of the test. In contrast, for the walls with higher shear stress level, the overall trend was opposite, with slightly increasing percentages of shear deformation with increasing lateral drift ratio.

6) Effective secant flexural stiffness values of $0.85E_cI_g$ and $0.4E_cI_g$ were noted for uncracked and cracked walls, respectively, in the case where slip and extension deformations were modeled explicitly. The corresponding values where slip and extension were incorporated into the effective flexural stiffness are $0.65E_cI_g$ for uncracked walls and $0.3E_cI_g$ for cracked walls. Effective secant shear stiffness values of $0.2E_cA_w$ and $0.1E_cA_w$ were derived for uncracked and cracked walls, respectively. These flexural and shear rigidity values are lower than those recommended by ASCE 41-06, including Supplement No.1, and FEMA 356.

7) Models that exclude and include shear-flexure interaction, but with monotonic material relations, tend to overestimate both lateral load capacity and lateral stiffness of reinforced concrete structural walls. The overestimation is more significant for the uncoupled model

when the drift level approaches first yielding of boundary longitudinal reinforcement, indicating that the interaction of flexural and shear responses becomes more significant at these drift levels.

8) The wall specimens were designed such that nonlinear shear deformations were expected to contribute significantly to lateral displacement responses, which might lead to significant interaction of flexure and shear. Therefore, the detailed response information obtained from these five, heavily-instrumented test specimens is valuable for the development and validation of analytical models, including models that account for cyclic nonlinear shear-flexure interaction.

A. APPENDIX A CRACKS-RELATED DATA

A.1 Crack Patterns

The crack patterns of wall specimens at each lateral load or drift level are shown in Figures A-1 to A-4 (specimen RW-A20-P10-S38, or Test 1), Figures A-5 to A-8 (specimen RW-A20-P10-S63, or Test 2), Figures A-9 to A-13 (specimen RW-A15-P10-S51, or Test 3), Figures A-14 to A-17 (specimen RW-A15-P10-S78, or Test 4), and Figures A-18 to A-22 (specimen RW-A15-P2.5-S64, or Test 5).

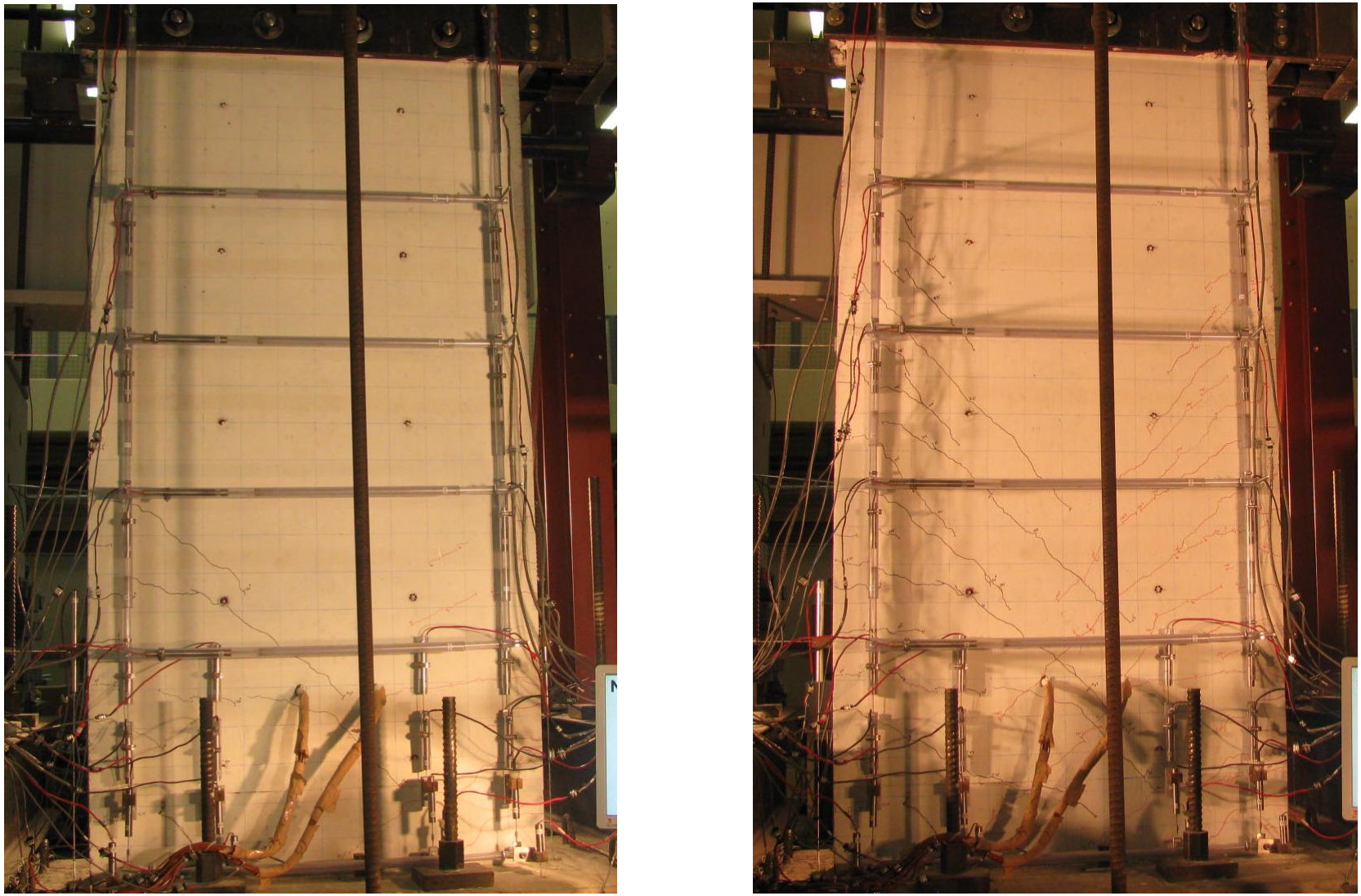

Figure A-1 Crack patterns for RW-A20-P10-S38: (a) V=50 kips, and (b) 0.38% Drift

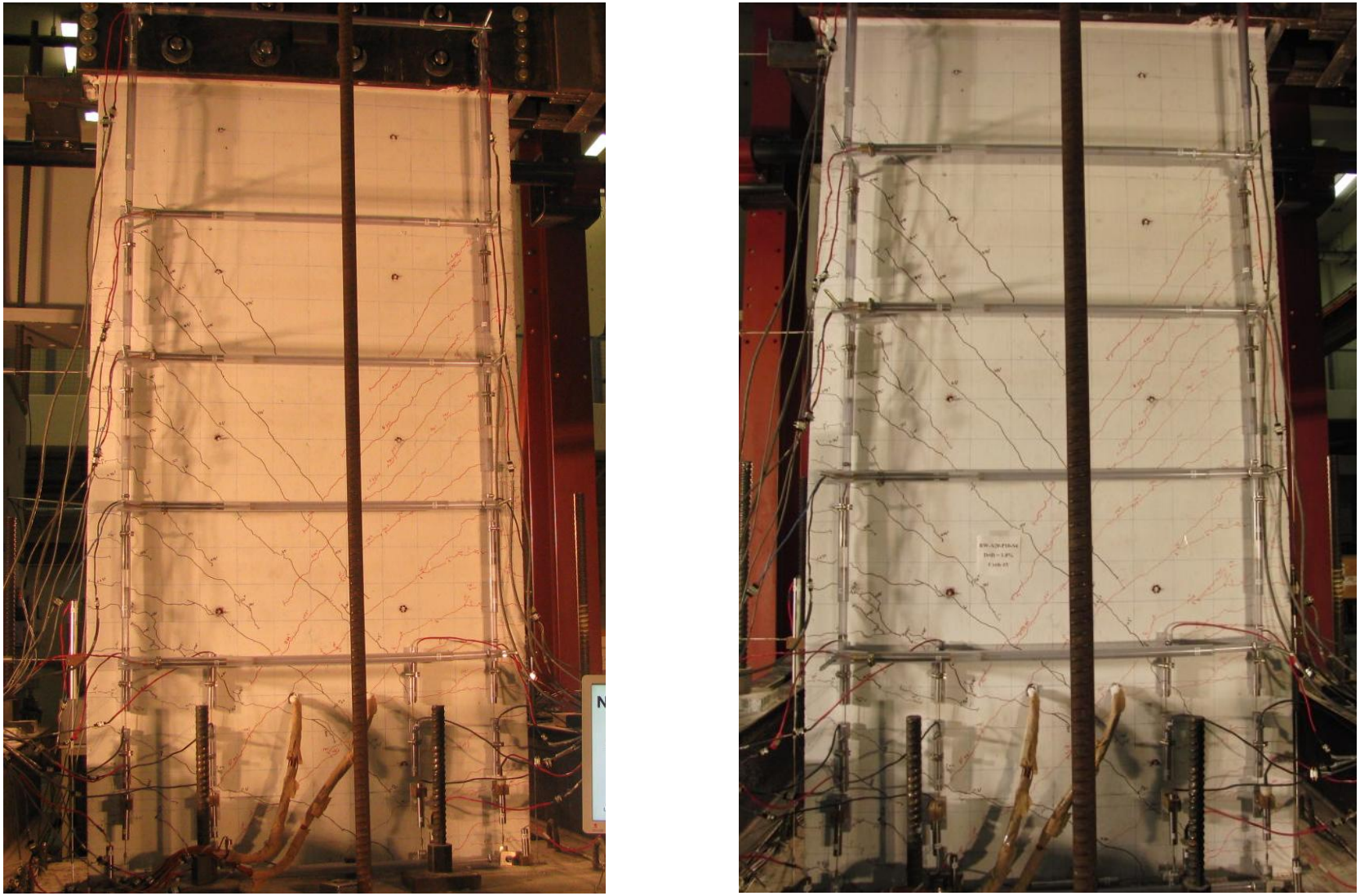

Figure A-2 Crack patterns for RW-A20-P10-S38: (a) 0.56% Drift, and (b) 0.75% Drift

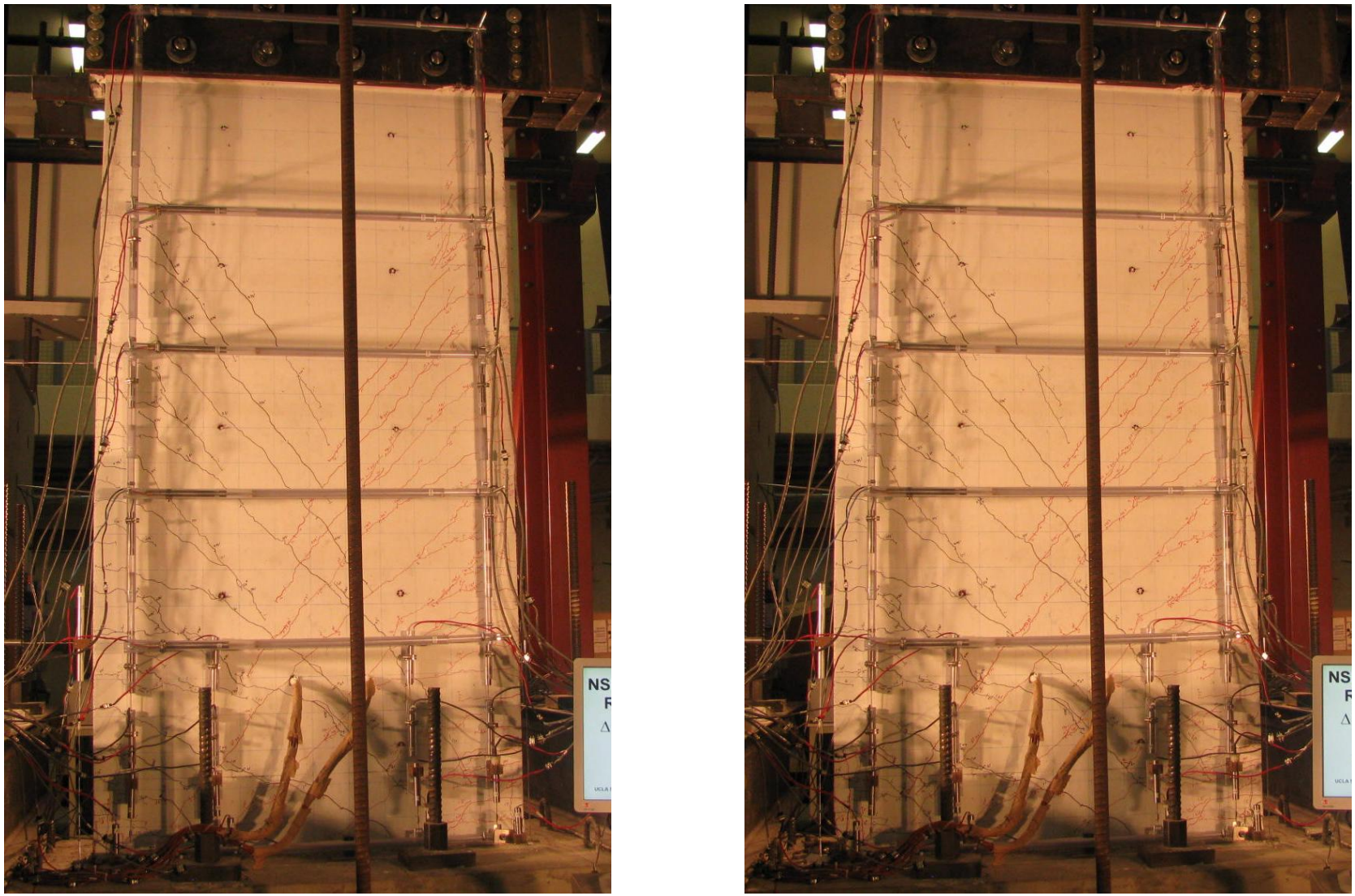

Figure A-3 Crack patterns for RW-A20-P10-S38: (a) 1.1% Drift, and (b) 1.5% Drift

Figure A-4 Crack patterns for RW-A20-P10-S38: (a) 2.3% Drift, and (b) At end of test

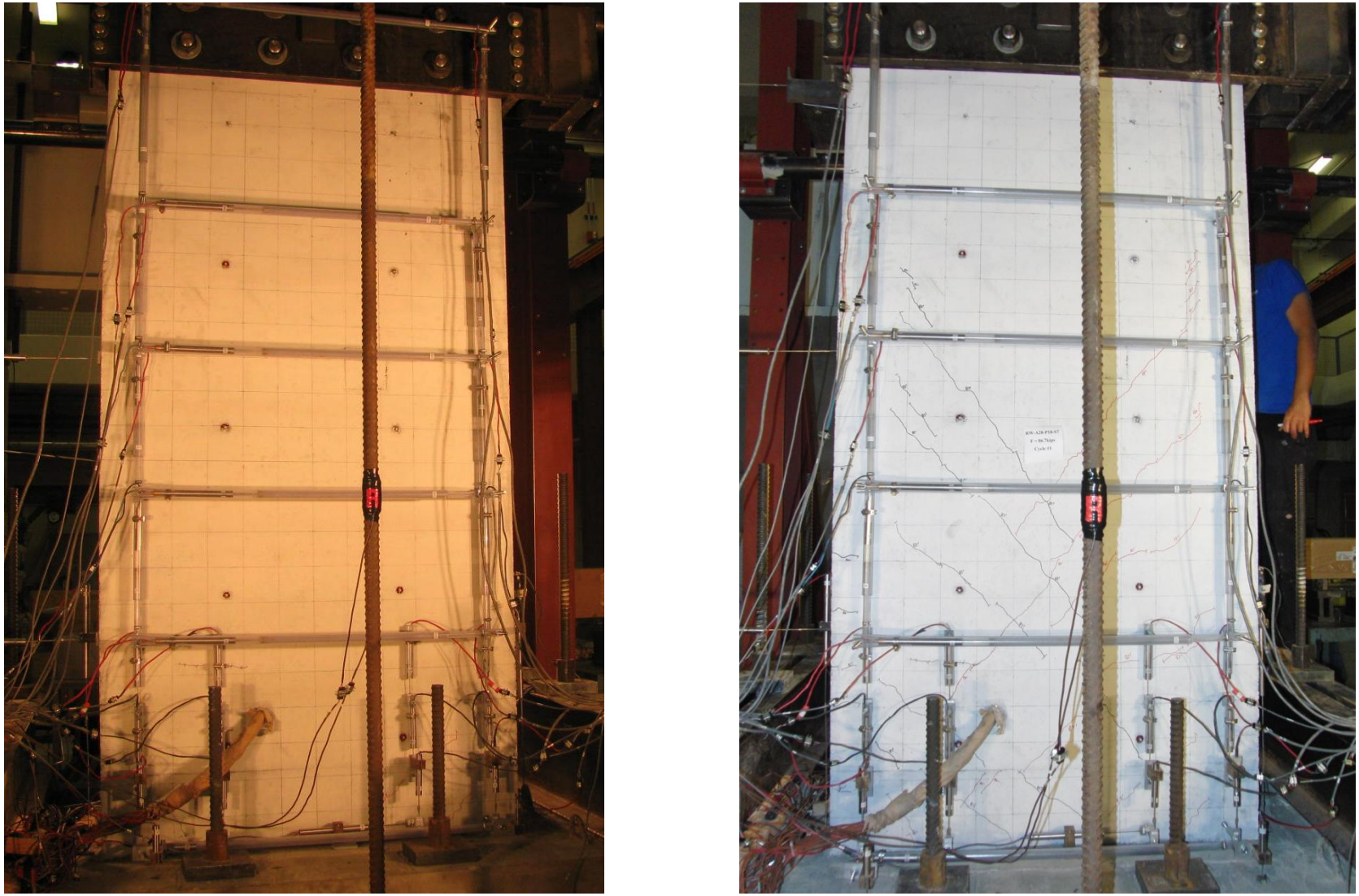

Figure A-5 Crack patterns for RW-A20-P10-S63: (a) V=43.3 kips, and (b) V=86.7 kips

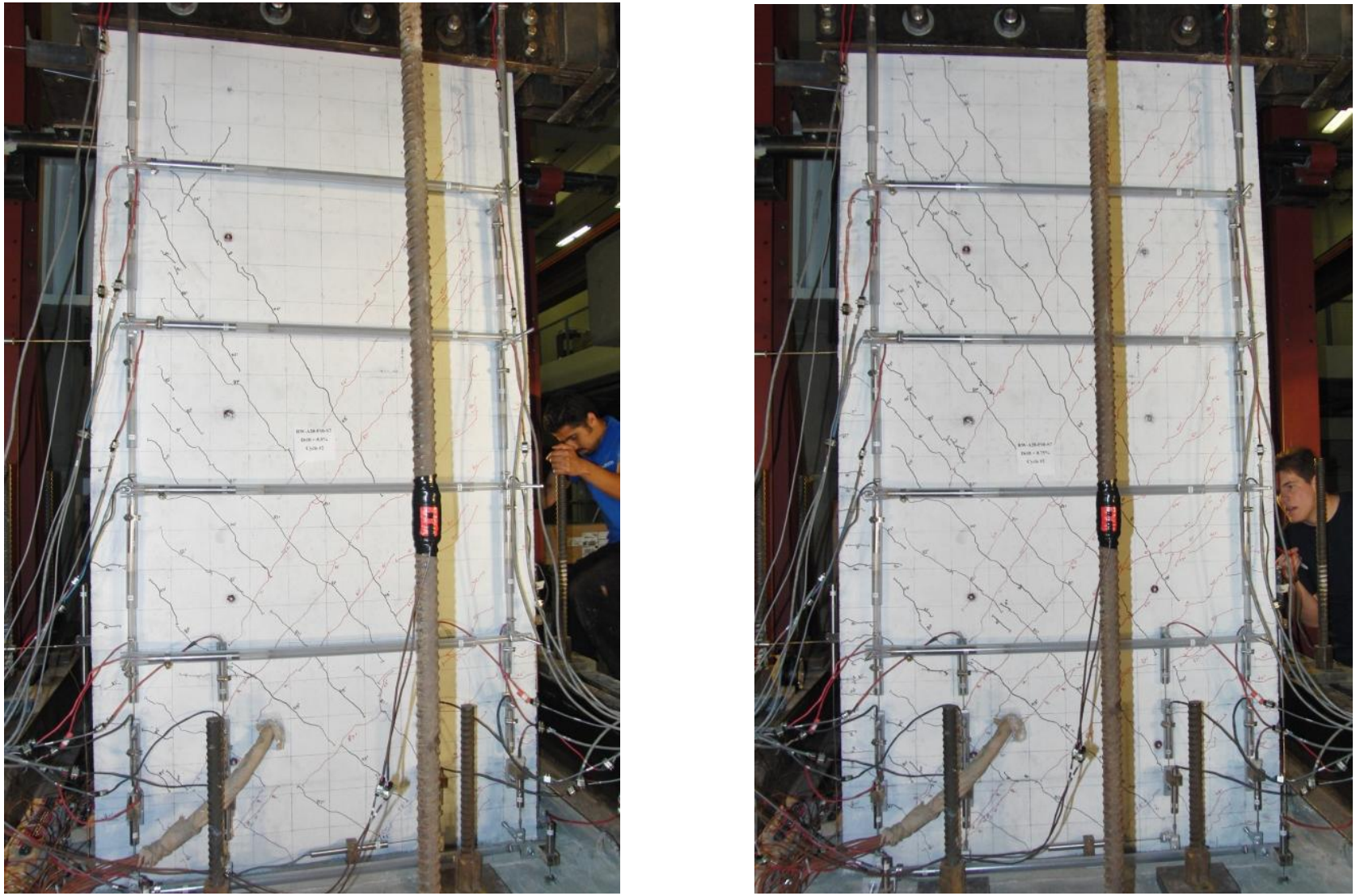

Figure A-6 Crack patterns for RW-A20-P10-S63: (a) 0.50% Drift, and (b) 0.75% Drift

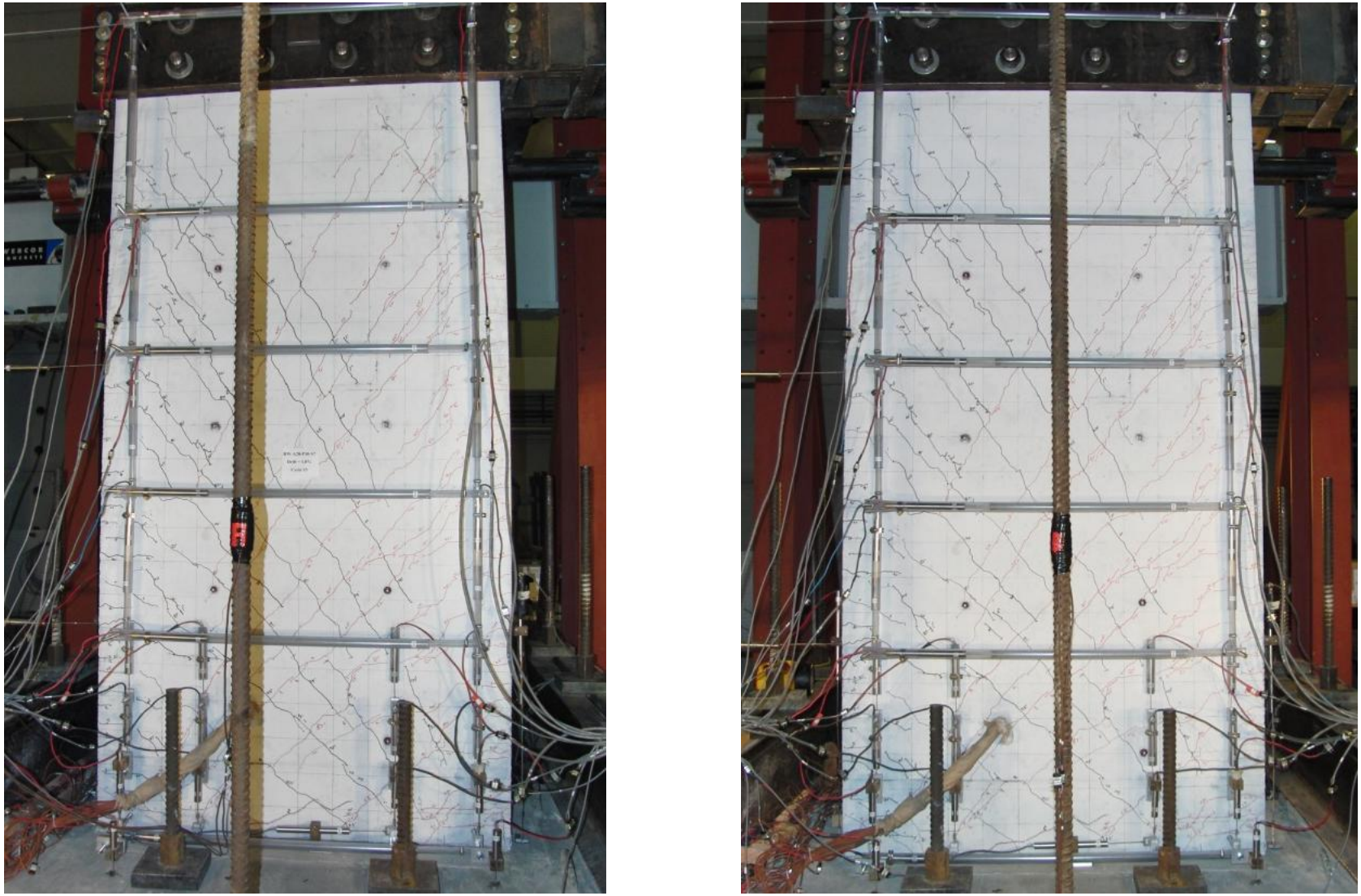

Figure A-7 Crack patterns for RW-A20-P10-S63: (a) 1.0% Drift, and (b) 1.5% Drift

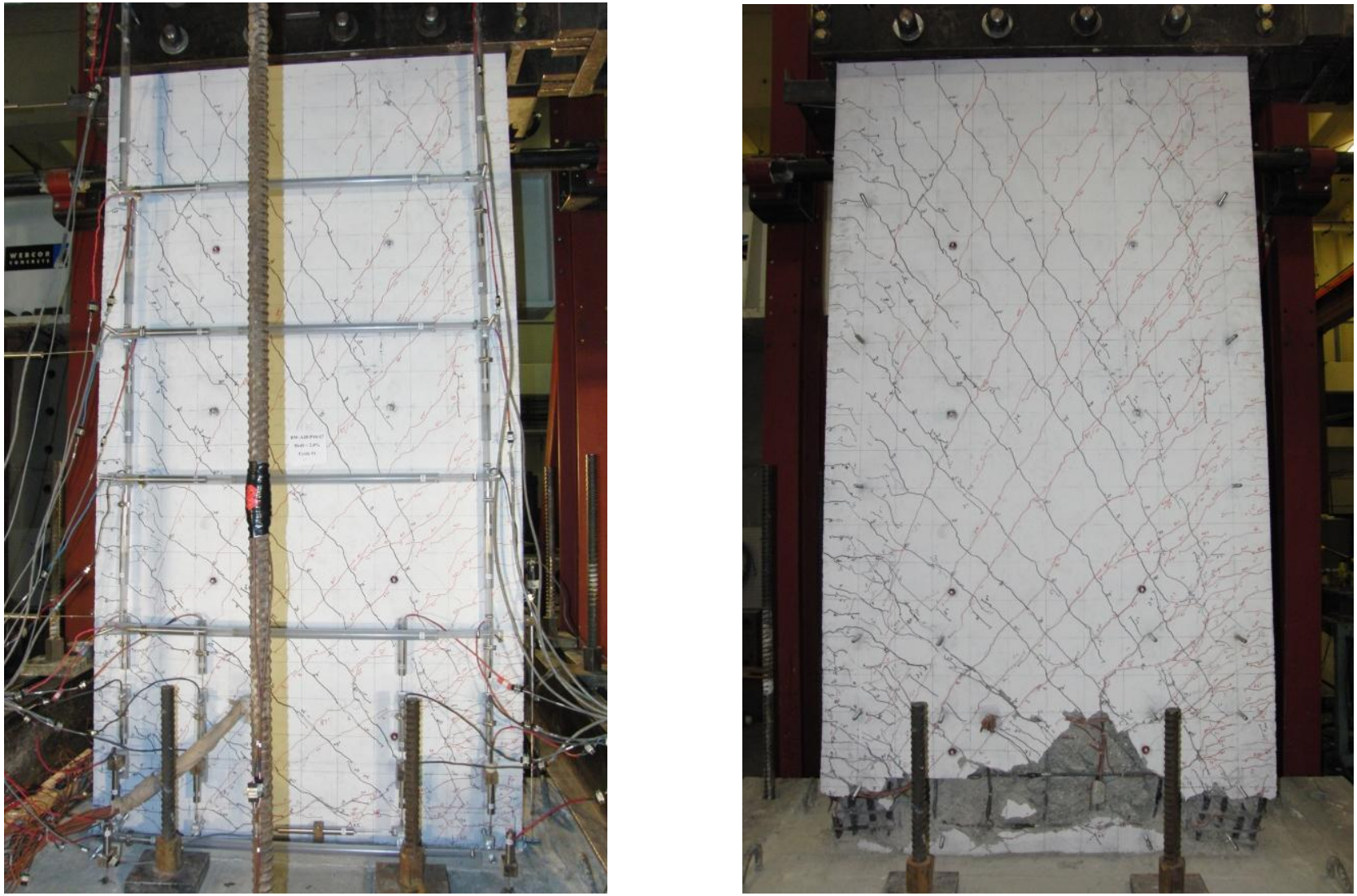

Figure A-8 Crack patterns for RW-A20-P10-S63: (a) 2.0% Drift, and (b) At end of test

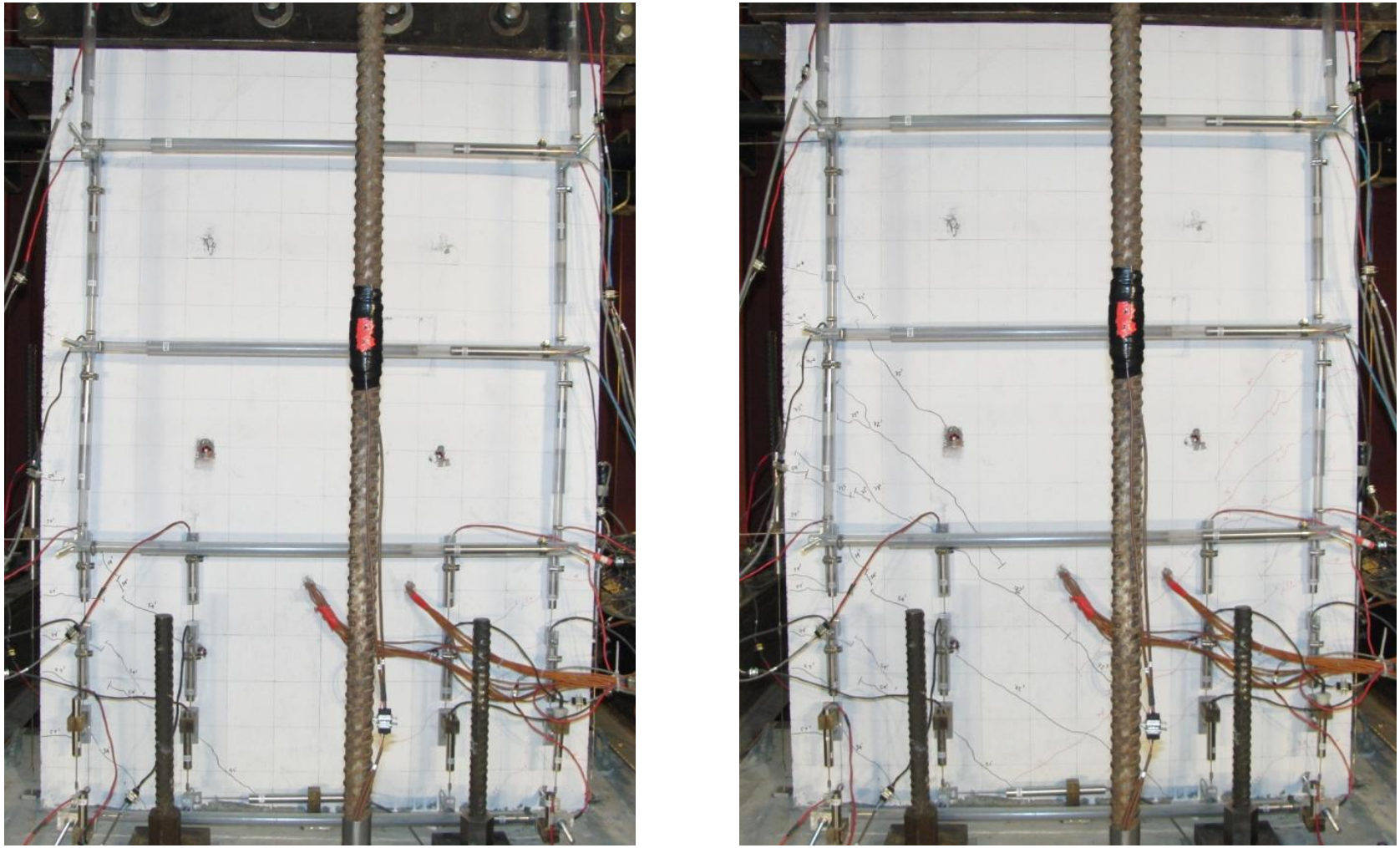

Figure A-9 Crack patterns for RW-A15-P10-S51: (a) V=54 kips, and (b) V=72 kips

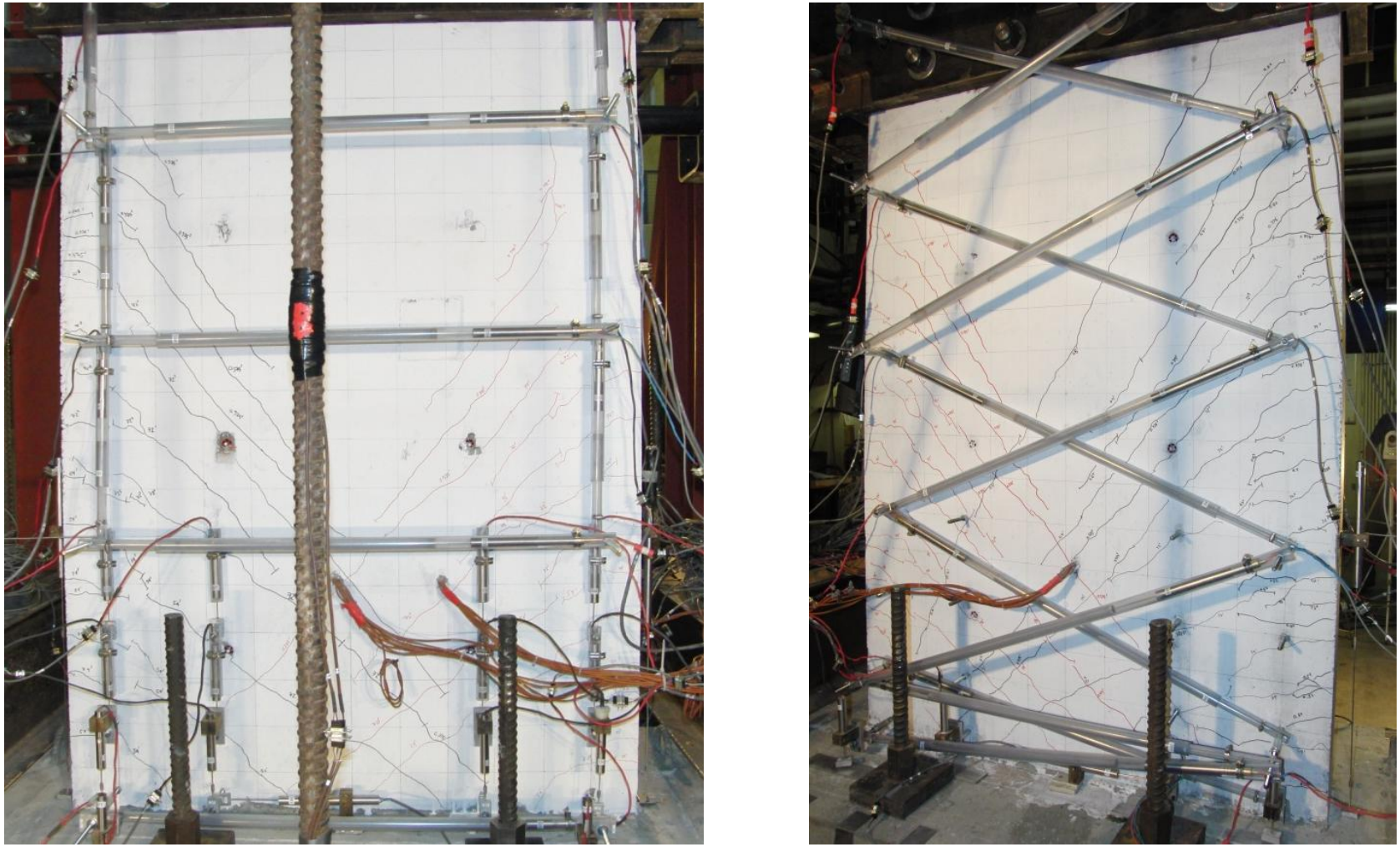

Figure A-10 Crack patterns for RW-A15-P10-S51: (a) 0.375% Drift, and (b) 0.5% Drift

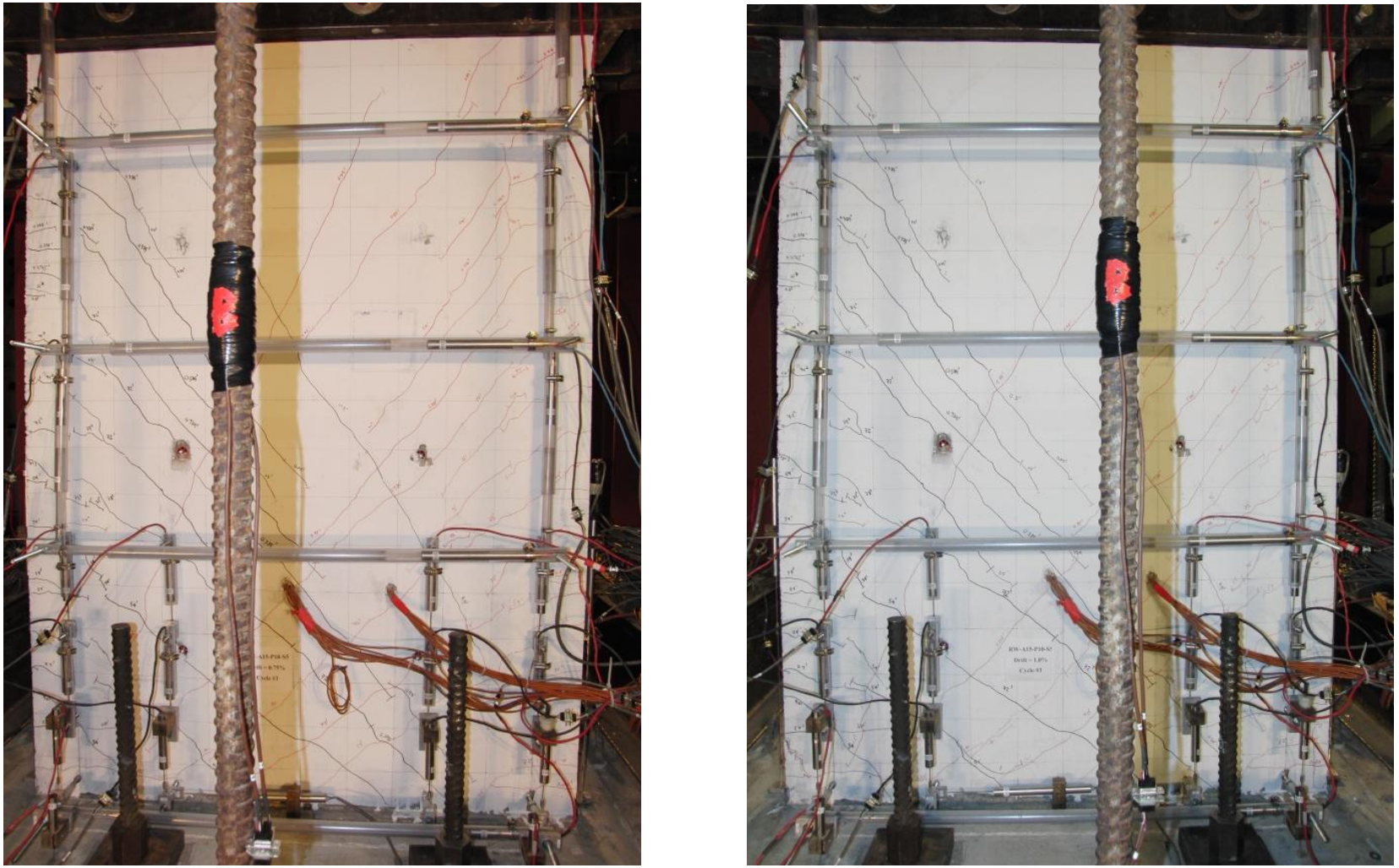

Figure A-11 Crack patterns for RW-A15-P10-S51: (a) 0.75% Drift, and (b) 1.0% Drift

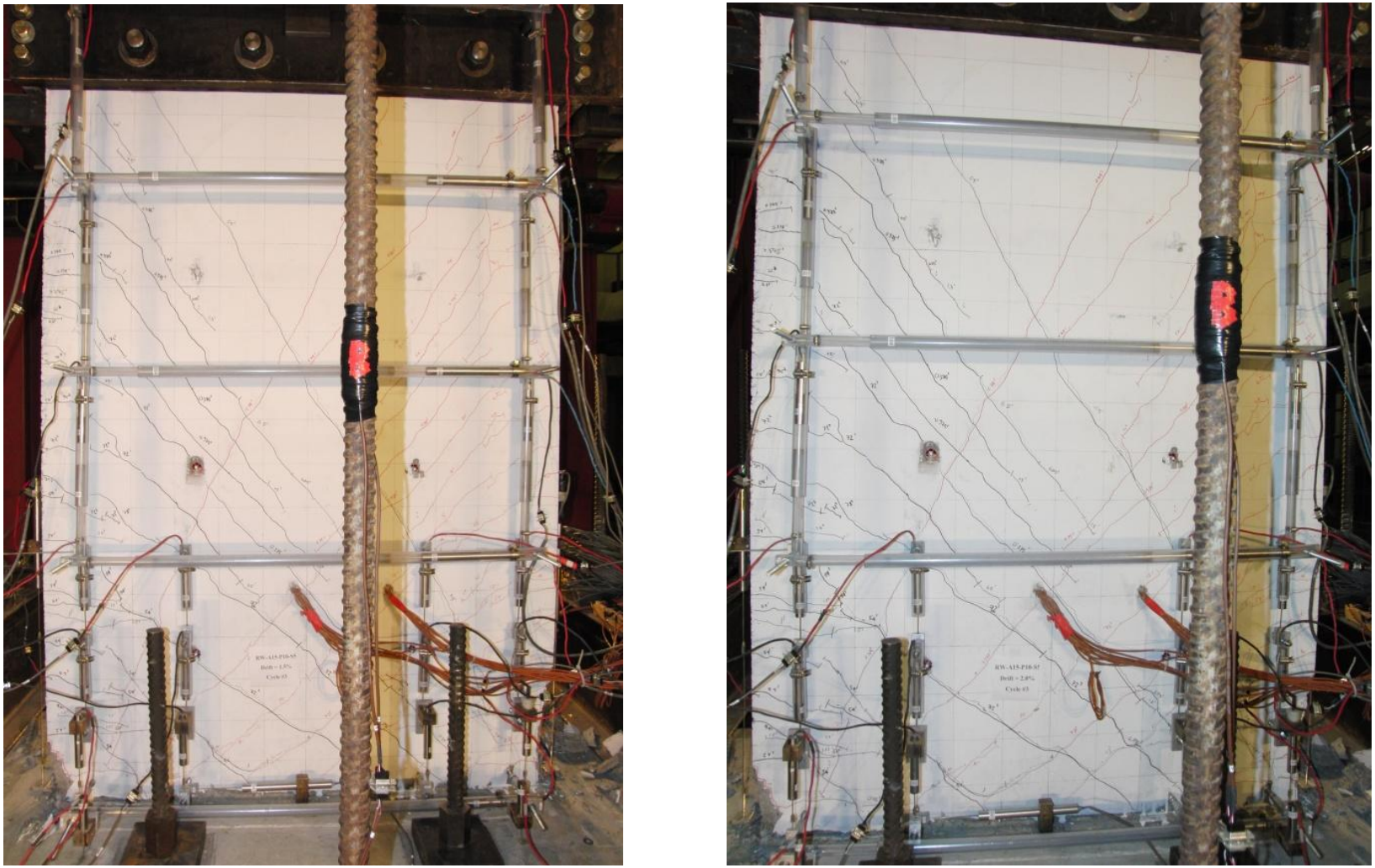

Figure A-12 Crack patterns for RW-A15-P10-S51: (a) 1.5% Drift, and (b) 2.0% Drift

Figure A-13 Crack patterns for RW-A15-P10-S51: (a) 3.0% Drift, and (b) At end of test

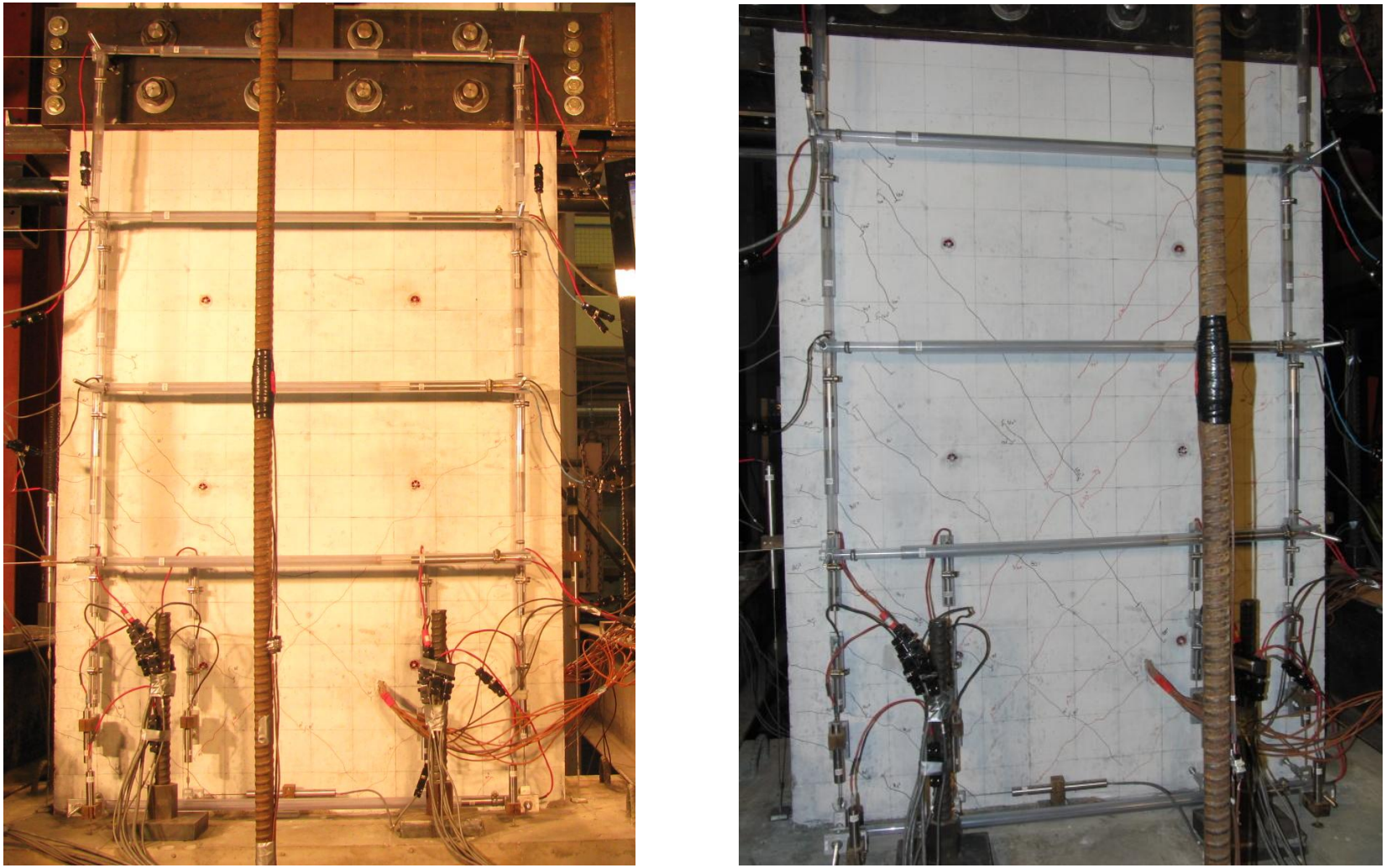

Figure A-14 Crack patterns for RW-A15-P10-S78: (a) V=80 kips, and (b) V=120 kips

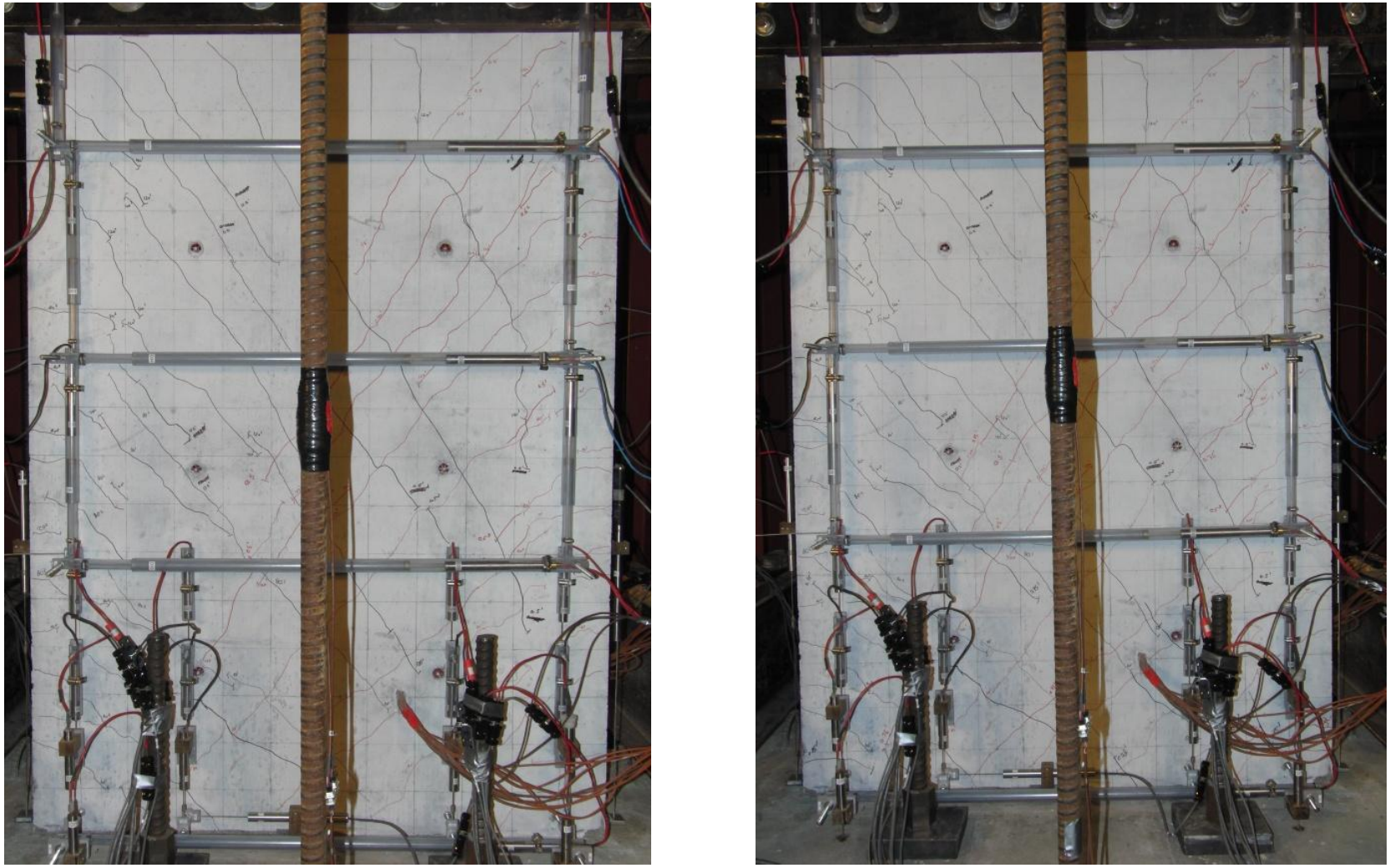

Figure A-15 Crack patterns for wall RW-A15-P10-S78: (a) 0.5% Drift, and (b) 0.75% Drift

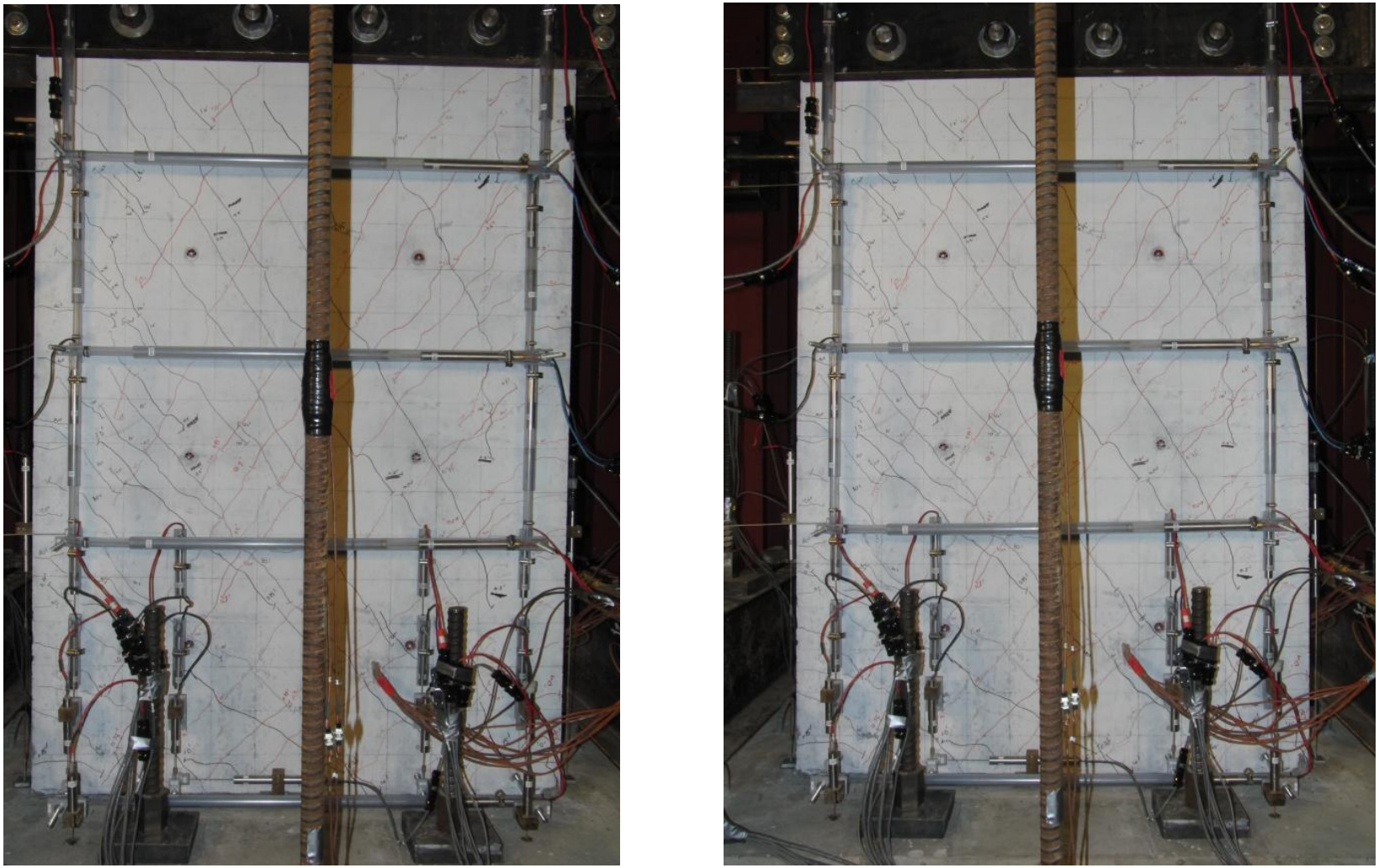

Figure A-16 Crack patterns for wall RW-A15-P10-S78: (a) 1.0% Drift, and (b) 1.5% Drift

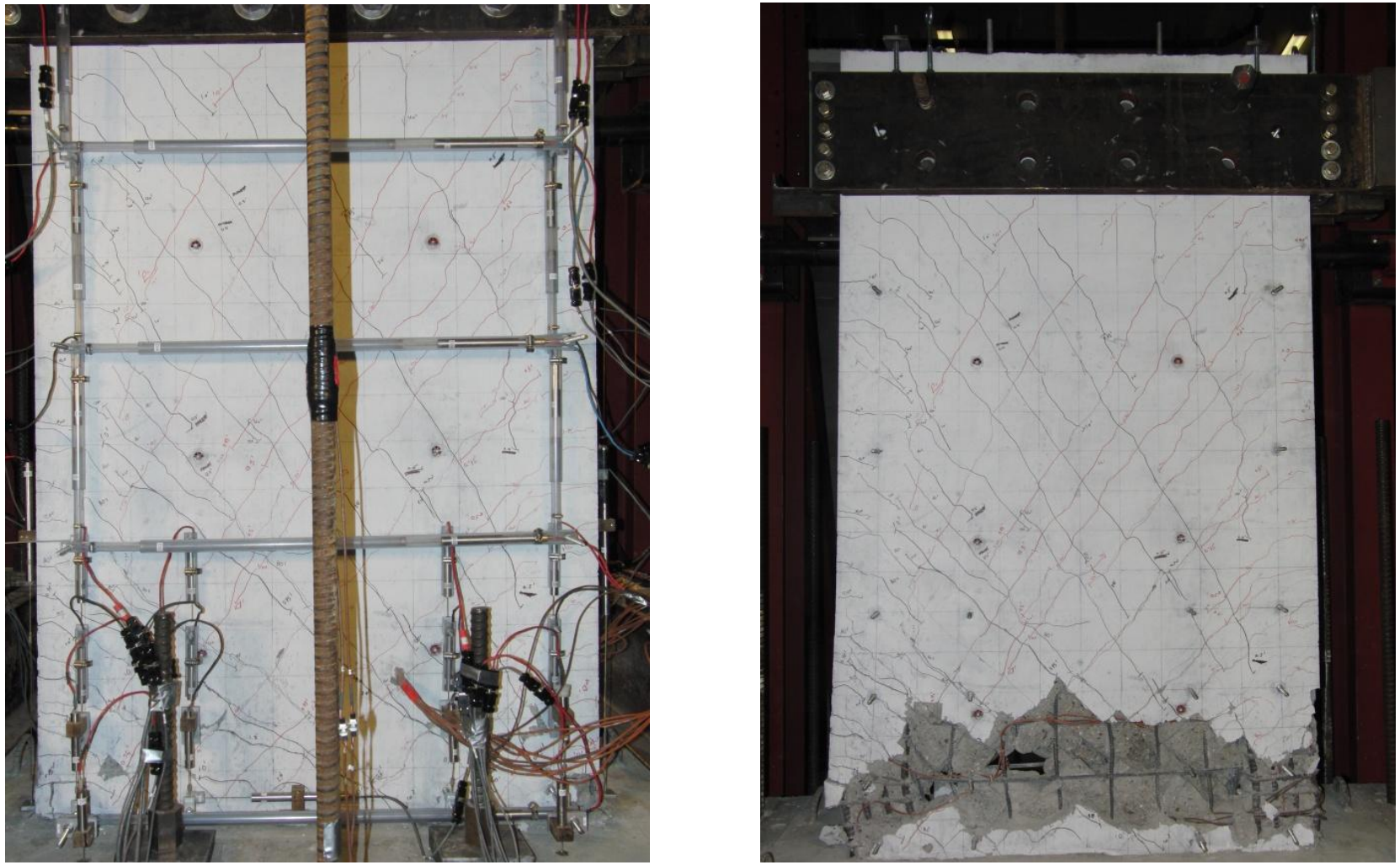

Figure A-17 Crack patterns for RW-A15-P10-S78: (a) 2.0% Drift, and (b) At end of test

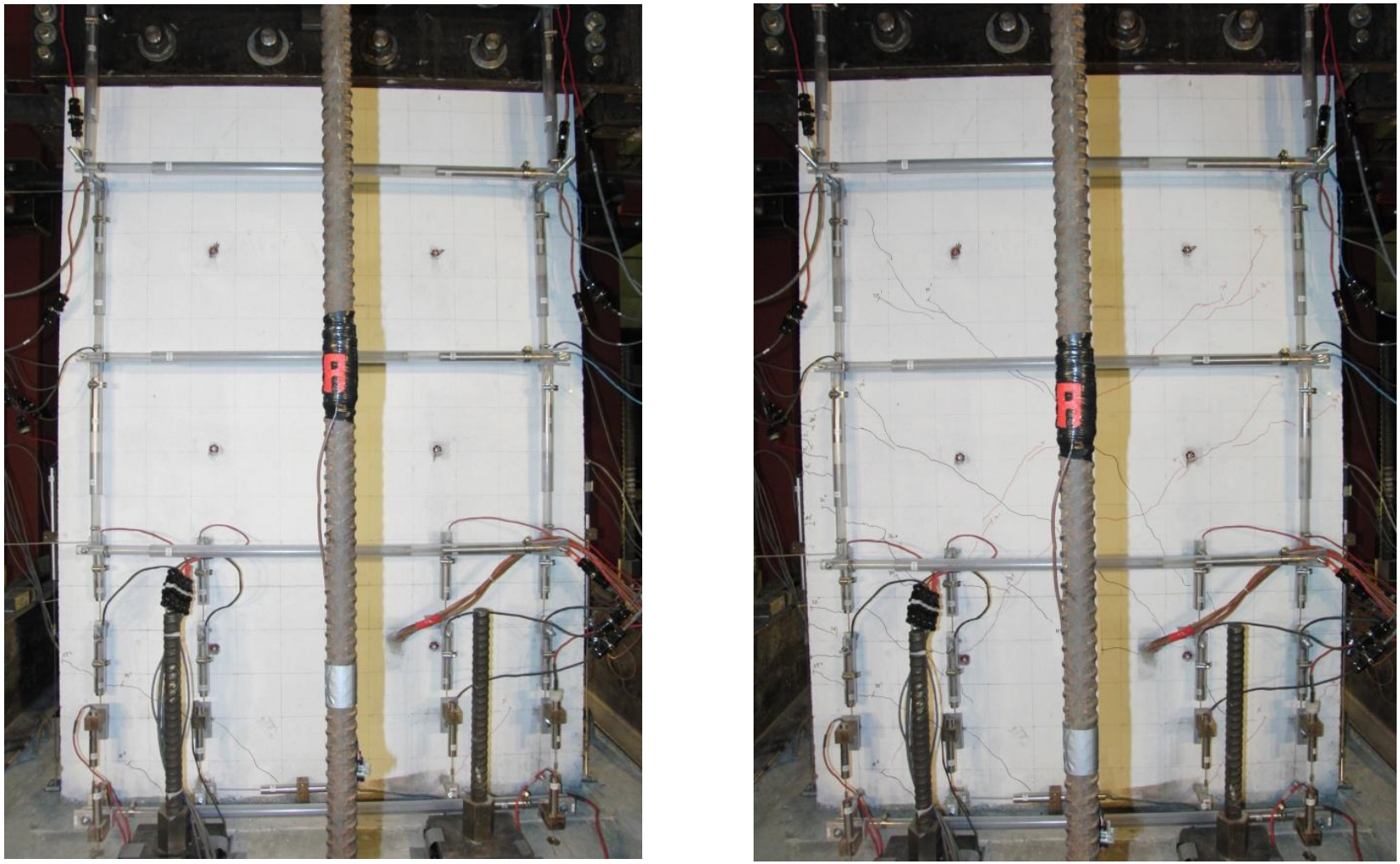

Figure A-18 Crack patterns for RW-A15-P2.5-S64: (a) V=35 kips, and (b) V=70 kips

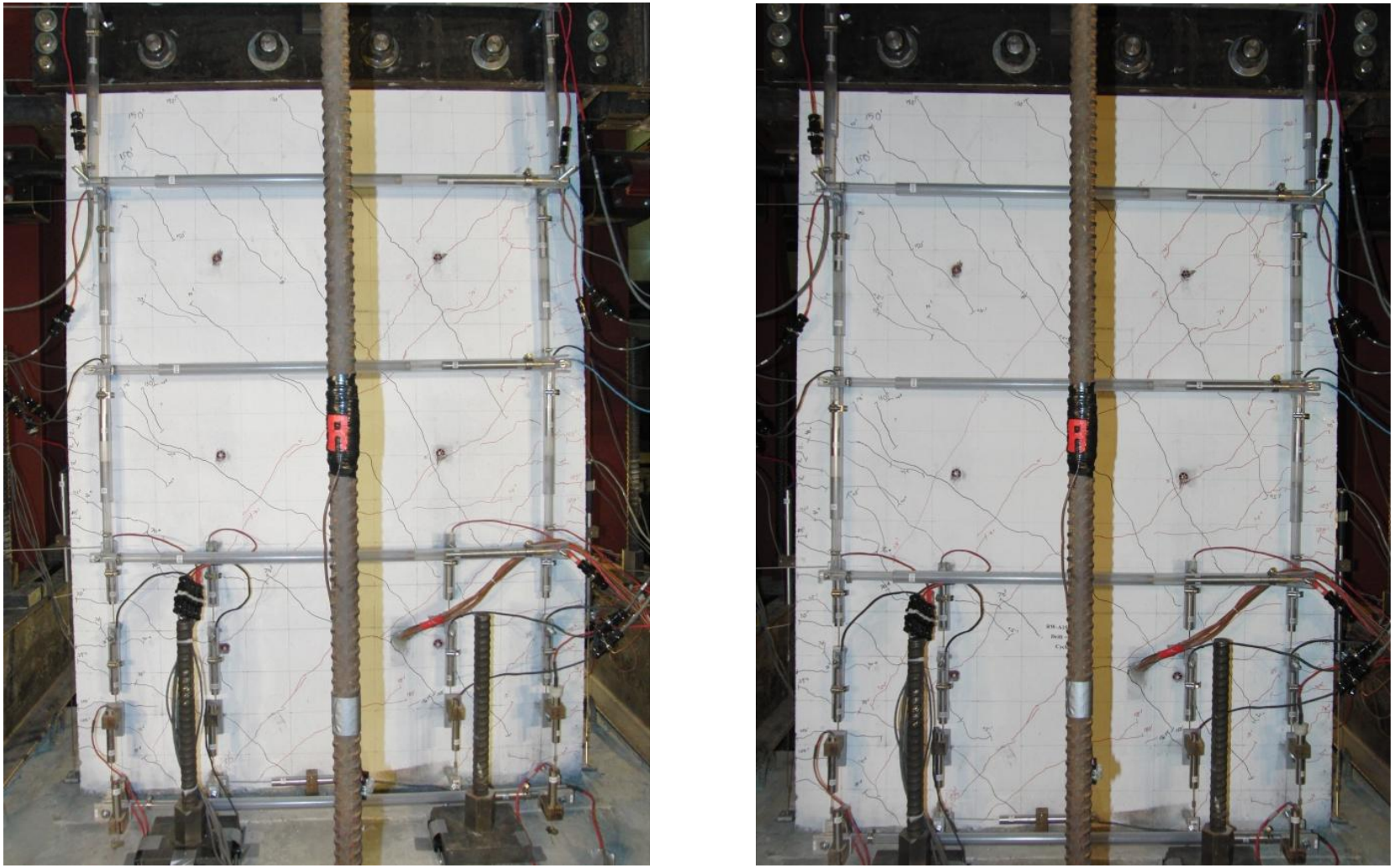

Figure A-19 Crack patterns for RW-A15-P2.5-S64: (a) V=105 kips, and (b) 0.5% Drift

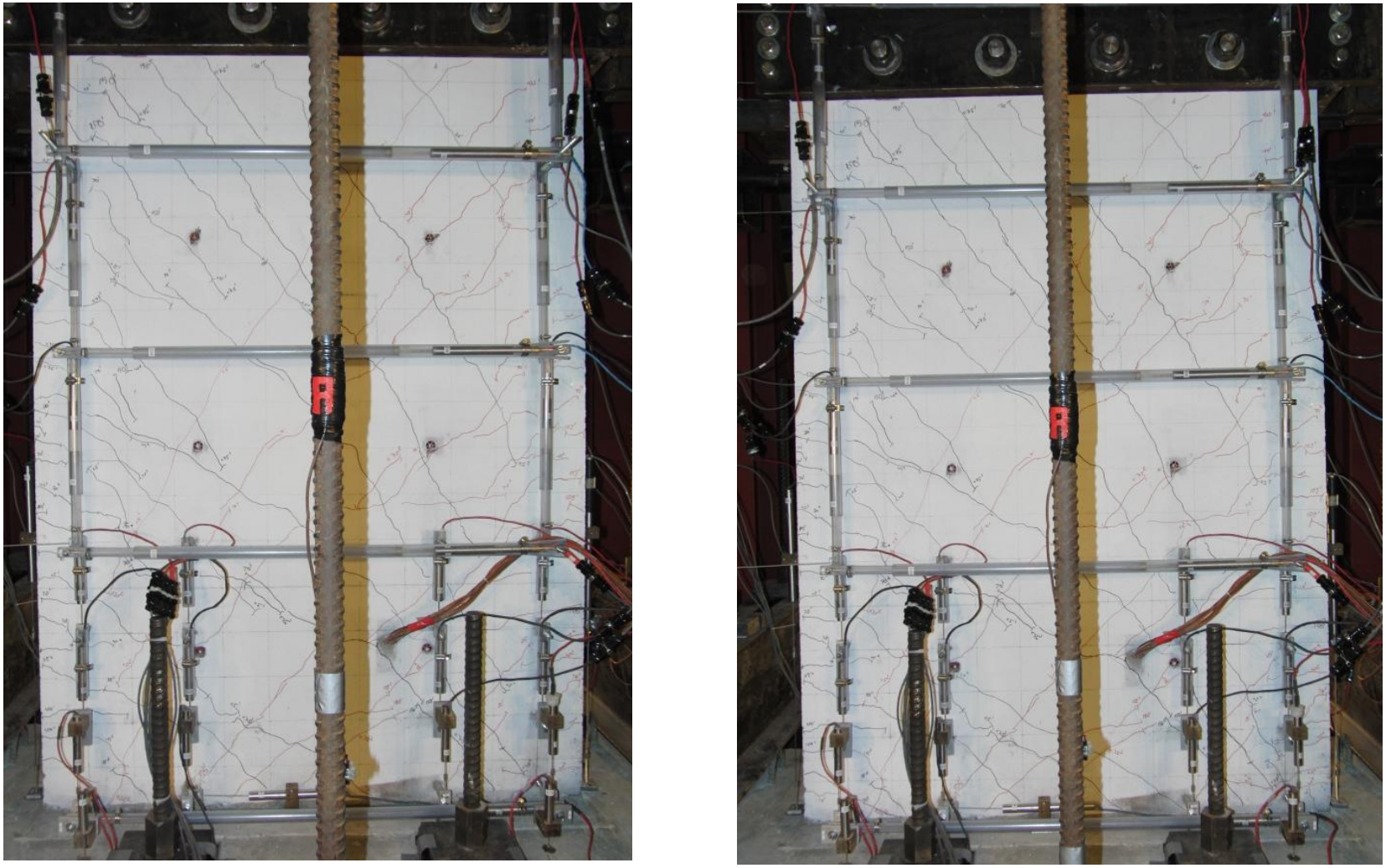

Figure A-20 Crack patterns for RW-A15-P2.5-S64: (a) 0.75% Drift, and (b) 1.0% Drift

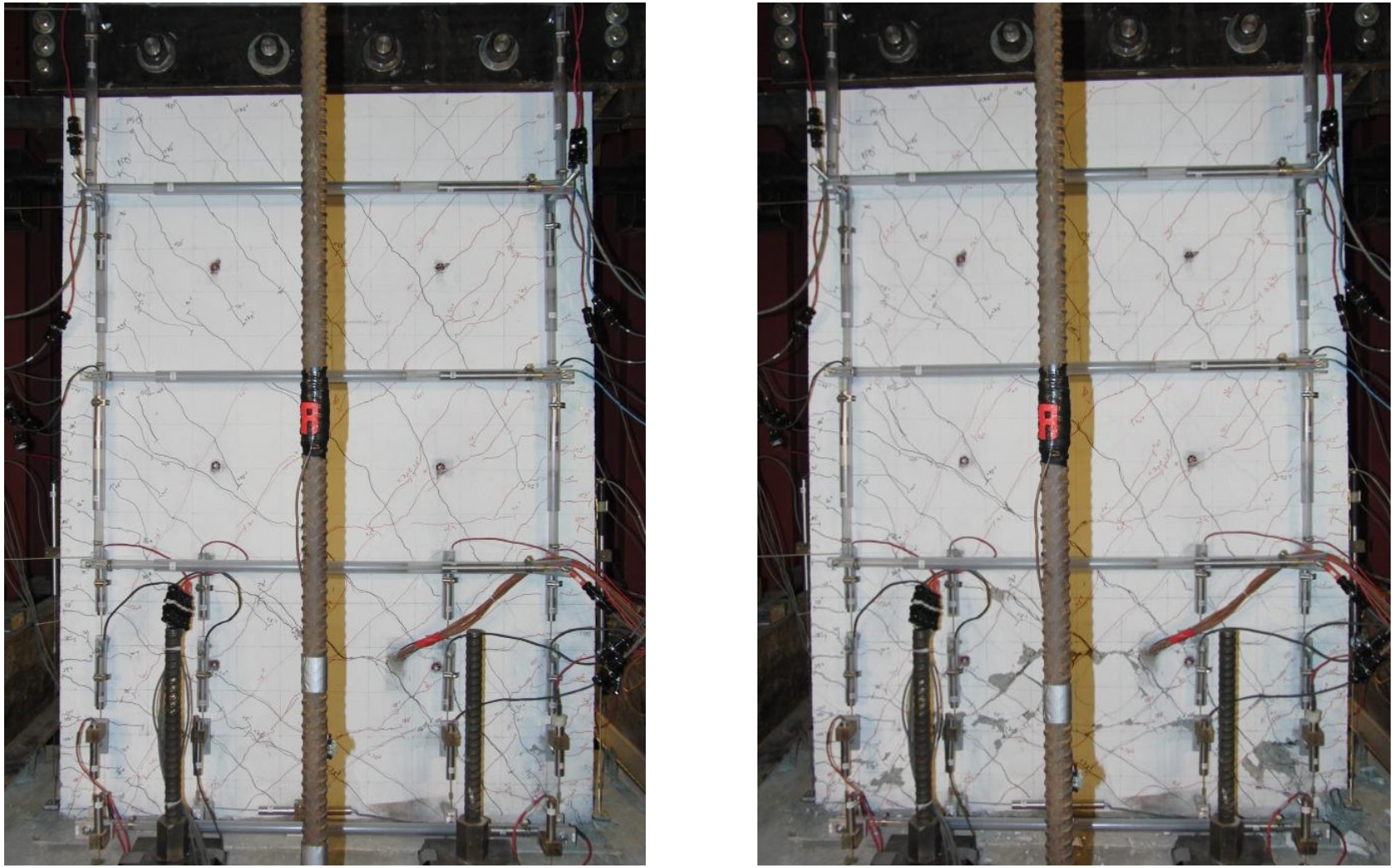

Figure A-21 Crack patterns for RW-A15-P2.5-S64: (a) 1.5% Drift, and (b) 2.0% Drift

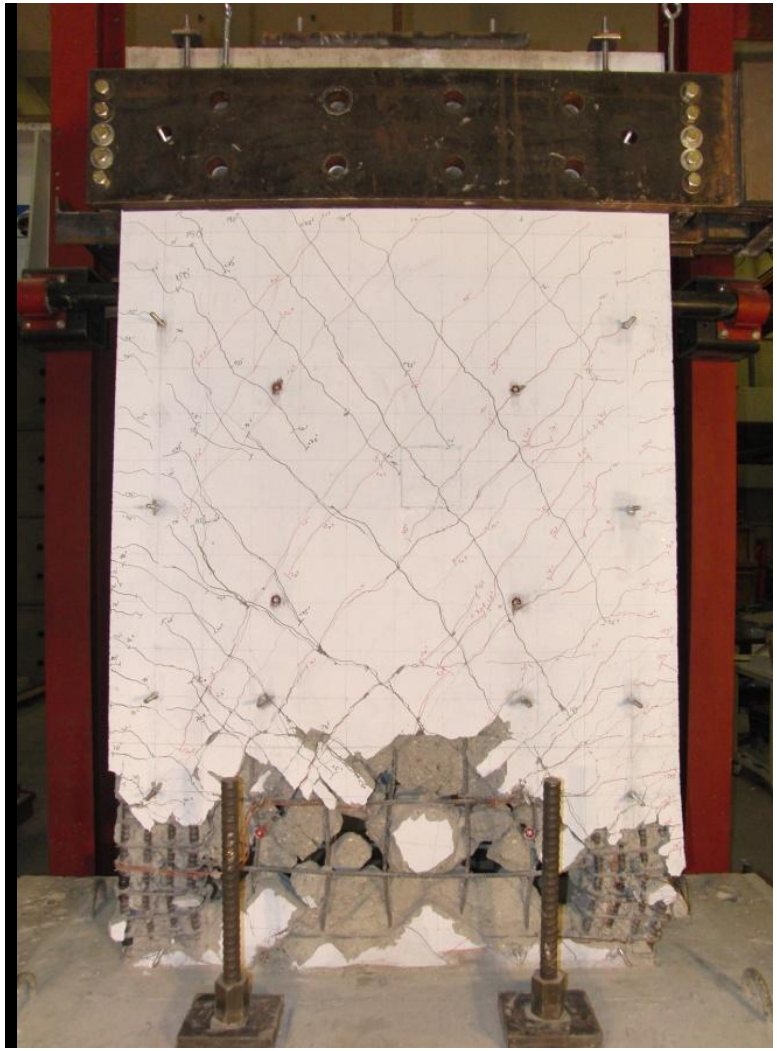

Figure A-22 Crack patterns for RW-A15-P2.5-S64: At end of test

A.2 Crack Widths

Typical horizontal flexural cracks and diagonal shear cracks on each wall specimen, under both positive and negative loadings, were numbered. Their maximum and residual crack widths, i.e., at maximum lateral load or displacement and zero lateral load, respectively, were measured and recorded. Figures A-23 through A-32 show these main cracks in five test specimens.

Cracks 1, 2, and 3 are not specific horizontal flexural cracks; they just represent the flexural cracks with the maximum crack width over the height from 0 to 8 in. (0 to 203 mm), 8 to 16 in. (203 to 406 mm), and 16 to 24 in. (406 to 610 mm), respectively. The remainder of cracks, which were numbered in their sequence of appearance from 4 to 9 or 11, are diagonal shear cracks. Maximum and residual crack widths (in mm unit) of these typical cracks are presented in Tables A-1 to A-5 for Tests 1 to 5, respectively.

For specimen RW-A20-P10-S38 (Test 1), only residual, not maximum, crack widths were recorded at drift ratios of 2.3% and 3.1%, due to a safety problem. As well, for specimen RW-A15-P2.5-S64 (Test 5), both maximum and residual crack widths were not available at 3.0% drift.

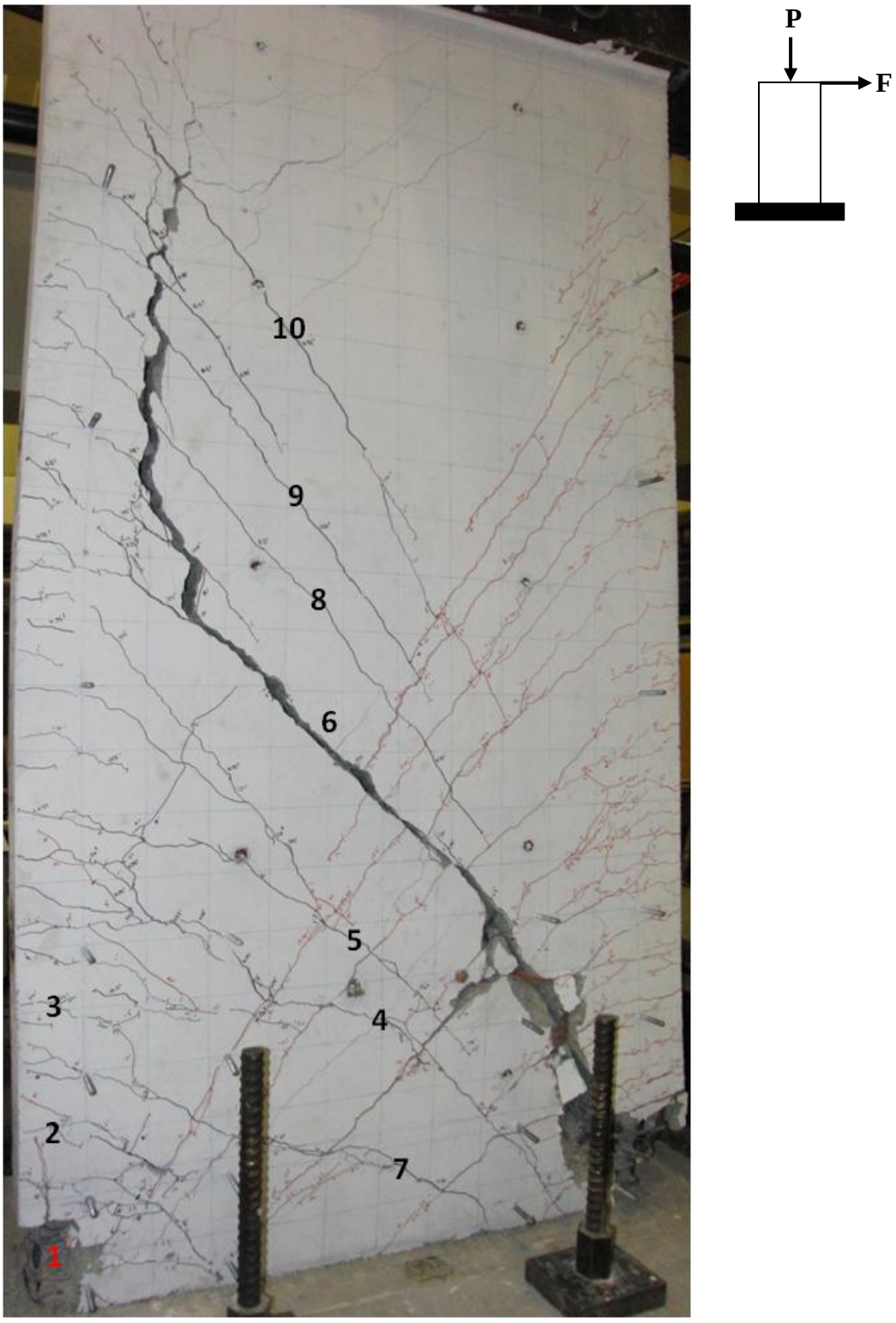

Figure A-23 RW-A20-P10-S38: Main cracks under positive loading

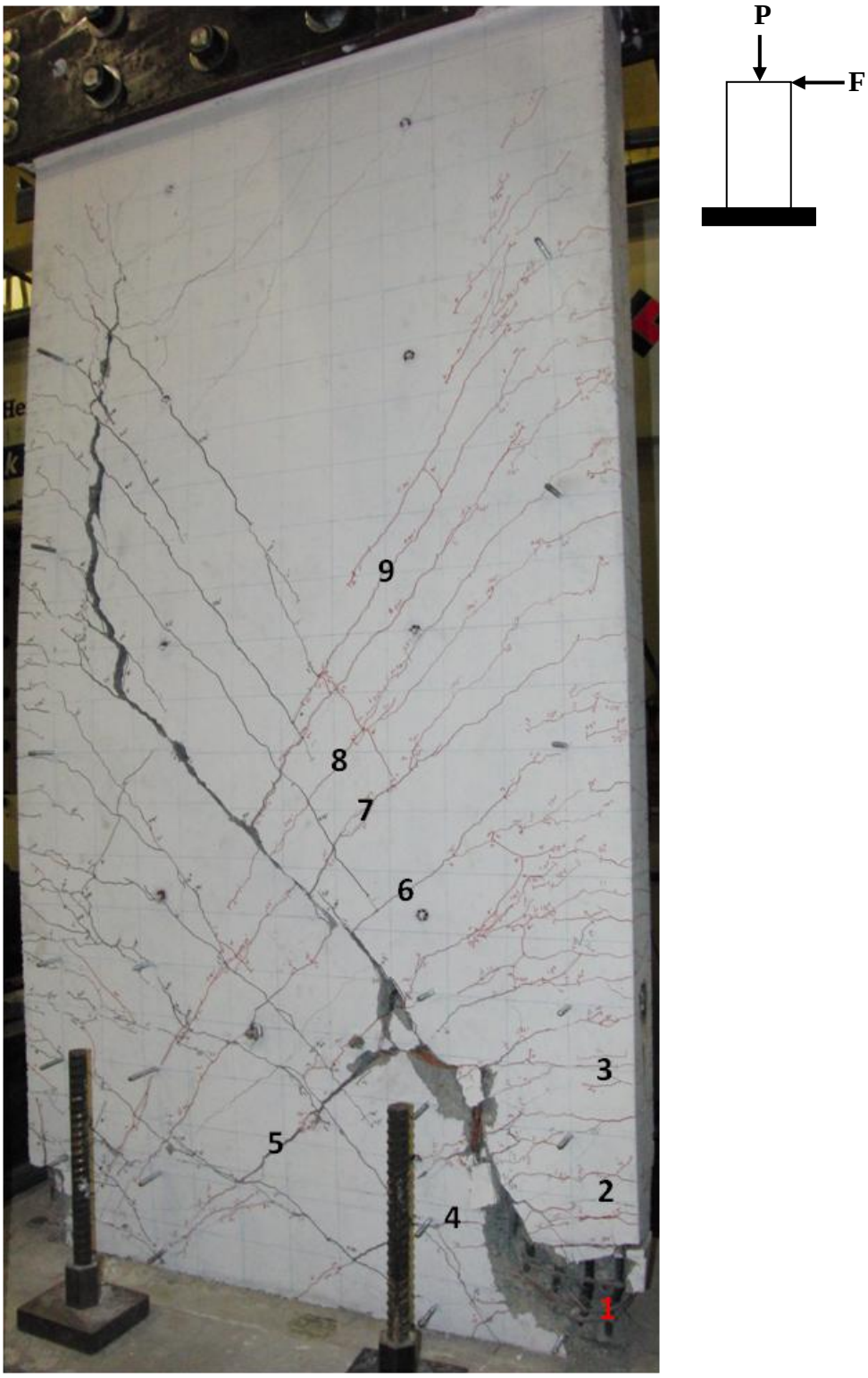

Figure A-24 RW-A20-P10-S38: Main cracks under negative loading

Table A-1 Crack widths in specimen RW-A20-P10-S38

Crack	Drift ratio (%) - Positive loading					
	0.56%	0.75%	1.1%	1.5%	2.3%	3.1%
1 (H*)	0.15/0.1*	0.6/0.15	1.25/0.2	1.5/0.3	/0.8	/1.0
2 (H)	0.15/0.1	0.3/0.1	1.0/0.2	1.25/0.2	/0.3	/0.4
3 (H)	0.15/0.1	0.2/0.1	0.3/0.1	0.5/0.15	/0.25	/0.35
4 (D*)	0.5/0.1	0.6/0.1	1.0/0.1	1.5/0.15	/1.0	/1.25
5 (D)	0.5/0.1	0.6/0.1	0.8/0.15	1.25/0.2	/0.4	/0.6
6 (D)	0.5/0.1	0.6/0.15	0.7/0.15	0.8/0.2	/0.5	/0.6
7 (D)	0.25/0.1	0.5/0.1	1.0/0.1	1.5/0.15	/1.0	/1.25
8 (D)	0.5/0.1	0.6/0.1	0.7/0.15	0.8/0.2	/0.5	/0.6
9 (D)	0.4/0.1	0.4/0.1	0.5/0.1	0.6/0.15	/0.2	/0.3
10 (D)	0.25/0.1	0.3/0.1	0.35/0.1	0.5/0.15	/0.15	/0.2
Crack	Drift ratio (%) - Negative loading					
	0.56%	0.75%	1.1%	1.5%	2.3%	3.1%
1 (H)	0.15/0.1	0.3/0.1	0.6/0.15	1.25/0.2	/0.8	/1.0
2 (H)	0.15/0.1	0.2/0.1	0.5/0.1	0.8/0.15	/0.3	/0.4
3 (H)	0.15/0.1	0.2/0.1	0.4/0.1	0.5/0.15	/0.3	/0.4
4 (D)	0.4/0.1	0.5/0.1	0.5/0.1	0.8/0.1	/0.35	/0.8
5 (D)	0.6/0.1	0.8/0.1	1.0/0.1	1.5/0.15	/0.8	/1.25
6 (D)	0.4/0.1	0.4/0.1	0.5/0.1	0.7/0.1	/0.35	/0.8
7 (D)	0.4/0.1	0.5/0.1	0.5/0.1	0.6/0.1	/0.1	/0.4
8 (D)	0.3/0.1	0.3/0.1	0.3/0.1	0.5/0.1	/0.1	/0.25
9 (D)	0.25/0.1	0.3/0.1	0.4/0.1	0.5/0.1	/0.1	/0.2

Notes (*): H is Horizontal flexural cracks; D is Diagonal shear cracks; X/Y presents the maximum and residual crack widths of X (mm) and Y (mm), respectively.

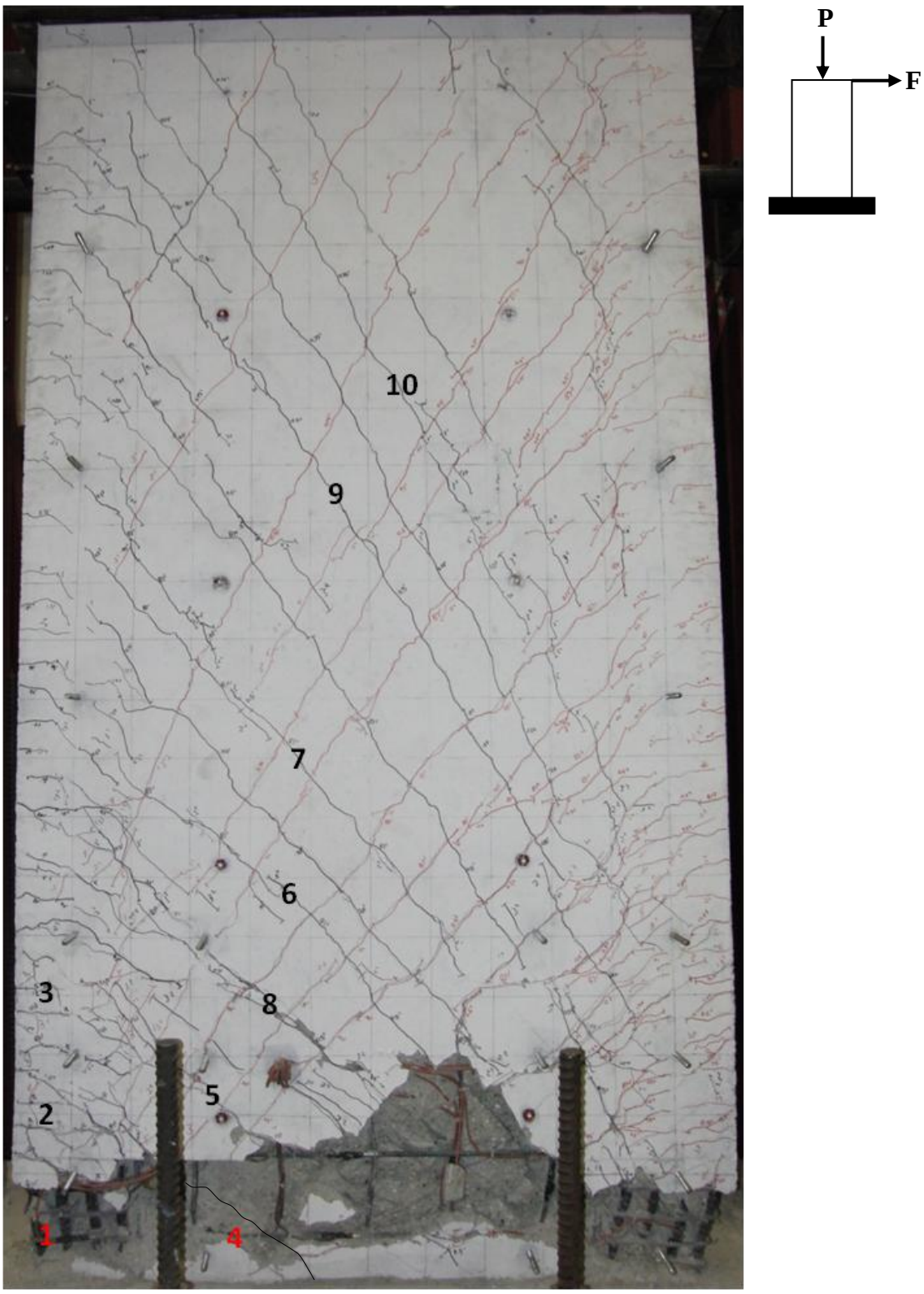

Figure A-25 RW-A20-P10-S63: Main cracks under positive loading

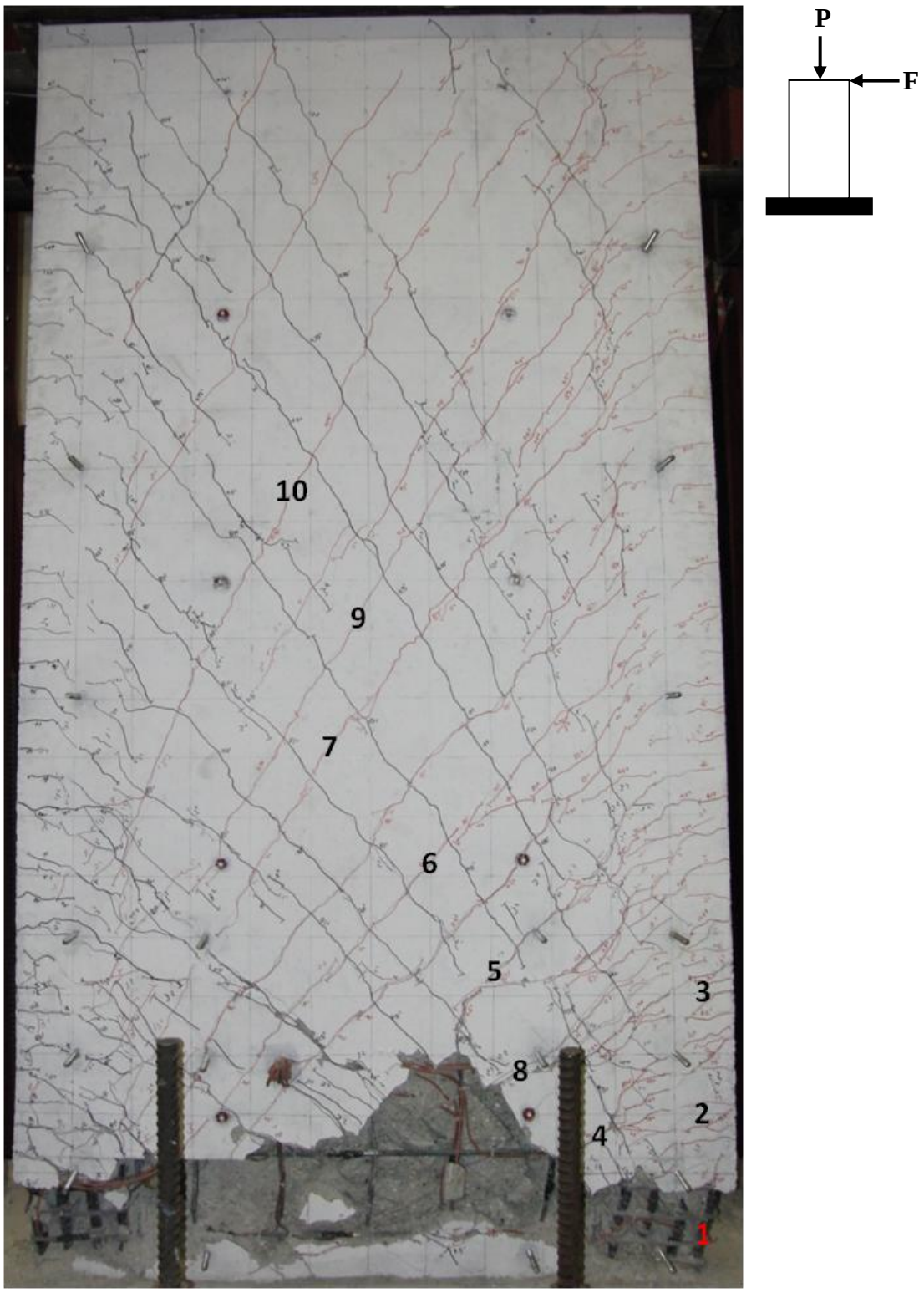

Figure A-26 RW-A20-P10-S63: Main cracks under negative loading

Table A-2 Crack widths in specimen RW-A20-P10-S63

Crack	Drift ratio (%) - Positive loading					
	0.5%	0.75%	1.0%	1.5%	2.0%	3.0%
1 (H)	0.15/0.1	0.3/0.1	0.8/0.5	0.9/0.5	1.0/0.6	1.5/0.6
2 (H)	0.15/0.1	0.15/0.1	0.15/0.1	0.8/0.3	1.0/0.4	1.5/0.5
3 (H)	0.15/0.1	0.15/0.1	0.15/0.1	0.5/0.4	0.6/0.4	1.0/0.5
4 (D)	0.25/0.1	0.35/0.1	0.8/0.2	1.25/0.4	1.5/0.5	2.5/0.6
5 (D)	0.3/0.1	0.4/0.1	0.5/0.1	2.0/0.5	2.5/0.6	3.5/1.0
6 (D)	0.4/0.1	0.4/0.1	0.5/0.1	0.5/0.1	0.6/0.1	1.0/0.1
7 (D)	0.4/0.1	0.4/0.1	0.5/0.1	0.5/0.1	0.6/0.1	0.6/0.1
8 (D)	0.3/0.1	0.4/0.1	0.5/0.1	0.6/0.1	1.25/0.1	3.0/0.1
9 (D)	0.3/0.1	0.3/0.1	0.35/0.1	0.35/0.1	0.4/0.1	0.4/0.1
10 (D)	-	0.1/0.1	0.1/0.1	0.15/0.1	0.15/0.1	0.2/0.1
Crack	Drift ratio (%) - Negative loading					
	0.5%	0.75%	1.0%	1.5%	2.0%	3.0%
1 (H)	0.15/0.1	0.3/0.1	0.8/0.4	0.9/0.4	1.0/0.5	1.5/0.6
2 (H)	0.15/0.1	0.2/0.1	0.25/0.1	0.4/0.2	0.6/0.3	0.6/0.5
3 (H)	0.15/0.1	0.15/0.1	0.25/0.1	0.5/0.4	0.6/0.5	0.8/0.5
4 (D)	0.3/0.1	0.4/0.1	0.8/0.2	2.0/0.6	2.5/1.0	3.0/1.0
5 (D)	0.3/0.1	0.35/0.1	0.4/0.1	0.8/0.1	1.25/0.1	2.0/0.1
6 (D)	0.3/0.1	0.35/0.1	0.4/0.1	0.5/0.1	0.6/0.1	1.0/0.2
7 (D)	0.4/0.1	0.4/0.1	0.5/0.1	0.6/0.1	0.8/0.1	1.0/0.1
8 (D)	0.3/0.1	0.5/0.1	0.6/0.1	0.8/0.3	1.0/0.4	1.5/0.4
9 (D)	0.25/0.1	0.3/0.1	0.3/0.1	0.35/0.1	0.4/0.1	0.5/0.1
10 (D)	0.15/0.1	0.2/0.1	0.3/0.1	0.35/0.1	0.4/0.1	0.4/0.1

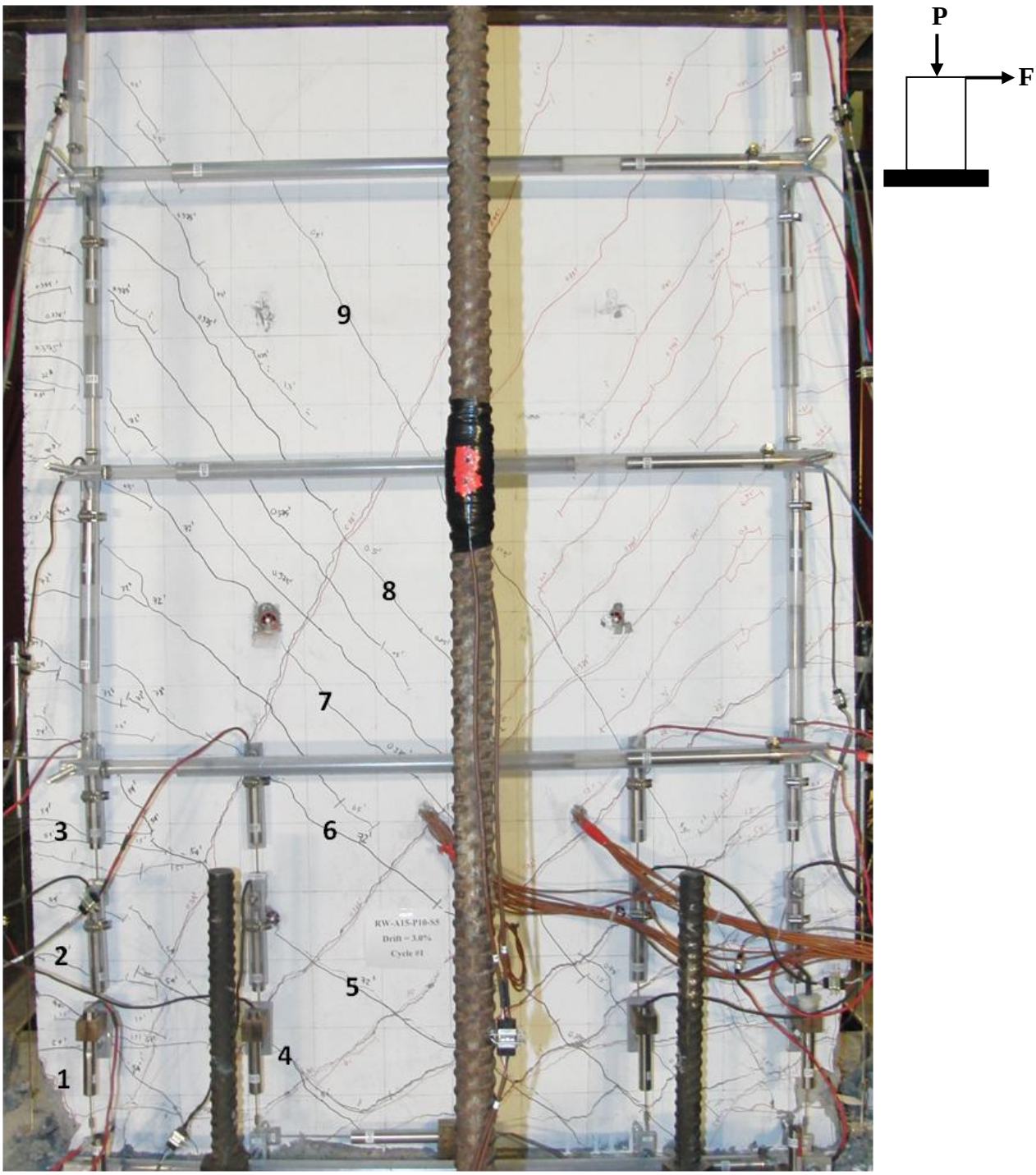

Figure A-27 RW-A15-P10-S51: Main cracks under positive loading

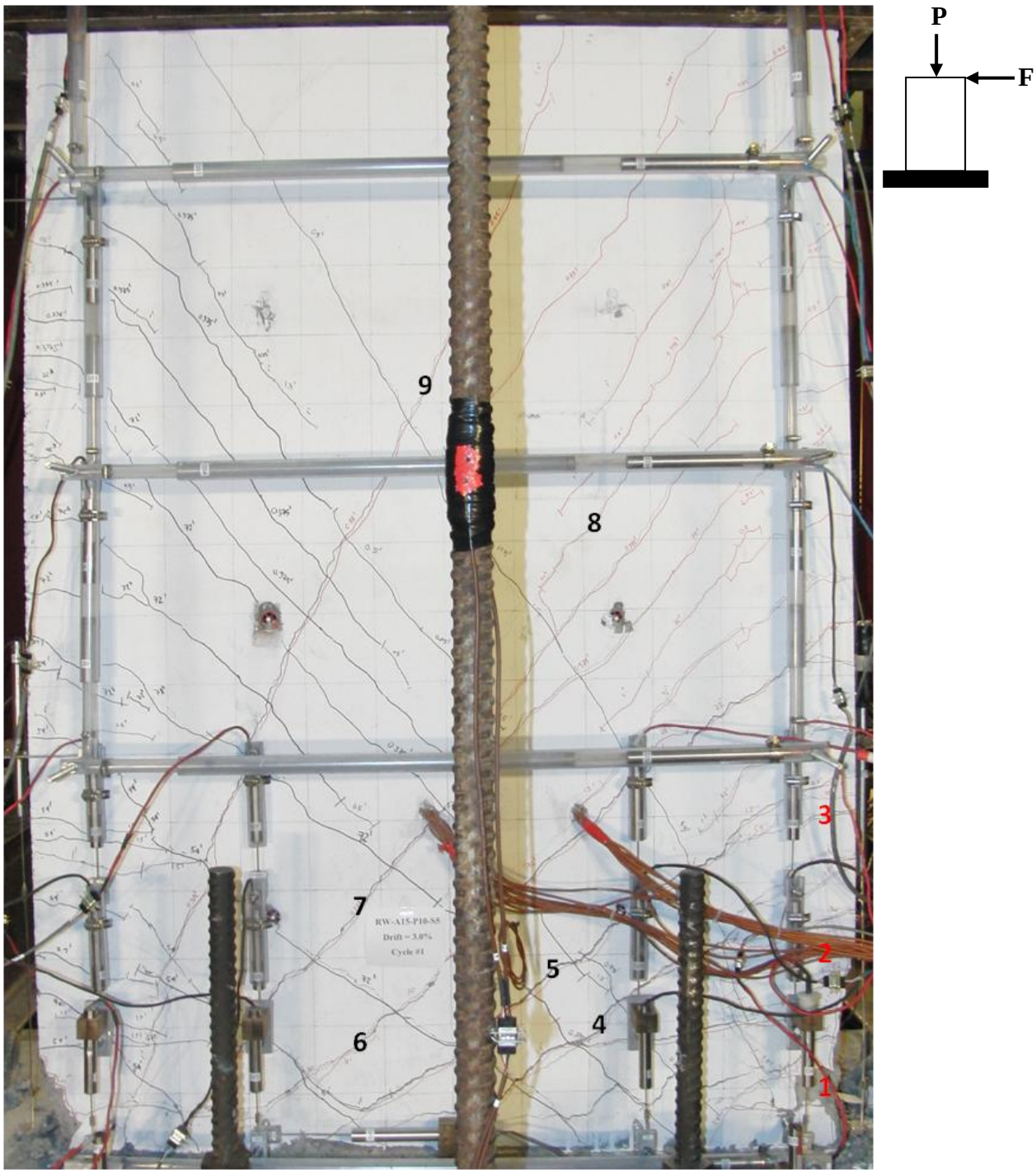

Figure A-28 RW-A15-P10-S51: Main cracks under negative loading

Table A-3 Crack widths in specimen RW-A15-P10-S51

Crack	Drift ratio (%) - Positive loading					
	0.5%	0.75%	1.0%	1.5%	2.0%	3.0%
1 (H)	0.15/0.1	0.5/0.1	1.25/0.2	1.25/0.3	1.5/0.4	2.0/0.8
2 (H)	0.15/0.1	0.3/0.1	0.8/0.2	1.0/0.3	1.25/0.35	1.5/0.4
3 (H)	0.15/0.1	0.2/0.1	0.6/0.1	1.0/0.4	1.5/0.6	2.0/0.8
4 (D)	0.2/0.1	0.3/0.1	0.4/0.1	1.25/0.15	1.5/0.5	3.0/0.8
5 (D)	0.2/0.1	0.4/0.1	1.0/0.1	2.0/0.3	2.5/0.6	3.0/0.8
6 (D)	0.5/0.1	0.6/0.1	0.8/0.1	1.25/0.1	1.5/0.15	2.25/0.3
7 (D)	0.4/0.1	0.5/0.1	0.6/0.1	0.8/0.1	1.0/0.1	1.5/0.1
8 (D)	0.4/0.1	0.4/0.1	0.5/0.1	0.5/0.1	0.5/0.1	0.5/0.25
9 (D)	0.4/0.15	0.5/0.1	0.6/0.1	0.7/0.2	0.8/0.25	1.25/0.3
Crack	Drift ratio (%) - Negative loading					
	0.5%	0.75%	1.0%	1.5%	2.0%	3.0%
1 (H)	0.15/0.1	0.6/0.15	0.8/0.2	1.0/0.3	1.25/0.4	1.5/0.5
2 (H)	0.15/0.1	0.4/0.1	0.6/0.1	0.7/0.2	0.8/0.3	1.25/0.6
3 (H)	0.15/0.1	0.15/0.1	0.2/0.1	0.8/0.3	1.0/0.4	1.25/0.5
4 (D)	0.3/0.1	0.6/0.1	0.8/0.1	2.0/0.4	2.5/0.5	3.0/0.6
5 (D)	0.25/0.1	0.5/0.1	0.8/0.1	1.25/0.1	1.75/0.3	3.0/0.8
6 (D)	0.5/0.1	0.6/0.1	0.6/0.1	0.8/0.1	1.25/0.3	1.75/0.4
7 (D)	0.4/0.1	0.5/0.1	0.6/0.1	0.8/0.1	1.0/0.1	1.75/0.4
8 (D)	0.25/0.1	0.3/0.1	0.4/0.1	0.4/0.1	0.5/0.15	0.6/0.2
9 (D)	0.25/0.1	0.4/0.15	0.6/0.3	0.8/0.3	1.0/0.4	1.5/0.5

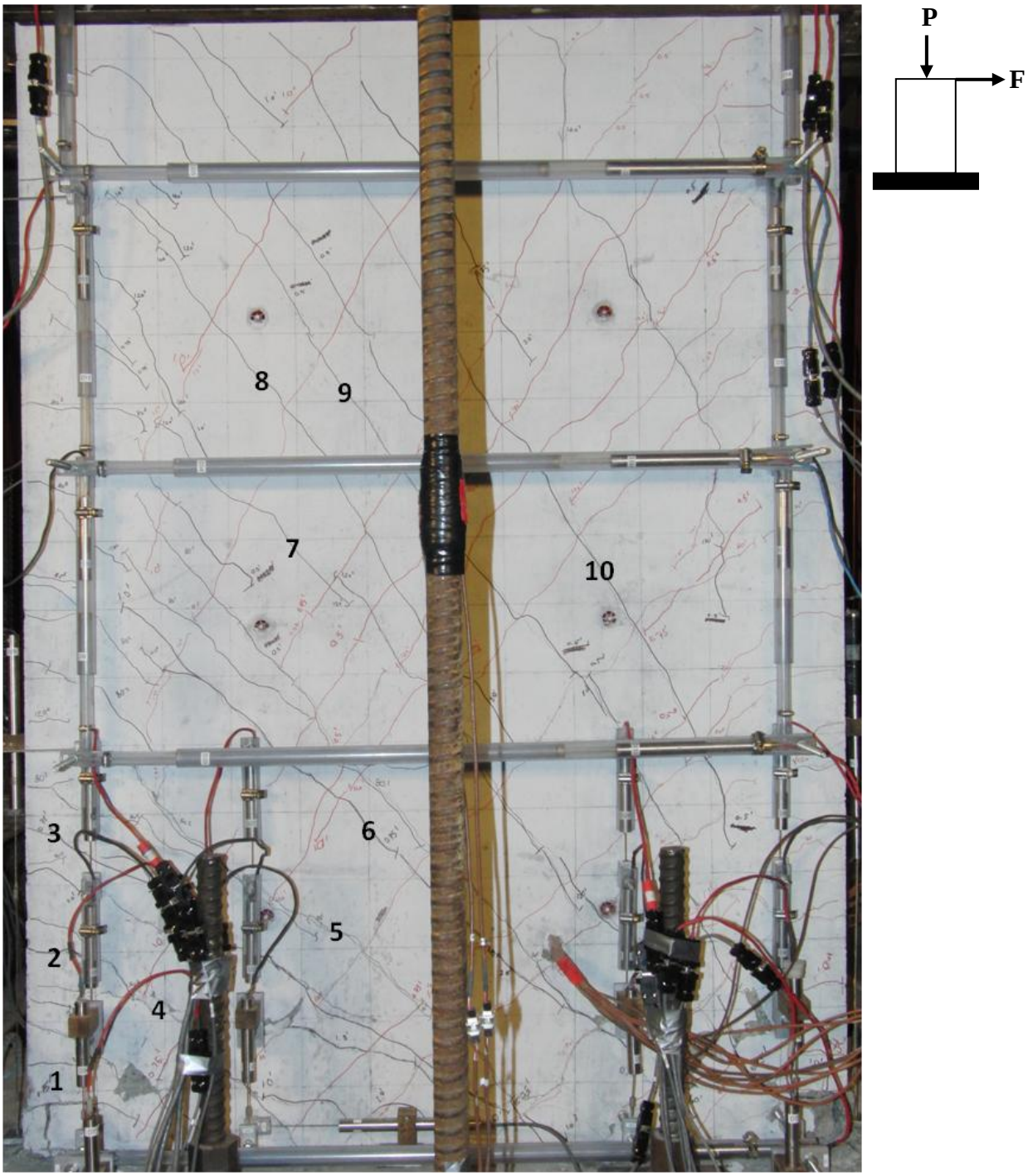

Figure A-29 RW-A15-P10-S78: Main cracks under positive loading

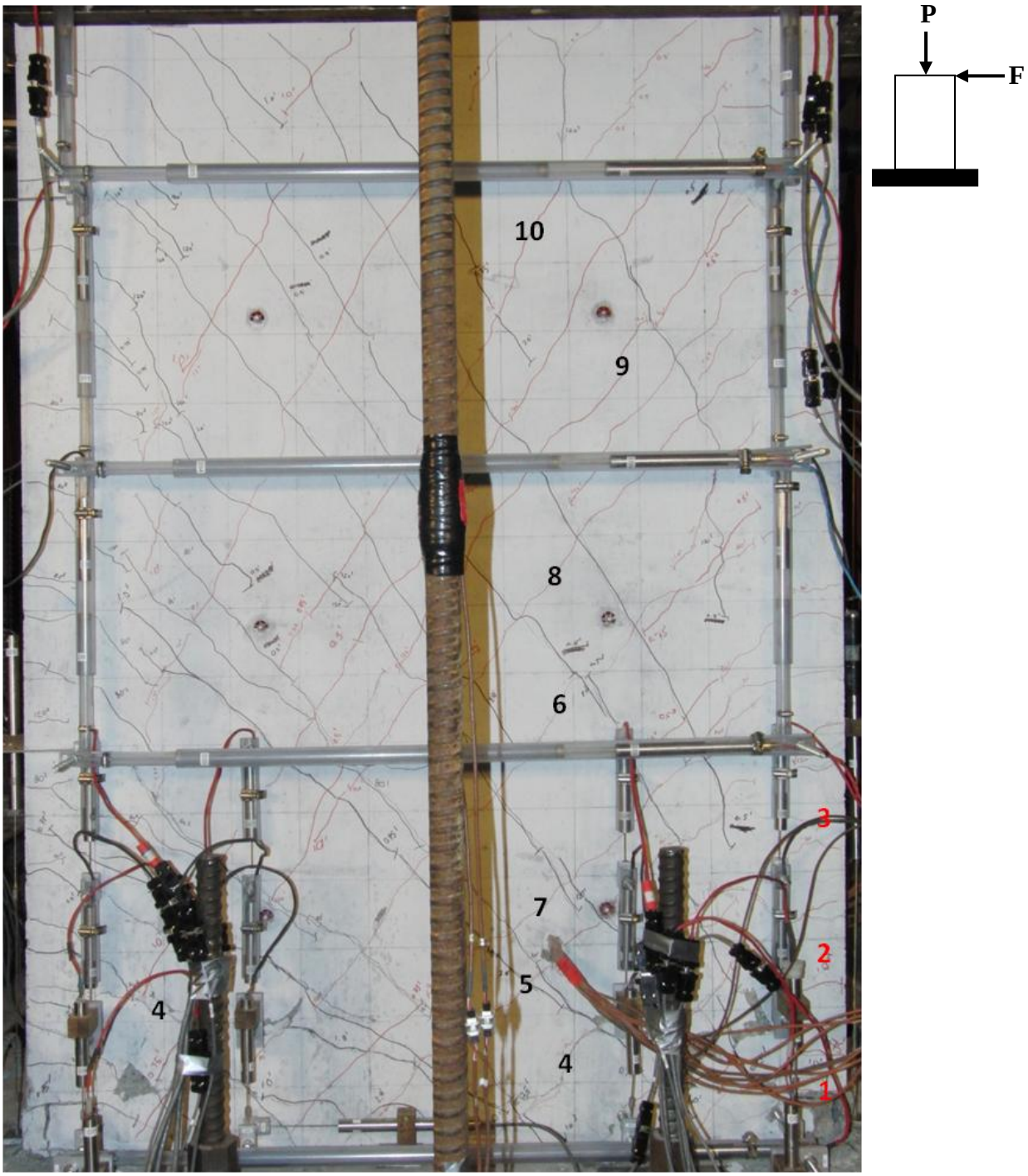

Figure A-30 RW-A15-P10-S78: Main cracks under negative loading

Table A-4 Crack widths in specimen RW-A15-P10-S78

Crack	Drift ratio (%) - Positive loading					
	0.5%	0.75%	1.0%	1.5%	2.0%	3.0%
1 (H)	0.15/0.1	0.2/0.1	1.0/0.2	1.25/0.4	1.5/0.5	2.0/1.0
2 (H)	0.15/0.1	0.15/0.1	0.2/0.1	1.0/0.2	1.25/0.4	1.5/1.0
3 (H)	0.15/0.1	0.25/0.1	0.3/0.1	0.4/0.1	1.5/0.5	2.0/0.8
4 (D)	0.2/0.1	0.25/0.1	0.8/0.2	1.5/0.6	2.0/0.7	2.5/0.8
5 (D)	0.3/0.1	0.4/0.1	0.5/0.1	0.6/0.4	1.5/1.0	2.5/1.25
6 (D)	0.25/0.1	0.3/0.1	0.4/0.1	0.5/0.2	0.8/0.4	1.75/0.5
7 (D)	0.4/0.1	0.4/0.1	0.5/0.1	1.0/0.3	1.25/0.4	1.5/0.4
8 (D)	0.25/0.1	0.4/0.1	0.5/0.1	0.5/0.15	0.5/0.15	0.8/0.15
9 (D)	0.25/0.1	0.3/0.1	0.4/0.1	0.4/0.1	0.5/0.1	0.5/0.1
10 (D)	0.25/0.1	0.3/0.1	0.4/0.1	0.4/0.1	0.5/0.15	0.6/0.2
Crack	Drift ratio (%) - Negative loading					
	0.5%	0.75%	1.0%	1.5%	2.0%	3.0%
1 (H)	0.15/0.1	0.2/0.1	0.8/0.4	0.8/0.5	1.5/1.25	(*)
2 (H)	0.15/0.1	0.2/0.1	0.6/0.3	0.8/0.4	1.25/1.0	1.5/1.0
3 (H)	0.15/0.1	0.15/0.1	0.2/0.1	0.8/0.4	1.0/0.5	1.25/1.0
4 (D)	0.2/0.1	0.3/0.1	0.5/0.1	1.0/0.6	1.25/0.7	1.5/0.8
5 (D)	0.2/0.1	0.4/0.1	0.4/0.1	1.0/0.1	1.5/0.25	2.0/0.8
6 (D)	0.3/0.1	0.4/0.1	0.4/0.1	0.5/0.1	1.25/0.2	3.0/1.25
7 (D)	0.3/0.1	0.35/0.1	0.4/0.1	1.0/0.1	1.5/0.3	3.0/0.8
8 (D)	0.3/0.1	0.4/0.1	0.5/0.1	0.5/0.1	0.5/0.1	1.0/0.2
9 (D)	0.25/0.1	0.3/0.1	0.3/0.1	0.4/0.1	0.4/0.1	0.8/0.1
10 (D)	0.2/0.1	0.25/0.1	0.3/0.1	0.35/0.1	0.4/0.1	0.6/0.1

Notes: (*) Crack widths were not available at this location during cycles to 3.0% drift due to a concrete crushing.

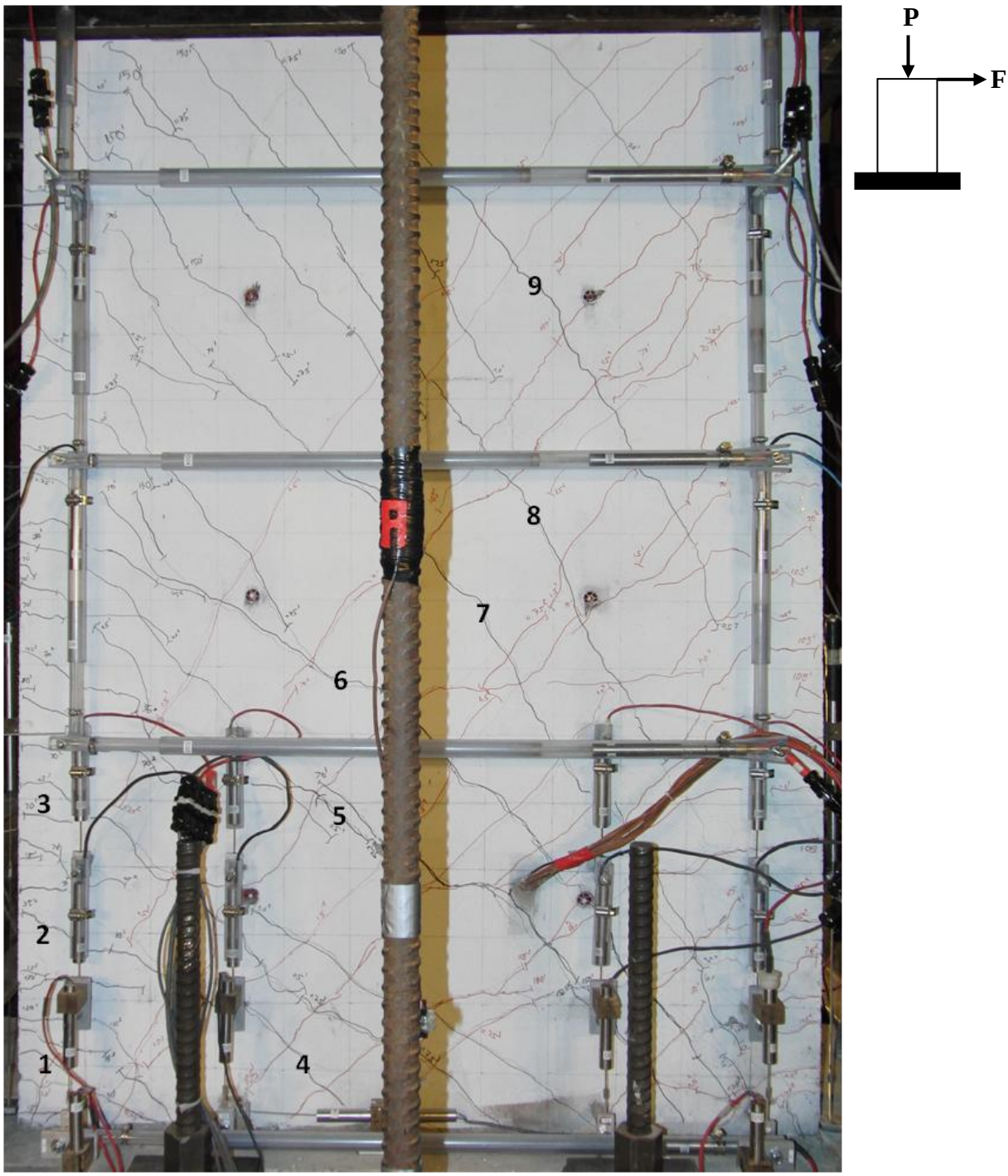

Figure A-31 RW-A15-P2.5-S64: Main cracks under positive loading

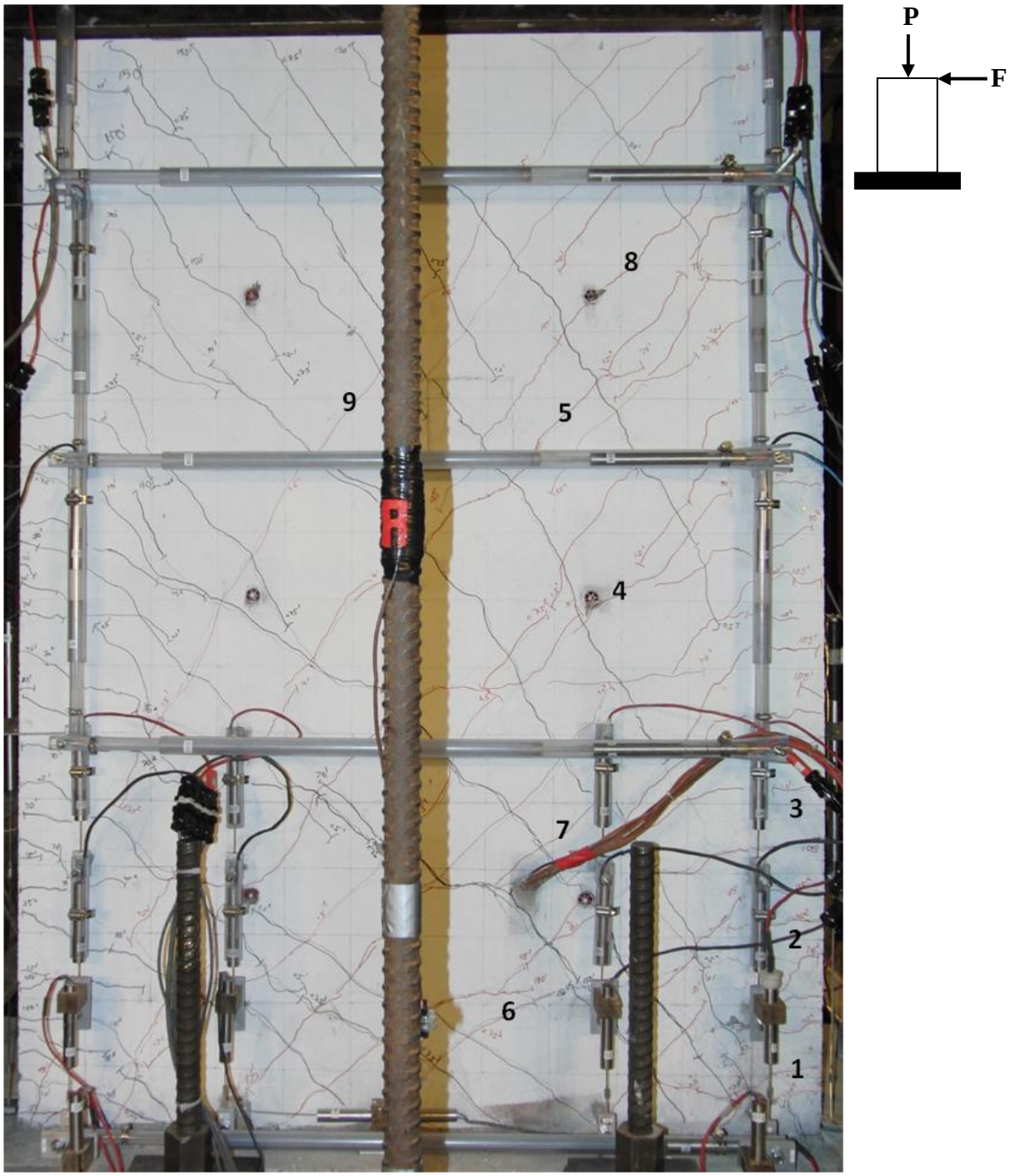

Figure A-32 RW-A15-P2.5-S64: Main cracks under negative loading

Table A-5 Crack widths in specimen RW-A15-P2.5-S64

Crack	Drift ratio (%) - Positive loading					
	0.5%	0.75%	1.0%	1.5%	2.0%	3.0%
1 (H)	0.15/0.1	0.2/0.1	0.8/0.6	1.0/0.8	1.25/0.8	NA
2 (H)	0.15/0.1	0.2/0.1	0.6/0.3	1.0/0.8	1.25/1.0	NA
3 (H)	0.15/0.1	0.15/0.1	0.2/0.1	0.8/0.5	1.0/0.8	NA
4 (D)	0.3/0.1	0.4/0.1	0.8/0.2	1.5/0.4	2.0/0.6	NA
5 (D)	0.5/0.1	0.6/0.1	0.8/0.2	1.25/0.3	3.0/1.0	NA
6 (D)	0.5/0.1	0.6/0.1	0.7/0.1	1.0/0.3	3.0/1.0	NA
7 (D)	0.6/0.1	0.7/0.1	0.8/0.1	1.0/0.2	1.25/0.35	NA
8 (D)	0.3/0.1	0.3/0.1	0.35/0.1	0.35/0.1	0.4/0.1	NA
9 (D)	0.25/0.1	0.25/0.1	0.3/0.1	0.3/0.1	0.4/0.1	NA
Crack	Drift ratio (%) - Negative loading					
	0.5%	0.75%	1.0%	1.5%	2.0%	3.0%
1 (H)	0.15/0.1	0.15/0.1	1.0/0.8	1.25/1.0	1.5/1.0	NA
2 (H)	0.15/0.1	0.15/0.1	0.15/0.1	1.0/0.8	1.25/1.0	NA
3 (H)	0.15/0.1	0.15/0.1	0.15/0.1	0.15/0.1	0.8/0.6	NA
4 (D)	0.5/0.1	0.6/0.1	0.7/0.1	1.0/0.25	1.25/0.4	NA
5 (D)	0.6/0.1	0.7/0.2	0.8/0.2	1.0/0.3	1.25/0.5	NA
6 (D)	0.25/0.1	0.35/0.1	0.8/0.15	2.0/0.7	3.0/1.0	NA
7 (D)	0.4/0.1	0.6/0.1	0.8/0.2	1.5/0.2	3.0/0.8	NA
8 (D)	0.4/0.1	0.5/0.1	0.5/0.1	0.6/0.1	1.5/0.5	NA
9 (D)	0.25/0.1	0.3/0.1	0.3/0.1	0.4/0.1	1.25/0.4	NA

B. APPENDIX B SENSORS-RELATED DATA

B.1 Axial Load

Axial load histories, i.e., axial load versus data point relations, for specimens RW-A20-P10-S63 (Test 2), RW-A15-P10-S51 (Test 3), RW-A15-P10-S78 (Test 4), and RW-A15-P2.5-S64 (Test 5) are presented in Figures B-1 through B-4. Although axial load was not recorded for specimen RW-A20-P10-S38 (Test 1), it was monitored during the test by checking pressure in the hand pump connected to the two hydraulic cylinders. The axial load was adjusted by adding or releasing the pressure to ensure that its magnitude was almost equal to the design axial load.

The design axial loads were 144 kips (641 kN) for Tests 1 to 4 and 36 kips (160kN) for Test 5. The actual axial load, defined as the average axial load throughout the test, were 148 kips (658 kN), 157 kips (698 kN), 149 kips (663 kN), and 38 kips (169 kN) for Tests 2 to 5, respectively. The actual axial load for Test 1 was approximately 144 kips (641 kN).

Axial load versus lateral load relations for Tests 2 to 5 are shown in Figures B-5, B-7, B-9, and B-11; whereas axial load versus lateral displacement responses for Tests 2 to 5 are shown in Figures B-6, B-8, B-10, and B-12, respectively.

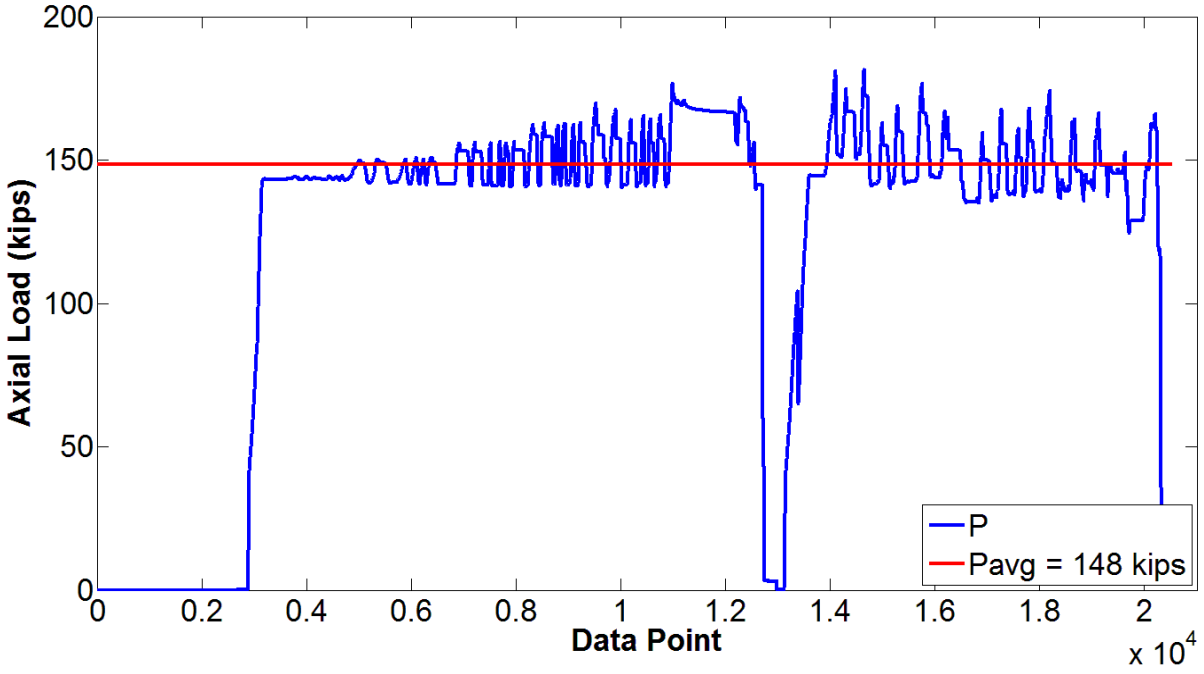

Figure B-1 Axial load history: RW-A20-P10-S38 (Test 2)

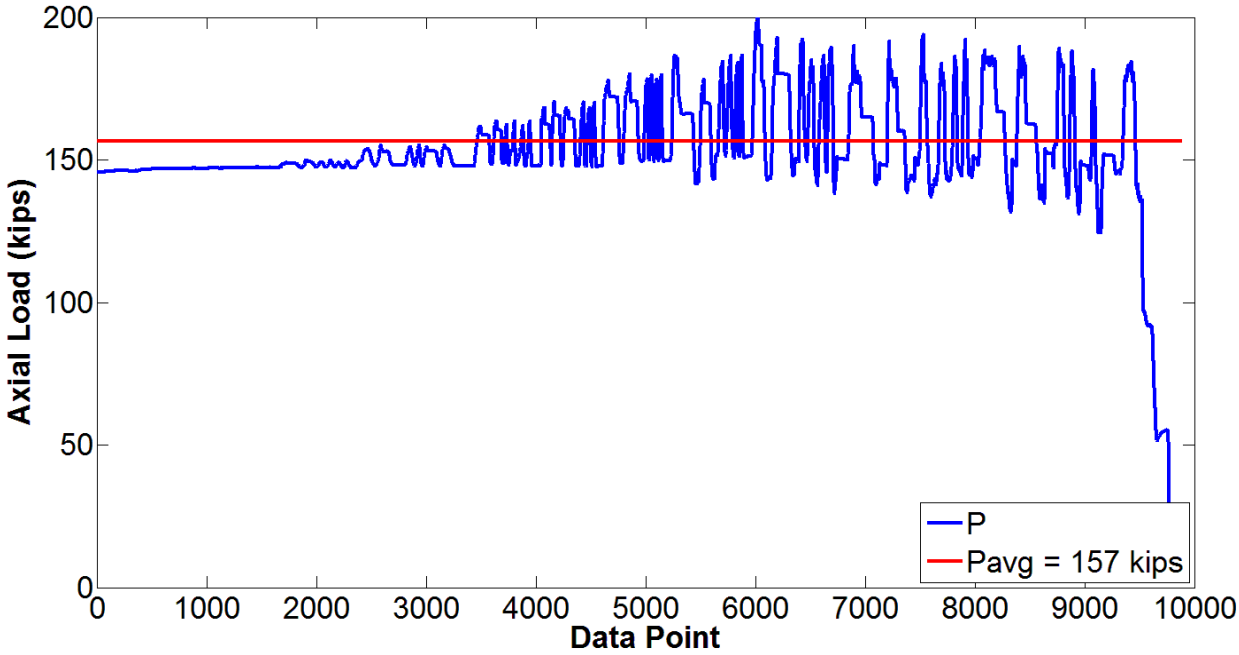

Figure B-2 Axial load history: RW-A15-P10-S51 (Test 3)

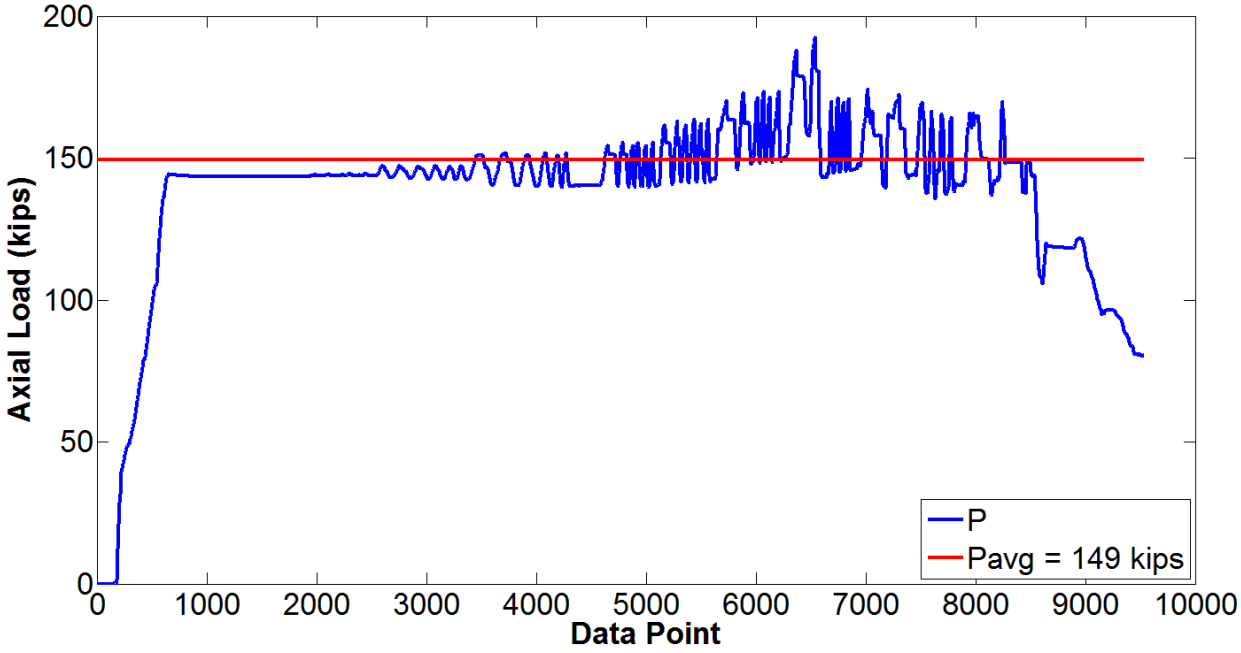

Figure B-3 Axial load history: RW-A15-P10-S78 (Test 4)

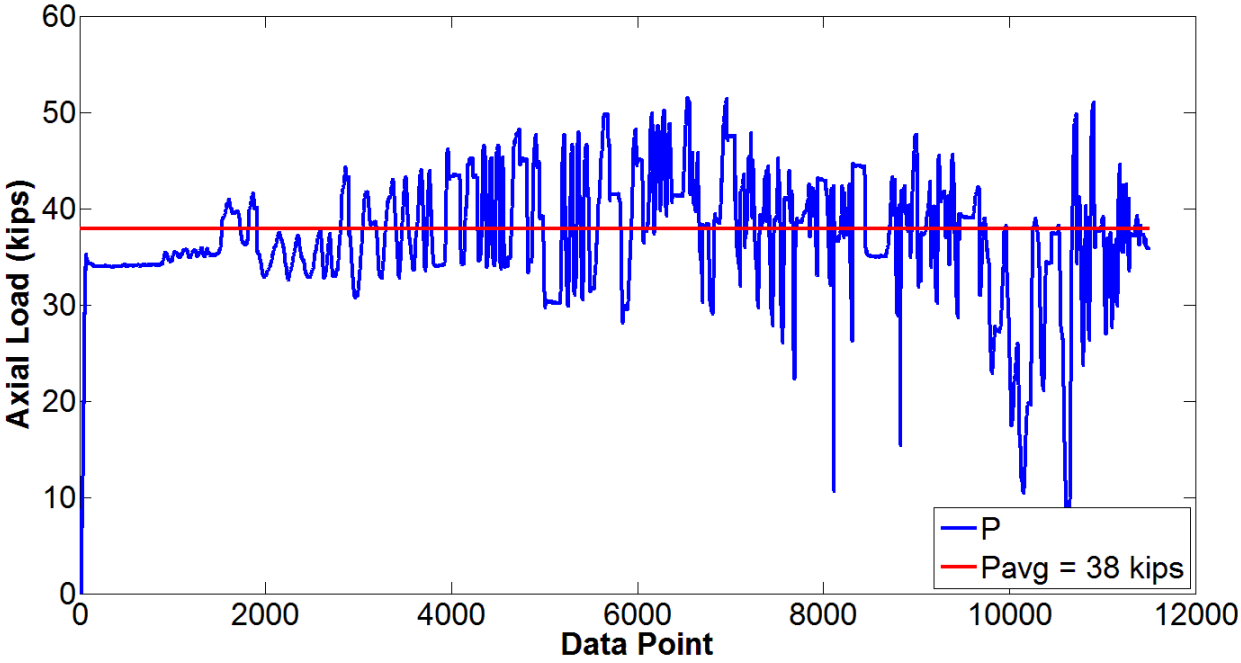

Figure B-4 Axial load history: RW-A15-P2.5-S64 (Test 5)

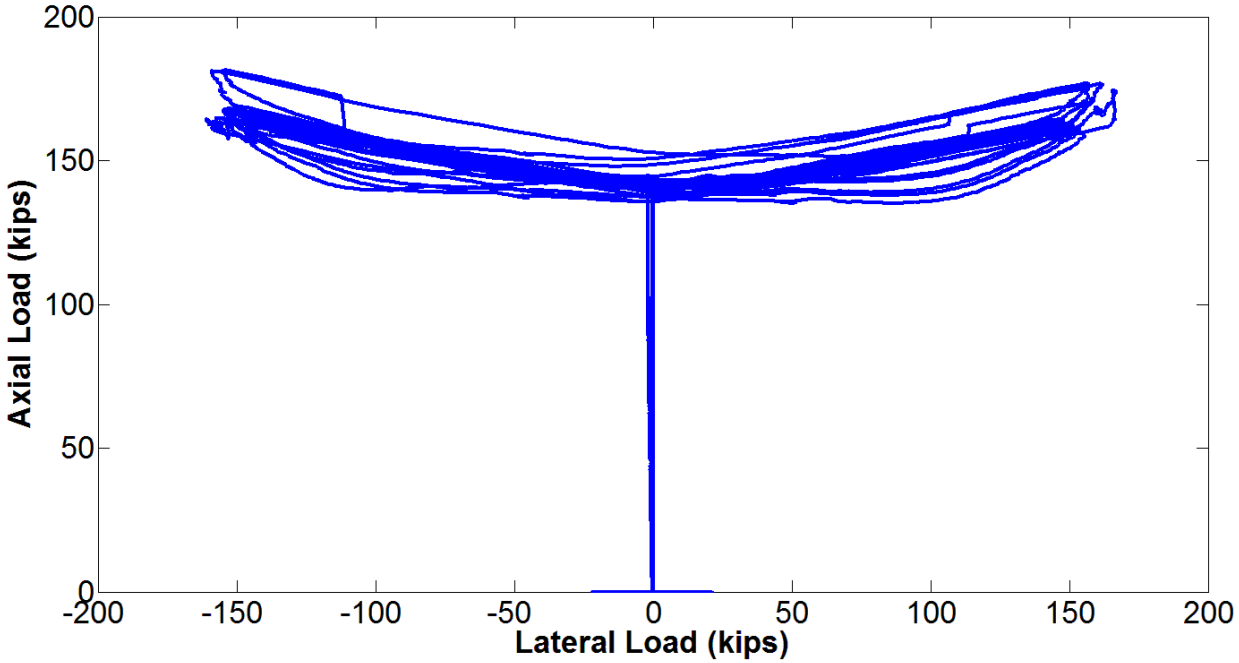

Figure B-5 RW-A20-P10-S63 (Test 2): Axial load versus lateral load relation

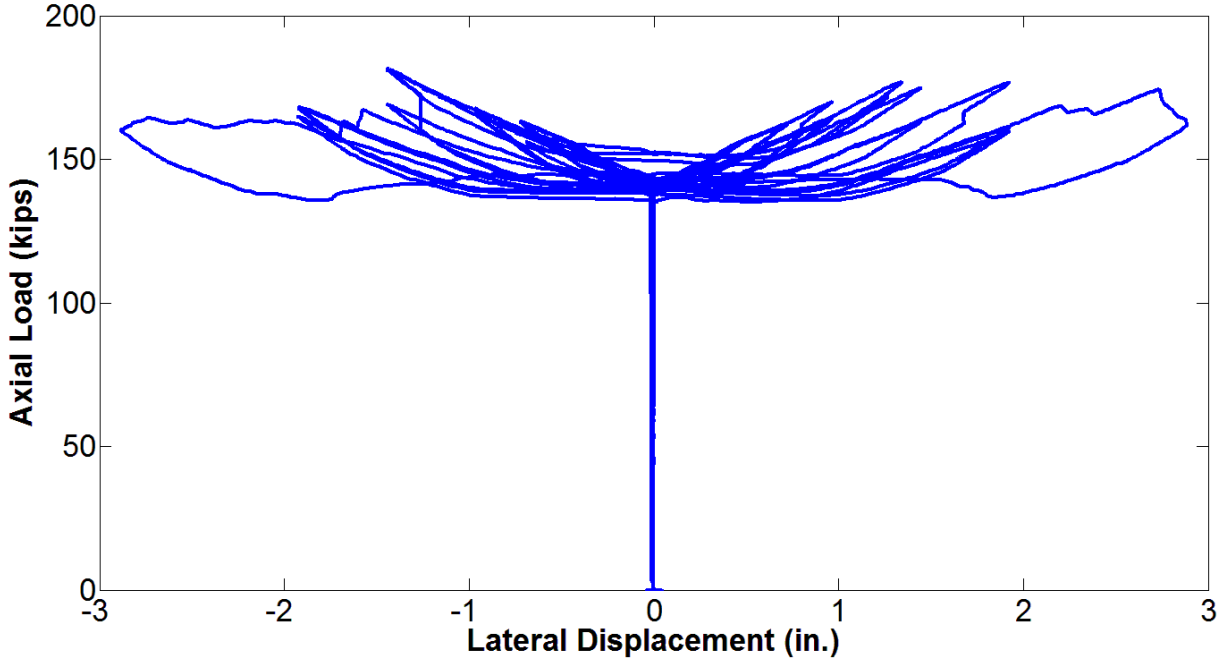

Figure B-6 RW-A20-P10-S63 (Test 2): Axial load versus lateral displacement relation

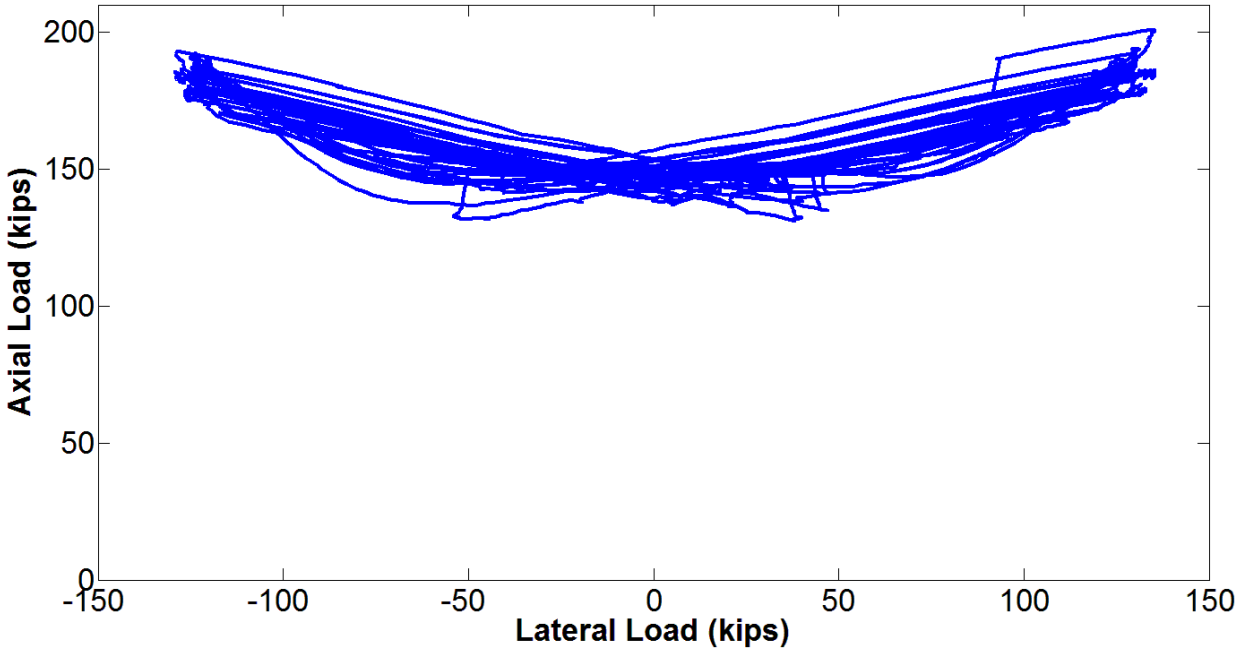

Figure B-7 RW-A15-P10-S51 (Test 3): Axial load versus lateral load relation

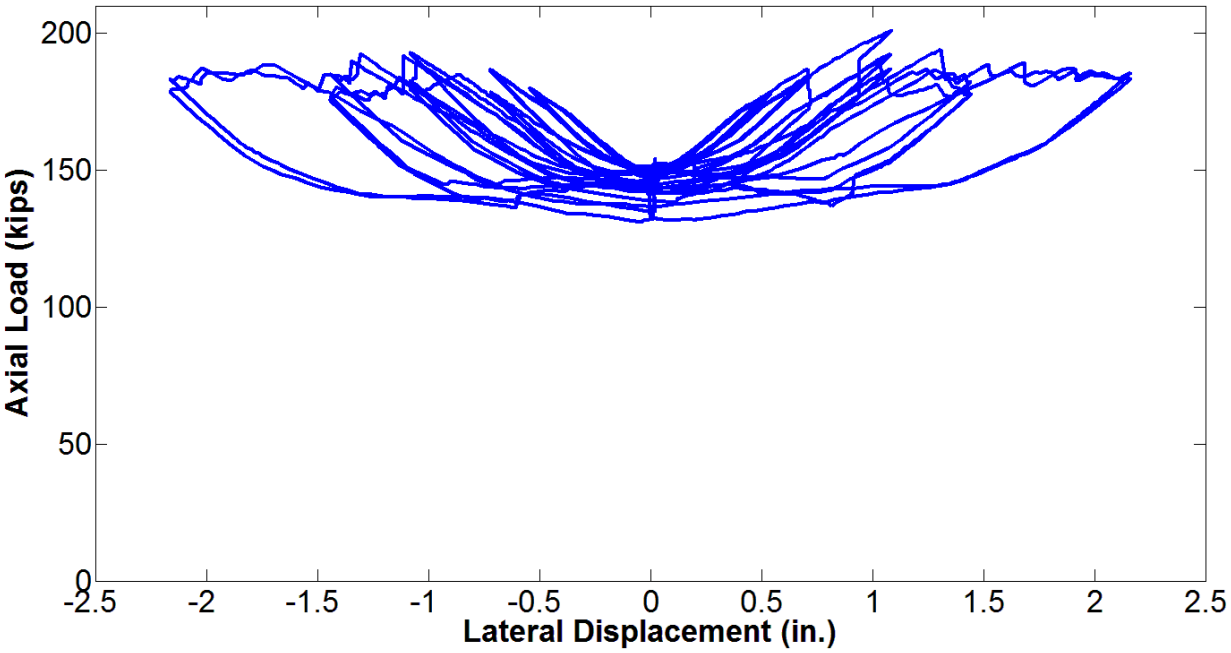

Figure B-8 RW-A15-P10-S51 (Test 3): Axial load versus lateral displacement relation

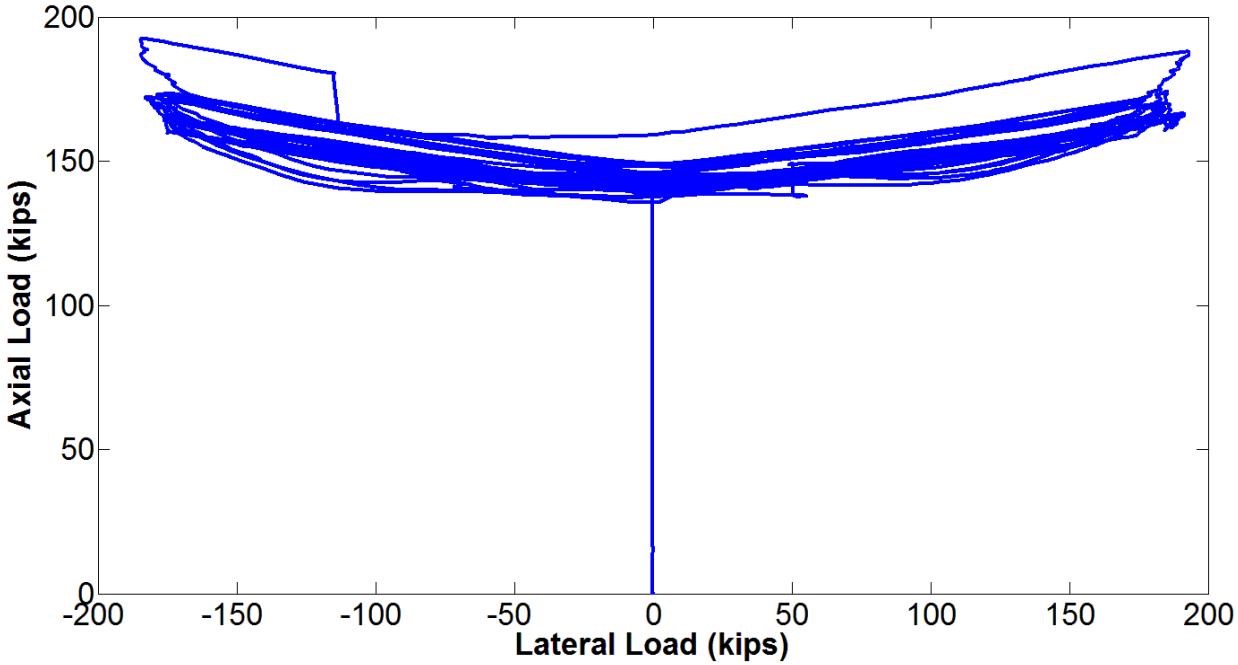

Figure B-9 RW-A15-P10-S78 (Test 4): Axial load versus lateral load relation

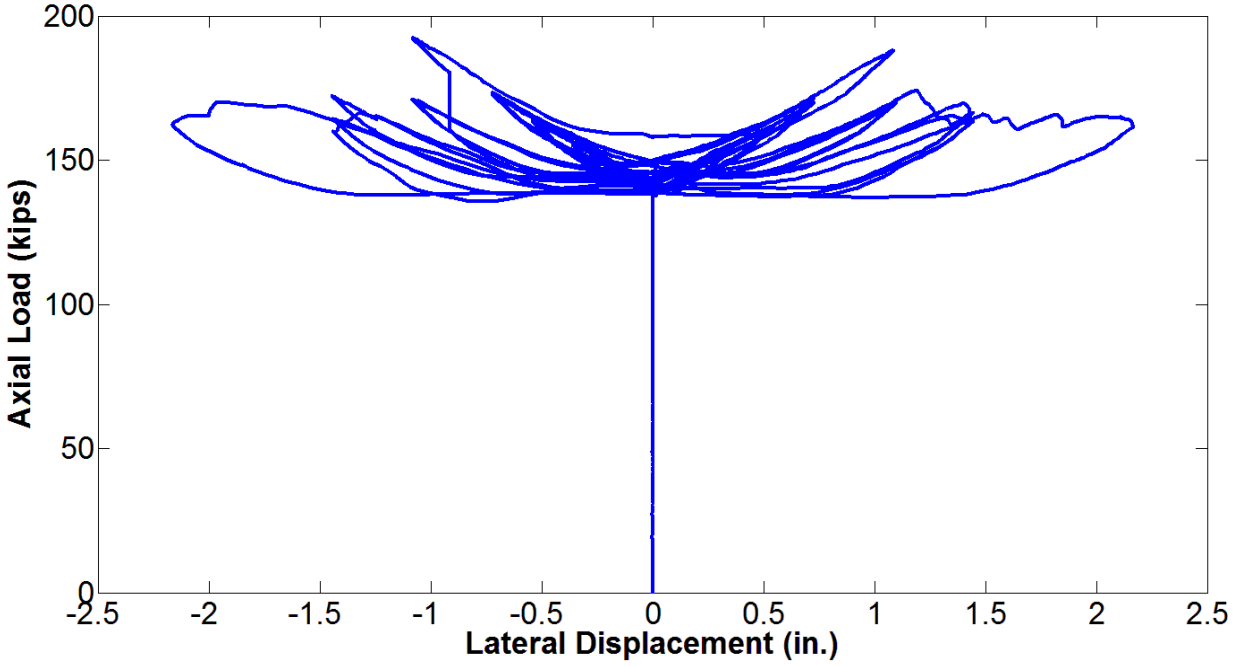

Figure B-10 RW-A15-P10-S78 (Test 4): Axial load versus lateral displacement relation

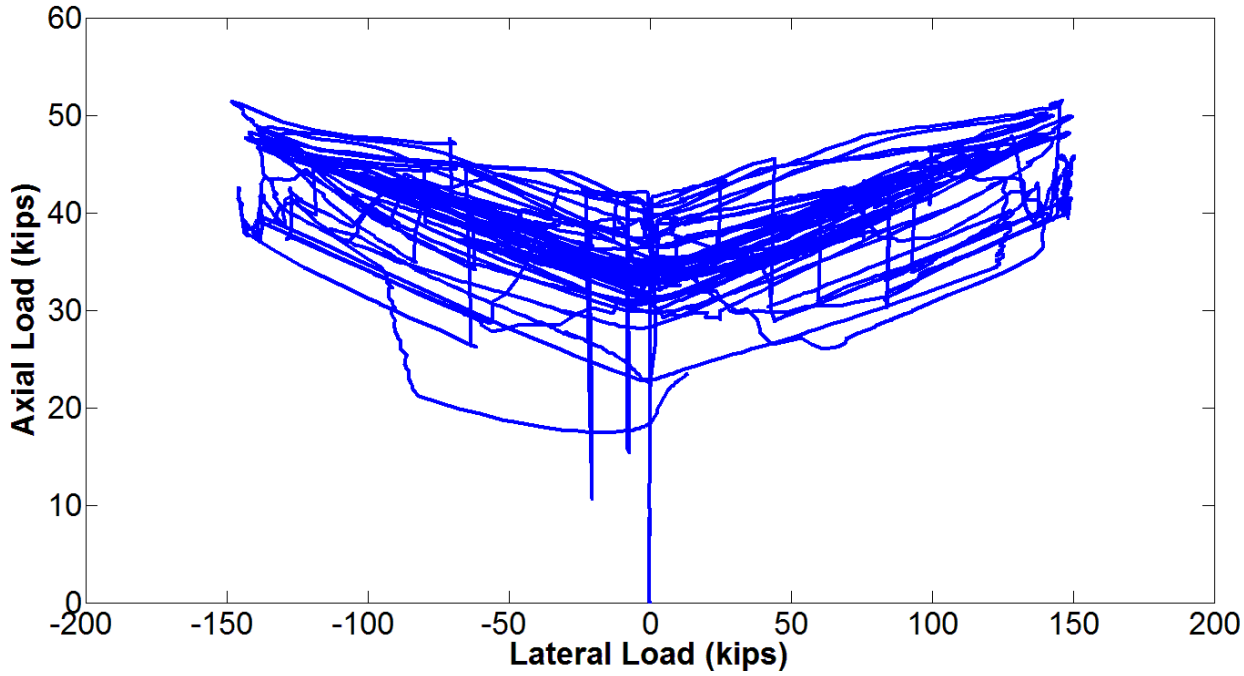

Figure B-11 RW-A15-P2.5-S64 (Test 5): Axial load versus lateral load relation

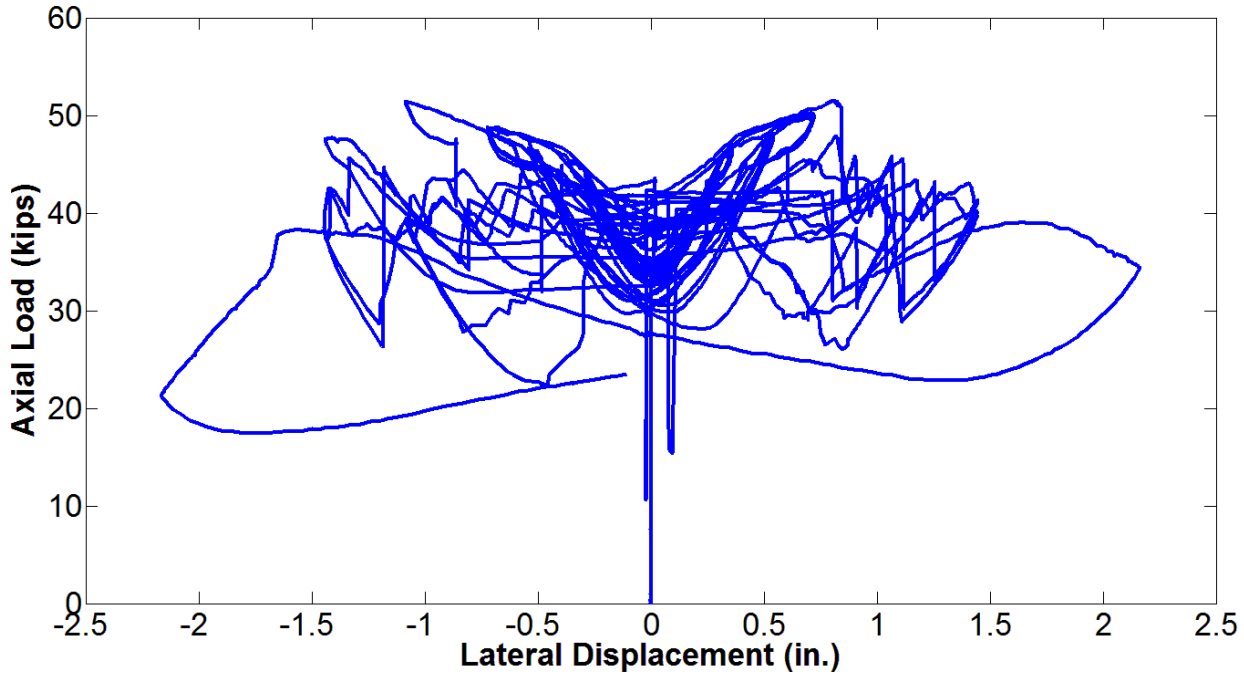

Figure B-12 RW-A15-P2.5-S64 (Test 5): Axial load versus lateral displacement relation

B.2 Reinforcing Steel Strain History

The reinforcing steel strain histories for all strain gauges installed in five wall specimens are shown in Figures B-13 through B-16 (specimen RW-A20-P10-S38, or Test 1), Figures B-17 to B-20 (specimen RW-A20-P10-S63, or Test 2), Figures B-21 to B-24 (specimen RW-A15-P10-S51, or Test 3), Figures B-25 to B-28 (specimen RW-A15-P10-S78, or Test 4), and Figures B-29 to B-32 (specimen RW-A15-P2.5-S64, or Test 5). The plots are grouped in terms of strain gauges affixed on boundary longitudinal reinforcement, web vertical reinforcement, web horizontal reinforcement, and boundary transverse reinforcement.

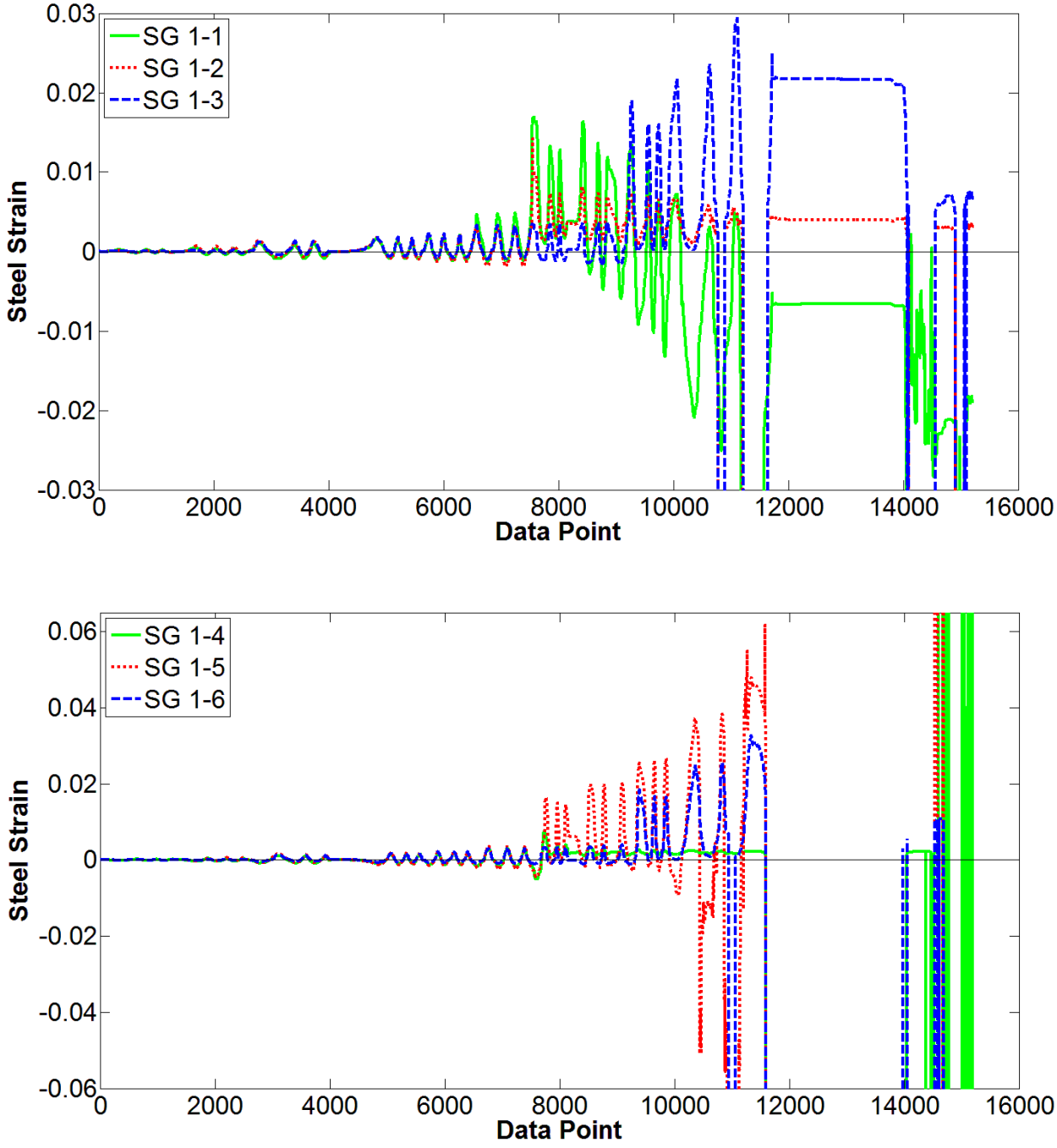

Figure B-13 RW-A20-P10-S38: Strain gage histories at boundary longitudinal reinforcement

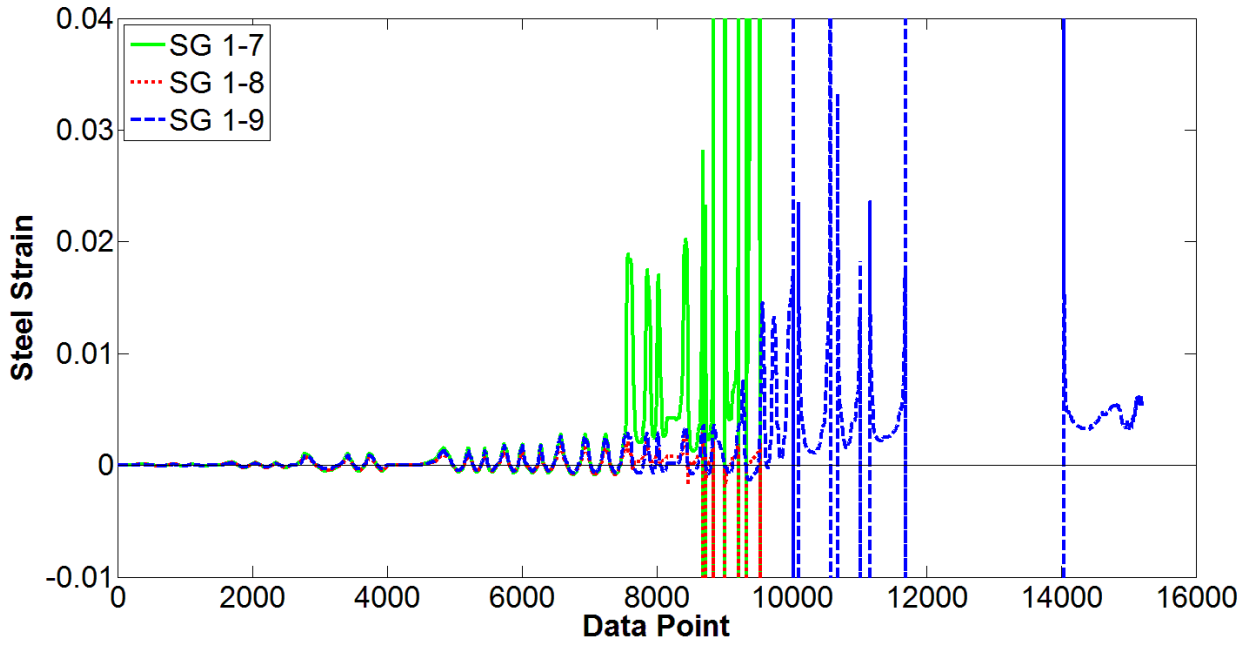

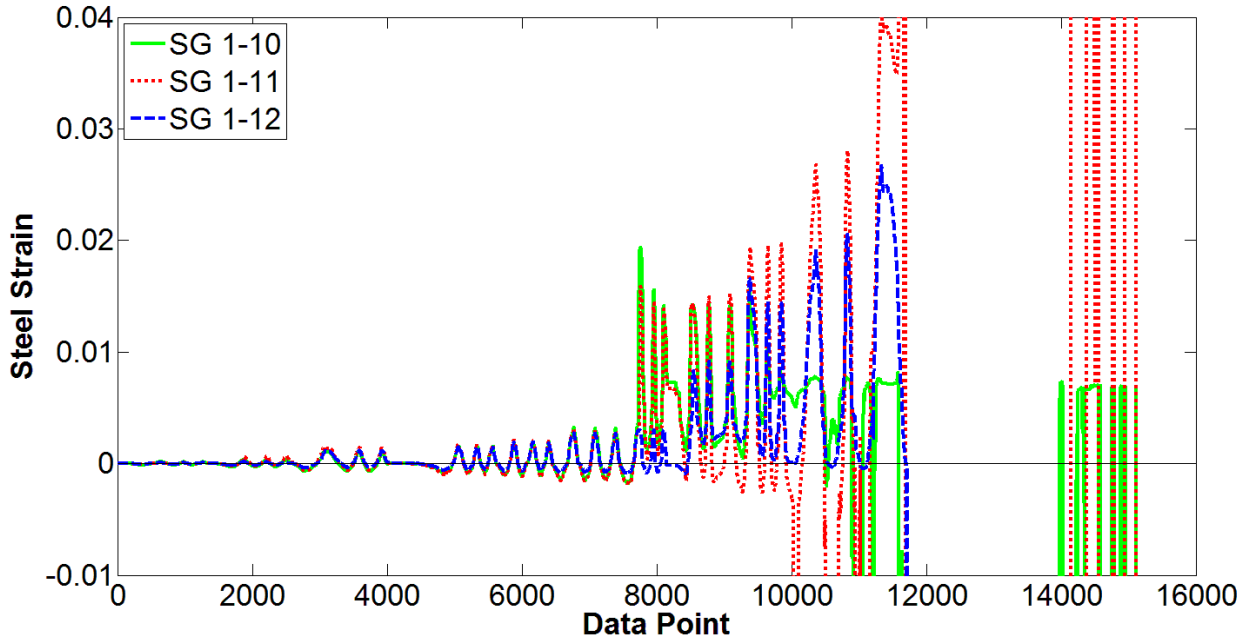

Figure B.13 (cont.)

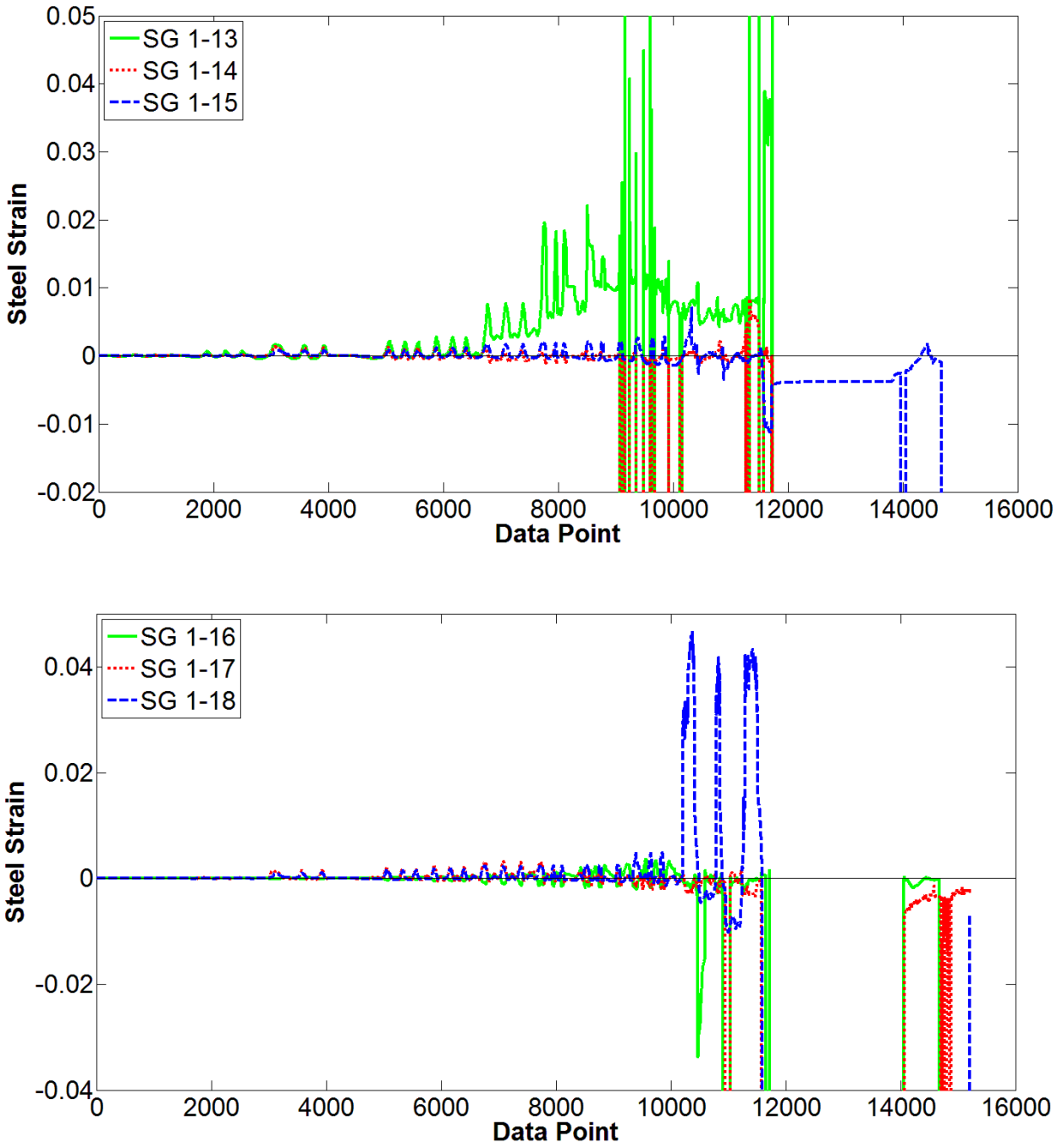

Figure B-14 RW-A20-P10-S38: Strain gage histories at web vertical reinforcement

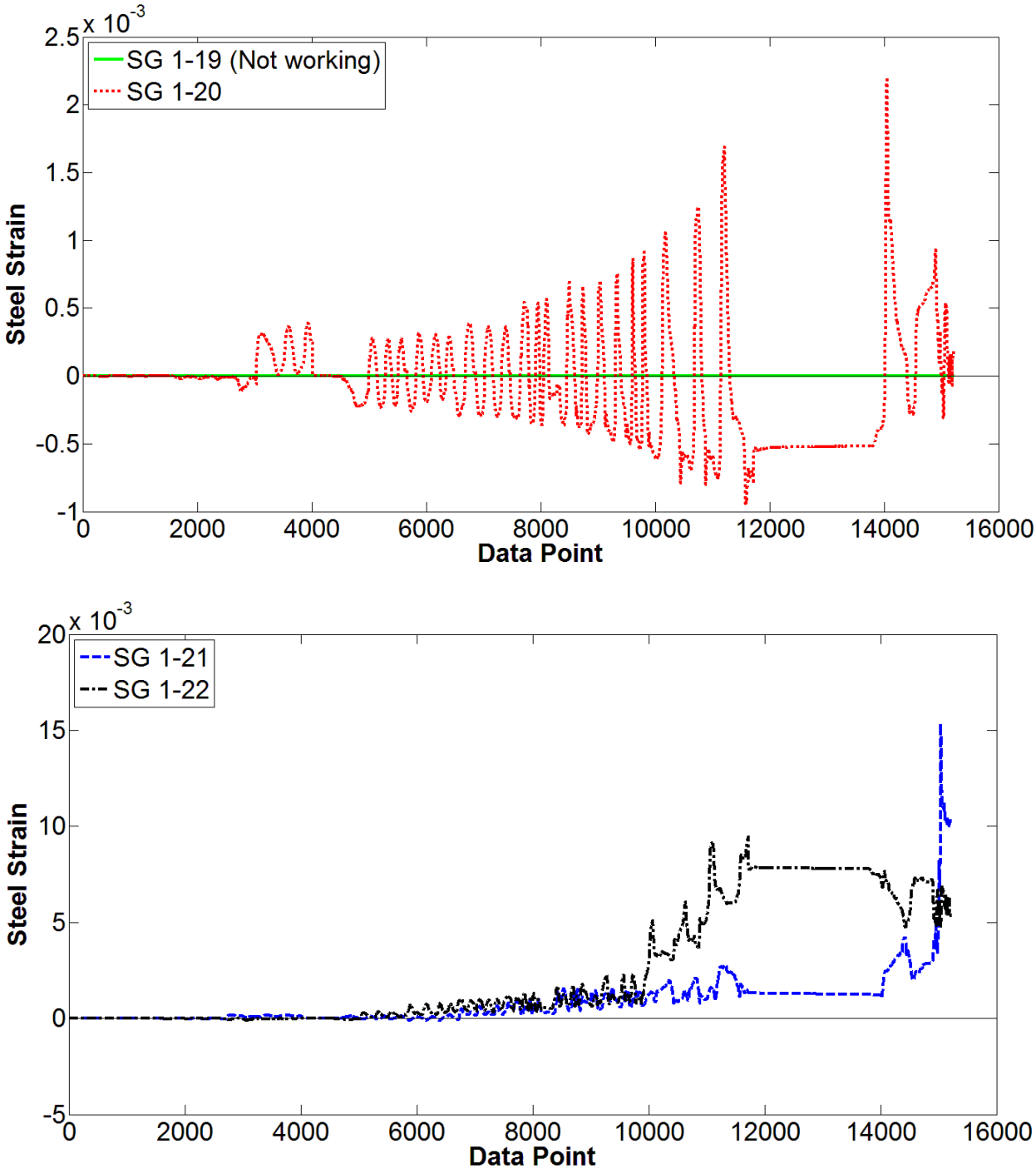

Figure B-15 RW-A20-P10-S38: Strain gage histories at web horizontal reinforcement

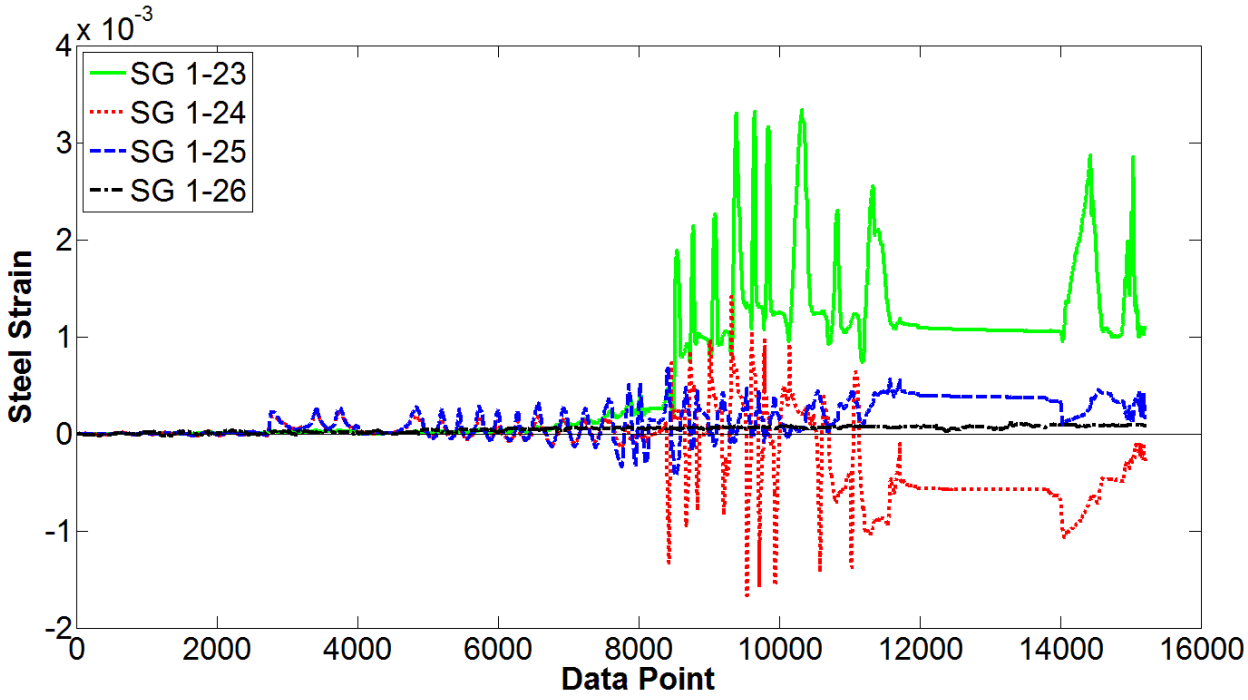

Figure B-16 RW-A20-P10-S38: Strain gage histories at boundary transverse reinforcement

Notes: SG 1-27, SG 1-28, SG 1-29, and SG 1-30 were not working.

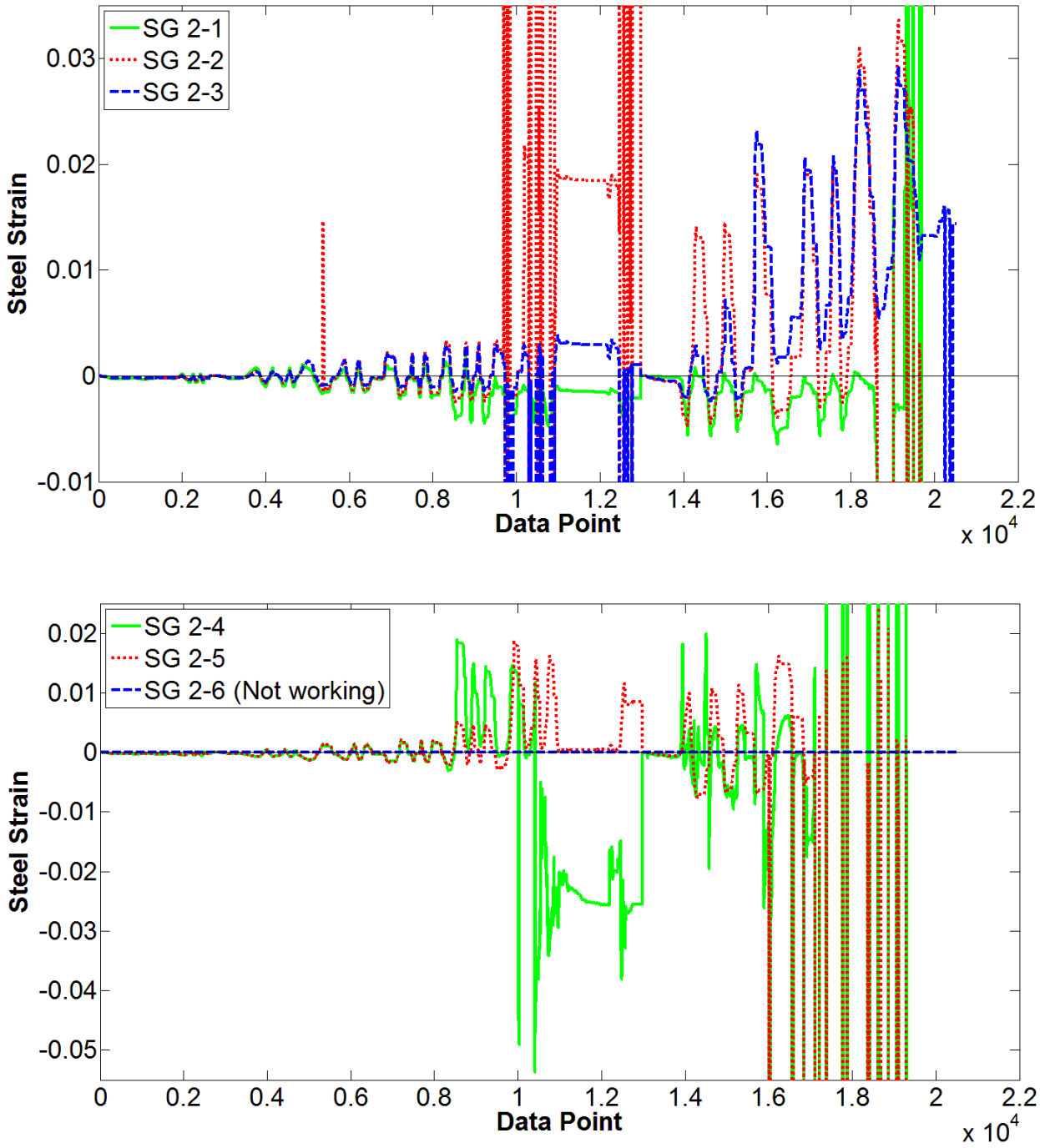

Figure B-17 RW-A20-P10-S63: Strain gage histories at boundary longitudinal reinforcement

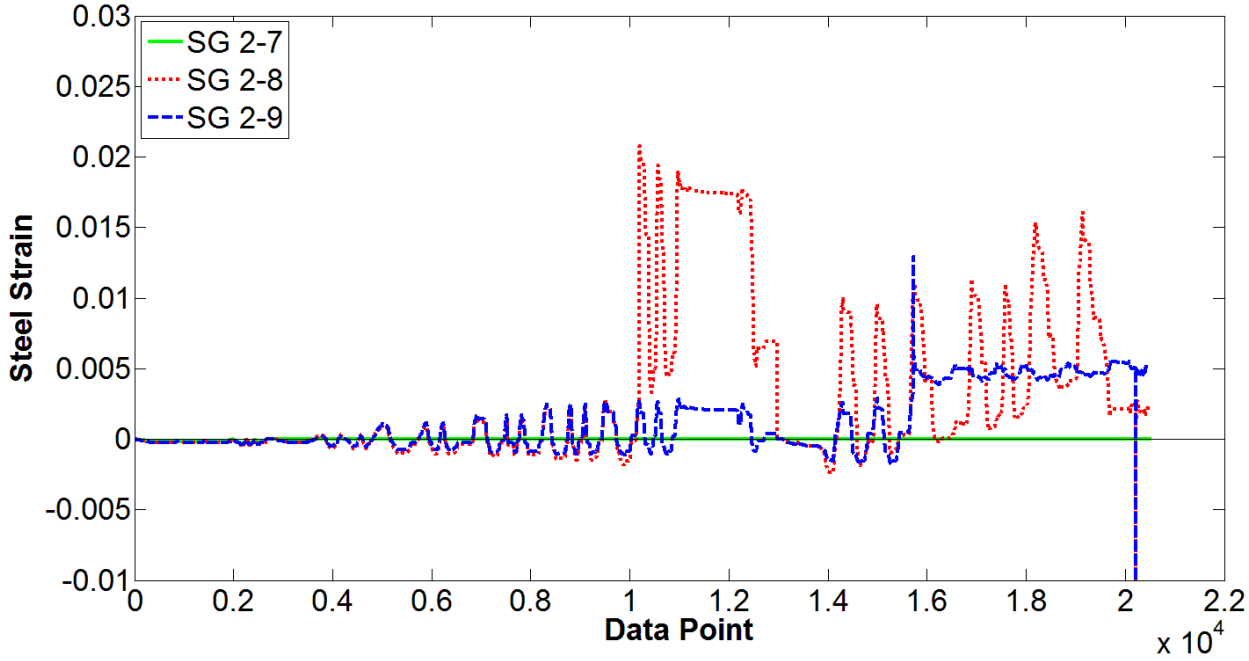

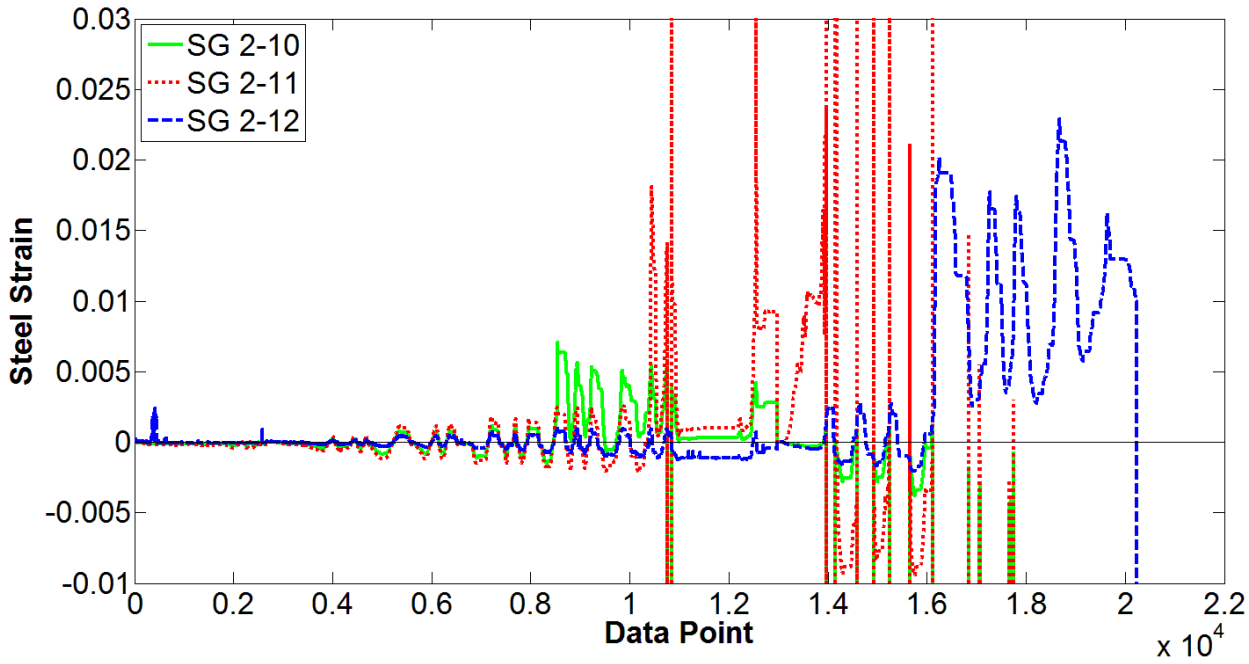

Figure B.17 (cont.)

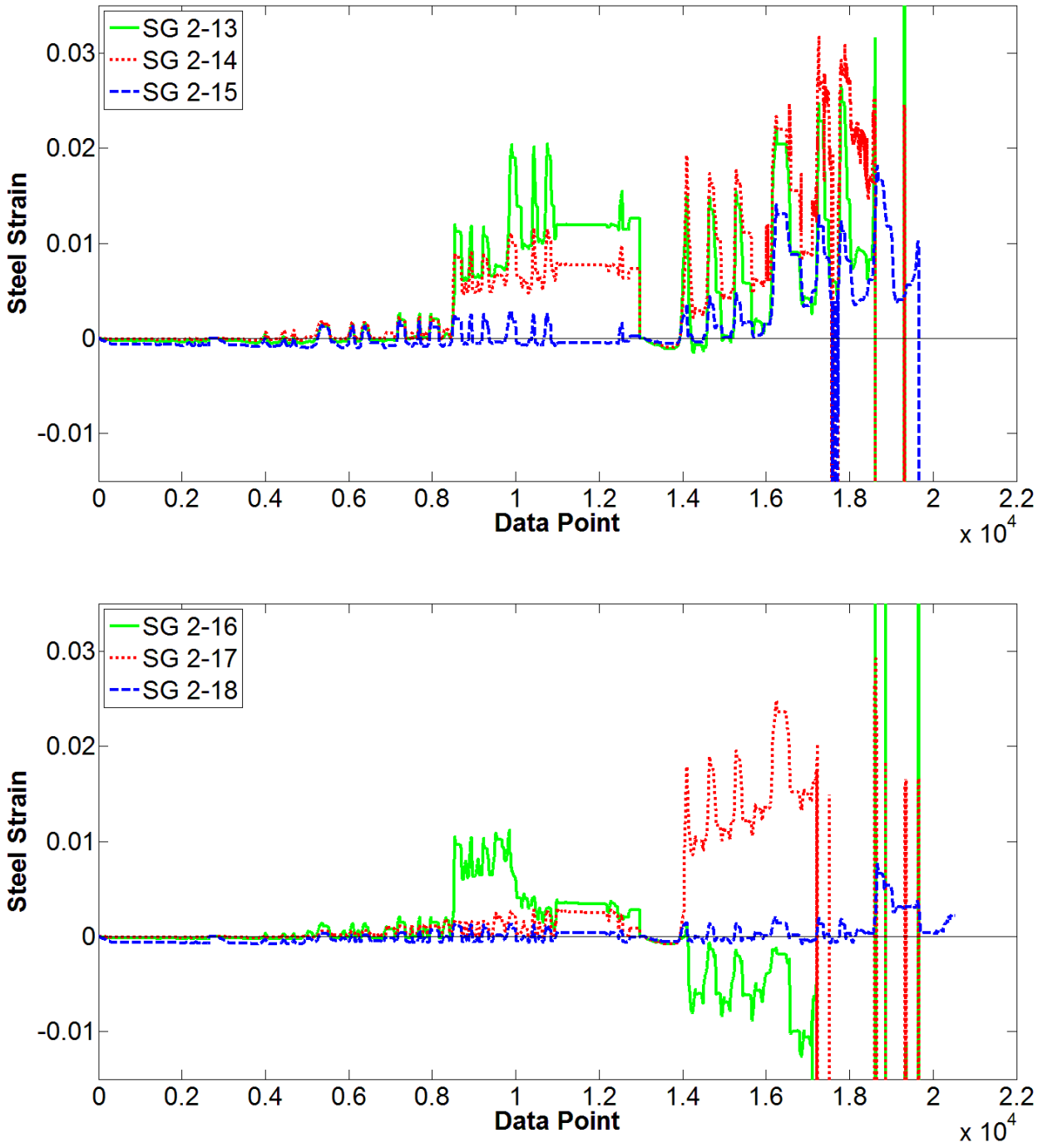

Figure B-18 RW-A20-P10-S63: Strain gage histories at web vertical reinforcement

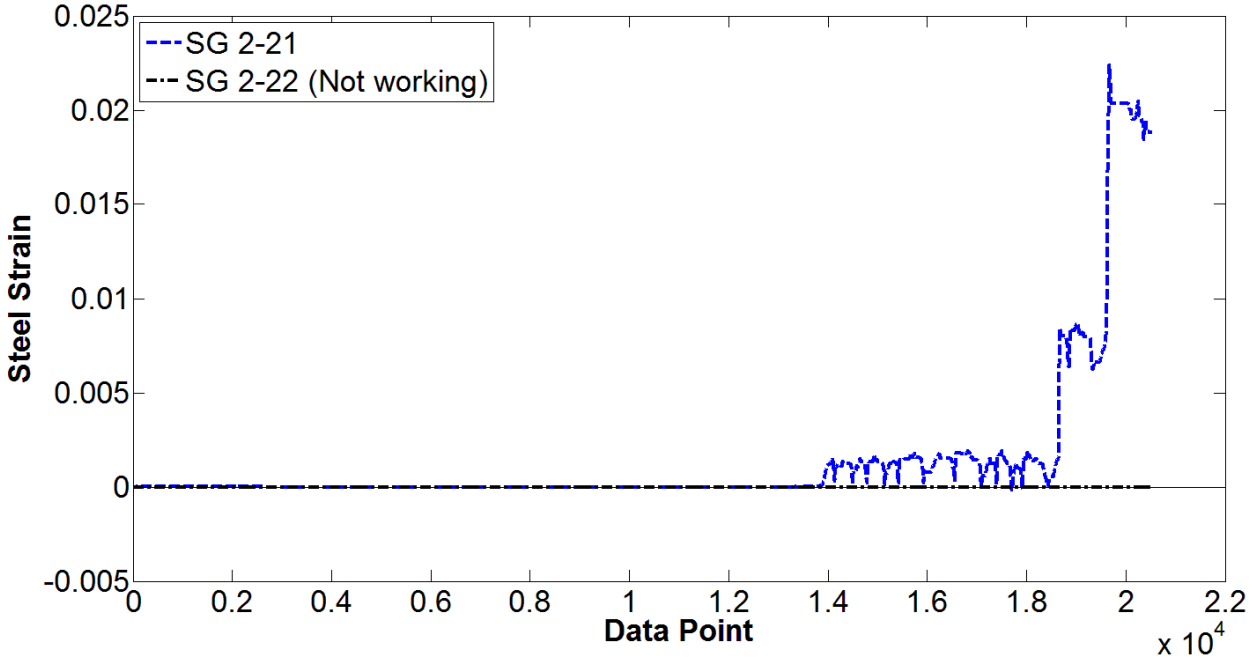

Figure B-19 RW-A20-P10-S63: Strain gage histories at horizontal web reinforcement

Notes: SG 2-19 and SG 2-20 were not working.

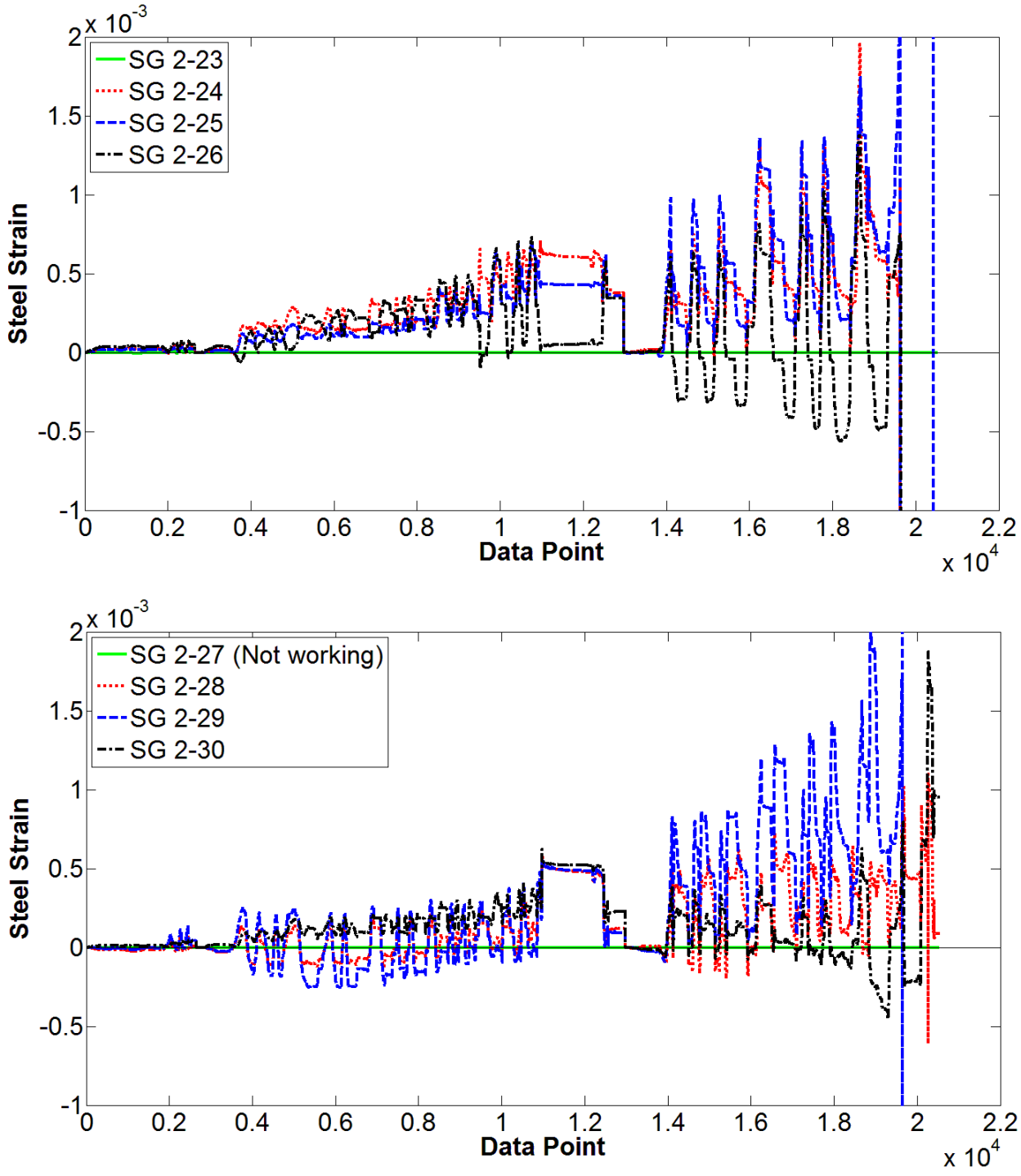

Figure B-20 RW-A20-P10-S63: Strain gage histories at boundary transverse reinforcement

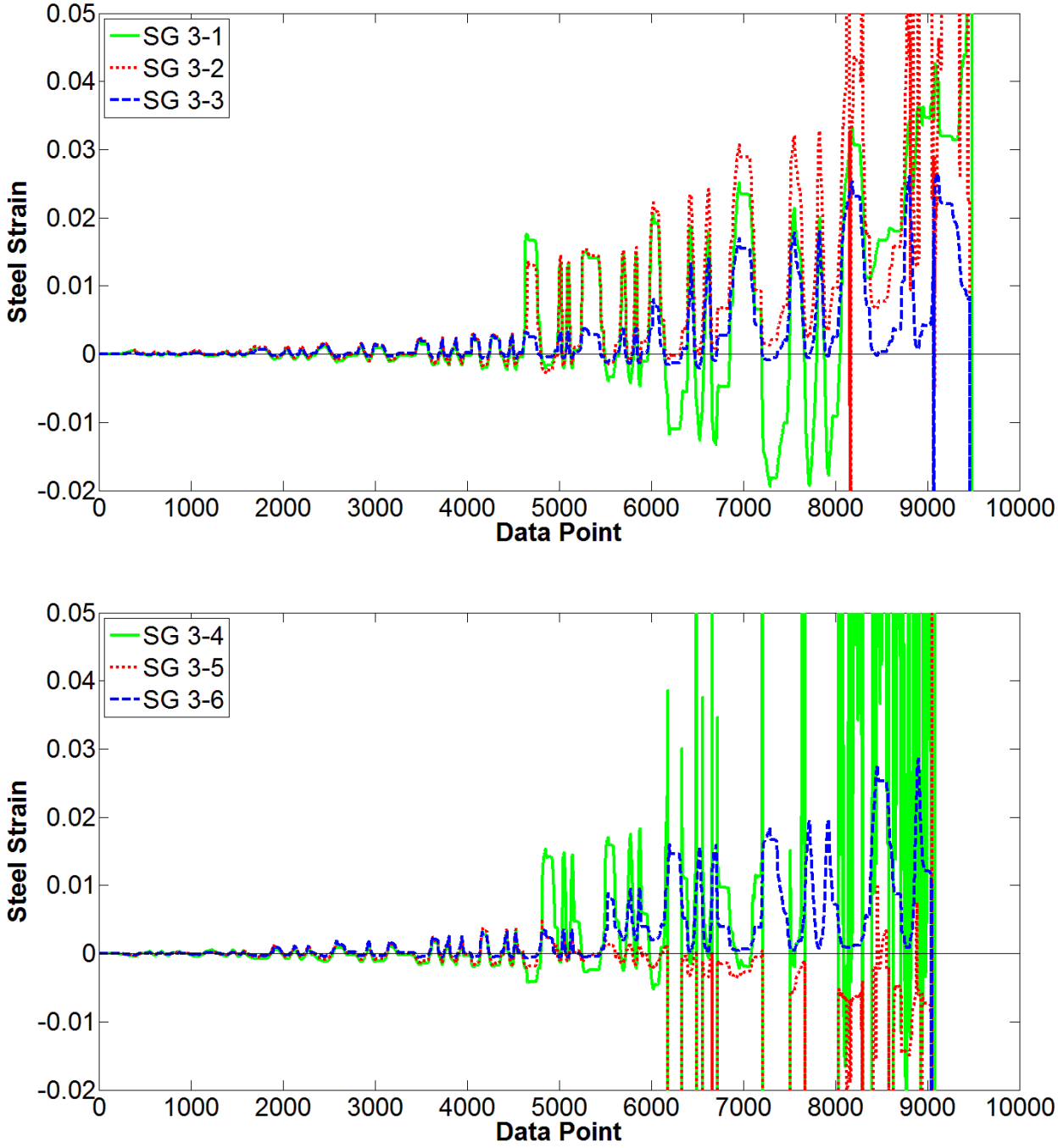

Figure B-21 RW-A15-P10-S51: Strain gage histories at boundary longitudinal reinforcement

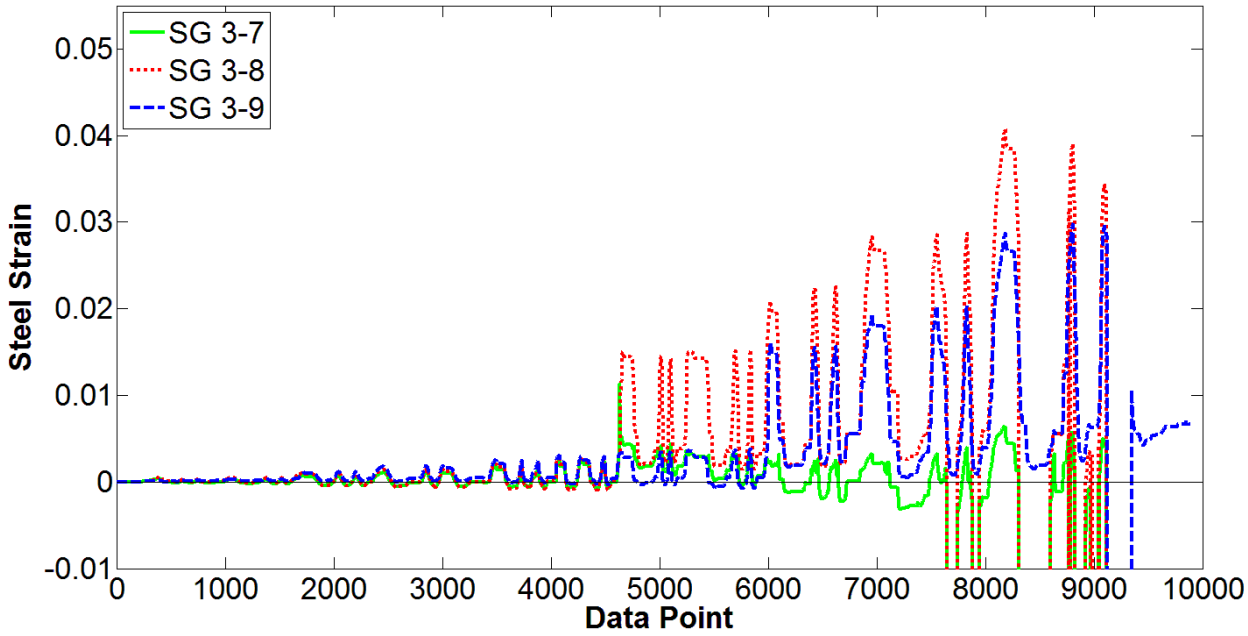

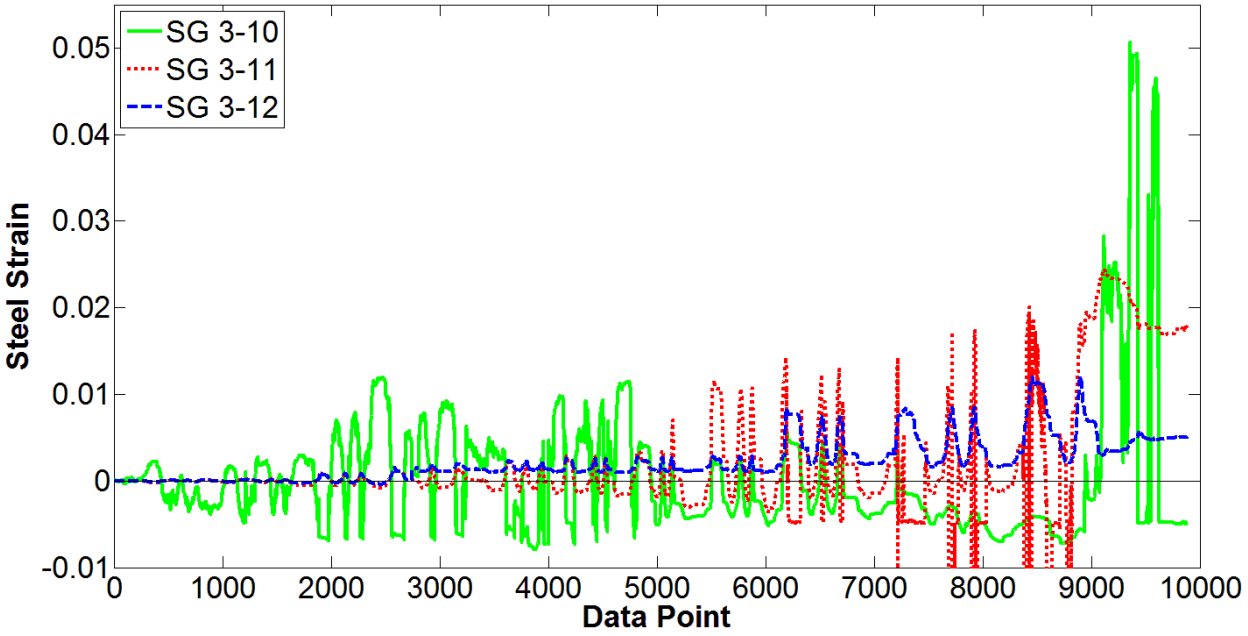

Figure B.21 (cont.)

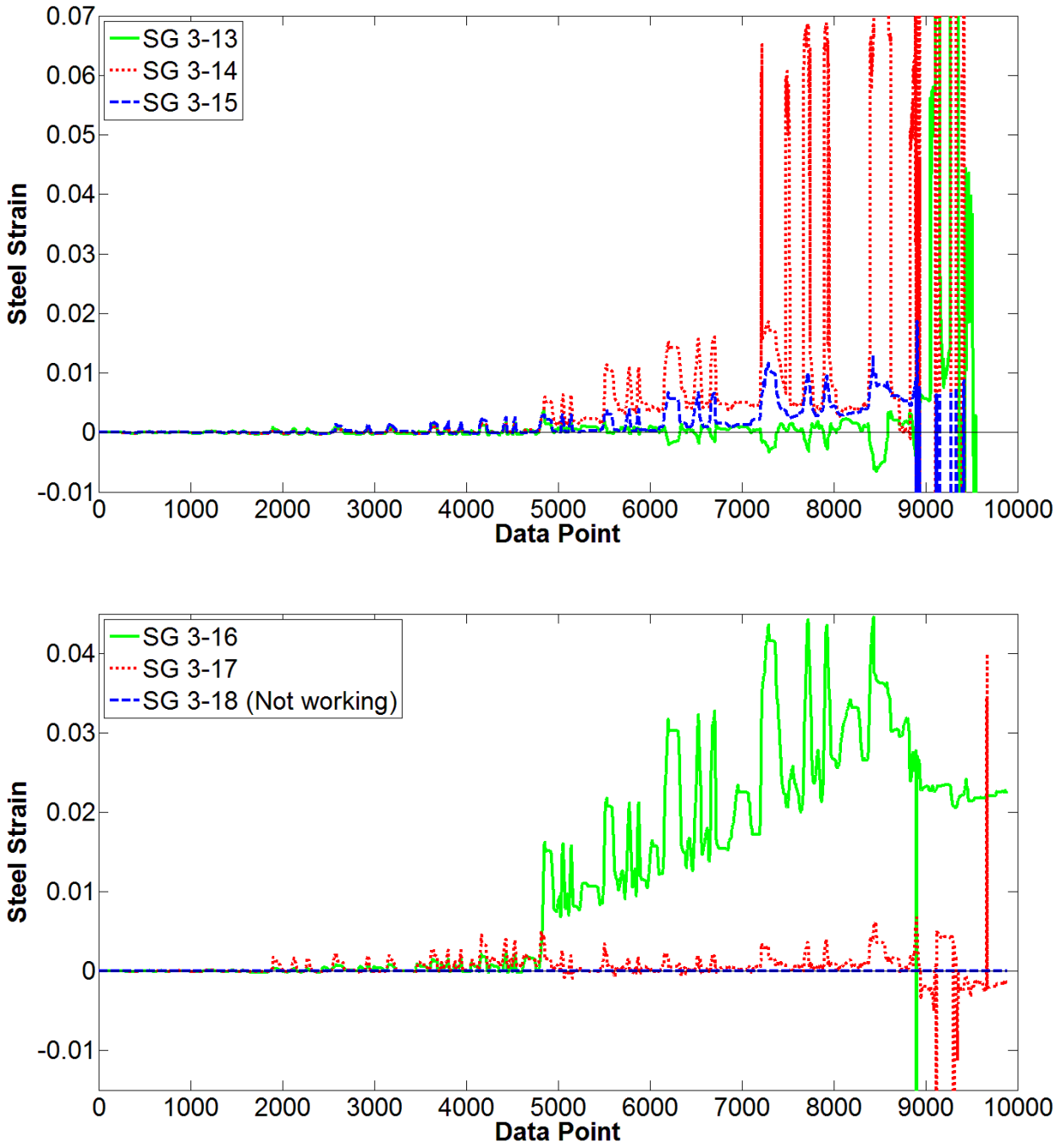

Figure B-22 RW-A15-P10-S51: Strain gage histories at web vertical reinforcement

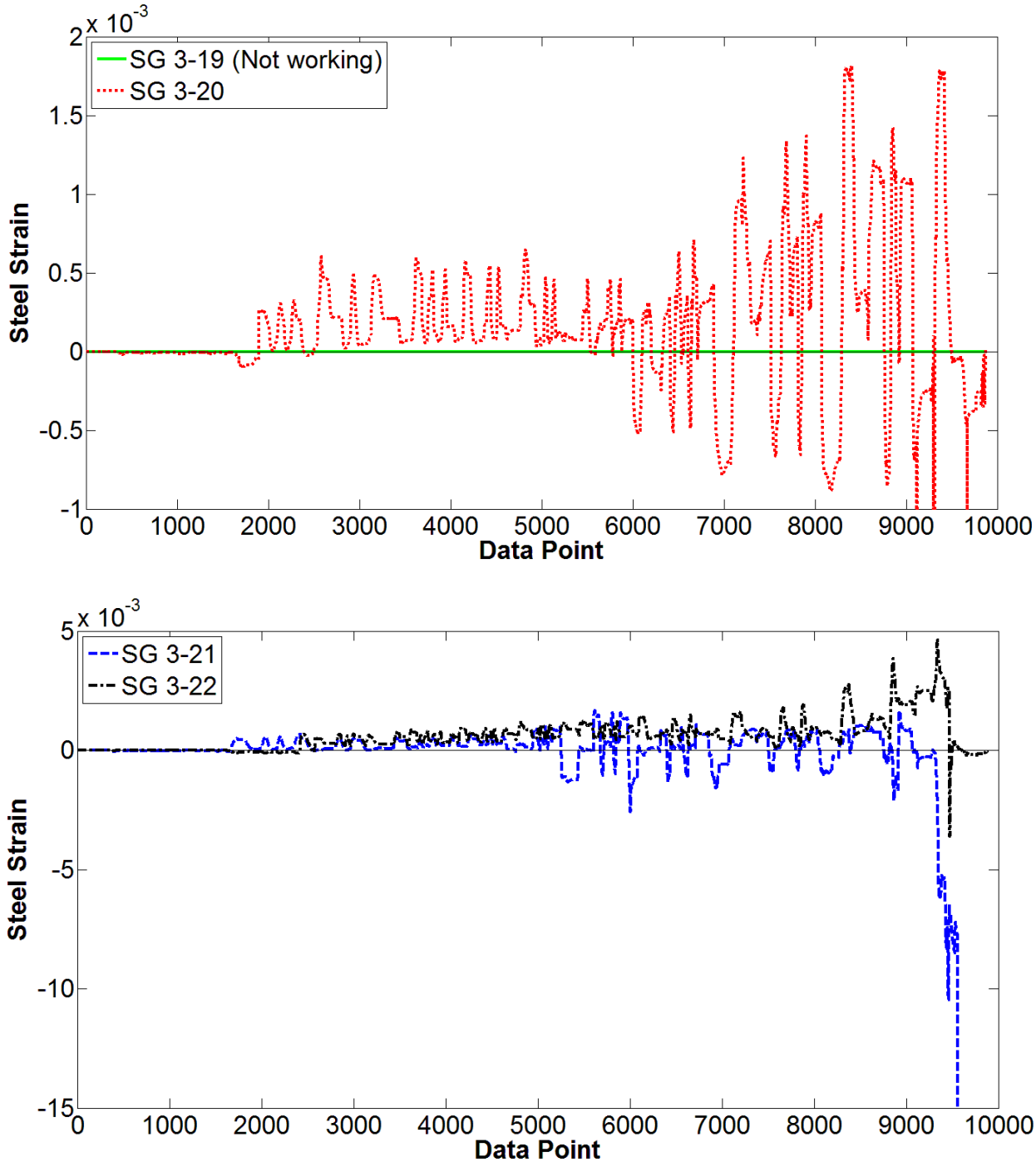

Figure B-23 RW-A15-P10-S51: Strain gage histories at web horizontal reinforcement

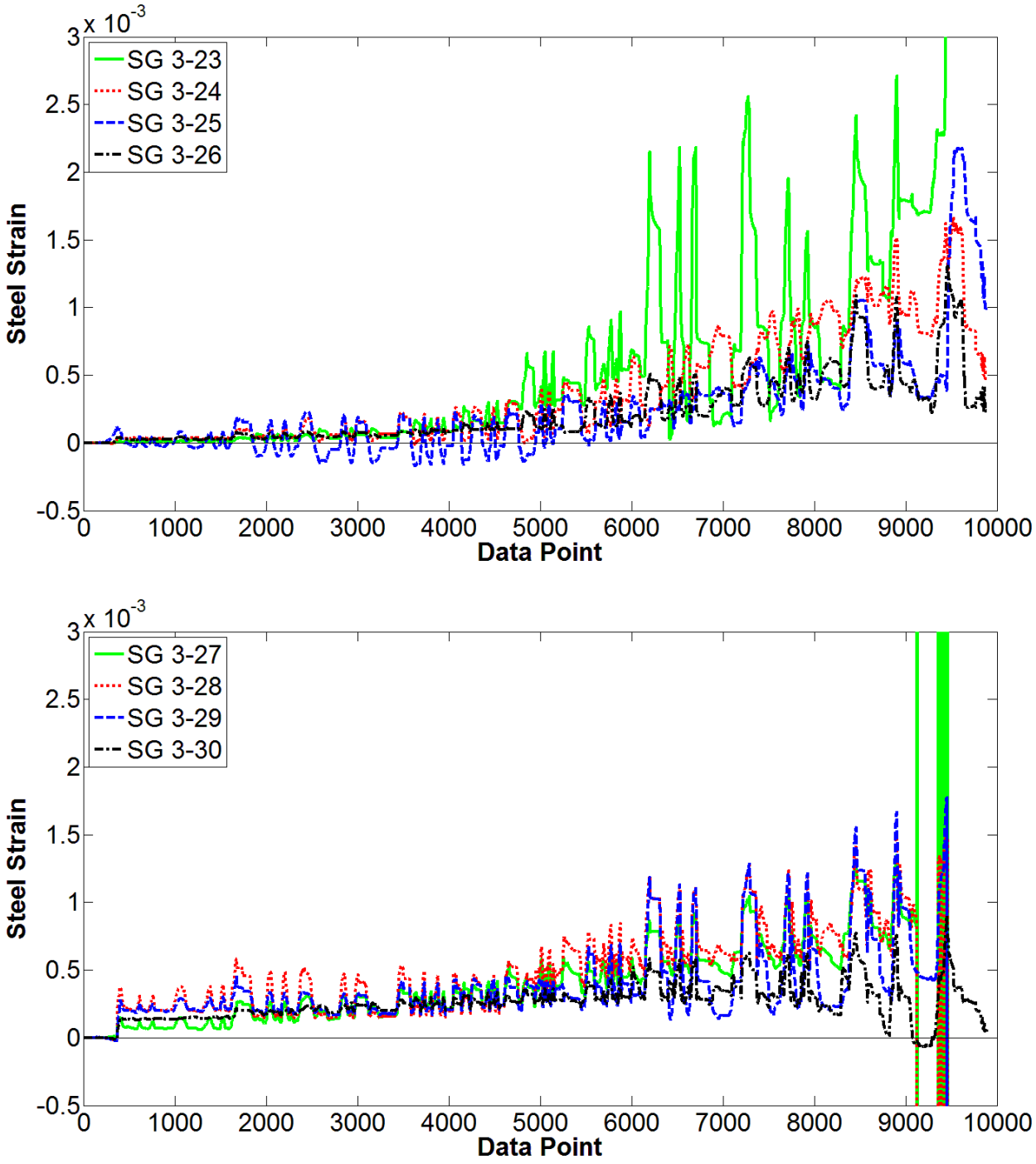

Figure B-24 RW-A15-P10-S51: Strain gage histories at boundary transverse reinforcement

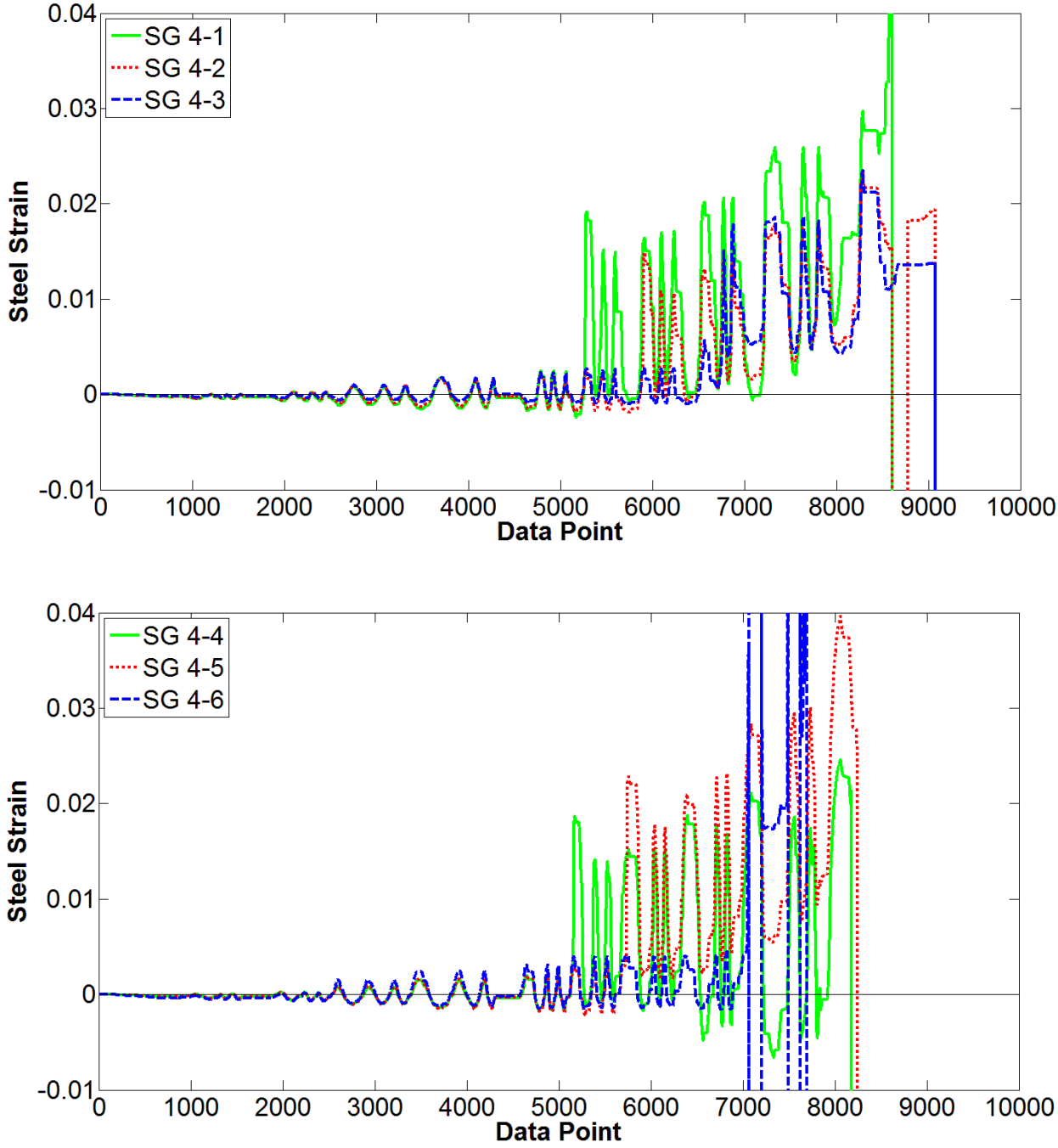

Figure B-25 RW-A15-P10-S78: Strain gage histories at boundary longitudinal reinforcement

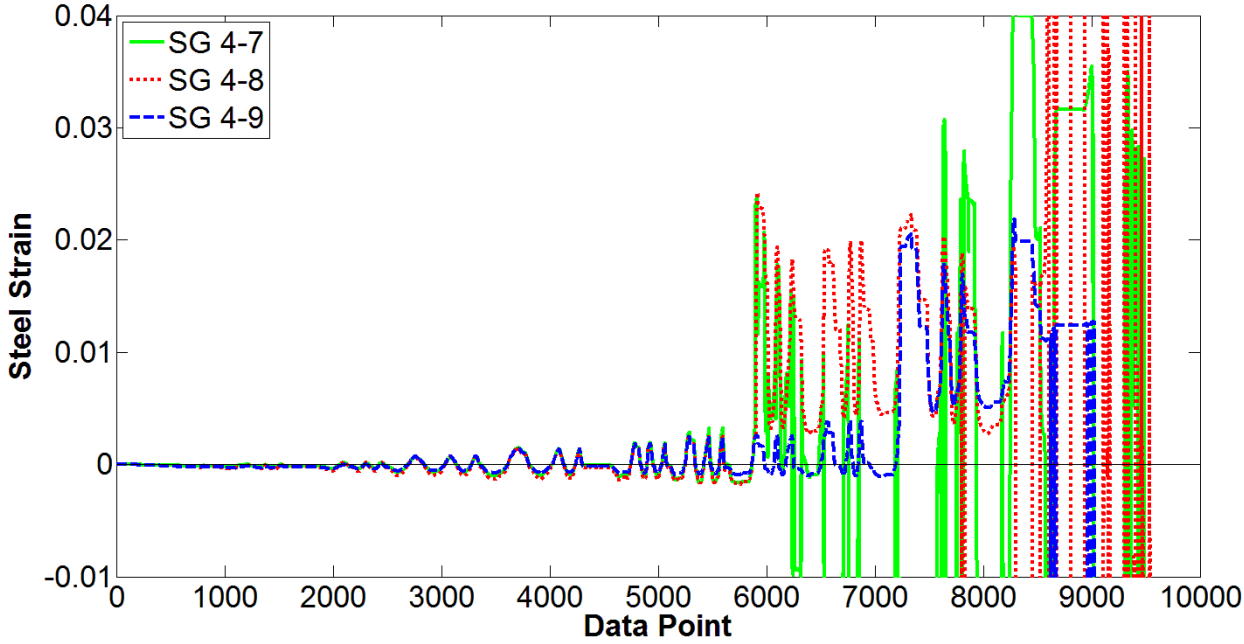

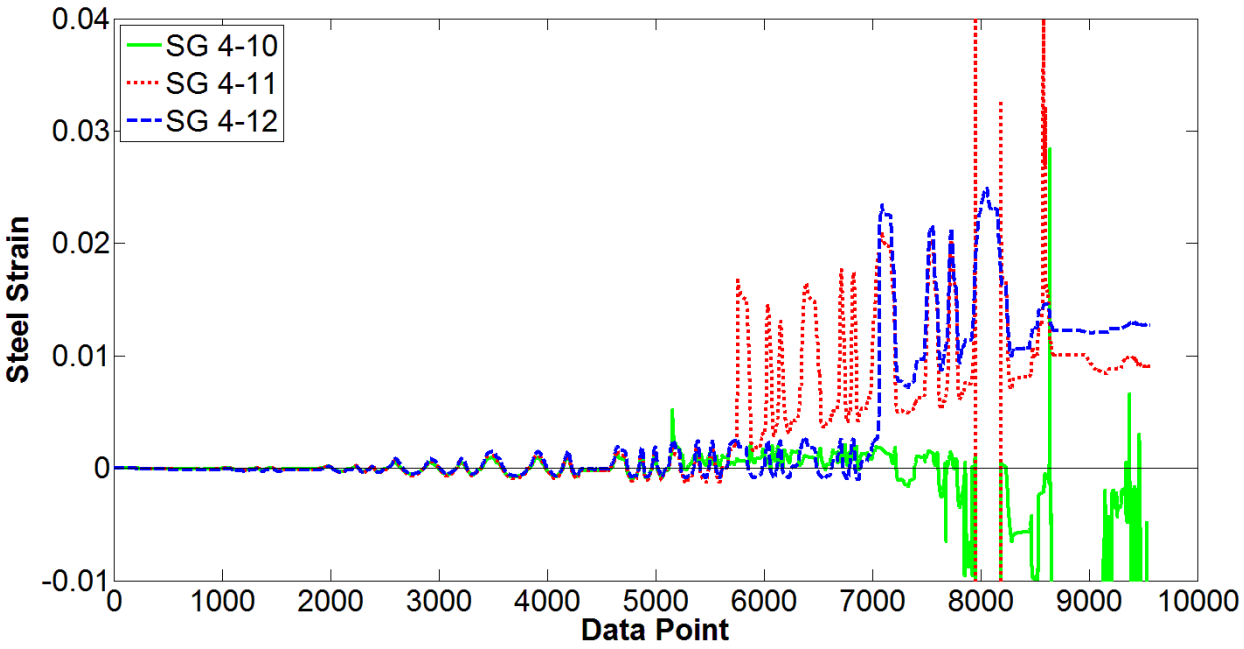

Figure B.25 (cont.)

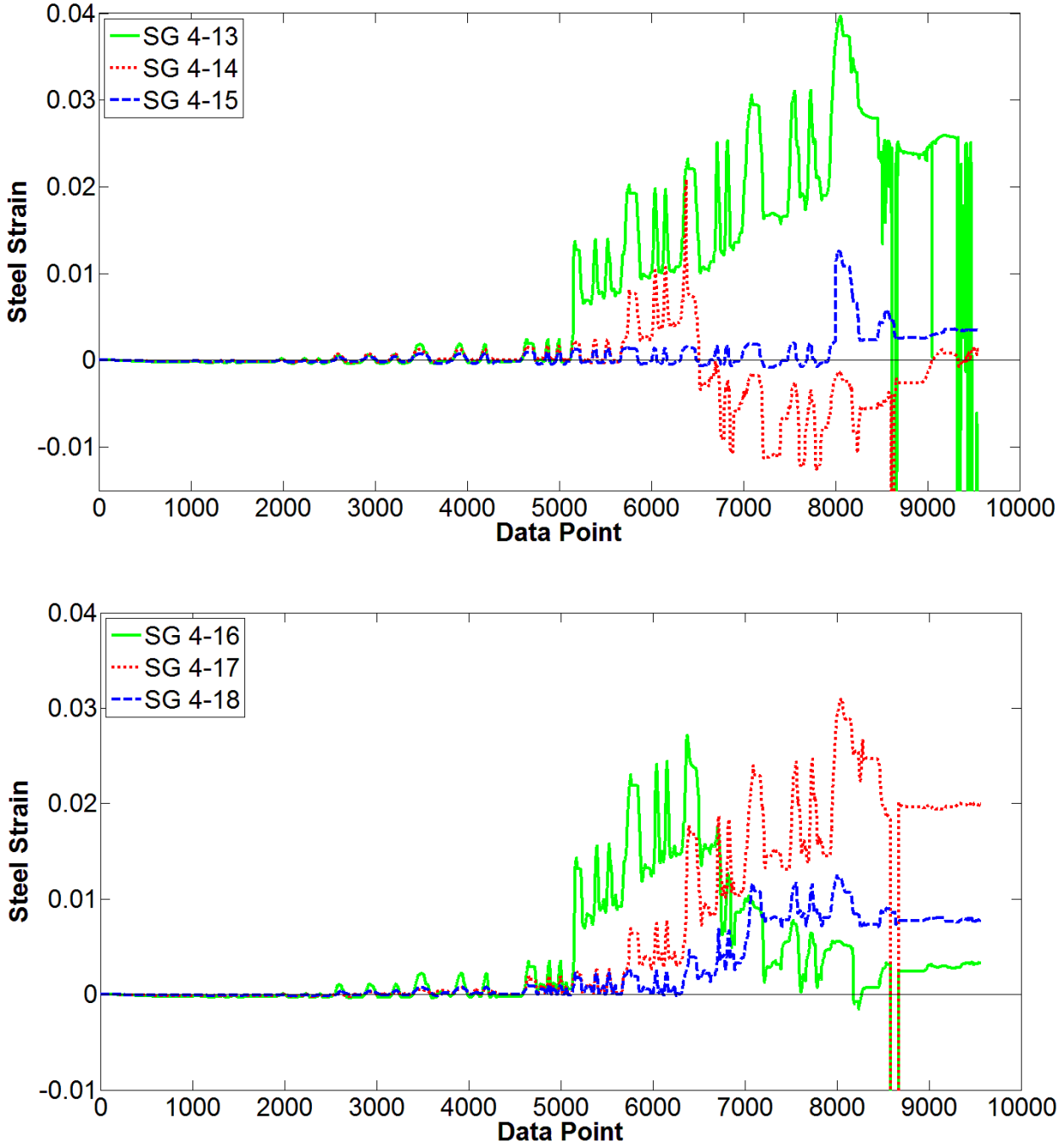

Figure B-26 RW-A15-P10-S78: Strain gage histories at web vertical reinforcement

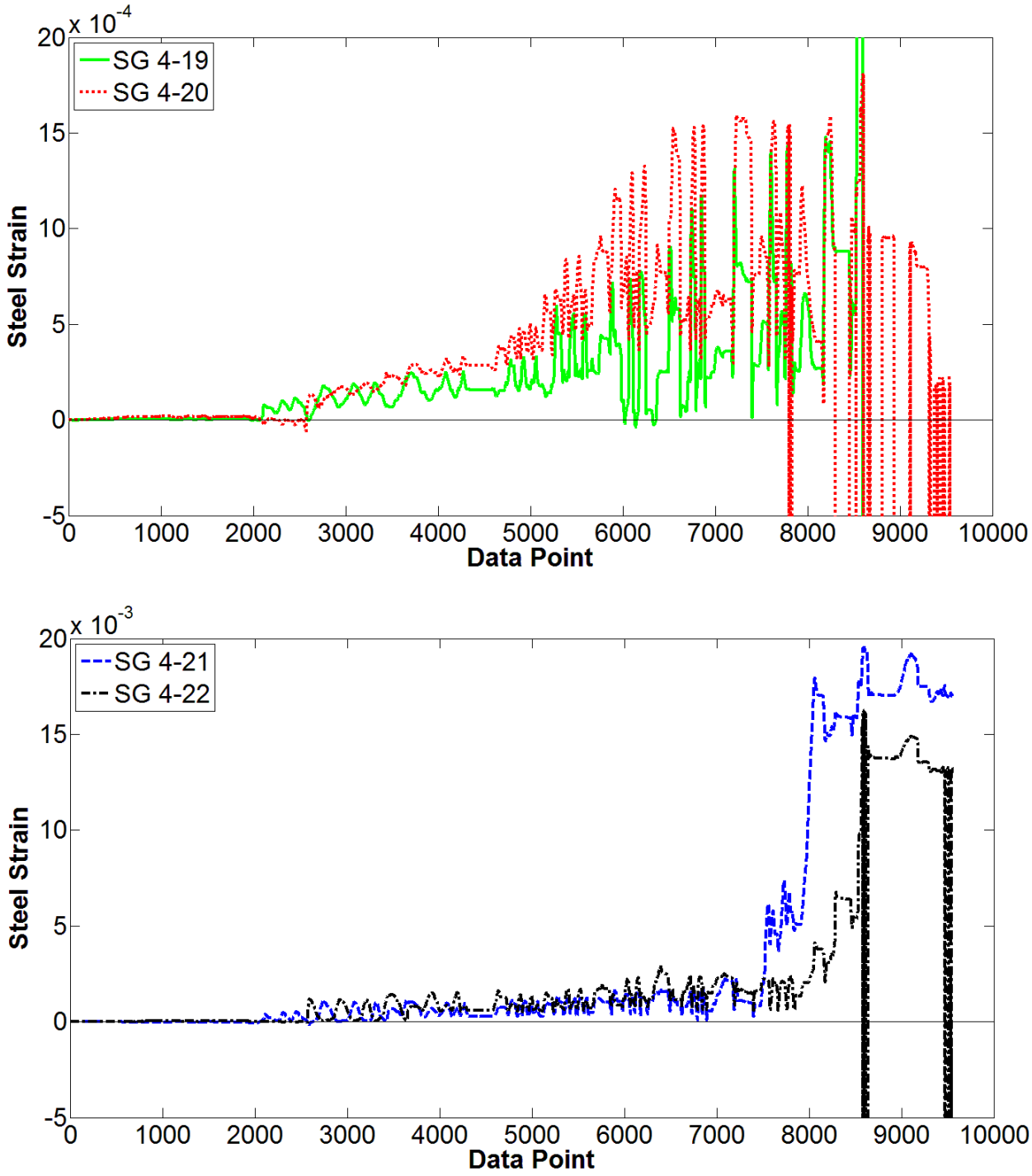

Figure B-27 RW-A15-P10-S78: Strain gage histories at web horizontal reinforcement

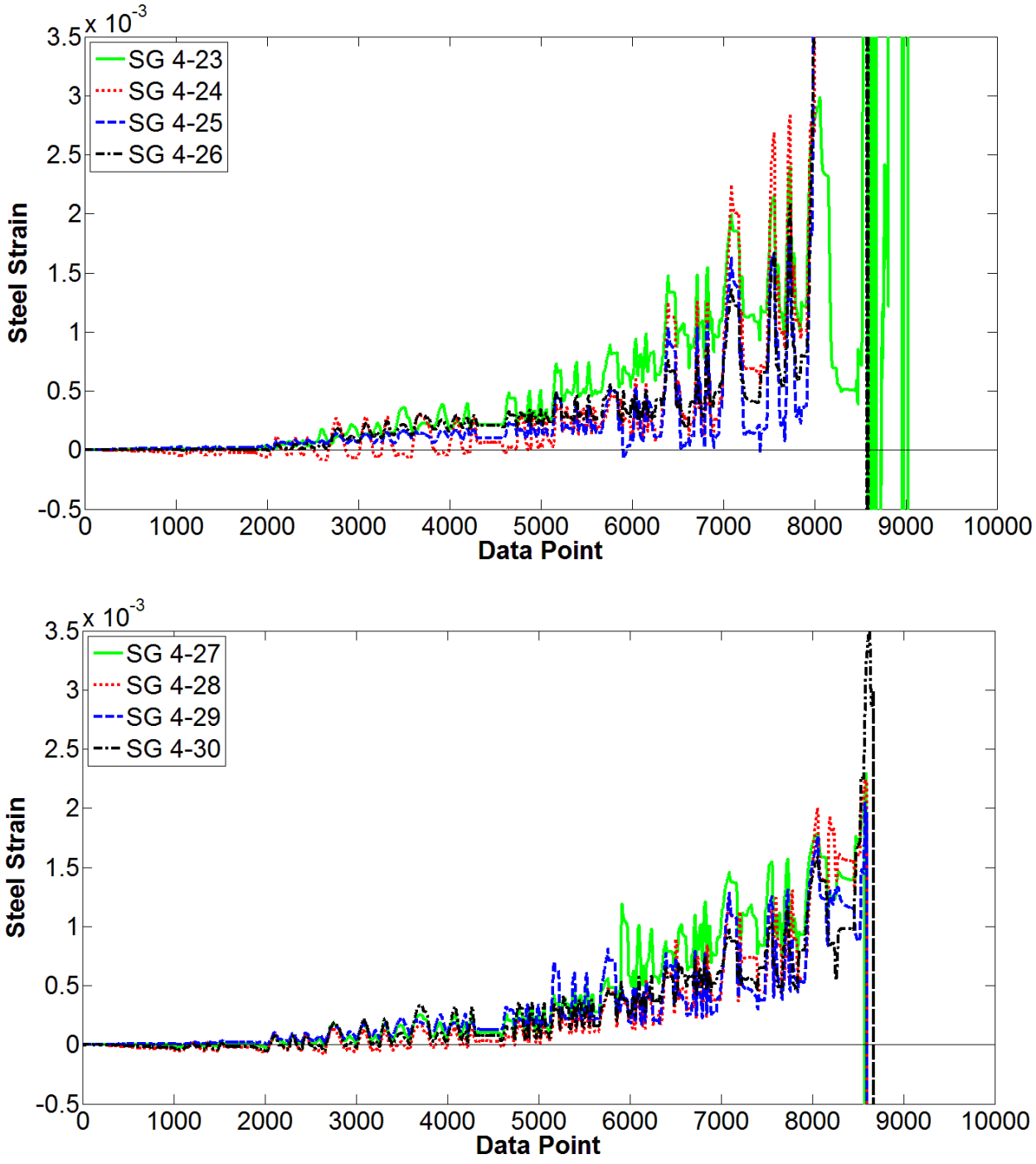

Figure B-28 RW-A15-P10-S78: Strain gage histories at boundary transverse reinforcement

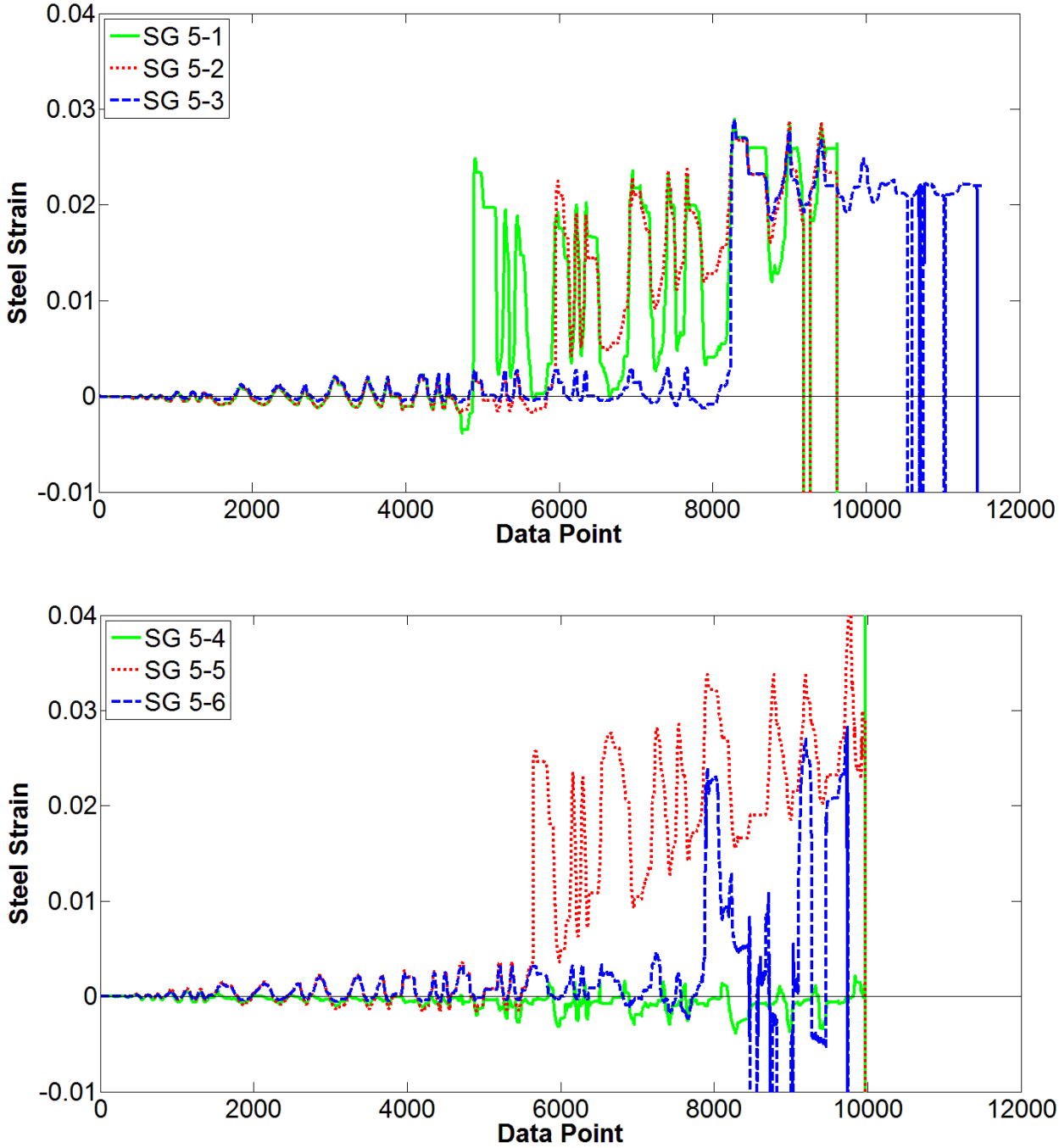

Figure B-29 RW-A15-P2.5-S64: Strain gage histories at boundary longitudinal reinforcement

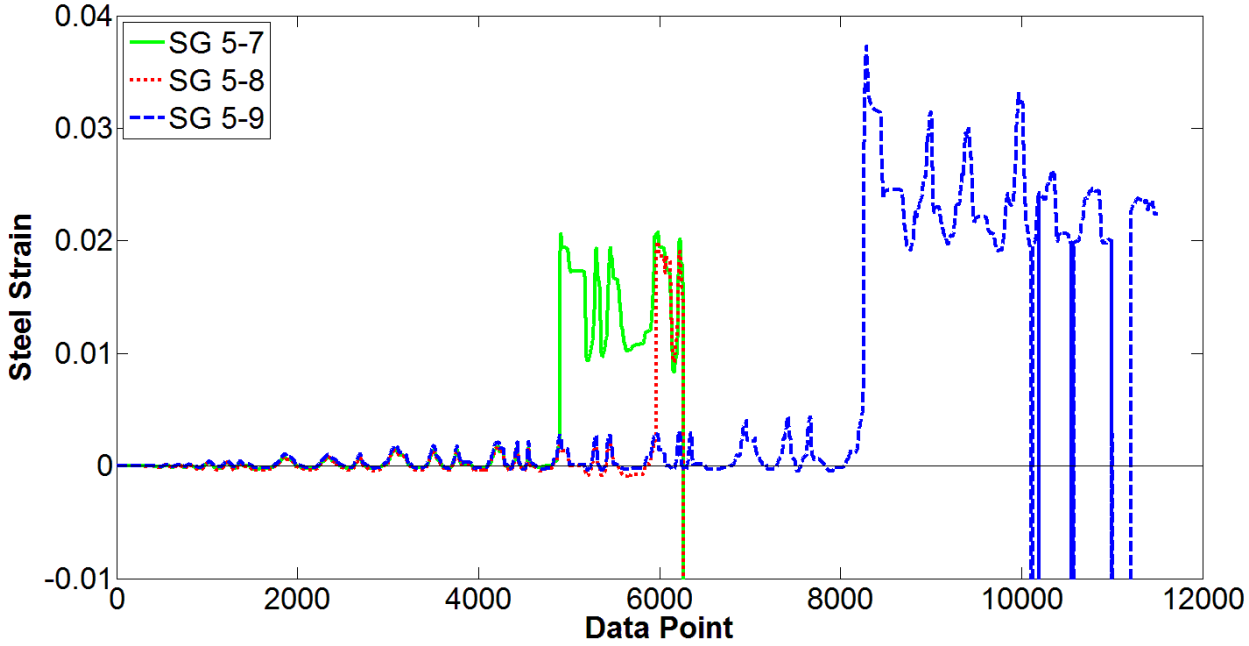

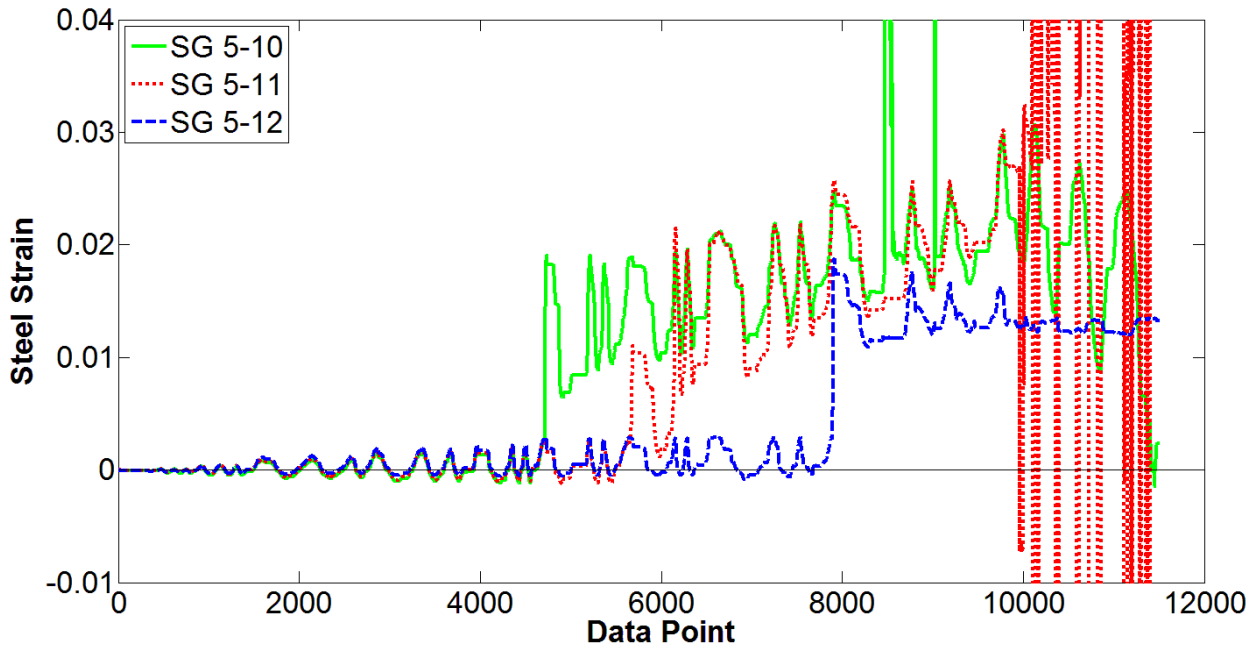

Figure B.29 (cont.)

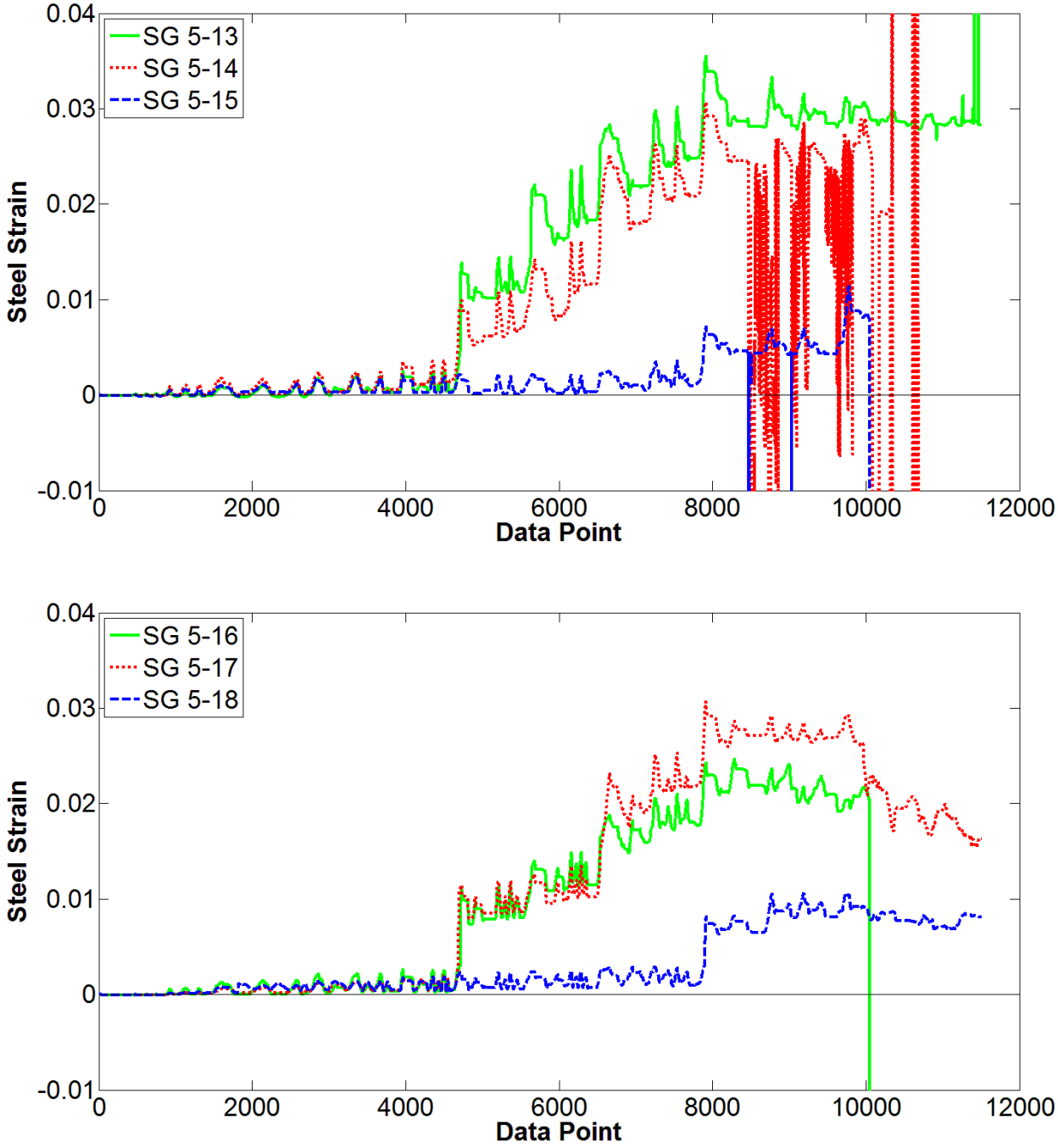

Figure B-30 RW-A15-P2.5-S64: Strain gage histories at web vertical reinforcement

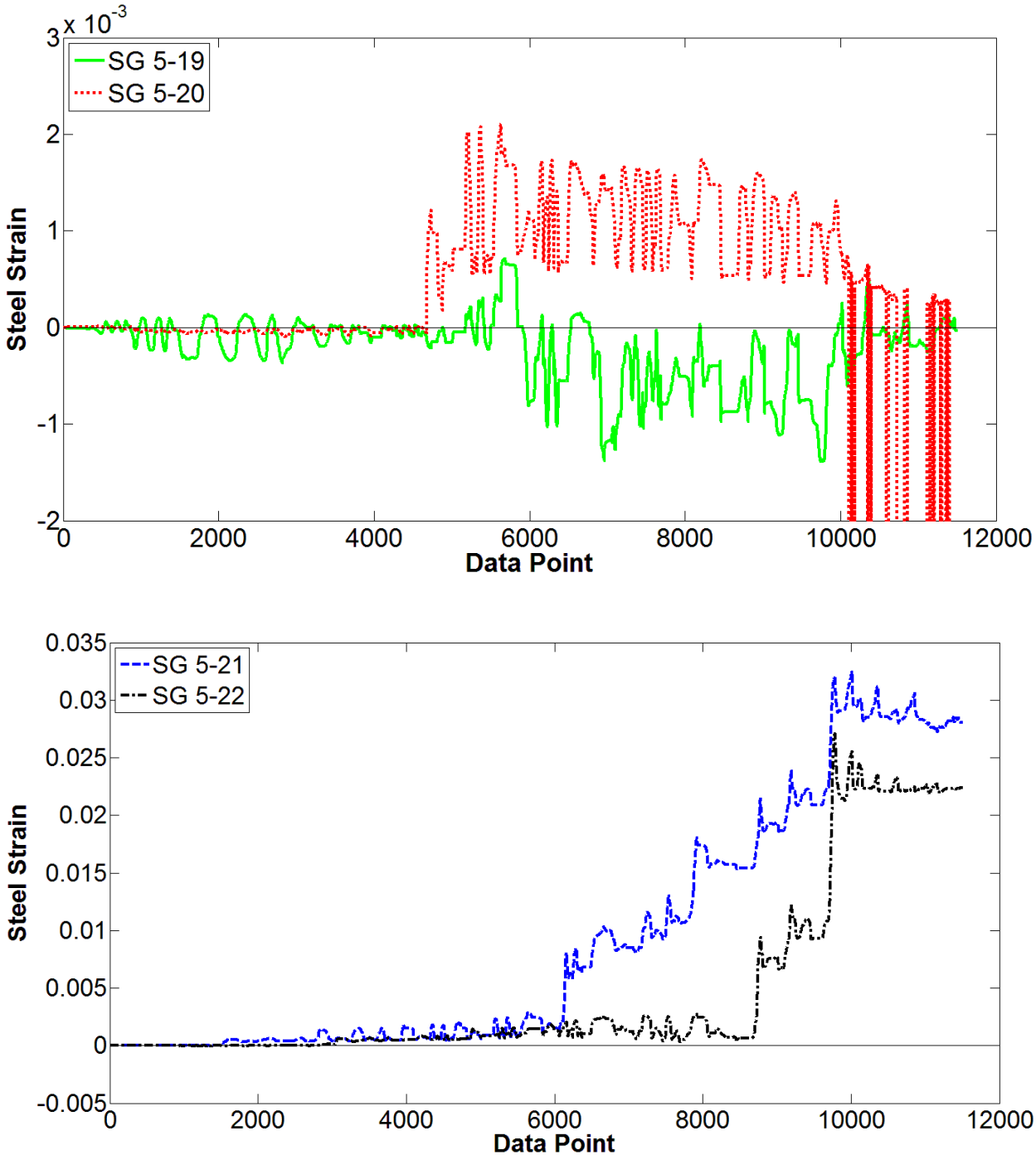

Figure B-31 RW-A15-P2.5-S64: Strain gage histories at web horizontal reinforcement

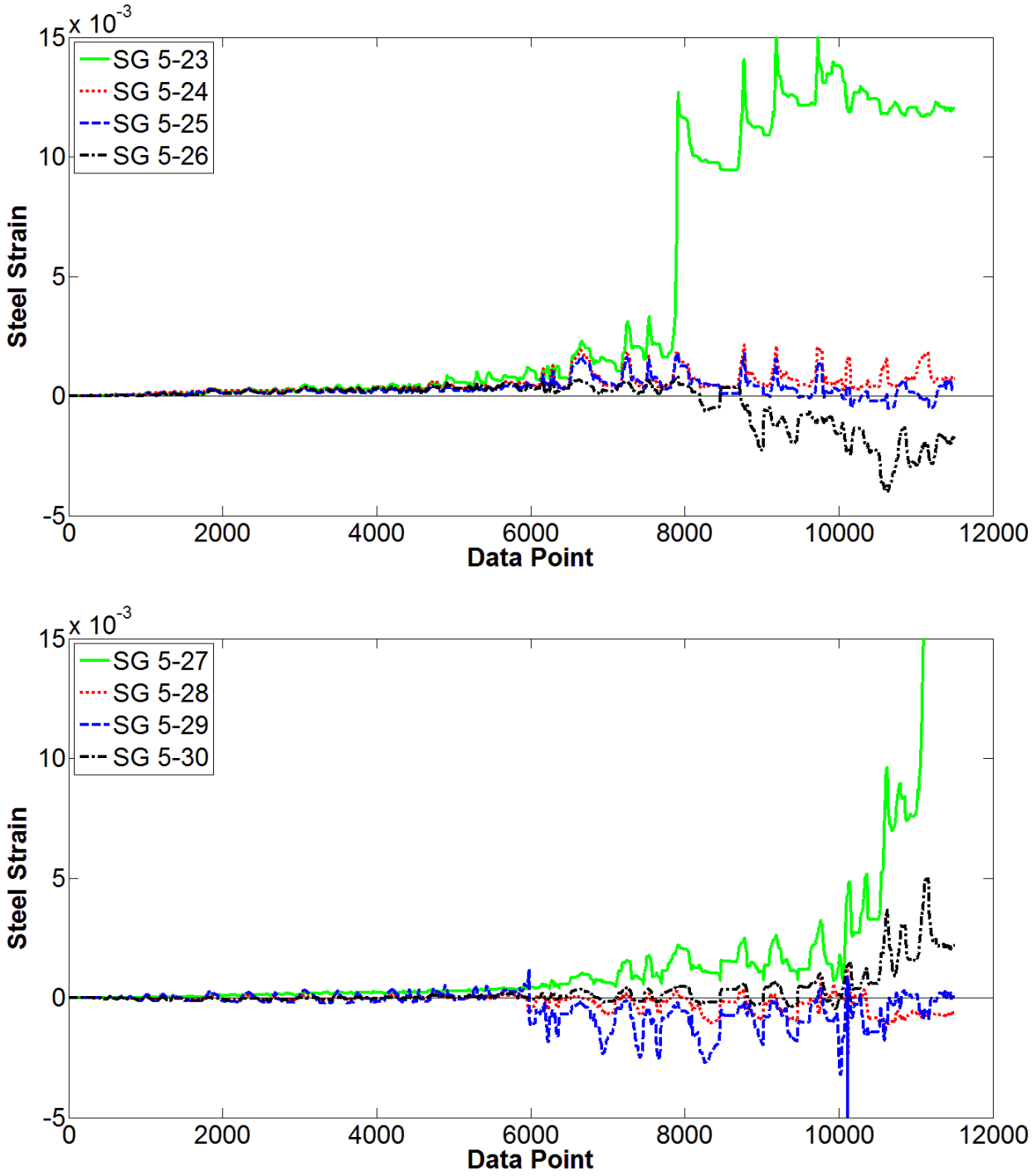

Figure B-32 RW-A15-P2.5-S64: Strain gage histories at boundary transverse reinforcement

B.3 Wall Top Rotation

The rotations at the top of five wall specimens, determined by two lines of LVDTs near the wall edges, i.e., sensors 1 to 16 for 2.0 aspect ratio walls and sensors 1 to 14 for 1.5 aspect ratio walls, are shown in Figures B-33 through B-37.

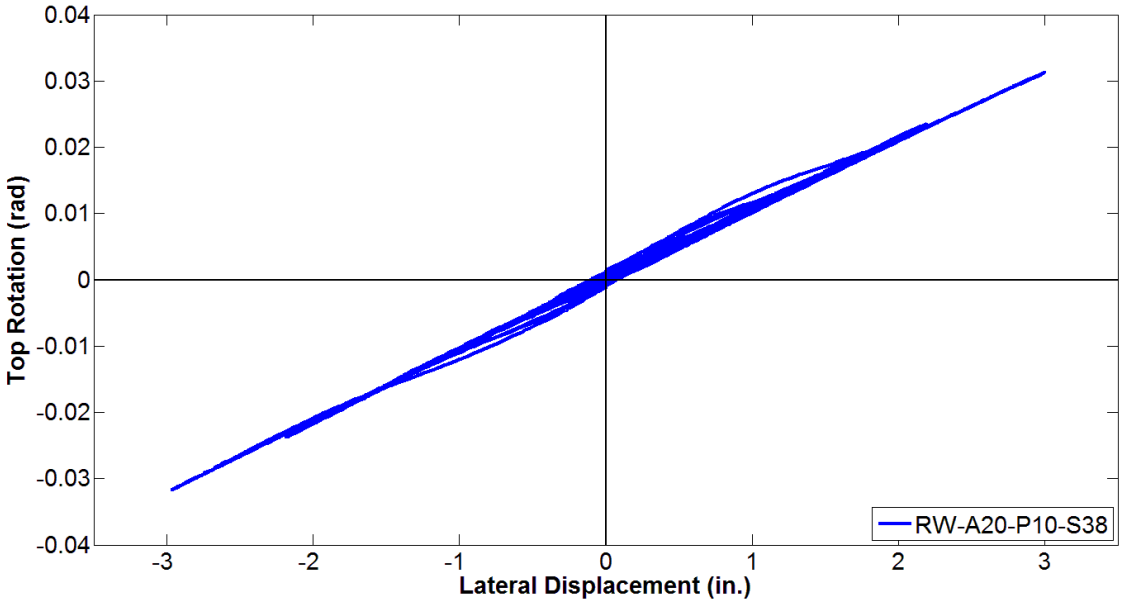

Figure B-33 Wall top rotation for Test 1, RW-A20-P10-S38

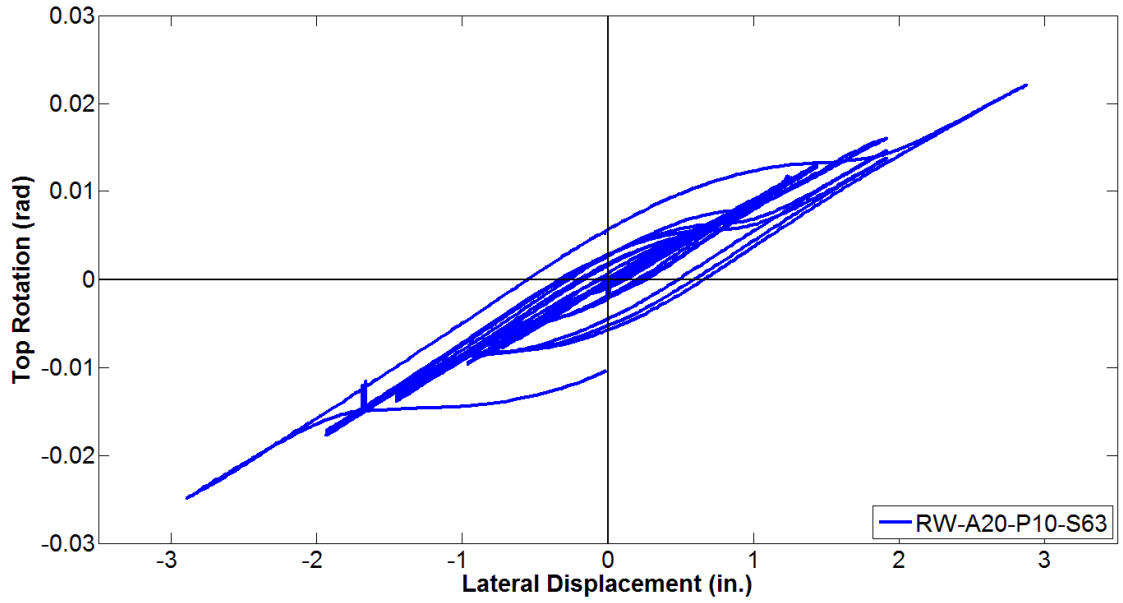

Figure B-34 Wall top rotation for Test 2, RW-A20-P10-S63

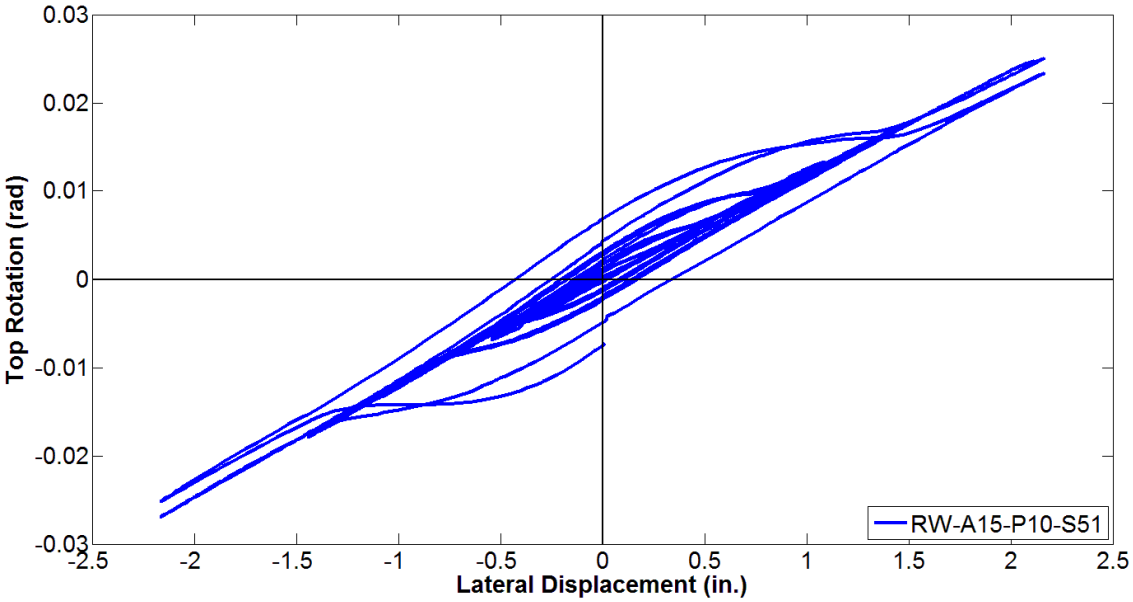

Figure B-35 Wall top rotation for Test 3, RW-A15-P10-S51

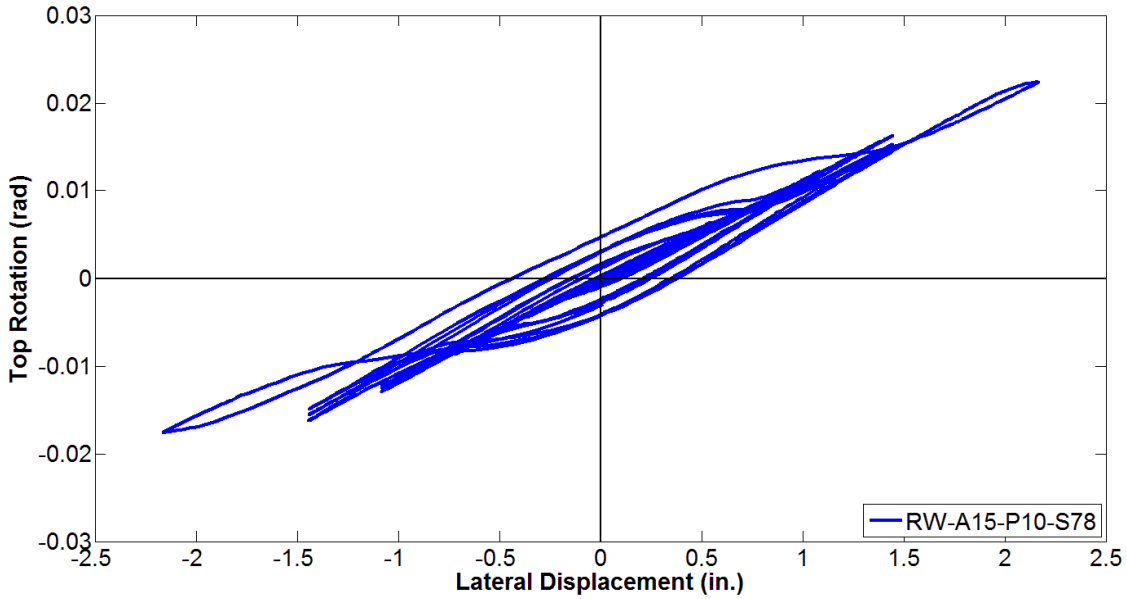

Figure B-36 Wall top rotation for Test 4, RW-A15-P10-S78

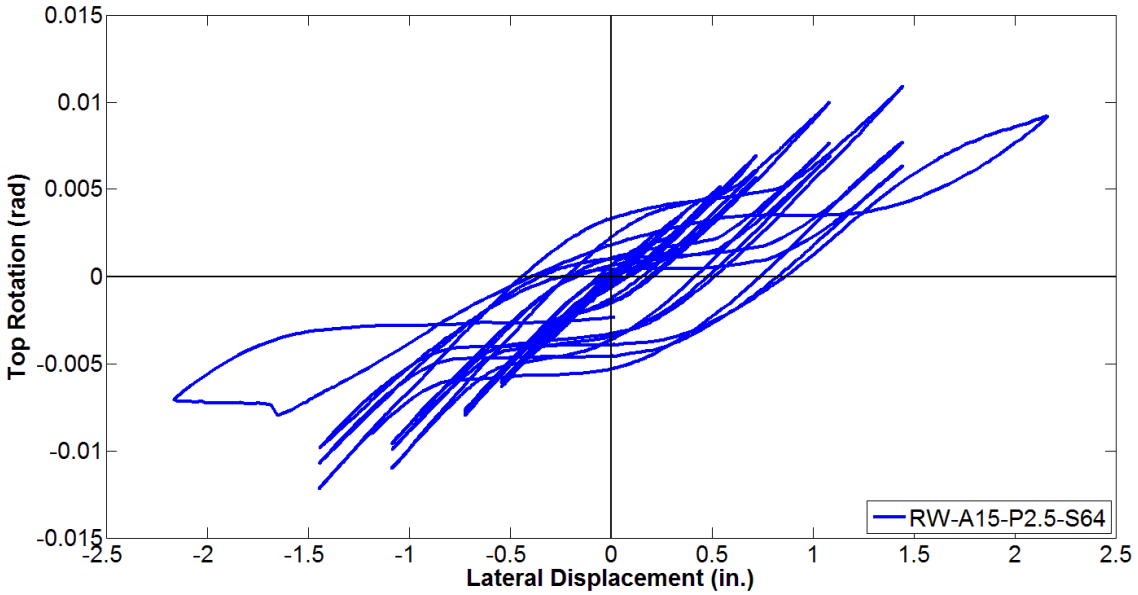

Figure B-37 Wall top rotation for Test 5, RW-A15-P2.5-S64

C. APPENDIX C MATERIALS-RELATED DATA

C.1 Mix Design for Concrete

Concrete placement for the foundation blocks took place on July 26th, 2010, while concrete for the wall sections was poured on December 7th, 2010. Tables C-1 and C-2 show the concrete mix for the foundation blocks and shear walls, respectively.

Table C-1 Concrete mix for the foundation blocks

MIX: GE50P5 — 5000 psi @ 28 Days. 3/8" Gravel Pump/Place Mix. 5 ± 1 Inches Slump.

GRADATIONS — with VULCAN , San Gabriel Valley (Relience) Aggregates.

Aggregates	2"	1 1/2"	1"	3/4"	1/2"	3/8"	#4	#8	#16	#30	#50	#100	#200
W.C. SAND						100	96	81	62	41	18	6	2
3/8 AGGR					100	92	10	4	2	0	0	0	0
COMBINED	100	100	100	100	100	97	66	54	41	27	12	4	1

Materials	BATCH WEIGHTS 1 CU YD @ SSD		SPECIFIC GRAVITY			ABSOLUTE VOLUME
CEMENT - TYPE II	689 lbs	8.62 equiv.	3.15	X	62.4	3.51
FLYASH	121 lbs		2.35	X	62.4	0.83
W.C. Sand	1696 lbs	65.0 %	2.66	X	62.4	10.22
3/8" G	909 lbs	35.0 %	2.65	X	62.4	5.5
WATER (MAXIMUM)	407.3 lbs	48.9 gals	1	X	62.4	6.53
WRDA 64	24.30 ozs					
1.5% ENTRAPPED AIR			1.50%	X	27	0.41
TOTALS	3822.3 lbs					27.0

METHOD: Uniform Building Code (UBC) 1905.3.3.2 and 2007 CBC Title 24 1905.3

WATER/CEMENT RATIO: 5.7 gals/sack (0.50)

STRENGTH RESULTS: 4375 psi @ 7 Days, 6745 psi @ 28 Days with Laboratory Prepared Cylinders.

Table C-2 Concrete mix for the shear walls

MIX: GE50P2S7 — 5000 psi @ 28 Days. 3/8" Gravel Pump/Place Mix. 7 ± 1 Inches Slump.

GRADATIONS — with VULCAN , San Gabriel Valley (Reliance) Aggregates.

Aggregates	2"	1 1/2"	1"	3/4"	1/2"	3/8"	#4	#8	#16	#30	#50	#100	#200
W.C. SAND						100	96	81	62	41	18	6	2
3/8 AGGR					100	92	10	4	2	0	0	0	0
COMBINED	100	100	100	100	100	97	66	54	41	27	12	4	1

Materials	BATCH WEIGHTS 1 CU YD @ SSD		SPECIFIC GRAVITY			ABSOLUTE VOLUME
CEMENT - TYPE II/V	689 lbs	8.62 equiv.	3.15	X	62.4	3.51
FLYASH	121 lbs		2.35	X	62.4	0.83
W.C. Sand	1789 lbs	65.0 %	2.66	X	62.4	10.78
3/8" G	959 lbs	35.0 %	2.65	X	62.4	5.8
WATER (MAXIMUM)	354.0 lbs	42.5 gals	1	X	62.4	5.67
WRDA 64	24.60 ozs					
GRACE ADVA SUP	32.40 ozs					
1.5% ENTRAPPED AIR			1.50%	X	27	0.41
TOTALS	3912 lbs					27.0

METHOD: California Building Code (CBC) Title 24 1905.3 - 2007 Edition

WATER/CEMENT RATIO: 4.9 gals/sack (0.44)

STRENGTH RESULTS: 4820 psi @ 7 Days, 6540 psi @ 28 Days with Laboratory Prepared Cylinders.

C.2 Stress-Strain Response of Concrete in Compression

For each wall specimen, three 6×12 in. (152×305 mm) concrete cylinders were tested in compression at the UCLA material testing laboratory at or closed to the test day. Stress-strain relations of concrete for all five shear walls are presented in Figures C-1 through C-5. For specimen RW-A20-P10-S38, the test data for cylinder No.3 was not reliable; therefore, only results from the first two cylinders were considered.

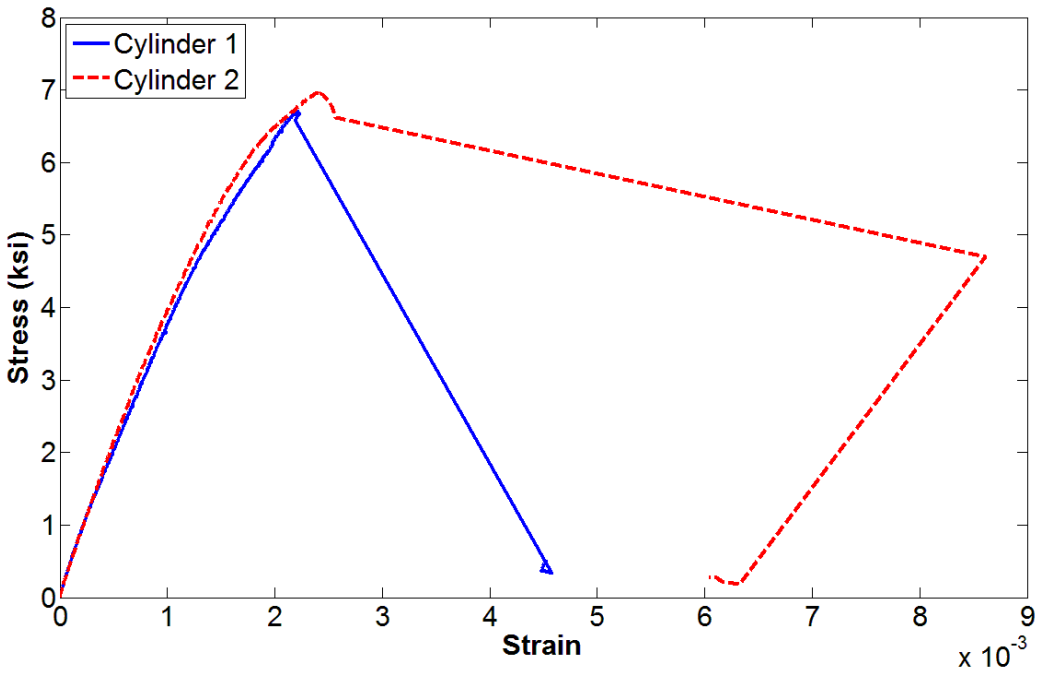

Figure C-1 Stress-strain relations of concrete in compression for RW-A20-P10-S38

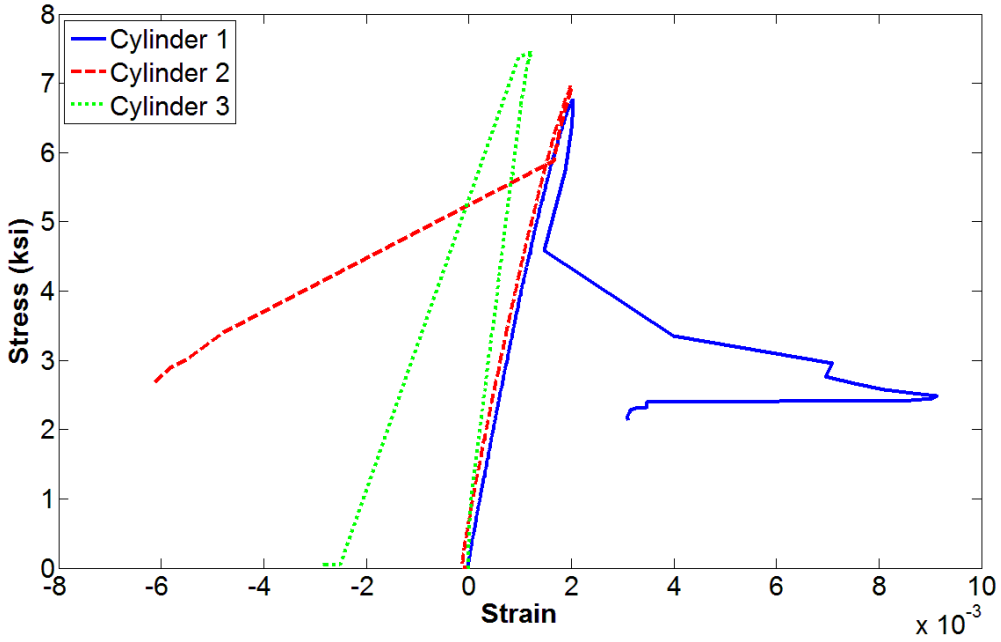

Figure C-2 Stress-strain relations of concrete in compression for RW-A20-P10-S63

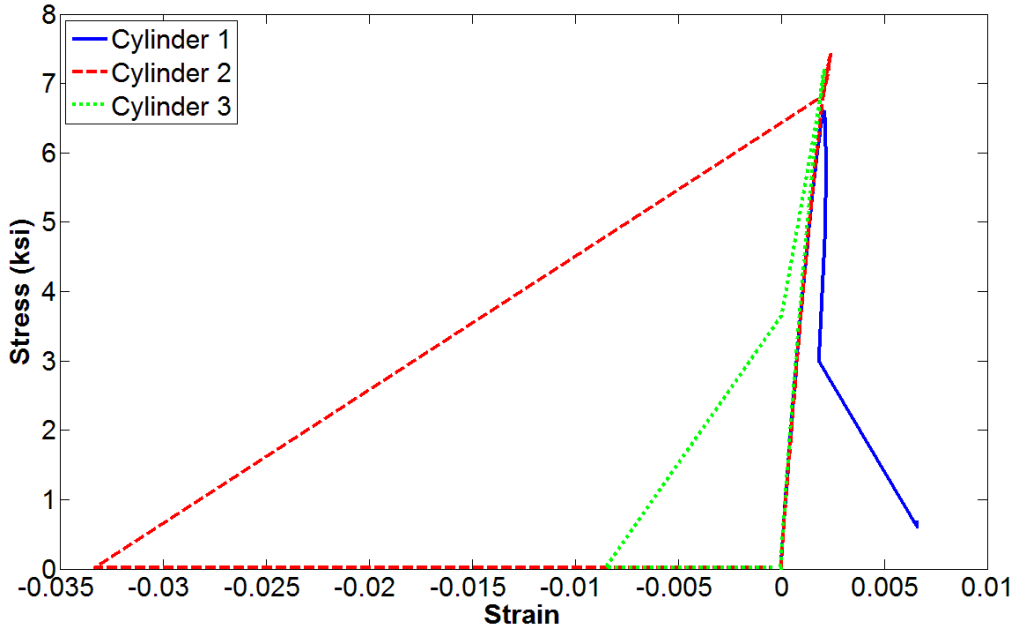

Figure C-3 Stress-strain relations of concrete in compression for RW-A15-P10-S51

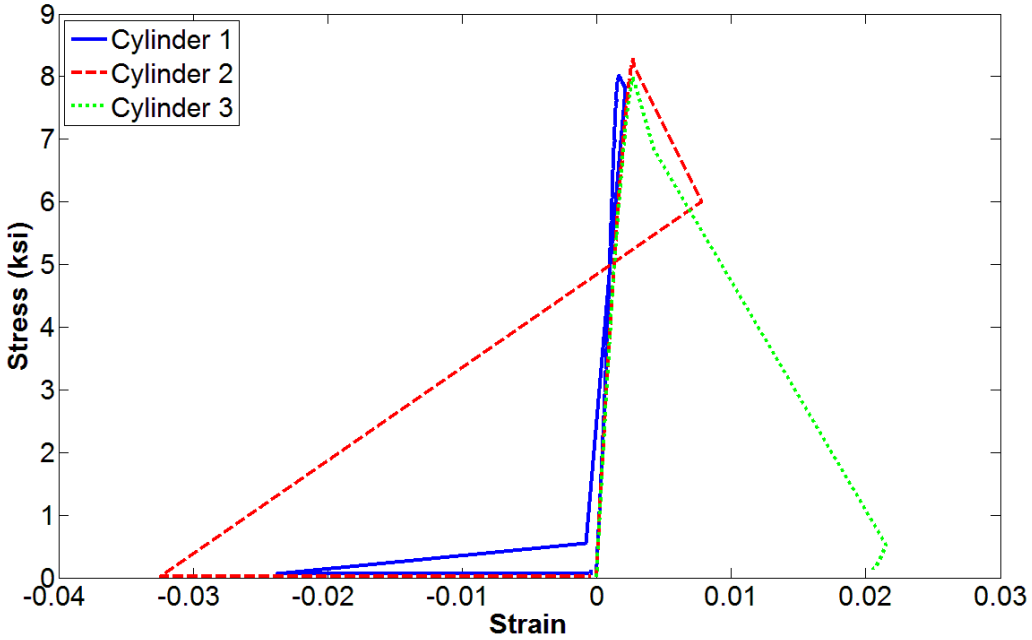

Figure C-4 Stress-strain relations of concrete in compression for RW-A15-P10-S78

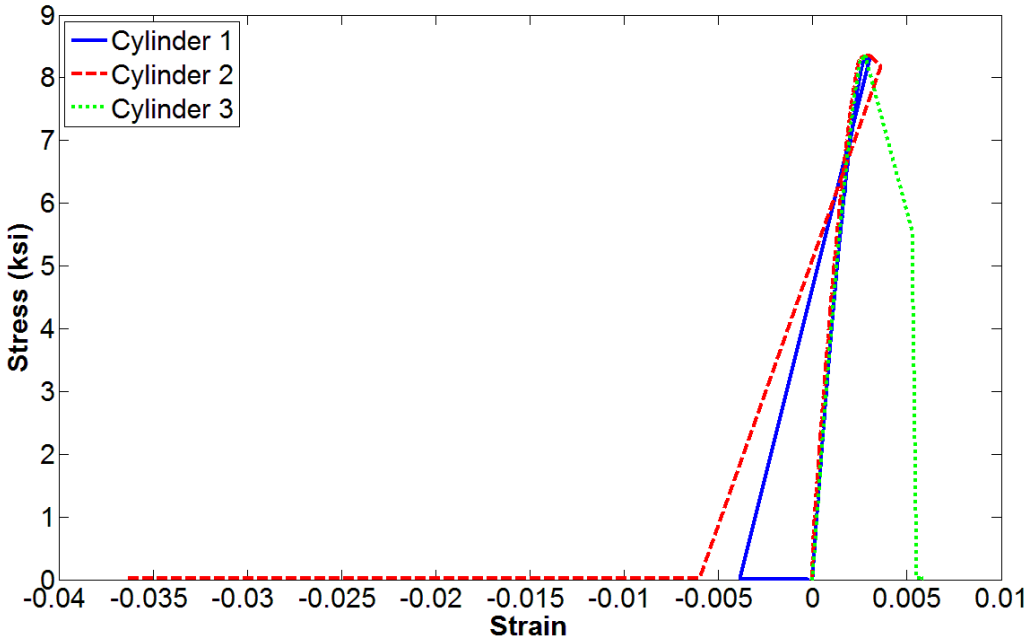

Figure C-5 Stress-strain relations of concrete in compression for RW-A15-P2.5-S64

The compressive strength and strain at peak stress, together with their average values, of all concrete cylinders are summarized in Table C-3.

Table C-3 Compressive strength and strain at peak stress of concrete at the day of testing

No	Specimen	Compressive strength ksi (MPa)	Average compressive strength ksi (MPa)	Strain at peak stress ($x10^3$)	Average strain at peak stress ($x10^3$)
Test 1	RW-A20-P10-S38	Cyl. 1: 6.70 (46.22) Cyl. 2: 6.95 (47.93) Cyl. 3: Unreliable	6.83 (47.1)	Cyl. 1: 2.212 Cyl. 2: 2.421 Cyl. 3: Unreliable	2.317
Test 2	RW-A20-P10-S64	Cyl. 1: 6.75 (46.57) Cyl. 2: 6.95 (47.95) Cyl. 3: 7.44 (51.33)	7.05 (48.6)	Cyl. 1: 2.030 Cyl. 2: 1.999 Cyl. 3: Unreliable	2.014
Test 3	RW-A15-P10-S51	Cyl. 1: 6.59 (45.46) Cyl. 2: 7.42 (51.15) Cyl. 3: 7.21 (49.71)	7.07 (48.8)	Cyl. 1: 2.110 Cyl. 2: 2.393 Cyl. 3: 2.103	2.202
Test 4	RW-A15-P10-S78	Cyl. 1: 8.01 (55.25) Cyl. 2: 8.27 (57.03) Cyl. 3: 7.98 (55.02)	8.09 (55.8)	Cyl. 1: 1.681 Cyl. 2: 2.704 Cyl. 3: 2.729	2.371
Test 5	RW-A15-P2.5-S65	Cyl. 1: 8.33 (57.44) Cyl. 2: 8.35 (57.54) Cyl. 3: 8.34 (57.49)	8.34 (57.5)	Cyl. 1: 3.029 Cyl. 2: 2.911 Cyl. 3: 2.795	2.912

C.3 Stress-Strain Response of Steel Bars

Stress-strain relations for #3 (0.375 in. or 9.5 mm), #2 (0.25 in. or 6.4 mm), D6a (6mm), and D6b (6mm) bars are presented in Figures C-6 to C-9, respectively. Due to an uncertainty about the relatively low ductility level of D6b deformed bars from Australia, eight rebar samples were tested to get accurate mechanical properties. For the remainder of rebars, from three to five samples were used for the tension test for each type of reinforcement.

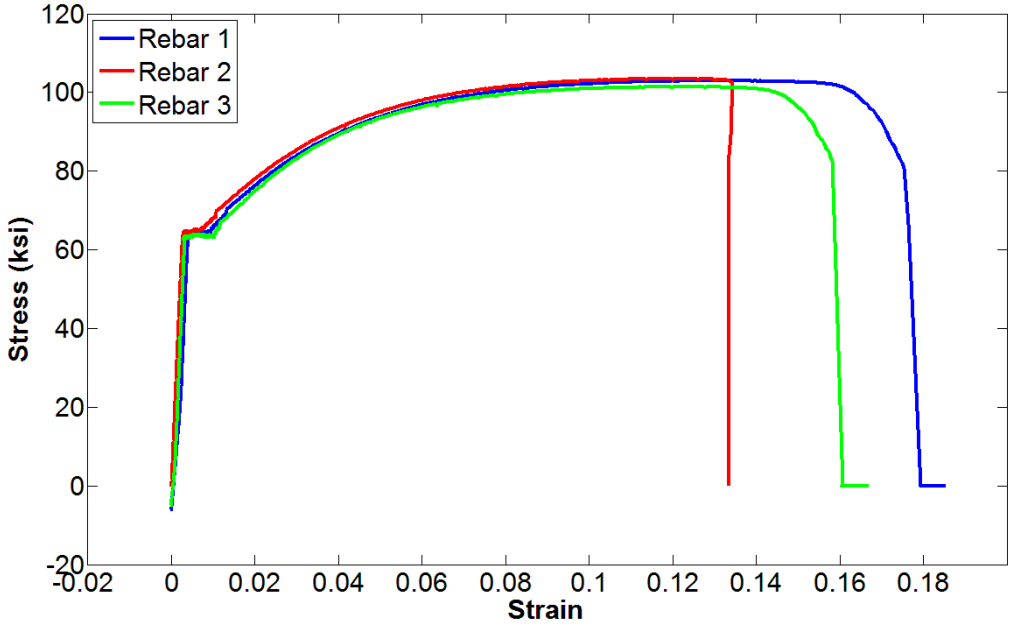

Figure C-6 Stress-strain relations of #3 bars

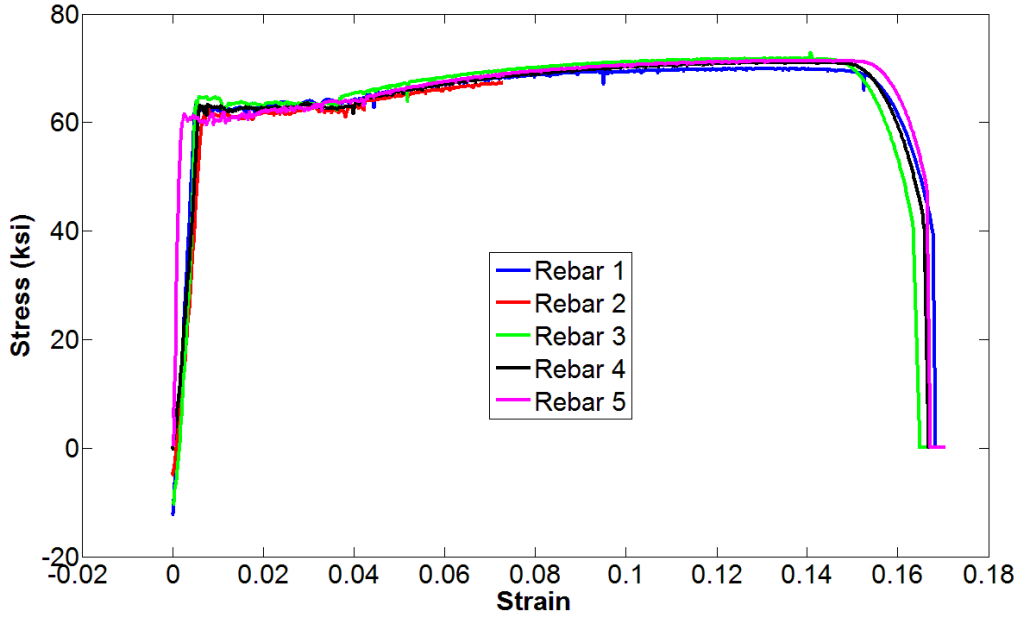

Figure C-7 Stress-strain relations of #2 bars

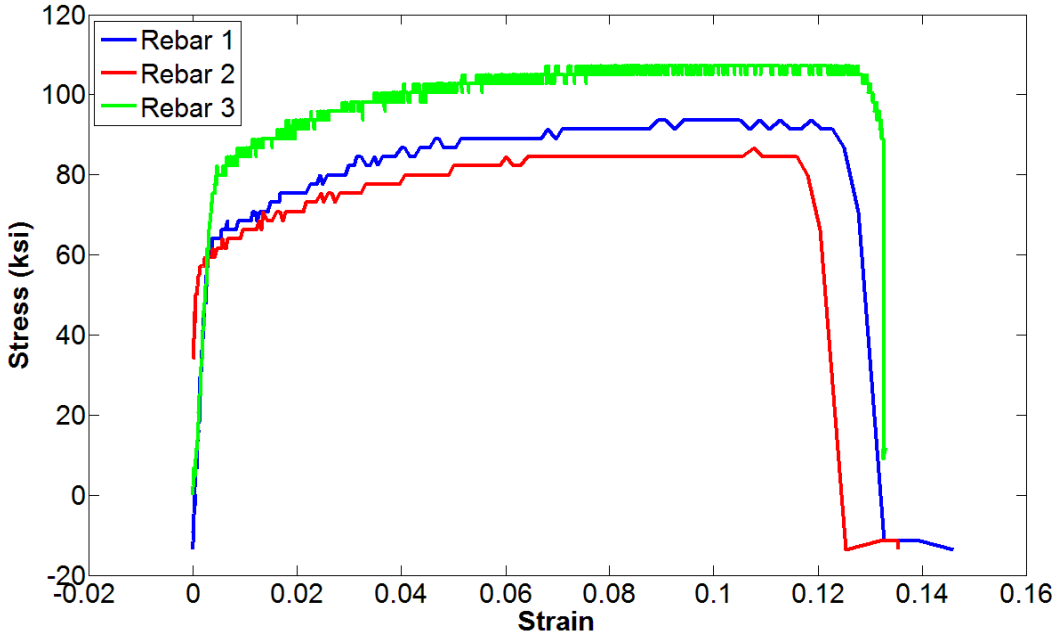

Figure C-8 Stress-strain relations of D6a bars

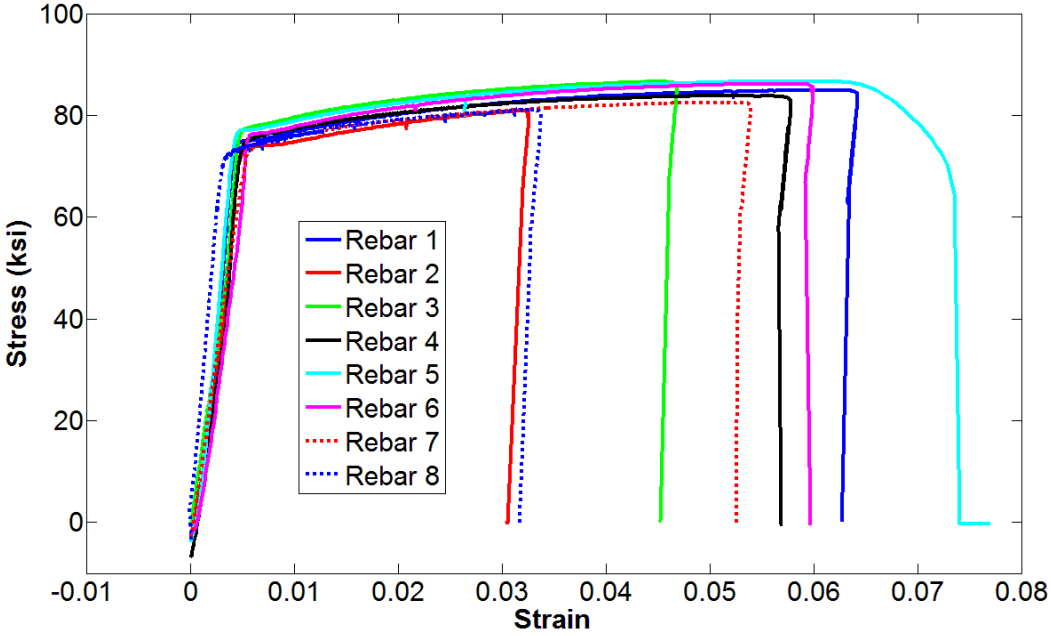

Figure C-9 Stress-strain relations of D6b bars

For headed bars, mill certificates were available; therefore, reinforcing steel strengths were specified without testing. Table C-4 provides typical mechanical properties of #4, #5, and #6 headed bars used in the test specimens.

Table C-4 Mechanical properties of headed bars

CMC Rebar

2755 South Willow Ave. Bloomington, CA 92316
Ph. (909)873-3060 Fax (909) 873-3020

Shipper Number : 095171
Customer Name : ERICO PRODUCTS INC
Job Number : BM099059
Job Name : ERICO MISC. ORDER
Releases : 00006

Material: REINFORCING STEEL

RECORD OF PHYSICAL AND CHEMICAL TEST REPORT

Mill Co.	Heat #	Size	Grade	C	MN	P	S	SI	CR	NI	CU	MO	V	CE	Yield	Tens	EL	BD
CMC Steel	4000346	4/13	A706	.20	.94	.008	.033	.200	.100	.140	.320	.040	.016	.380	68400	88900	19.0	OK
CMC Steel	4000109	5/16	A706	.27	1.06	.008	.017	.220	.090	.080	.280	.020	.028	.470	68700	89900	15.0	OK
CMC Steel	4000486	6/19	A706	.28	1.00	.013	.040	.220	.100	.080	.300	.010	.014	.470	69200	92400	18.0	OK

REFERENCES

1. ACI Committee 318 (1999). "Building Code Requirements for Structural Concrete (ACI 318-99) and Commentary (ACI 318R-99)," American Concrete Institute, Farmington Hills, Michigan, 391 pp.
2. ACI Committee 318 (2011). "Building Code Requirements for Structural Concrete (ACI 318-11) and Commentary (ACI 318R-11)," American Concrete Institute, Farmington Hills, Michigan, 503 pp.
3. Adebar, P.; Ibrahim, A. M. M.; and Bryson, M. (2007). "Test of High-Rise Core Wall - Effective Stiffness for Seismic Analysis," ACI Journal Proceedings, V. 104, Issue 5, pp. 549-559.
4. Ali, A. and Wight, J. K. (1990). "Reinforced Concrete Structural Walls with Staggered Opening Configurations under Reversed Cyclic Loading," Report No. UMCE 90-05, Department of Civil Engineering, University of Michigan, 241 pp.
5. Ali, A. and Wight, J. K. (1991). "Reinforced Concrete Structural Walls with Staggered Door Openings," Journal of Structural Engineering, ASCE, V. 117, No. 5, pp. 1514–1531.
6. American Society of Civil Engineers (2007). "ASCE/SEI Standard 41-06, Seismic Rehabilitation of Existing Buildings," Reston, Virginia, 411 pp.
7. Barda, F.; Hanson, J. M.; and Corley, W. G. (1977). "Shear Strength of Low-Rise Walls with Boundary Elements," ACI-SP53-08, American Concrete Institute, Farmington Hills, MI, pp. 149-202.

8. Belarbi, A. and Hsu, T. T. C. (1994). “Constitutive Laws of Concrete in Tension and Reinforcing Bars Stiffened by Concrete,” ACI Structural Journal, V. 91, No. 4, pp. 465-474.
9. Belarbi, A. and Hsu, T. T. C. (1995). “Constitutive Laws of Softened Concrete in Biaxial Tension-Compression,” ACI Structural Journal, V. 92, No. 5, pp. 562-573.
10. Beyer, K.; Dazio, A.; and Priestley, M. J. N. (2011). "Shear Deformations of Slender Reinforced Concrete Walls under Seismic Loading," ACI Structural Journal, V. 108, No. 2, pp. 167-177.
11. Birely, A.; Lehman, D.; Lowes, L.; Kuchma, D.; Hart, C.; and Marley, K. (2008). “Investigation of the Seismic Behavior and Analysis of Reinforced Concrete Structural Walls," Proceedings, 14th World Conference on Earthquake Engineering, Beijing, China, October 12-17, 2008.
12. Birely, A.; Lehman, D.; Lowes, L.; Kuchma, D.; Hart, C.; and Marley, K. (2010). “Investigation of the Seismic Response of Planar Concrete Walls,” Proceedings, Paper 773, 9th U.S. National Conference and 10th Canadian Conference on Earthquake Engineering, Ontario, Canada, July 25-29, 2010.
13. Brueggen, B. L. (2009). “Performance of T-shaped Reinforced Concrete Structural Walls under Multi-Directional Loading,” PhD Dissertation, Department of Civil Engineering, University of Minnesota, 498 pp.
14. Brueggen, B. L. and French, C. W. (2010). “Simplified Modeling of Non-Rectangular RC Structural Walls,” Proceedings, Paper 1713, 9th U.S. National Conference and 10th Canadian Conference on Earthquake Engineering, Ontario, Canada, July 25-29, 2010.
15. Cardenas, A. E.; Hanson, J. M.; Corley, W. G.; and Hognestad, E. (1973). "Design Provisions for Shear Walls," ACI Journal Proceedings. V. 70, Issue 3, pp. 221-230.

16. Chang, G. A. and Mander, J. B. (1994). “Seismic Energy Based Fatigue Damage Analysis of Bridge Columns: Part I - Evaluation of Seismic Capacity,” Technical Report No. NCEER–94–0006, State University of New York, Buffalo, New York.
17. Colotti, V. (1993). “Shear Behavior of RC Structural Walls,” Journal of Structural Engineering, ASCE, V. 119, No. 3, pp. 728-746.
18. Corley, W. G.; Fiorato, A. E.; and Oeserle, R. G. (1981). "Structural Walls," ACI Special Publication-72, American Concrete Institute, Farmington Hills, MI, 1981, pp. 77-131.
19. Dazio, A.; Beyer, K.; and Bachmann, H. (2009). "Quasi-static Cyclic Tests and Plastic Hinge Analysis of RC Structural Walls," Engineering Structures, V. 31, pp. 1556-1571.
20. Eberhard, M. O. and Meigs, B. E. (1995). “Earthquake-Resisting System Selection Statistics for Reinforced Concrete Buildings,” Earthquake Spectra, V. 11, No. 1, pp. 19-36.
21. Elwood, K. J. (2002). "Shake Table Tests and Analytical Studies on the Gravity Load Collapse of Reinforced Concrete Frames," PhD Dissertation, University of California, Berkeley, 419 pp.
22. Farvashany, F. E.; Foster, S. J.; and Rangan, B. V. (2008). "Strength and Deformation of High-Strength Concrete Shearwalls," ACI Structural Journal, V. 105, No. 1, pp. 21-29.
23. Federal Emergency Management Agency (2000). "Prestandard and Commentary for the Seismic Rehabilitation of Buildings (FEMA-356)," ASCE, 518 pp.
24. Filippou, F. C.; Popov, E. G.; and Bertero, V. V. (1983). “Effects of bond deterioration on hysteretic behavior of reinforced concrete joints,” EERC Report No. UCB/EERC–83/19, Earthquake Engineering Research Center, University of California, Berkeley, California.
25. Fischinger, M.; Vidic, T.; Selih, J.; Fajfar, P.; Zhang. H. Y.; and Damjanic, F.B. (1990). “Validation of a Macroscopic Model for Cyclic Response Prediction of RC Walls,” in N.B.

Bicanic and H. Mang (eds.), “Computer Aided Analysis and Design of Concrete Structures,” V. 2, Pineridge Press, Swansea, pp. 1131-1142.

26. Fischinger, M.; Vidic, T.; and Fajfar, P. (1992). “Nonlinear Seismic Analysis of Structural Walls Using the Multiple-Vertical-Line-Element Model,” in H. Krawinkler and P. Fajfar (eds.), “Nonlinear Seismic Analysis of RC Buildings,” Elsevier Science Publishers Ltd., London and New York, pp. 191-202.
27. Gupta, A. and Rangan, B. V. (1998). "High-Strength Concrete Structural Walls," ACI Structural Journal, V. 95, No. 2, pp. 194-203.
28. Hidalgo, P. A.; Ledezma, C. A.; and Jordan, R. M. (2002). "Seismic Behavior of Squat Reinforced Concrete Shear Walls," Earthquake Spectra, V. 18, No. 2, pp. 287–308.
29. Hiraishi, H. (1984). “Evaluation of Shear and Flexural Deformations of Flexural Type Shear Walls,” Bulletin of the New Zealand National Society for Earthquake Engineering, V. 17, No. 2, pp. 135-144.
30. Hsu, T. T. C. (1993). "Unified Theory of Reinforced Concrete," CRC Press Inc., Boca Raton, Fla., 336 pp.
31. Jiang, H. and Kurama, Y. C. (2010). "Analytical Modeling of Medium-Rise Reinforced Concrete Shear Walls," ACI Structural Journal, V. 107, No. 4, pp. 400-410.
32. Johnson, B. (2010). “Anchorage Detailing Effects on Lateral Deformation Components of R/C Shear Walls," MS Thesis, Department of Civil Engineering, University of Minnesota, 353 pp.
33. Kabeyasawa, T.; Shiohara, H.; Otani, S.; and Aoyama, H. (1983). “Analysis of the Full-scale Seven-story Reinforced Concrete Test Structure,” Journal of the Faculty of Engineering, University of Tokyo, V. 37, No. 2, pp. 432-478.

34. Kabeyasawa, T. (1997). “Design of RC Shear Walls in Hybrid Wall System,” Proceedings, Fourth Joint Technical Coordinating Committee, U.S.-Japan Cooperative Seismic Research on Composite and Hybrid Structures, Monterey, California.
35. Kabeyasawa, T. and Hiraishi, H. (1998). "Tests and Analyses of High-strength Reinforced Concrete Shear Walls in Japan," ACI-SP176-13, American Concrete Institute, Farmington Hills, MI, pp. 281-310.
36. Massone, L. M. and Wallace, J. W. (2004). "Load-Deformation Responses of Slender Reinforced Concrete Walls," ACI Structural Journal, V. 101, No. 1, pp. 103-113.
37. Massone, L. M. (2006). "RC Wall Shear-Flexure Interaction: Analytical and Experimental Responses," PhD Dissertation, Department of Civil and Environmental Engineering, University of California, Los Angeles, 398 pp.
38. Massone, L. M.; Orakcal, K.; and Wallace, J. W. (2006). “Modeling Flexural/Shear Interaction in RC Walls, ACI-SP-236, Deformation Capacity and Shear Strength of Reinforced Concrete Members under Cyclic Loadings," American Concrete Institute, Farmington Hills, MI, Paper 7, pp. 127-150.
39. Massone, L. M.; Orakcal, K.; and Wallace, J. W. (2009). “Modeling of Squat Structural Walls Controlled by Shear,” ACI Structural Journal, V. 106, No. 5, pp. 646-655.
40. Mazzoni, S.; McKenna, F.; Scott, M. H.; Fenves, G. L. (2007). "OpenSees Command Language Manual," The Regents of the University of California, 451 pp.
41. Menegotto, M. and Pinto, E. (1973). “Method of Analysis for Cyclically Loaded Reinforced Concrete Plane Frames Including Changes in Geometry and Non-Elastic Behavior of Elements under Combined Normal Force and Bending,” Proceedings, IABSE Symposium. Lisbon, Portugal.

42. Mickleborough, N. C.; Ning, F.; and Chan, C. (1999). "Prediction of Stiffness of Reinforced Concrete Shearwalls under Service Loads," ACI Structural Journal, V. 96, No. 6, pp. 1018-1026.
43. Ning, F. (1998). "Lateral Stiffness Characteristics of Tall Reinforced Concrete Buildings under Service Loads," PhD Dissertation, Hong Kong University of Science and Technology.
44. Oesterle, R. G.; Fiorato, A. E.; Johal, L. S.; Carpenter, J. E.; Russel, H. E.; and Corley, W. G. (1976). "Earthquake Resistant Structural Walls - Tests of Isolated Walls," Report to the National Science Foundation, Construction Technology Laboratories, Portland Cement Association, Skokie, IL., 315 pp.
45. Oesterle, R. G.; Aristizabal-Ochoa, J. D.; Fiorato, A. E.; Russel, H. E.; and Corley, W. G. (1979). "Earthquake Resistant Structural Walls - Tests of Isolated Walls - Phase II," Report to the National Science Foundation, Construction Technology Laboratories, Portland Cement Association, Skokie, IL., 325 pp.
46. "OpenSees - Open System for Earthquake Engineering Simulation", The Regents of the University of California.
47. Orakcal, K. (2004). "Nonlinear Modeling and Analysis of Slender Reinforced Concrete Walls," PhD Dissertation, Department of Civil and Environmental Engineering, University of California, Los Angeles, 224 pp.
48. Orakcal, K.; Conte, J. P.; and Wallace, J. W. (2004). "Flexural Modeling of Reinforced Concrete Structural Walls - Model Attributes," ACI Structural Journal, V. 101, No. 5, pp. 688-698.
49. Orakcal, K. and Wallace, J. W. (2006). "Flexural Modeling of Reinforced Concrete Walls - Experimental Verification," ACI Structural Journal, V. 103, No. 2, pp. 196-206.

50. Orakcal, K.; Massone, L. M.; and Wallace, J. W. (2006). “Analytical Modeling of Reinforced Concrete Walls for Predicting Flexural and Coupled-Shear-Flexural Responses,” PEER Report No. 2006/07, Pacific Earthquake Engineering Research Center, 213 pp.
51. Orakcal, K.; Massone, L. M.; and Wallace, J. W. (2009). "Shear Strength of Lightly Reinforced Wall Piers and Spandrels," ACI Structural Journal, V. 106, No. 4, pp. 455-465.
52. Palermo, D. and Vecchio, F. J. (2002). " Behavior of Three-Dimensional Reinforced Concrete Shear Walls," ACI Structural Journal, V. 99, No. 1, pp. 81-89.
53. Palermo, D. and Vecchio, F. J. (2003). "Compression Field Modeling of Reinforced Concrete Subjected to Reversed Loading: Formulation", ACI Structural Journal, V. 100, No. 5, pp. 616-625.
54. Pang, X. B. D. and Hsu, T. T. C. (1995). “Behavior of Reinforced Concrete Membrane Elements in Shear," ACI Structural Journal, V. 92, No. 6, pp. 665-679.
55. Paulay, T.; Priestley, M. J. N.; and Synge, A. J. (1982). "Ductility in Earthquake Resisting Squat Shearwalls," ACI Journal, July-August, 1982, pp. 257-269.
56. Petrangeli, M.; Pinto, P. E.; and Ciampi, V. (1999). “Fiber Element for Cyclic Bending and Shear of RC Structures. I: Theory,” Journal of Engineering Mechanics, ASCE, V. 125, No. 9, pp. 994-1001.
57. Petrangeli, M. (1999). “Fiber Element for Cyclic Bending and Shear of RC Structures. II: Verification,” Journal of Engineering Mechanics, ASCE, V. 125, No. 9, pp. 1002-1009.
58. Pilakoutas, K. and Elnashai, A. (1995). "Cyclic Behavior of Reinforced Concrete Cantilever Walls, Part I: Experimental Results," ACI Structural Journal, V. 92: No. 3, pp. 271-281.

59. Pilakoutas, K. and Elnashai, A. (1995). "Cyclic Behavior of Reinforced Concrete Cantilever Walls, Part II: Discussions and Theoretical Comparisons," ACI Structural Journal, V. 92: No. 4, pp. 425-433.

60. Popovics, S. (1973). "A Numerical Approach to the Complete Stress-Strain Curve of Concrete," Cement and Concrete Research, V. 3, No. 4, pp. 583-599.

61. Salonikios, T. N.; Kappos, A. J.; Tegos, I. A.; and Penelis, G. G. (1999). "Cyclic Load Behavior of Low-Slenderness Reinforced Concrete Walls: Design Basis and Test Results," ACI Structural Journal, V. 96: No. 4, pp. 649-660.

62. Salonikios, T. N.; Kappos, A. J., Tegos, I. A., and Penelis, G. G. (2000). "Cyclic Load Behavior of Low-Slenderness Reinforced Concrete Walls: Failure Modes, Strength and Deformation Analysis, and Design Implications," ACI Structural Journal, V. 97: No. 1, pp. 132-142.

63. Taylor, C. P.; Cote, P. A.; and Wallace, J. W. (1998). “Design of Slender Reinforced Concrete Walls with Openings.” ACI Structural Journal, V. 95, No. 4, pp. 420–433.

64. Thomsen, J. H. and Wallace, J. W. (1995). "Displacement-Based Design of RC Structural Walls - An Experimental Investigation of Walls with Rectangular and T-Shaped Cross-Sections". Report No. CU/CEE-95/06, Department of Civil Engineering, Clarkson University, Potsdam, New York, 353 pp.

65. Thomsen, J. H. and Wallace, J. W. (2004). "Displacement-Based Design Procedures for Slender Reinforced Concrete Structural Walls - Experimental Verification," Journal of Structural Engineering, ASCE, V. 130, No. 4, pp. 618-630.

66. Vecchio, F. J. and Collins, M. P. (1986). "The Modified Compression-Field Theory for Reinforced Concrete Elements Subjected to Shear," ACI Journal Proceedings, V. 83, Issue 2, pp. 219-231.

67. Vulcano, A. and Bertero, V. V. (1987). "Analytical Models for Predicting the Lateral Response of RC Shear Walls: Evaluation of Their Reliability," Report No. UCB/EERC-87/19, Earthquake Engineering Research Center, University of California, Berkeley.

68. Vulcano, A.; Bertero, V. V.; and Colotti, V. (1988). "Analytical Modeling of RC Structural Walls," Proceedings, 9th World Conference on Earthquake Engineering, V. 6, Tokyo-Kyoto, Japan, pp. 41-46.

69. Vulcano, A. (1992). "Macroscopic Modeling for Nonlinear Analysis of RC Structural Walls," in H. Krawinkler and P. Fajfar (eds.), "Nonlinear Seismic Analysis of RC Buildings," Elsevier Science Publishers Ltd., London and New York, pp. 181-190.

70. Wallace, J. W. (1994). "New Methodology for Seismic Design of RC Shear Walls," Journal of Structural Engineering, ASCE, V. 120, No. 3, pp. 863-884.

71. Wallace, J. W. (1995). "Seismic Design of RC Shear Walls. Part I: New Code Format," Journal of Structural Engineering, ASCE, V. 121, No. 1, pp. 75-87.

72. Wallace, J. W. and Thomsen, J. H. (1995). "Seismic Design of RC Shear Walls. Part II: Applications," Journal of Structural Engineering, ASCE, V. 121, No. 1, pp. 88-101.

73. Wallace, J. W. (2007). "Modeling Issues for Tall Reinforced Concrete Core Wall Buildings," The Structural Design of Tall and Special Buildings, Wiley InterScience, 16, pp. 615-632.

74. Wallace, J. W. (2012). "Behavior, Design, and Modeling of Structural Walls and Coupling Beams - Lessons from Recent Laboratory Tests and Earthquakes," International Journal of Concrete Structures and Materials, V. 6, No. 1, pp. 3-18.

75. Wight, J. K.; Wood, S. L.; Moehle, J. P.; and Wallace, J. W. (1996). “On Design Requirements for Reinforced Concrete Structural Walls,” ACI Special Publication-162, American Concrete Institute, Farmington Hills, MI, 1996, pp. 431-456.

76. Wood, S. L. (1990). "Shear Strength of Low-Rise Reinforced Concrete Walls," ACI Structural Journal, V. 87, No. 1, pp. 99-107.

77. Wood, S. L. and Sittipunt, C. (1996). “Cyclic Response of Reinforced Concrete Walls,” ACI Special Publication-162, American Concrete Institute, Farmington Hills, MI, 1996, pp. 399-429.

78. Zhang, Y. and Wang, Z. (2000). " Seismic Behavior of RC Shear Walls Subjected to High Axial Loading," ACI Structural Journal, V. 97, No. 5, pp. 739-750.